12-2018

Mesoscopic Organization and Dynamics in Structured Liquids

James Tyler Cosby
University of Tennessee

To the Graduate Council:

I am submitting herewith a dissertation written by James Tyler Cosby entitled "Mesoscopic Organization and Dynamics in Structured Liquids." I have examined the final electronic copy of this dissertation for form and content and recommend that it be accepted in partial fulfillment of the requirements for the degree of Doctor of Philosophy, with a major in Chemical Engineering.

Joshua R. Sangoro, Major Professor

We have read this dissertation and recommend its acceptance:

Roberto Benson, Bamin Khomami, Alexei Sokolov

Accepted for the Council:

Dixie L. Thompson

Vice Provost and Dean of the Graduate School

(Original signatures are on file with official student records.)

Mesoscopic Organization and Dynamics in Structured Liquids

A Dissertation Presented for the

Doctor of Philosophy

Degree

The University of Tennessee, Knoxville

James Tyler Cosby

December 2018

Dedicated to my parents, Kim and Alan Cosby, and my friends, Sean and Cassidy Britt, for their constant support and encouragement.

And the Scenes Gone By and the Scenes to Come flow
blending together in the sea-green deep while Now
spreads in circles on the surface.
—Ken Kesey, Sometimes a Great Notion

Acknowledgments

I am deeply indebted to my research advisor, Prof. Joshua Sangoro, without his patient guidance none of this would have been possible. Many of the experiments were conducted at Oak Ridge National Laboratory where Dr. Yangyang Wang was of immense help. I extend a heartfelt thanks to Prof. Katsuhiko Tsunashima for synthesizing a portion of the ionic liquids and to Utkarsh Kapoor and Prof. Jindal Shah for their detailed molecular dynamics simulations of the binary ionic liquid mixtures. I am grateful to the National Science Foundation, Army Research Office, and the GAANN research fellowship program for their monetary support. I would like to thank Profs. Bamin Khomami, Alexei Sokolov, and Roberto Benson for serving on my doctoral committee. I also appreciate the numerous doctoral students who have aided me along the way, Dr. Philip Griffin and Dr. Adam Holt for helping me get started, Dr. Maximilian Heres for being a constant companion in the lab, and Tom Kinsey, Stephanie Spittle, and postdoctoral researcher Dr. Emmanuel Mapesa for numerous discussions and their willingness to read this document. I have also had the pleasure of working with a number of outstanding undergraduate researchers, especially Zachariah Vicars, who was of considerable help in the analysis of dielectric data.

Abstract

An increasing number of liquids of both natural and technological importance are known to exhibit spatial and dynamic heterogeneity at the mesoscale due to specific non-covalent intermolecular interactions such as hydrogen-bonding, coulombic interactions, or solvophobic exclusion. However, there is little understanding as to how the organization and dynamics at the mesoscale influence the physical and chemical properties of the bulk liquids.

In this dissertation, two classes of materials, ionic liquids and imidazoles, are selected as case studies and investigated by a combination of experimental techniques which provide insight into the interplay of mesoscale organization, dynamics, and physicochemical properties. The mesoscale organization in these materials originates primarily from two different types of non-covalent interactions. For ionic liquids (ILs), this interaction is the solvophobic exclusion of extended aliphatic chains substituted on the cation from regions occupied by the polar ions. Here, new experimental signatures of mesoscale solvophobic aggregate dynamics are identified in the dielectric and dynamic-mechanical spectra. Using these signatures, it is found for instance, in phosphonium-based ionic liquids, that the formation of long-lived aggregates depends not only on the volume fraction of aliphatic groups, but also on the formation of a well-defined polar phase through strong coulombic interactions of the cation and anion charge centers. Finally, the ability to tune physicochemical properties, notably the static dielectric permittivity, by composition-dependent control of mesoscale aggregate morphology and dynamics in binary IL mixtures, is demonstrated. In imidazoles, the organization is driven by intermolecular hydrogen-bonds resulting in supramolecular chains of imidazole molecules. The existence of these chains is commonly believed to promote proton conductivity by a fast intermolecular proton transfer mechanism. A detailed analysis of neat 2-ethyl-4-methylimidazole and mixtures with minute amounts of levulinic acid and butyramide reveal an inverse relation between the average hydrogen-bonded chain length

and conductivity with no direct correlation between the static dielectric permittivity and proton conductivity. In addition, an unusual temperature dependence of static dielectric permittivity is attributed to the formation of antiparallel alignment of neighboring hydrogen-bonded chains, a degree of previously unrecognized mesoscale organization.

Table of Contents

List of Tables

List of Figures

Chapter 1

Introduction

1.1 Motivation

Strong noncovalent interactions in soft condensed matter give rise to correlations over lengthscales considerably longer than the dimensions of a single molecule.[28, 29, 30, 31, 32, 33] The noncovalent interactions which contribute to this long-range organization may arise from one or more classes of molecular forces including coulombic, hydrogen-bonding, halogen-bonding, dipole-dipole, van der Waals, π-bonding, and solvophobic effects.[34, 35] These correlations can lead to the emergence of random spatial heterogeneity or more organized hierarchical structures which pervade numerous classes of soft materials including proteins and nucleic acids, microphase-separated block copolymers and polymer blends, supramolecular gels and colloids, and aqueous surfactant solutions including microemulsions and worm-like surfactant micelles.[36, 37] The dimensions of these self-assembled structures typically lie between fifty and hundreds or thousands of nanometers, far larger than local molecular dimensions. Pure, single-component liquids, by comparison, have long been considered to be homogeneous, coherent, and essentially irregular.[38, 39] Within this framework, only very short-range correlations and the correspondingly fast molecular motions at those lengthscales are expected to influence the physical and chemical properties.[32] More recently however, we have begun to gain a greater appreciation that many liquids previously considered to be amorphous are in fact capable of forming intermediate correlations at the mesoscale, that is, at distances larger than the molecular dimensions, but smaller than the macroscopic lengthscales typical of the soft materials mentioned previously.[28, 29, 30,

31, 32, 33] Perhaps the most familiar example is the ability for intermolecular hydrogen-bonding to give rise to supramolecular hydrogen-bonded networks. The organization and orientation of molecules within the mesostructure as well as the overall mesoscale and macroscopic dynamics, are thought to play significant roles in determining the physicochemical properties of these complex liquids.[40, 24, 41, 42] However, a fundamental understanding of the impact of these intermediate range correlations on the physicochemical properties is still lacking. Elucidating the influence of these correlations on the physicochemical properties of soft materials, therefore, requires investigations over very broad time- and lengthscales. In this dissertation, two classes of materials are selected as case studies to further elucidate the interplay of mesoscale organization and dynamics, namely, (i) Ionic Liquids, and (ii) Imidazoles.

Ionic liquids (ILs) are a special category of complex fluids comprised entirely of ions and conventionally characterized by melting points below 100 °C.[43, 44, 45, 46] Due to their unique features such as low vapor pressures, wide liquidus ranges, high thermal stability, tunability, high ionic conductivity and wide electrochemical stability windows, they are under investigation for use as potential electrolytes in safe, high efficiency batteries, fuel cells, and super-capacitors.[47, 48, 49, 50, 51] A key advantage of ILs is the large variety of cations and anions available, providing a possibility to design billions of chemically distinct materials with desirable properties for different uses.[52] This vast number of chemical structures necessitates the development of structure-property relationships to aid in the design and synthesis of each new ionic liquid. This challenging task is further complicated by the mounting experimental evidence that many ionic liquids exhibit pronounced organization at the mesoscale.[32] This organization arises from the solvophobic segregation of non-polar aliphatic groups attached to the ions which leads to the formation of mesoscale aggregates characterized by the existence of distinct polar and non-polar domains.[13, 53, 54, 15, 55, 56] A potential advantage of the mesoscale organization is that it can impart special characteristics on the IL which improve performance and suitability for certain applications such as polymerization, organic synthesis and catalysis, as well as nanoparticle growth.[32, 57, 58, 59, 60, 61, 62, 63] However, a fundamental understanding of the impact of structural organization at the mesoscale on charge transport and dynamics in ILs necessary to formulate rational design strategies is still lacking. *How long-lived are these mesoscopic aggregates and how do they influence the physicochemical properties of ILs?* To address these questions,

we have employed experimental techniques which can probe detailed signatures of the mesoscale aggregates and their dynamics over much broader timescales.

Imidazoles are a unique class of hydrogen-bonded liquids capable of forming at least two intermolecular hydrogen-bonds (H-bonds) per molecule.[6, 8, 7] These bonds give rise to three-dimensional hydrogen-bonded networks which are expected to significantly alter their mechanical and transport properties. In bulk, liquid imidazoles and low concentration acid solutions as well as certain other liquids such as water, phosphoric acid, triazole and pyrazole, proton transport is hypothesized to occur, at least in part, via a Grotthuss-type mechanism in which protons are shuttled along the network at rates faster than molecular diffusion.[64, 65, 66, 67] Understanding the mechanisms of proton-transport in amorphous materials is crucial for numerous applications ranging from proton-exchange membranes to biological processes. The intrinsically proton-conducting liquid imidazoles, which form linear, H-bonded chains, provide a new and unique opportunity to probe the influence of H-bonded networks on proton conduction. A fundamental understanding of how the existence of these H-bonded chains influence proton transport in neat as well as acid-doped liquid imidazoles remains elusive. *How does temperature and acid concentration influence the imidazole hydrogen-bonded network and in turn how does the network influence proton transport?* To address these questions, we have utilized experimental techniques capable of probing dynamic signatures of the H-bonded chains as well as other complimentary techniques.[68]

This dissertation seeks to address the following fundamental questions:

1. How do the chemical structures of ionic liquids alter organization and dynamics at the mesoscale?

2. In turn, how do changes to the mesoscale organization and dynamics alter the physical and chemical properties of ionic liquids?

3. What design strategies can be formulated which allow the physicochemical properties of ionic liquids to be tuned via control of mesoscale aggregate morphology and dynamics?

4. How do temperature, chemical structure, and acid concentration influence the size and dynamics of mesoscale hydrogen-bonded chains in liquid imidazoles?

5. What is the influence of the size and dynamics of mesoscale hydrogen-bonded chains on proton transport in liquid imidazoles?

The overarching goal of this research is to develop a fundamental basis for the rational design of novel, safe, efficient, and environmentally benign electrolytes for current and future energy technologies. The central emphasis is on obtaining an understanding of the correlation between the chemical structure, mesoscopic organization, and dynamics and how these relationships determine the physicochemical and electrochemical properties of non-aqueous electrolytes. We investigate how the remarkable properties of matter emerge from complex correlations of atomic and molecular constituents and how we can control these properties to engineer more efficient electrolytes.

1.2 Outline

This dissertation is organized in the following manner. First, an overview of the relevant experimental methods is provided. In the following two chapters, the results of the case studies are presented starting with the ionic liquids and then the imidazoles. Finally, a brief summary of the results is given redressing the fundamental scientific questions outlined above, followed by a discussion of the future outlook for these researches.

Chapter 2 introduces the relevant experimental methods. These methods include broadband dielectric spectroscopy, dynamic mechanical spectroscopy, differential scanning calorimetry, Fourier transform infrared spectroscopy, and x-ray scattering. The modes of operation and the application of these methods to our studies of mesoscale organization and dynamics are discussed.

Chapter 3 presents the results of our case study on ionic liquids. In section 3.2, we highlight the discovery of new experimental signatures of mesoscale aggregate dynamics in the broadband dielectric and dynamic mechanical spectra of imidazolium ionic liquids. Following this, we employ binary ionic liquid mixtures as a strategy for tuning the mesoscale aggregate morphology and dynamics. It is found that the control of morphology and dynamics leads to a 100% increase in the static dielectric permittivities, ε_s, otherwise known as "dielectric constant". Therefore, a strategy emerges whereby ε_s can be enhanced by simply mixing two ILs with low intrinsic static permittivities. In section 3.4, our investigation is extended to quaternary phosphonium-based ionic liquids. In these systems it is found that long-lived mesoscale aggregation is not linked directly

to the volume fraction of aliphatic groups but is sensitive to the overall chemical structure and perhaps especially to strong interactions within the polar ionic domain. Afterwards, in section 3.5 the influence of anion chemical structure on charge transport and dynamics in a series of quaternary phosphonium ILs is investigated.

Chapter 4 turns to hydrogen-bonded liquids and our case study on imidazoles. Here we show that the addition of very small amounts of levulinic acid cause the disruption of mesoscale hydrogen-bonded imidazole chains. In addition, the temperature and composition-dependent trends in the static dielectric permittivities and mesoscale relaxation dynamics indicate that imidazoles have a unique mesoscale organization characterized by an antiparallel alignment of neighboring mesoscale hydrogen-bonded chains. It is suggested that the potential for π-bonding between imidazole heterocycles may contribute to such organization. The lack of correlation between dc ionic conductivity, hydrogen-bonded chain length, and static dielectric permittivity suggests that the hydrogen-bonded chains may not play a significant role in the conduction of protons in liquid imidazoles.

Chapter 5 presents a brief summary of the results of the two case studies. The fundamental scientific questions posed in the introduction are addressed. The future outlook of this research direction is discussed.

Chapter 2

Experimental Methods

In this chapter, the following experimental techniques are discussed: (i) broadband dielectric spectroscopy, (ii) dynamic mechanical spectroscopy, (iii) differential scanning calorimetry, (iv) Fourier transform infrared spectroscopy and (v) small-angle x-ray scattering. The broadband dielectric and dynamic mechanical spectroscopies as well as differential scanning calorimetry provide complementary insight into the dynamics at mesoscopic and more local lengthscales. Fourier transform infrared spectroscopy is utilized as a sensitive probe of the local environment in hydrogen-bonded networks. Small-angle x-ray scattering is utilized to investigate the mesoscale aggregate morphologies in solvophobically-aggregating ionic liquids.

2.1 Broadband Dielectric Spectroscopy

The history of dielectric spectroscopy begins with the pioneering experiments of Michael Faraday (1791-1867) and the earlier, but long unpublished, work of Henry Cavendish (1731-1810).[69, 70] With regards to dielectric spectroscopy, a significant accomplishment of these two men was the realization that the amount of charge, q, stored within a Leyden jar (an early capacitor) at a constant applied voltage, V, is dependent upon the type of insulating material placed between the conducting plates. The ratio of charge stored to applied voltage is known as capacitance, $C = q/V$. Faraday referred to the intrinsic ability for a material to store electrical energy as its specific inductive capacity defined as the ratio of the material's capacitance, C, to the capacitance of a reference, C_0, in the same capacitor geometry. Today, this is termed the relative dielectric permittivity, $\varepsilon = C/C_0$.

The values of relative permittivity are dependent on the reference material used for C_0. Cavendish utilized a series of specially made glass plates, Faraday utilized an empty capacitor, and today we use the capacitance of a vacuum.

In the course of his experiments, Faraday became convinced that the inductive effects he observed were not due to the motion of some electric substance, a popular opinion at the time, but rather were caused by the action of contiguous particles within the insulating material itself. This perceived ability for insulating materials to transmit electrical energy is the origin of the word dielectric; a combination of the Greek "dia-" meaning "through" and "elektra-" referring to electricity.[1] His inability to experimentally isolate an electric substance, Faraday wrote, "dwelt on my mind, and made me wish and search for a clearer view than any that I was acquainted with, of the way in which electrical powers and the particles of matter are related; especially in inductive actions, upon which almost all others appeared to rest."[69] His desire to understand how "electrical powers and particles of matter are related" has continued to be a primary motivation for generations of dielectric spectroscopists. However, before this understanding could develop, a more fundamental theory of electric phenomena was required.

Luckily, the wait was short. Just as Faraday was finishing his career, James Clerk-Maxwell took up the reins and, building upon Faraday's enormous quantity of experimental results, developed a succinct theory which accounts not only for observations of electric, but also magnetic and light phenomena in his unified electromagnetic theory. This theory may be briefly stated in the form of four equations:

$$\nabla \cdot \mathbf{B} = 0 \tag{2.1}$$

$$\nabla \times \mathbf{E} = -\frac{\partial}{\partial t}\mathbf{B} \tag{2.2}$$

$$\nabla \cdot \mathbf{D} = \rho_e \tag{2.3}$$

$$\nabla \times \mathbf{H} = \vec{j} + \frac{\partial}{\partial t}\mathbf{D} \tag{2.4}$$

where $\mathbf{H}$ and $\mathbf{E}$ are the magnetic and electric fields, $\mathbf{B}$ the magnetic induction, $\mathbf{D}$ the dielectric displacement, $\vec{j}$ the electric current, and ρ_e the charge density. The dielectric displacement, $\mathbf{D}$, is

[1] Coined by William Whewell in an 1837 letter to Faraday.[71] Whewell also originated the terms scientist and physicist in an 1840 letter, however Faraday felt physicist would never catch on due to the three consecutive ess sounds being "too much."

the key concept which encapsulates the influence of an applied electric field on matter. It arises from the displacement of free and bound charges on the electrode surfaces and within the dielectric and is directly proportional to the dielectric permittivity, $\mathbf{D} = \varepsilon^* \varepsilon_0 \mathbf{E}$. The polarization, $\mathbf{P}$, is the portion of dielectric displacement which arises solely from the motion of charges within the dielectric itself. It is defined as the difference of dielectric displacement in a filled and empty capacitor:

$$\mathbf{P} = \mathbf{D} - \boldsymbol{D_0} = \varepsilon^* \varepsilon_0 \mathbf{E} - \varepsilon_0 \mathbf{E} = (\varepsilon^* - 1)\varepsilon_0 \mathbf{E} \tag{2.5}$$

Studying the microscopic origin of polarization and utilizing it to obtain useful information concerning the dielectric material under study is the purview of dielectric spectroscopy. In general, this is accomplished by making careful measurements of the complex relative dielectric permittivity, $\varepsilon^* = \varepsilon' - i\varepsilon''$, while systematically varying the chemical structure of the dielectric and correlating/attributing changes in the dielectric spectrum to changes in polarization arising from the modified chemical structure.

A major accomplishment of Maxwell's theory is the identification of light as an electromagnetic wave. As a result, one prediction which emerged is that permittivity should equal the square of the index of refraction, $\varepsilon' = n^2$.[2] As physicists began testing this prediction, they noticed strong discrepancies when measuring the permittivities of liquids at low frequencies using the frequency-dependent ac-fields developed by Heinrich Hertz. The finding that the dielectric response is strongly frequency dependent precipitated the first real efforts into elucidating the different molecular origins of dielectric polarization and led to the development of theories which continue to illuminate the discussion and interpretation of dielectric spectra to this day.

Prior to introducing these theories, it will be beneficial to introduce how a dielectric experiment may actually be accomplished. That is, how do we measure the dielectric permittivity? There are several measurement methods, each applicable to a certain E-field frequency range. For the sake of brevity we will focus on the method employed in our lab and utilized to obtain the dielectric spectra presented in this dissertation.

The primary dielectric spectrometer in our lab is a Novocontrol High Resolution α-analyzer which combines several measurement capabilities in one integrated dielectric analyzer to allow for precise measurement of samples with broadly varying impedances over the widest possible

Figure 2.1: Novocontrol High Resolution α-analyzer. The sample capacitor is at the bottom of the metal apparatus on the right. The dielectric analyzer is on the left.

frequency range, see Figure 2.1. Using this instrument, and a Quatro temperature control system, the complex dielectric permittivity may be measured over a frequency range of $10^{-6} - 10^{7}$ Hz and temperature range $-160\,°\mathrm{C} - 400\,°\mathrm{C}$. A diagram of the simplest measurement circuit is illustrated in Figure 2.2. The sample is placed between two metal electrodes to form a simple capacitor. A frequency-dependent voltage, $U^*(\omega)$ is then applied to this capacitor and the resultant current is measured. The ratio of the applied voltage and measured current is the complex impedance, $Z^*(\omega) = U^*(\omega)/I^*(\omega)$, which is related to the inverse of complex capacitance by $Z^*(\omega) = \frac{1}{i\omega C^*(\omega)}$. We may then obtain the complex dielectric permittivity by the previously given definition, $\varepsilon^*(\omega) = \frac{C^*(\omega)}{C_0}$, where C_0 is the vacuum capacitance of the given capacitor geometry.

This simple apparatus is modified in modern instruments by the addition of dielectric converters consisting of a variable resistor and electrometer amplifier with variable gain for measurement of a sample voltage rather than a current and the use of reference capacitors in parallel with the sample capacitor. The combined effect being a significant increase in accuracy and reduction of noise giving the ability to measure the loss angle, $\tan\delta = \varepsilon''/\varepsilon'$, with an accuracy better than 10^{-4}.

Upon application of an electric field, the charges contained within a dielectric may be displaced, producing a polarization, **P**. This polarization is dependent on the frequency of the applied electric field, with different mechanisms contributing at different frequencies. Within our current understanding of the basic building blocks of matter, i.e. elementary particles, atoms, and molecules, the fundamental frequency-dependent mechanisms of polarization may be defined, as illustrated in Figure 2.3.[1, 72] Starting at the highest frequencies (shortest times), the electric

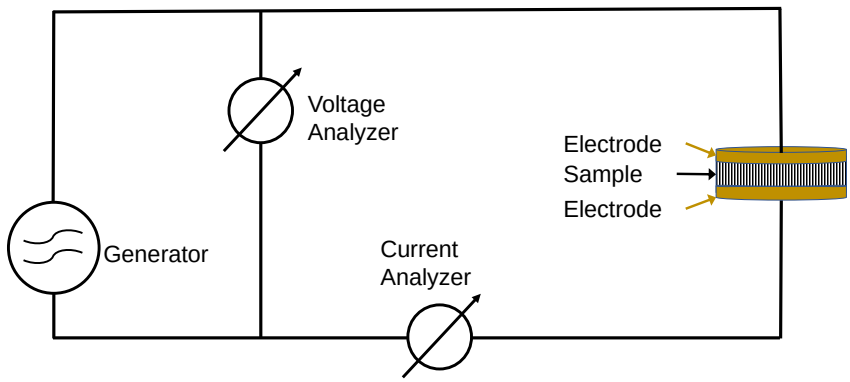

Figure 2.2: Illustration of a simplified dielectric spectroscopy measurement apparatus. The sample is placed between two metallic electrodes, a frequency-dependent potential is applied, and the resultant current is measured. The complex dielectric permittivity is then obtained as $\varepsilon^*(\omega) = \frac{C^*(\omega)}{C_0} = \frac{1}{i\omega Z^*(\omega)} = \frac{I^*}{i\omega U^* C_0}$.

field displaces electrons relative to the atomic nuclei resulting in induced dipole moments. This is termed *electronic polarization*. Following this, at lower frequencies, atoms within a molecule or crystal lattice are displaced relative to one another creating an *atomic polarization*. In addition, to these *induced* dipole moments many molecules contain regions of higher or lower electron densities and therefore form *permanent* molecular dipoles with a dipole moment μ defined as charge q multiplied by their separation distance d. These dipoles may be reoriented within the electric field creating *orientational* or *dipolar polarization*. When the dielectric contains ions two additional polarizations occur. The first is *ion-hopping polarization*, the translational hopping of charged ions which can lead to long-range ion diffusion. The second is an accumulation of charges at either the electrodes or internal interfaces within the material producing an *interfacial polarization*. The contributions of orientational, ion hopping, and interfacial polarizations in liquids with strong intermolecular interactions resulting in mesoscale organization are the primary focus of this work. Beginning with induced and orientational polarization, a more detailed introduction into the underlying mechanisms will now be provided.

The polarization due to the material response is given by $\mathbf{P} = (\varepsilon^* - 1)\varepsilon_0\mathbf{E}$. The real and imaginary parts of complex dielectric permittivity, $\varepsilon^*(\omega) = \varepsilon'(\omega) - i\varepsilon''(\omega)$, for the well-studied dipolar liquid glycerol at 210 K are shown *versus* frequency in Figure 2.4. Focusing on the real

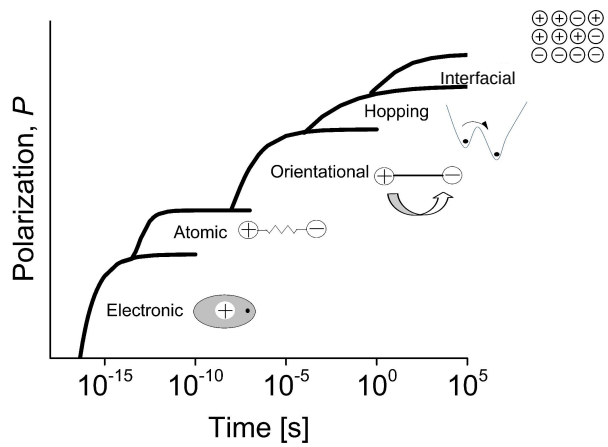

Figure 2.3: Mechanisms of dielectric polarization *versus* the time a dc electric field is applied. Shorter times correspond to higher frequencies of an ac field.

part, $\varepsilon'(\omega)$, we can identify some characteristic features: (i) a high-frequency limiting value, (ii) a low-frequency plateau value, and (iii) a transition region where the permittivity is frequency dependent. The high frequency limiting value, ε_∞, contains the total contributions from atomic and electronic polarizations. In the frequency-dependent, transition region the permanent molecular dipoles are orienting in the direction of the applied field. This characteristic frequency provides insight into the dynamics of the molecular dipoles as discussed later. The lower-frequency plateau value, known as the static dielectric permittivity, ε_s, or dielectric constant, is determined by the equilibrium contribution of orientational polarization and ε_∞.

The total polarization can be rewritten by separating the polarization components as $\mathbf{P}_\mu + \mathbf{P}_\infty = (\varepsilon - 1)\varepsilon_0\mathbf{E}$, where $\mathbf{P}_\mu$ and $\mathbf{P}_\infty$ are the orientational and induced polarizations, respectively. For the moment, we are neglecting the frequency-dependence of permittivity and simply take ε to indicate a frequency-independent value of the real part of the complex dielectric permittivity. The frequency dependence will be considered later. The induced polarization is given by $\mathbf{P}_\infty = \sum_k n_k \alpha_k (\boldsymbol{E_i})_k$, where n is the number density of molecules, α the polarizability, and the $\mathbf{E}_i$ is the local electric field. Polarization has units of Coulomb per meter squared [$\mathrm{C\,m^{-2}}$] and can be treated as the average dipole moment of N dipoles per unit volume. The orientational polarization can therefore be written as, $\mathbf{P}_\mu = \sum_k n_k \overline{\boldsymbol{\mu_d}}$, where n is the number density of dipoles and $\overline{\boldsymbol{\mu_d}}$ the average dipole moment due to orientational polarization. Orientational polarization arises from a torque experienced by the permanent dipoles in the applied electric field. This torque is counterbalanced

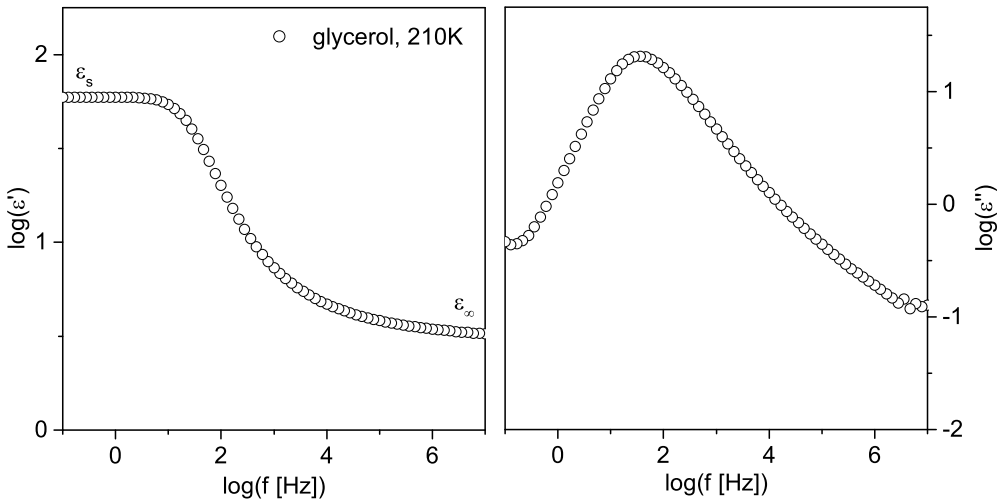

Figure 2.4: The real and imaginary parts of the complex dielectric permittivity, $\varepsilon^*(\omega) = \varepsilon'(\omega) - i\varepsilon''(\omega)$, of glycerol at 210K as measured by the Novocontrol α-analyzer.

by thermal fluctuations which tend to randomize the orientation of dipoles. Consequently, the average dipole moment due to orientational polarization is a statistical equilibrium.[72] Under certain approximations the equilibrium dipole moment due to orientation polarization may be estimated. These assumptions are (i) the permanent molecular dipole moment is independent of temperature and electric field, (ii) the interactions of dipoles may be neglected, and (iii) the dipoles may freely rotate with respect to the field direction. In this case, the interaction energy of a dipole, $\boldsymbol{\mu}$, at an angle θ with the electric field is, U $=\boldsymbol{\mu} \cdot \boldsymbol{E_d} = -|\boldsymbol{\mu}||\boldsymbol{E_d}|\cos\theta$. According to Boltzmann's statistics the average dipole moment due to orientational polarization is given by:

$$\overline{\boldsymbol{\mu_d}} = \frac{\int_0^\pi A\ \exp(\frac{|\boldsymbol{\mu}||\boldsymbol{E_d}|\ \cos\ \theta})(\boldsymbol{\mu}\ \cos\ \theta)\, 2\pi\ \sin\ \theta\ d\theta}{\int_0^\pi A\ \exp(\frac{|\boldsymbol{\mu}||\boldsymbol{E_d}|\ \cos\ \theta})\, 2\pi\ \sin\ \theta\ d\theta} \tag{2.6}$$

Substituting x $= \frac{|\boldsymbol{\mu}||\boldsymbol{E_d}|}{kT}$ allows us to perform the integration to find:

$$\frac{\overline{\boldsymbol{\mu_d}}}{\boldsymbol{\mu}} = \coth\ x - \frac{1}{x} \tag{2.7}$$

This result is shown in graphical form in Figure 2.5. At low field strengths, the average dipole moment due to orientational polarization varies linearly as $\overline{\boldsymbol{\mu_d}} = \frac{|\boldsymbol{\mu}|^2}{3kT}\boldsymbol{E_d}$. The orientational polarization is now written as, $\mathbf{P}_\mu = \sum_k n_k \frac{|\boldsymbol{\mu}|^2}{3kT}\boldsymbol{E_d}$. The orientational and induced polarizations

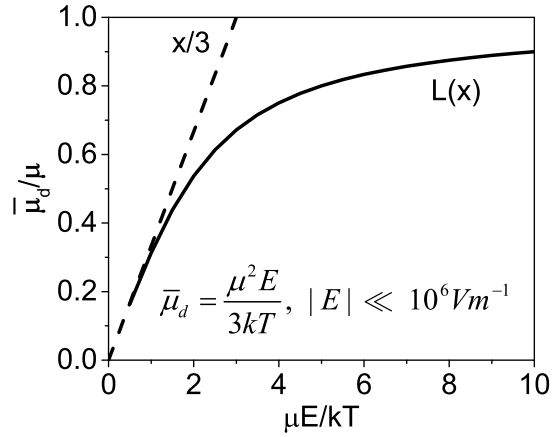

Figure 2.5: Langevin function for the orientational dipole moment.[1, 2, 3]

are combined to give a fundamental equation for the response of polar dielectrics to an external field, Equation 2.8.[2]

$$(\varepsilon - 1)\varepsilon_0 \boldsymbol{E} = \sum_k n_k \left[\alpha_k (\boldsymbol{E}_i)_k + \frac{|\boldsymbol{\mu}|^2}{3kT} \boldsymbol{E}_d \right] \tag{2.8}$$

In the original approach of Peter Debye, the internal and directing fields, $\boldsymbol{E}_i$ and $\boldsymbol{E}_d$, are set equal to the Lorentz field, which is itself derived by conceptualizing a spherical vacuum cavity inside a dielectric with constant permittivity. The applied field polarizes the inner surface of the dielectric giving a modified internal field, $\boldsymbol{E}_i = \boldsymbol{E} + (\varepsilon + 2)\boldsymbol{E}/3$. Substituting this electric field into Equation 2.8 gives the classic Debye formula, Equation 2.9, where ε is the low-frequency limit of the real part of complex dielectric permittivity, n is the number density of dipoles, α the polarizability, and μ the permanent molecular dipole moment.[2, 3, 73]

$$\frac{\varepsilon - 1}{\varepsilon + 2} = \frac{n}{3\varepsilon_0} \left(\alpha + \frac{\mu^2}{3kT} \right) \tag{2.9}$$

For non-polar dielectrics as well as polar dielectrics in the high-frequency limit, the orientational polarization component can be removed, giving the Clausius-Mossotti formula for the high frequency limiting permittivity, ε_∞, Equation 2.10.[2, 3, 73]

$$\frac{\varepsilon_\infty - 1}{\varepsilon_\infty + 2} = \frac{n\alpha}{3\varepsilon_0} \tag{2.10}$$

The Debye formula estimation of ε yields accurate values of the low-frequency static dielectric permittivity, ε_s, or equivalently the molecular dipole moment, μ, for polar molecules in the gas phase and in dilute solution with a non-polar solvent; however, it fails for liquid, polar dielectrics. This is due to a failure of the Lorentz field to accurately approximate the effective local field. Onsager developed a modified approach which accounts for an additional polarization due to the reaction of the surrounding dielectric to a point dipole inside the Lorentz cavity.[2, 1] The Onsager cavity more accurately represents the local electric field and yield the Onsager equation, Equation 2.11, which accurately predicts values of ε_s, or alternatively μ, for many pure dipolar liquids.[2, 1, 74]

$$\varepsilon_s - \varepsilon_\infty = \frac{3\varepsilon_s}{2\varepsilon_s + \varepsilon_\infty}\left(\frac{\varepsilon_\infty + 2}{3}\right)^2 \frac{n\,\mu^2}{3kT} \tag{2.11}$$

However, it fails for what are known as "associating" dipolar liquids. These liquids form strong intermolecular interactions which tend to orient dipoles in particular directions with respect to one another.[2, 3, 75] The effect of this local orientation of dipoles is approximated by introducing an additional term, $z\overline{cos\,\gamma}$, to the Onsager equation, where z is the average number of a dipoles nearest neighbors and $\overline{cos\,\gamma}$ is the average of the cosine of the angle between their dipole moments.[75] This modification was introduced by Kirkwood and Fröhlich to give Equation 2.12.

$$\varepsilon_s - \varepsilon_\infty = \frac{3\varepsilon_s}{2\varepsilon_s + \varepsilon_\infty}\left(\frac{\varepsilon_\infty + 2}{3}\right)^2 \frac{n\,\mu^2}{3kT}(1 + z\overline{cos\,\gamma}) \tag{2.12}$$

The final term in this equation, $(1 + z\overline{cos\,\gamma})$, differentiates it from the Onsager equation.[75] This term is known as the Kirkwood-Fröhlich correlation factor, g_k. Values of g_k greater than one indicate a preferential parallel alignment of the nearest dipoles and an increase in ε_s above the prediction of the Onsager equation, while values less than one indicate antiparallel alignment and a decrease in ε_s relative to the Onsager equation.[75]

These estimations of the dielectric permittivity take into account only the long-time, equilibrium distribution of dipole moments. Application of a dc electric field for a period of time will give this equilibrium polarization. If the electric field is then removed, the polarization will begin to decrease with a time decay originating in the motion of molecular dipoles. Dielectric spectroscopy therefore joins a host of other experimental techniques capable of providing information on dynamics in soft materials including dynamic mechanical spectroscopy, nuclear magnetic resonance spectroscopy,

and calorimetry. At low field strengths, the polarization is linearly related to the step change in the electric field strength by Equation 2.13.[3, 76]

$$\boldsymbol{P}(t) = \boldsymbol{P}_{\infty} + \varepsilon_0 \int_{-\infty}^{t} \varepsilon(t - t') \frac{d\boldsymbol{E}(t')}{dt'} dt' \tag{2.13}$$

In this regime, the molecular fluctuations due to the perturbation by the applied electric field are equivalent to the spontaneous equilibrium fluctuations. This equivalence between response function and thermal fluctuations makes dielectric relaxation spectroscopy a particular case of the fluctuation dissipation theorem.[76]

When the applied electric field is oscillating at a particular frequency, $\boldsymbol{E}(t)(\omega) = E_0 \exp(-i\omega t)$, then the frequency-dependent complex dielectric permittivity is related to the time-dependent dielectric function by Equation 2.14.[3]

$$\varepsilon^*(\omega) = \varepsilon'(\omega) - i\varepsilon''(\omega) = \varepsilon_{\infty} + \int_0^{\infty} \exp(-i\omega t) \left[-\frac{d\varepsilon(t)}{dt} \right] dt \tag{2.14}$$

The simplest approximation for the time decay in dielectric permittivity assumes it follows an exponential form with a correlation function given by, $\phi(t) = \exp(-t/\tau)$, where t is time and τ is the characteristic dipole relaxation time. The dielectric spectra are more easily measured in the frequency domain and so we perform a Laplace transform into the frequency domain to find the Debye equation for dipolar relaxations, Equation 2.15:

$$\varepsilon^*(\omega) = \Delta\varepsilon \int_0^{\infty} \exp(-i\omega t) \left[-\frac{d\phi(t)}{dt} \right] dt \; + \; \varepsilon_{\infty} = \frac{\Delta\varepsilon}{1 + i\omega\tau} + \varepsilon_{\infty} \tag{2.15}$$

where $\Delta\varepsilon$ is the dielectric strength, $\omega = 2\pi f$ the oscillation frequency of the applied electric field, τ the molecular dipole relaxation time, and ε_{∞} the high frequency limiting permittivity.[72, 1, 3] Debye tested his model against experimental data for primary alcohols and found excellent agreement.[72, 77] Over time it was realized that the exponential decay of the dielectric relaxation of alcohols, and certain other hydrogen-bonded systems, is the exception rather than the norm, with dielectric relaxations typically displaying quite broad distributions of relaxation times.[3, 31] In the time domain, such relaxations may be fit with stretched exponential functions such as the Kohlrausch-Williams-Watts equation, $g(t) = \exp[(t/\tau)^{\beta}]$, where β is a stretching parameter. Since

dielectric spectra are typically measured and displayed in the frequency domain, the fitting functions utilized are "stretched" versions of the Debye-equation known as the Cole-Cole, Cole-Davidson, and Havriliak-Negami functions depending on the combination of stretching parameters which are utilized.[78, 79, 79, 80, 81] With its two stretching parameters, β and γ, the Havriliak-Negami function, Equation 2.16, is the most general.[3]

$$\varepsilon^* = \frac{\Delta\varepsilon}{[1 + (i\omega\tau_{HN})^{\beta}]^{\gamma}} + \varepsilon_{\infty} \tag{2.16}$$

It should be noted that the model relaxation rates provided by the Havriliak-Negami fitting function, $\omega_{HN} = 1/\tau_{HN}$, do not correspond to the frequency of the peak maximum. The frequency of the peak maximum, or molecular relaxation rate, is related to the shape parameters β and γ by Equation 2.17.[3]

$$\omega_{max} = \frac{1}{\tau_{HN}} \left[\sin \frac{\beta\pi}{2 + 2\gamma}\right]^{1/\beta} \left[\sin \frac{\beta\gamma\pi}{2 + 2\gamma}\right]^{-1/\beta} \tag{2.17}$$

As an example of a fit using these model functions, the dielectric spectra of the monohydroxy alcohol 1-propanol is presented in Figure 2.6 at 130 K. The dominant lower frequency peak is well described by the Debye equation which was initially taken as proof of its accuracy. However, two additional, but much weaker relaxations are also present at higher frequencies. These are referred to as the α and β relaxations. The Debye relaxation is observed in many monohydroxy alcohols as well as several other hydrogen-bonded liquids.[31] Over time, the origin of this relaxation has been determined to be the reorientation of supramolecular dipoles which arise from the association of neighboring alcohols via intermolecular hydrogen-bonding.[31] The three dielectric relaxations are well-described by a combination of a Debye, Cole-Davidson, and Cole-Cole fitting functions to describe the Debye-like, α, and β relaxations, respectively, see Equation 2.18 with fit parameters provided in Table 2.1.[82, 83]

$$\varepsilon^* = \frac{\Delta\varepsilon_{Debye}}{[1 + (i\omega\tau_{Debye})]} + \frac{\Delta\varepsilon_{\alpha}}{[1 + (i\omega\tau_{\alpha})]^{\gamma}} + \frac{\Delta\varepsilon_{\beta}}{[1 + (i\omega\tau_{\beta})^{\beta}]} + \varepsilon_{\infty} \tag{2.18}$$

In addition to these dipolar relaxations, the dielectric spectra of ion conducting liquids have contributions arising from the motion of ions. These contributions are typically represented in the

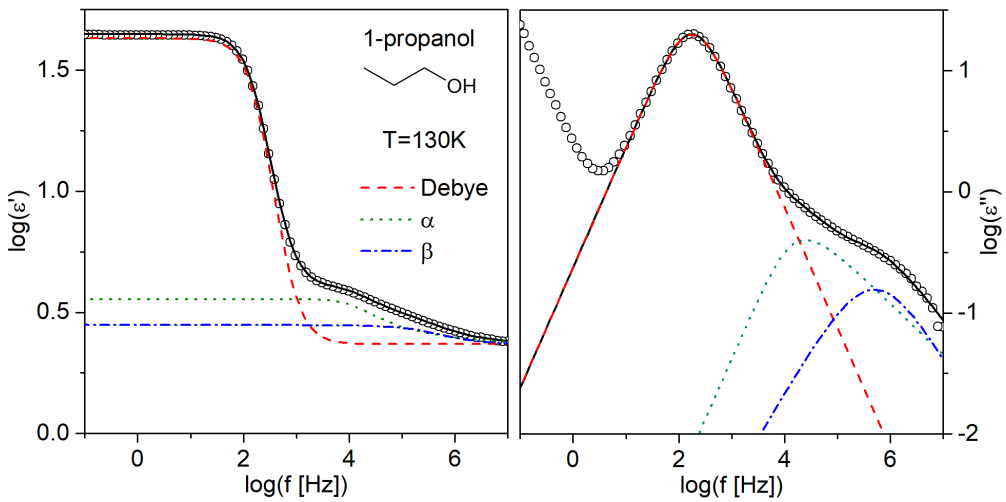

Figure 2.6: The real and imaginary parts of the complex dielectric permittivity, $\varepsilon^*(\omega) = \varepsilon'(\omega) - i\varepsilon''(\omega)$, of propanol at 130K as measured by the Novocontrol α-analyzer. The frequency-dependent spectrum is well described by a combination of three fitting functions, Equation 2.18. Fit parameters are provided in Table 2.1.

Table 2.1: Fit parameters from Equation 2.18 for the dielectric spectra of 1-propanol at 130 K.

Relaxation	$\Delta\varepsilon$	τ	γ	β
Debye	40.4	9.0×10^{-4}	1	1
α	1.2	1.3×10^{-5}	1	0.42
β	0.5	3.2×10^{-7}	0.80	1

real part of the complex conductivity, $\sigma^*(\omega) = \sigma'(\omega) + i\sigma''(\omega)$, which is related to the complex dielectric permittivity as $\sigma^* = i\omega\varepsilon_0\varepsilon^*$. As an example, the spectra of the prototypical ionic liquid 1-propyl-3-methylimidazolium bis(trifluoromethylsulfonyl)imide (C_3MIm NTf_2) is provided in Figure 2.7. The transport of ions between the electrodes through a percolated ion conducting pathway leads to a frequency independent plateau in the real part of complex conductivity. This plateau value is the dc ionic conductivity, σ_0, characteristic of the material at a given temperature. At frequencies above the plateau the real part of complex conductivity increases, while below the plateau it decreases. The high frequency response is due to ac conduction and the low frequency response is characteristic of the buildup of charges at the electrodes. The electrode polarization is not an intrinsic characteristic of the material, but depends strongly upon the material of the electrodes and will not be discussed further.[84] Other than the electrode polarization region, the charge transport contribution to the real part of complex conductivity is well described by the theoretical approach originated by Dyre known as the random barrier model (RBM). In this model, an ion is taken to be hopping in a randomly varying energy landscape. The onset of dc ionic conductivity, σ_0, corresponds to the time, τ_e it takes for an ion to overcome the largest energy barrier and form a percolated conducting path. Solving within the continuous time random walk approximation gives an analytical expression for the complex dielectric permittivity, Equation 2.19.[4] This model describes the frequency dependence of conductivity for C_3MIm NTf_2 quite well with only the two parameters σ_0 and τ_e as shown by the fit lines in Figure 2.7(a).

$$\varepsilon^*(\omega) = \frac{\sigma_0}{i\omega\varepsilon_0}\frac{i\omega\tau_e}{\ln(1 + i\omega\tau_e)} \tag{2.19}$$

The complex conductivity is directly related to the complex dielectric permittivity as $\sigma^* = i\omega\varepsilon_0\varepsilon^*$. The real part of conductivity therefore contributes strongly to the imaginary part of the complex dielectric permittivity, $\varepsilon'' = \sigma'/\omega\varepsilon_0$, as a low frequency increase with a slope of minus one in a double logarithmic plot *versus* frequency, see solid symbols in Figure 2.7(b). This contribution obscures any additional dielectric relaxations which occur in the vicinity of charge transport. To reveal these underlying relaxations a derivative representation may be employed, $\varepsilon''_{der} =$

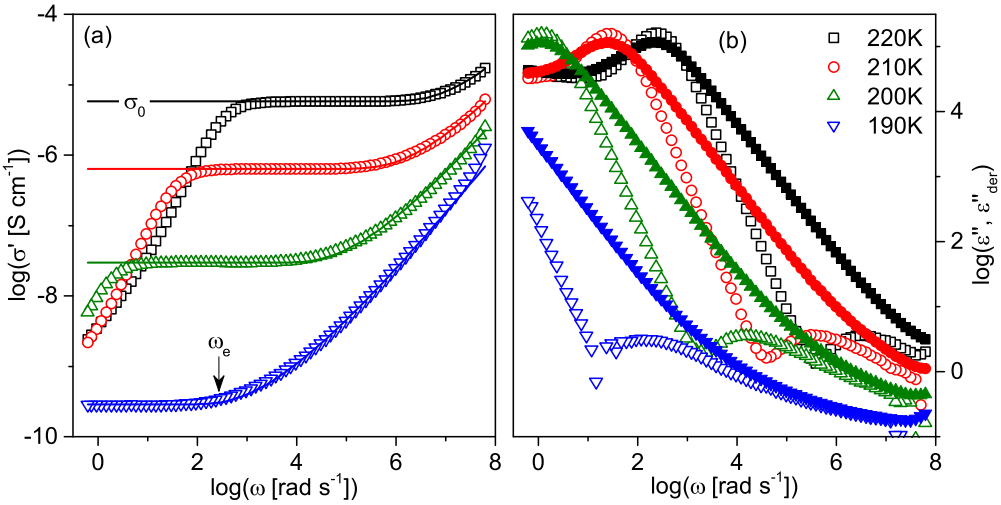

Figure 2.7: (a) Real part of the complex conductivity, σ', of the ionic liquid 1-propyl-3-methylimidazolium bis(trifluoromethylsulfonyl)imide. Lines correspond to fits by the random barrier model (RBM), Equation 2.19.[4] The two fit parameters of the RBM, σ_0 and $\omega_e = 1/\tau_e$ are indicated at 210K and 190K, respectively. (b) The imaginary part of complex dielectric permittivity, ε'' (closed symbols), and its derivative representation, $\varepsilon''_{der} = (-\pi/2)[\partial\varepsilon'/\partial\ln(f)]$ (open symbols).

$(-\pi/2)[\partial\varepsilon'/\partial\ln(f)]$. This derivative representation of ε'' is an approximation of the Kramers-Kronig relation between the real an imaginary parts of complex dielectric permittivity.[85, 86] In the case of C_3MIm NTf_2, only a single underlying relaxation is observed.

2.2 Dynamic Mechanical Spectroscopy

In general, dynamic mechanical spectroscopy consists of applying a strain and measuring the stress response of a material. Where dielectric spectroscopy measures a materials frequency-dependent response to an applied oscillatory electric field, dynamic mechanical spectroscopy probes the response to an oscillatory mechanical shear. This response is governed by the type of motion which its molecules undergo within the applied experimental frequency range. The sensitivity of the stress response to different types and length scales of molecular motion allows us to investigate structure by mechanical measurement.[87, 88]

All liquids are viscoelastic, meaning they exhibit a combination of viscous and elastic response depending upon the oscillation frequency of the applied strain. At very high frequencies, below the timescale of molecular motion, they respond as an elastic solid with a shear stress σ given by

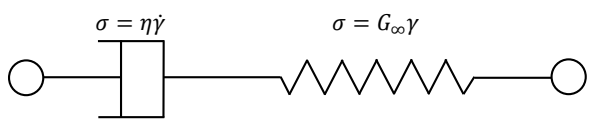

Figure 2.8: Maxwell model of a viscoelastic liquid. The response to an applied strain is captured by a Newtonian dashpot and Hookean spring connected in series.

Equation 2.20 where G is the shear modulus of the solid, and γ the strain.

$$\sigma = G\gamma \tag{2.20}$$

In this regime, the material is below its dynamic glass transition and is an amorphous glass. When the frequency is reduced below the rate of molecular motion, the molecules are able to slide past one another. Here, the material response consists entirely of a viscous component which, for a Newtonian fluid, is given by Newton's law of viscosity:

$$\sigma = \tau_{x,y} = \eta\frac{\partial v_x}{\partial y} = \eta\dot{\gamma} \tag{2.21}$$

where σ and $\tau_{x,y}$ are the shear stress, η the zero-shear viscosity, and $\frac{\partial v_x}{\partial y}$ and $\dot{\gamma}$ are the strain rate. To understand the viscoelastic response, we will first consider the simple Maxwell element which consists of a spring and dashpot connected in series, see Figure 2.8.[17] The Hookean spring responds in a purely elastic manner governed by Equation 2.20 while the dashpot flows as a viscous Newtonian fluid governed by Equation 2.21. When an instantaneous strain is applied to the system, the response at very short times is completely accounted for by the elastic spring. Then, gradually the dashpot will begin to flow and extend. At the longest times all of the response will be in the dashpot and the spring will return to its equilibrium position. Therefore, the long-time response is of a viscous liquid and the short time an elastic solid, satisfying the observed responses of a viscoelastic liquid. At any instant in time, the total strain, γ_0, is given by the summation of the strain in each element:

$$\gamma_0 = \gamma_E + \gamma_V \tag{2.22}$$

where the subscripts E and V denote the elastic and viscous response, respectively.

One of the simplest ways to obtain information regarding the viscoelastic response is to apply an oscillatory strain and measure the stress response. Then, for a Maxwell element undergoing a sinusoidal strain, $\gamma = \gamma_0 \sin(\omega t)$, the time derivative of the strain is given by,

$$\begin{aligned} \dot{\gamma} = \frac{\partial \gamma}{\partial t} &= \frac{\partial \gamma_E}{\partial t} + \frac{\partial \gamma_V}{\partial t} \\ \Rightarrow \omega \gamma_0 \cos(\omega t) &= \frac{1}{G_0}\frac{\partial \sigma}{\partial t} + \frac{1}{\eta_0}\sigma \end{aligned} \tag{2.23}$$

The solution to this differential equation is $\sigma(t) = A\ sin(\omega t) + B\ cos(\omega t)$. Inserting this solution into Equation 2.23, and solving for the coefficients gives Equation 2.24.[89, 90, 88]

$$\begin{aligned} \sigma(t) &= \frac{G_0\ \gamma_0\ \omega^2\ \tau^2}{\omega^2\ \tau^2 + 1}\sin(\omega t) + \frac{G_0 \gamma_0 \omega \tau}{\omega^2 \tau^2 + 1}\cos(\omega t) \\ \sigma(t) &= G' \gamma_0 \sin(\omega t) + G'' \gamma_0 \cos(\omega t) \end{aligned} \tag{2.24}$$

The frequency-dependent material response is captured by the two components G' and G''. The real part, G', termed the storage modulus, is the portion of the response which is in phase with applied strain and is therefore related to the elastic response. The imaginary part, G'', is known as the loss modulus and represents the portion of the material response which is 90° out of phase with applied shear and is therefore in phase with strain rate and must be related to the viscous response.[91, 90, 88, 92, 17] A mechanical spectroscopy measurement consists of measuring the frequency-dependence of G' and G''. In complex notation, the complex dynamic shear modulus is defined as, $G^*(\omega) = G'(\omega) + iG''(\omega)$.

The instrument utilized in this study is a TA instruments Discovery Hybrid Rheometer-2. The measurements were made in a parallel plate sample geometry with disposable aluminum plates. Temperature control was provided by an Environment Test Chamber also from TA Instruments with accuracy of ± 0.1 K. This instrument is a single-head rheometer where the motor, torque transducer, and position sensor (for measuring strain) are all mounted on the same plate on one side of the sample.[88] A simplified illustration of the instrument is provided in Figure 2.9. In our oscillatory shear measurements the maximum angular displacement (strain %) is preset and the torque required to achieve this strain is measured. When inertial forces can be neglected and the deformations are small enough to be within the linear regime, the stress/strain ratios, $\frac{\sigma}{\gamma}$, are

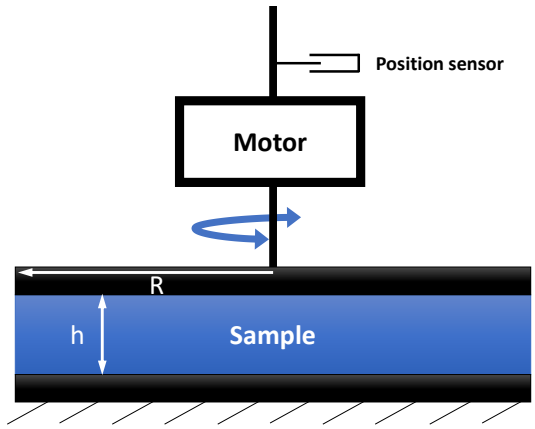

Figure 2.9: Illustration of the Ares HR-2 rheometer with parallel plate sample geometry where R defines the plate radius and h the sample thickness. As indicated, the HR-2 is a single-head rheometer with a fixed bottom plate and free top plate to which a motor and position sensor are affixed.

related to angular displacement/torque ratios, $\frac{S}{\alpha}$, by form factors which depend only on the sample geometry.[91, 92] This relationship is given in Equation 2.25 for parallel plate geometry, see Figure 2.9.

$$\frac{\sigma}{\gamma} = \frac{S}{\alpha}\frac{2h}{\pi R^4} \tag{2.25}$$

During measurement at a fixed frequency, the torque and therefore the shear tends to lag behind the oscillatory strain, see Figure 2.10. The shear stress is given by, $\sigma = \sigma_0 \sin(\omega t + \delta) = \sigma_0 \cos(\delta)\sin(\omega t) + \sigma_0 \sin(\delta)\cos(\omega t)$, where δ is the phase angle between the applied strain and measured stress response. Combined with Equation 2.24 this gives:

$$\begin{aligned} G' &= \frac{\sigma_0}{\gamma_0}\cos(\delta) \\ G'' &= \frac{\sigma_0}{\gamma_0}\sin(\delta) \end{aligned} \tag{2.26}$$

therefore, the real and imaginary parts of the complex dynamic shear modulus can be obtained by simply measuring the maximum amplitude of the applied shear strain and stress and their phase angle.[92] To ensure that measurements are within the linear response regime the amplitude of the strain may be reduced until strain-independent results are obtained.

The experimentally accessible frequency range for this type of oscillatory shear rheometer is much more limited than in the case of broadband dielectric spectroscopy. The Ares HR-2 has a

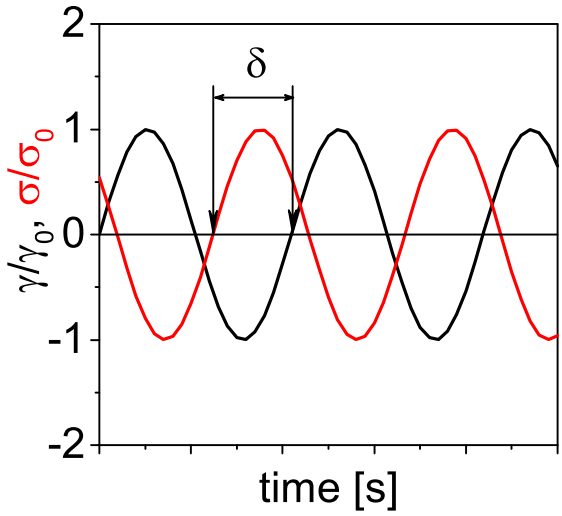

Figure 2.10: Time dependence of an applied sinusoidal shear strain and the measured stress-response at a fixed frequency. The maximum amplitudes of stress and strain and their measured phase shift, δ, are used obtain the real and imaginary parts of the complex dynamic shear modulus by Equation 2.26.

frequency range of $10^{-7} - 10^{2}\,\mathrm{rad\,s^{-1}}$. In practice, the available frequency range is limited by the material response. For viscous liquids, oscillatory shear measurements are only accurate near the viscoelastic transition where the torque is quite large. Therefore experiments must be carried out near the calorimetric glass transition temperature where the molecular relaxation times are at approximately $\tau = 10^{2}s$ or equivalently $\omega = 10^{-2}s^{-1}$.

The results of a measurement on the ionic liquid 1-hexyl-3-methylimidazolium tetrafluoroborate (C_6MIm BF_4) are presented in Figure 2.11. At each temperature, only a portion of the viscoelastic response is observed within the experimental frequency window. At the higher temperatures this is dominated by the viscous response with characteristic low-frequency slope of 1 and 2 in G'' and G', respectively. At the lowest temperatures and highest frequencies the elastic response begins to dominate with G' reaching a frequency-independent plateau value of $G_\infty = 10^9$ Pa, typical of an amorphous glass.[87, 88] The frequency at which the storage and loss moduli cross over one another corresponds to the characteristic structural relaxation rate of the liquid. This rate is directly accessed only at the lowest two temperatures in Figure 2.11. The analysis of the mechanical relaxation spectra can be extended by performing a time-temperature superposition of the experimental data. In this

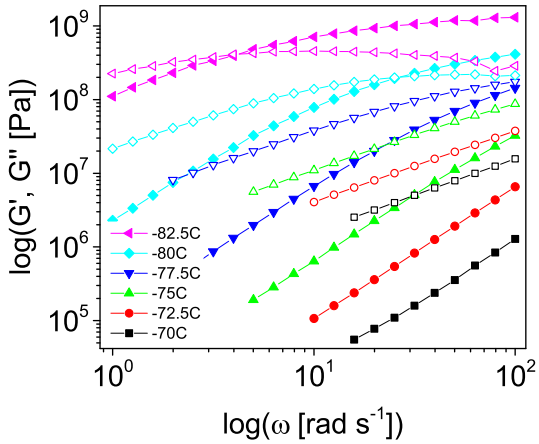

Figure 2.11: The real (closed symbols) and imaginary (open symbols) parts of complex dynamic shear modulus, $G^* = G' + iG''$, of 1-hexyl-3-methylimidazolium tetrafluoroborate (C_6MIm BF_4).

analysis, the data are shifted horizontally by shift factors, a_T, to give a master curve that is assumed to be representative of a reference temperature, T_{ref}.[17] It should be noted that this assumption holds only if time-temperature superposition is obeyed. The structural relaxation rates, ω_α, are then given by $\omega_\alpha = a_T\,\omega_{T_{ref}}$ where $\omega_{T_{ref}}$ is the relaxation rate at a specified reference temperature to which the other data is shifted. The master curve of the complex dynamic shear modulus of C_6MIm BF_4 is given in Figure 2.12.

The response encapsulated in Equation 2.24 defines the frequency dependence of G' and G'' as $G' = \frac{G_0\,\gamma_0\,\omega^2\,\tau^2}{\omega^2\,\tau^2+1}$ and $G'' = \frac{G_0\gamma_0\omega\tau}{\omega^2\tau^2+1}$. This response is derived for an idealized Maxwell element. The vast majority of viscoelastic materials do not follow this type of response, but rather exhibit relaxations stretched over wider frequency ranges. This is analogous to the "stretching" of typical dipolar relaxations in dielectric spectroscopy relative to the idealized Debye relaxation model.[3] We can modify the Maxwell relaxation model by introducing a stretching parameter which is analogous to the stretching parameter of the Cole-Davidson dielectric fitting function.[79, 93] This gives us a Cole-Davidson-modified Maxwell relaxation model for the real part of the complex dynamic shear modulus, Equation 2.27, where $Re[]$ indicates separation of the real part, G_∞ is the high frequency shear modulus, τ is the relaxation time, and γ is the stretching parameter.[94]

$$G' = Re\left[G_\infty\left(1 - \frac{1}{(1+i\omega\tau)^\gamma}\right)\right] \tag{2.27}$$

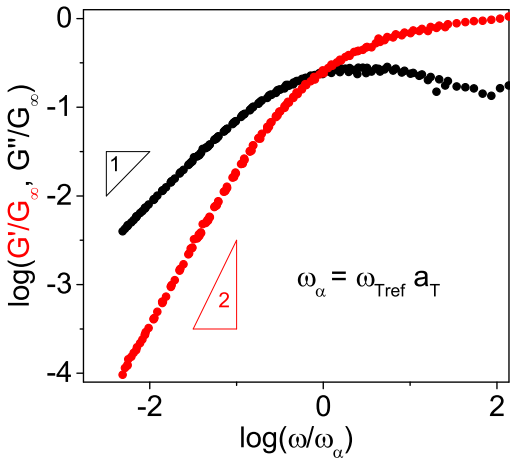

Figure 2.12: Master curve of the complex dynamic shear modulus for C_6MIm BF_4 obtained by time-temperature superposition at a reference temperature of $-82\,°C$. This curve is typical for a low molecular weight glass-forming liquid with the only mechanical relaxation being the structural relaxation of the liquid with relaxation rate ω_α.

2.3 Differential Scanning Calorimetry

Calorimetry is the science of measuring heat flow into and out of a sample as it undergoes various types of transitions including phyical transitions, e.g. melting, crystallization, mixing, etc..., as well as chemical transitions, i.e. chemical reaction. Differential scanning calorimetry (DSC) is a technique which emerged from this science in the middle part of the 20th century. DSC allows for rapid and, if properly calibrated, highly accurate measurement of the heat flow associated with phase transitions as well as heat capacity.[95] Due to the ease of measurement, the wealth of information supplied, and the small sample amounts required (milligrams), DSC has become ubiquitous in the study of amorphous, crystalline and semi-crystalline soft materials.[96]

In this intro to DSC, the operating principles will be established followed by an overview of its application to the study of glass-forming liquids. There are two types of DSC instruments with fundamentally different modes of operation. The first type was developed in the 1960s and is known as power compensation DSC.[97] This instrument consists of two separate calorimeters each with their own heaters and pans. One calorimeter contains the sample while the other is an empty reference. During a measurement the two heaters are operated such that the temperature in the sample and reference pans are maintained equal to one another. Due to the sample's heat capacity

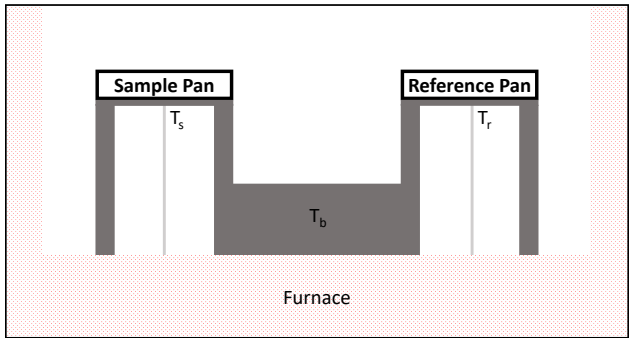

Figure 2.13: Illustration of a differential scanning calorimetry experimental apparatus. An aluminum reference and sample pan are placed on a constantan base. This base is subjected to heating/cooling ramps by a surrounding furnace. The temperature of the sample and reference pans as well as the base are recorded as a function of time. This allows a calculation of the sample heat capacity and heat flow rate.

and phase transitions the power supplied by the two heaters will be different. This difference is equal to the heat flow into the sample.

The instruments utilized in this study are Q1000 and Q2000 differential scanning calorimeters from TA instruments. These are both heat-flux rather power compensation calorimeters. An illustration of the experimental apparatus is presented in Figure 2.13. Here we see two aluminum pans set atop hollow platforms which are raised above and connected to a metal base. One pan is an empty reference and the other contains a small sample of the material to be measured. The base upon which the pans rest is made from constantan and forms one leg of a thermocouple. Inside the hollow platforms run chromel wires which form the other leg thereby allowing a precise measurement of both the reference pan and sample pan temperatures T_r and T_s, respectively. This entire assembly is enclosed, to minimize convection effects, and placed within a furnace which may be heated elecrically or cooled using either a liquid nitrogen purge gas stream (Q1000) or refrigerated air (Q2000). The temperature of the constantan base, T_0, is measured by a third thermocouple. This temperature is set via an electronic controller linked to the furnace which allows heating and cooling rates over a very wide range (0.1-100 K min^{-1}) while maintaining an accuracy of ± 0.1 K. During a measurement, the base temperature is ramped and the temperature difference between the sample and reference pans is measured. To obtain the heat flow into the sample requires a mathematical treatment of the heat flow paths within the whole system. The Q1000 and Q2000 calorimeters utilize an equivalent circuit approach, referred to as T_{zero}, which

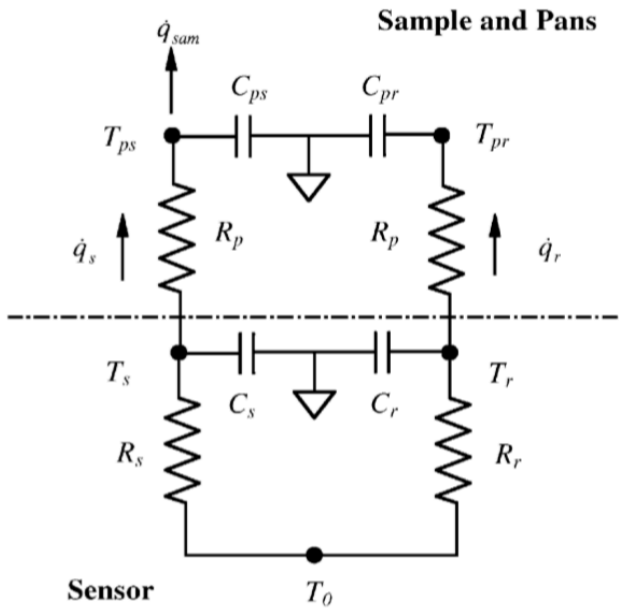

Figure 2.14: Equivalent circuit diagram of the heat-flux DSC assembly of Figure 2.13. The circuits above the dotted-dashed line account for the pan and sample effects while those below represent platform effects. As a result of this analysis and with careful calibration to account for the resistances and capacitances of the platforms and pans, the heat flow into the sample, q_{sam}, may be calculated. This diagram is reproduced from [5].

accounts for the thermal resistances and capacitances of the platforms as well as the sample and reference pans.

A diagram of the equivalent circuit corresponding to the experimental apparatus of Figure 2.13 is shown in Figure 2.14.[5] The circuit below the dotted line corresponds to the platform on which the two pans rest, where T_s, T_r, and T_0 are the measured temperatures, R_s is the resistance of sample platform, R_r the resistance of the reference platform, C_s the capacitance of the sample platform, C_r the capacitance of the reference platform. Accordingly, the heat flow rates into the sample and reference pans, q_s and q_r, are given by Equation 2.28.

$$\begin{aligned} q_s &= \frac{T_0 - T_s}{R_s} - C_s \frac{dT_s}{dt} \\ q_r &= \frac{T_0 - T_r}{R_r} - C_r \frac{dT_r}{dt} \end{aligned} \tag{2.28}$$

These heat flow rates may be subtracted to give an approximate heat flow rate into the sample. However, this neglects any effects from the platform/pan interfaces, the pans themselves, and the

thermocouple sensors. To account for these effects, we can first write expressions for the actual sample heat flow rate, q_{sam}, and the heat flow rate into the reference pan, q_r:

$$q_{sam} = q_s - m_{ps} c_{pan} \frac{dT_{ps}}{dt} \tag{2.29}$$

$$q_r = m_{pr} c_{pan} \frac{dT_{pr}}{dt} \Rightarrow c_{pan} = \frac{q_r}{m_{pr} \frac{dT_r}{dt}} \tag{2.30}$$

where m_{ps} and m_{pr} are the masses of the sample and reference pans and c_{pan} is the specific thermal capacity of the pan material. Now, inserting Equation 2.30 into Equation 2.29 gives Equation 2.31.

$$q_{sam} = q_s - q_r \left[\frac{m_{ps}(dT_{ps}/dt)}{m_{pr}(dT_{pr}/dt)} \right] \tag{2.31}$$

Equation 2.31 provides the actual heat flow rate into the sample as it undergoes a temperature ramp dT_o/dt. It is this heat flow rate which is the basic output of a typical DSC measurement. The heat flow rate *versus* temperature for the ionic liquid tributyl-dodecylphosphonium bis(trifluoromethylsulfonyl)imide is shown in Figure 2.15. Using this equation to obtain q_{sam} requires an estimate of the actual sample and reference pan temperatures T_{ps} and T_{pr}. This is accomplished using the expected resistances of the pans, sensors and their interface (approximated as an air gap) in the overall pan resistance, R_p. The temperatures are then given by Equation 2.32.

$$\begin{aligned} q_s &= \frac{T_s - T_{ps}}{R_p} \\ q_r &= \frac{T_r - T_{pr}}{R_p} \end{aligned} \tag{2.32}$$

Therefore, the sample heat flow rate, q_{sam}, can be accessed by measuring T_s and T_r during a temperature ramp, inputting the masses of the sample and reference pans and notifying the instrument software of which pan geometry and construction material is being used.[5]

During a temperature heating or cooling cycle the material under study may undergo a phase transition such as crystallization or melting. When such transitions occur, the sample will either absorb (endothermic) or expel heat (exothermic). This excess heat flow will result in either a positive or negative peak. The enthalpy of these phase transitions is equal to the areas of

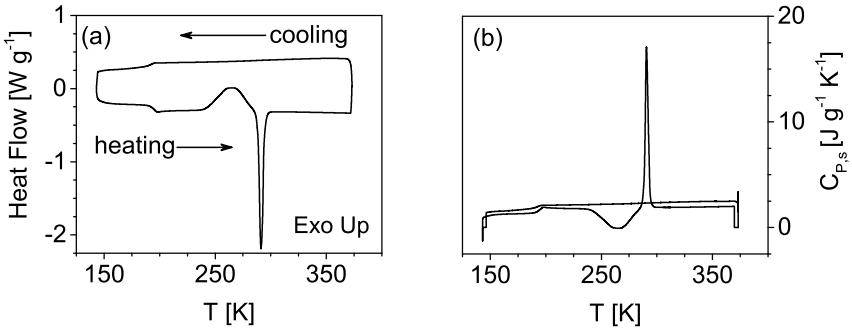

Figure 2.15: Result of a typical DSC experiment for the ionic liquid tributyl-dodecylphosphonium bis(trifluoromethylsulfonyl)imide $P_{4,4,4,12}$ NTf_2. (a) Heat flow *versus* temperature for a cooling and heating cycle at 10 °C min^{-1}, with exotherm up. (b) Sample heat capacity *versus* temperature on the same heating and cooling cycle. This sample has a glass transition at 195 K observed as a step in both heat flow and heat capacity. In addition, on the heating curve cold crystallization occurs (peak in heat flow and dip in heat capacity) with a maximum/minimum at 265 K followed by melting at 290 K

.

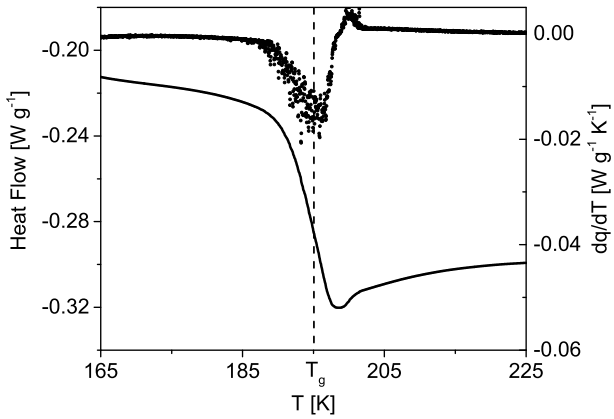

Figure 2.16: Calorimetric glass transition temperature, T_g, of $P_{4,4,4,12}$ NTf_2 on heating. The T_g is evident as a step-change in heat flow. The temperature assigned to T_g corresponds to the maximum in the temperature-derivative of heat flow (dashed line). The solid line corresponds to heat flow and the symbols to the derivative of heat flow with respect to temperature, dq/dT.

the transition peaks in a plot of heat flow *versus* temperature.[95, 96] In our study of glass-forming liquids, we are predominantly concerned with the calorimetric glass transition. The calorimetric glass transition temperature, T_g, is observed in a DSC experiment due to the change in sample heat capacity. It is evident as a step-change in both heat capacity and heat flow. The results of a single heat-cool cycle are presented for the ionic liquid tributyl-dodecyl-phosphonium bis(trifluoromethylsulfonyl)imide ($P_{4,4,4,12}$ NTf_2) as heat flow and heat capacity *versus* temperature in Figure 2.15. On cooling, only a step change is observed at approximately 195 K indicating the entire sample was super cooled to its glass transition without crystallization. On the heating trace, we observe a second step, again near 195 K, followed by two peaks. These peaks correspond to a cold crystallization event and subsequent melting. The two steps correspond to the calorimetric glass transition. This temperature range is examined in greater detail in Figure 2.16. Here we see that the step change spans several kelvin. The value recorded as the T_g may be defined as the temperature at the maximum in the derivative of the heat flow. The values of T_g are dependent upon whether they are recorded in the heating or cooling cycle and upon the heating and cooling rates.[17]

2.4 Fourier Transform Infrared Spectroscopy

As the name implies, Fourier transform infrared spectroscopy (FTIR) is concerned with the interaction of matter with electromagnetic radiation in the infrared frequency range.[98, 99, 100] The infrared extends from just beyond the visible light range, 12,500 cm^{-1}, down to the microwave region, 0.1 cm^{-1}. Note that wavenumber, inverse wavelength, is directly proportional to frequency as $1/\lambda = \nu/c$ where λ is wavelength, ν is frequency, and c is the speed of light. Measuring this entire frequency range requires a combination of several different types of infrared sources and sensors. The FTIR instrument types are therefore split into three categories which, in order of decreasing frequency, are near-IR, mid-IR, and far-IR.[99] The FTIR spectra in this work were collected using mid-IR spectrometers which cover the range 4000 - 400 cm^{-1}. These frequencies coincide with the vibrational and rotational modes of covalent bonds in organic molecules.[98, 99, 100] An isolated covalent bond of a particular type vibrates, or rotates, at a particular frequency and absorbs infrared radiation at that frequency. The measured absorbance is related to the concentration of the oscillator

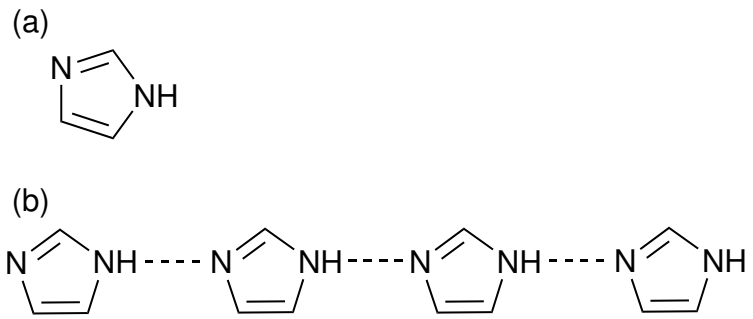

Figure 2.17: (a) Chemical structure of imidazole.[6] (b) Supramolecular aggregates of imidazole arising from intermolecular hydrogen-bonding. Dashed lines represent intermolecular hydrogen-bonds.[7, 8]

and its absorptivity by Beer's Law, Equation 2.33, where A is the absorbance, T the transmittance, a the absorptivity, b the thickness, and c the concentration of oscillator i.[99]

$$A(\nu) = \log_{10} \frac{1}{T(\nu)} = a_i(\nu) b c_i \tag{2.33}$$

The characteristic frequencies and relative absorbances of practically all types of covalent bonds have been investigated for a huge variety of organic molecules.[101] FTIR can therefore be used to identify the presence of different functional groups and molecules contained in a given sample. Such chemical structure identification was the original application of IR-spectroscopy although it has now been mostly superseded for this purpose by a combination of other techniques such as nuclear magnetic resonance spectroscopy (NMR), x-ray diffraction, and mass spectrometry.[99]

The frequency at which a covalent bond absorbs infrared radiation is sensitive not only to the type of bond, but also to its local environment and interactions with neighboring atoms of both the intra- and intermolecular variety. For instance, the IR spectra of the same material in its gas, liquid, and crystalline phases will be considerably different from one another. In condensed phases, all IR peaks are broadened and form distributions around a mean. The peak width, defined as the full-width at half-maximum (FWHM), as well as the frequency at its maximum are both sensitive reporters of the local environment especially if strong intermolecular interactions, such as hydrogen-bonding, occur.[98, 99, 100] FTIR is therefore useful as a probe of the local environment of different oscillators. As an example, we can consider the infrared spectra of imidazoles in dilute carbon tetrachloride solution in a study by Wolff in the 1970s.[9] Imidazole is a five-membered,

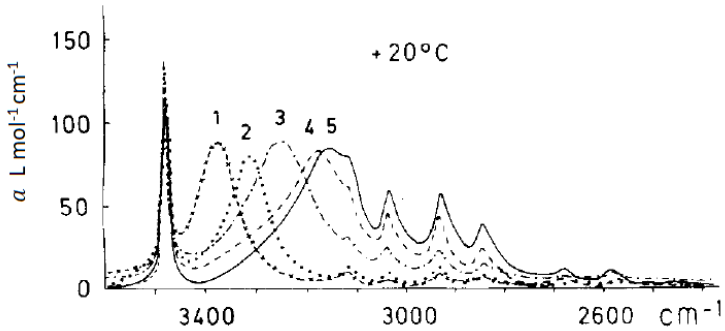

Figure 2.18: Infrared spectra of imidazole (0.0004 mol L^{-1}) and (1) trideuteroacetonitrile (0.399 mol L^{-1}), (2) octadeuterodioxane (0.396 mol L^{-1}), (3) hexadeuterodimethylsulfoxide (0.0158 mol L^{-1}), (4) pentadeuteropyridine (0.120 mol L^{-1}), and (5) N-methylimidazole (0.0204 mol L^{-1}). The free N-H stretch is located at 3500 cm^{-1}. This vibrational stretching band shifts to lower frequency, indicated roughly by the position of the labels, with increasing strength of the intermolecular hydrogen-bond formed between imidazole and the basic additives. This figure is reproduced from [9].

nitrogen-containing heterocycle with chemical structure given in Figure 2.17(a).[6]. The acidic and basic nitrogens on the heterocycle enable it to form intermolecular hydrogen-bonds which lead to suparmolecular aggregates of the type shown in Figure 2.17(b).[7, 8] The formation of these hydrogen-bonds will significantly alter the vibrational frequency of the N-H bond. Therefore, infrared spectroscopy is expected to be a sensitive tool to study supramolecular association in liquid imidazoles. In the extremely dilute limit in carbon tetrachloride solution, imidazole will exist as a free, unassociated molecule. The N-H vibration of "free" imidazole is located at $\approx 3500 cm^{-1}$, see Figure 2.18.[9] As the concentration of imidazole is increased they begin to form supramolecular hydrogen-bonded chains. In a supramolecular aggregate, only the N-H group of the imidazole on one end of the chain will continue to vibrate at 3500 cm^{-1}. The intensity of the "free" N-H vibration band will therefore be reduced as a function of imidazole concentration. Using Beer's law, the concentration dependence of the reduction in intensity can be used to estimate the degree of association in dilute imidazole solutions.[102] This approach indicates that imidazoles in saturated carbon tetrachloride solution exist with oligomers up to 13 molecules long.[102]

Upon forming an intermolecular hydrogen-bond, the N-H stretch band shifts to lower frequencies. The extent of this shift is influenced by the strength of the hydrogen-bond. This can be demonstrated by adding molecules of gradually increasing basicity to very dilute imidazole solutions. Such a study was accomplished by Wolff when he added trideuteroacetonitrile (pKa

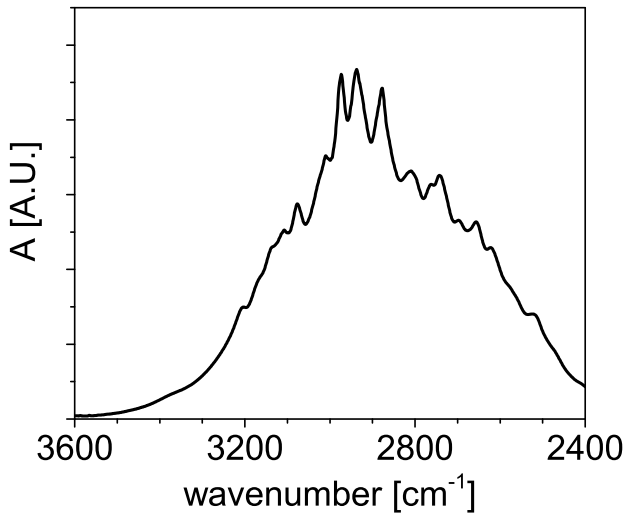

Figure 2.19: Infrared spectra of neat 2-ethyl-4-methylimidazole. The fundamental N-H stretching vibration is obscured by the existence of numerous sub-bands which arise due to Fermi resonance as shown in Figure 2.18.

≈ -10.0), octadeuterodioxane (pKa ≈ -3.2), hexadeuterodimethylsulfoxide (pKa ≈ 0), pentadeuteropyridine(pKa $\approx +5.4$), and N-methylimidazole(pKa $\approx +7.3$) to dilute imidazole/CCl_4 solutions.[9] The resulting IR spectra are provided in Figure 2.18. The shift for an imidazole dimer, corresponding to the strongest hydrogen-bond, is over 600 cm^{-1}.[9] In addition to the "free" and associated N-H stretch, numerous bands are located between 3200 cm^{-1} and 2400 cm^{-1}. Some of these are due to C-H stretching bands which arise in this region.[101] The majority, however, are sub-bands which arise due to Fermi interaction of the stretching vibrations with over and combination tones of intermolecular vibrations.[9, 103] In neat liquid imidazoles, these sub-bands are quite strong and obscure the contribution of the fundamental N-H stretching vibration as seen for liquid 2-ethyl-4-methylimidazole (2E4MIm) in Figure 2.19. These results show that the N-H stretch of imidazole cannot be used to probe hydrogen-bonding in neat 2E4MIm and highlight some of the difficulties in the application of FTIR to the study of mesoscale organization in liquids. Especially important is the ability to identify bands which are isolated and sensitive to the formation of non-covalent bonds.

Infrared spectra can be obtained in a number of different ways depending on how the infrared beam interacts with the sample and is subsequently passed to the detector. The primary methods are transmission, reflection, and attenuated-total reflectance. In transmission, the beam is passed

through a sample and collected into the detector. In reflectance, the beam passes through the sample, is reflected off of a surface on which the sample has been mounted back through the sample, and is then collected by the detector. Attenuated-total-reflectance (ATR) utilizes a special material known as an internal reflection element (IRE) to measure a sample without actually passing the beam through the sample. The IR-beam is directed into the IRE where it is internally reflected. One side of the IRE is in contact with the sample where an evanescent wave interacts with only with the topmost section of the sample. Afterwards, the beam leaves the other IRE and is collected into the detector. Each of these techniques is suited to different sample types and different experimental goals. ATR is one of the easiest to carry out, requiring the least sample preparation, and is therefore by far the most common technique seen in the literature today. The goal of our FTIR experiments are to probe the temperature and composition dependence of intermolecular interactions. The temperature of the sample is controlled by a Linkam Scientific THMS600 temperature stage. The design of this apparatus is geared toward transmission measurements and therefore all of our measurements were made by transmission.

2.5 X-ray Scattering

On a basic level, x-ray scattering operates on a similar principle as the familiar diffraction of visible light when it is passed through a grating.[104] Just as the diffraction pattern in that case is due to the spacing between holes, so, when x-rays are passed through matter the diffraction pattern is due to spacing between regions of varying electron density be it atoms, molecules, particles, etc.... The original application of x-ray scattering was the study of lattice structure in crystals.[105] The x-ray diffraction is governed by Bragg's Law, $\lambda = 2d \sin\theta$, where λ is the x-ray wavelength, 2θ the diffraction angle, and d the lattice spacing. X-ray wavelengths range between 0.01 and 10 nm.[106] In practice, the most common x-ray source for x-ray diffractometers is CuKα with a wavelength $\lambda = 1.54$ Å. Longer wavelengths are avoided due to their increased tendency to be absorbed by matter.[106] For crystal lattices, the local spacing between adjacent atoms or molecules ranges over a few angstroms. Therefore scattering angles at these lattice distances are quite large. This is the domain of wide-angle x-ray scattering. The angles are reduced as the spacing becomes larger. Accordingly, small-angle x-ray scattering is utilized in the study of long-range order. Small angle

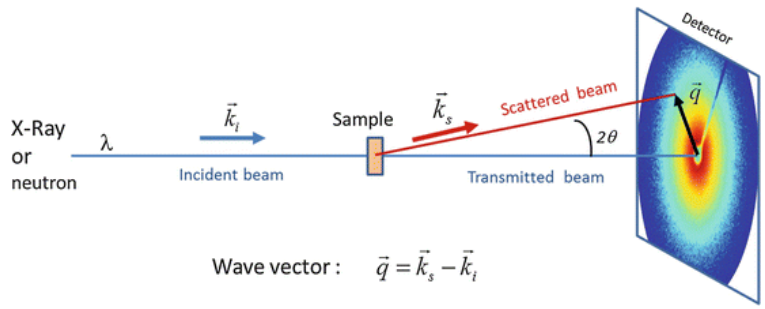

Figure 2.20: In this schematic of an x-ray scatttering beamline, a collimated x-ray beam is scattered upon passing through a sample. The intensity and wave vector of the scattered beam are recorded by an x-ray detector. The detector is mounted on a movable stage allowing a wide range of scattering vectors to be investigated. Reproduced from [10].

x-ray scattering has emerged as a useful tool in the study of a variety of amorphous materials including proteins, block copolymers, colloids, and microemulsions.[107]

The x-ray scattering instrument utilized in these investigations is a SAXSLAB Ganesha instrument equipped with a CuKα x-ray point source. A simplified illustration of the beamline in this instrument is provided in Figure 2.20.[10] In operation, a collimated x-ray beam is passed through a sample, where a portion of the beam is then scattered. Some distance away is an x-ray detector which records the position and intensity of the scattered beam. A wave vector, $\vec{q}$, is defined by the difference between the vectors corresponding to the scattered and incident beam, respectively. In the SAXSLAB Ganesha instrument, the detector is positioned on a movable stage so that the distance between the sample and the detector may be altered. In this way, by using a single instrument wide-, medium-, and small-angle scattering may be carried out in very short order. By doing so, order within the sample ranging from 0.2 to 100 nm can be investigated. The x-ray scattering profiles throughout the manuscript represent a combination of wide-, medium-, and small-angle x-ray scattering.

Incident x-rays are predominantly scattered by the electron clouds surrounding the atomic nuclei. If we consider the scattering from a region with electron density, $\rho(\vec{x})$, then the intensity, I, of scattered x-ray's can be defined in reciprocal, $\vec{q}$-space, by the Fourier transform, Equation 2.34.[106]

$$I(\vec{q}) = \int \rho(\vec{x}) e^{-i\vec{q}\cdot\vec{x}} d\vec{x} \tag{2.34}$$

The q-dependence of the scattering intensity can also be expressed in terms of a structure factor relating to the spacing between scattering particles, see Equation 2.35, where $S(q)$ is the structure factor, x_i is the mole fraction of atoms of type i, and f_i is their form factor.[13] This representation is especially helpful in comparisons with molecular dynamics simulations since the structure factors can be computed via the computationally derived radial distribution functions and compared with experimental scattering profiles.[13]

$$I(q) = S(q)\left[\sum_i x_i f_i(q)\right]^2 + \sum_i x_i f_i^2(q) \tag{2.35}$$

The magnitude of the wave vector is given by $q = 4\pi \sin\theta/\lambda$, where 2θ is the scattering angle. From Bragg's law, we then obtain the relation, $d = 2\pi/q$, as the distance between scatterers. Typically if there exist regular distances between regions of high electron density, then a peak will be evident in the x-ray scattering profile at a q-value corresponding to the distance separating the scattering regions. In our studies, x-ray scattering is employed to provide insight into the mesoscale organization of ionic liquds. In this case, x-ray profiles exhibit what is termed a pre-peak with values of d typically ranging from 12 to 25 Å. On the basis of numerous molecular dynamics simulations which reproduce this pre-peak, the origin is assigned to the existence of distinct polar and non-polar domains within the bulk liquid.[53, 54, 108] The distance, d, in this case is associated with the separation between polar domains separated by a non-polar domain.[32, 13]

Chapter 3

Ionic Liquids

In this chapter, the influence of chemical structure on mesoscale organization and dynamics is investigated for neat and binary mixtures of imidazolium-based ILs as well as neat phosphonium ILs. The chapter begins with a brief introduction to ionic liquids and a review of prior experimental evidence of mesoscopic organization. Following this, the results of detailed experiments on the mesoscale organization and dynamics of (i) neat imidazolium-based ILs, (ii) binary mixtures of imidazolium-based ILs, and (iii) neat phosphonium-based ILs are presented. The chapter concludes with a brief summary. It is found that the development of mesoscale organization, originating in the solvophobic aggregation of non-polar aliphatic chains, leads to the emergence of a slow dynamic response in the dielectric and dynamic mechanical spectra arising from fluctuations of the aggregates. As a result of these new dynamics, we are able to tune physicochemical properties, notably the static dielectric permittivity, through composition-dependent control of mesoscale aggregate morphology and dynamics in binary ionic liquid mixtures.

3.1 Introduction and Motivation

An ionic liquid at its most basic is simply a salt which is in the liquid state at the temperature and pressure of interest. However, commonly accepted terminology makes a clear distinction between an ionic liquid and other molten salts.[109] Ionic liquids are specifically defined as those salts having a melting point below 100 °C. There are several classes of ionic liquids including aprotic, protic, solvate, and purely inorganic. The materials studied in this chapter are all examples of organic

Ionic Liquid	Anions
$AlCl_3$ + PyrCl	$[AlCl_4]^-$ $[Al_2Cl_7]^-$
$FeCl_3$ + PyrCl	$[FeCl_4]^-$
$ZnCl_2$ + PyrCl	$[ZnCl_4]^-$
LiF + BeF_2	$[BeF_4]^{2-}$ $[BeF_7]^{3-}$

Pyr = 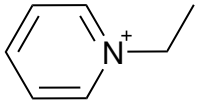

Figure 3.1: The first ionic liquids were eutectic mixtures usually consisting of a metal and organic salt. The most common were the chloroaluminates with a pyridinium salt (top entry). The reduction in melting point is due to the formation of the large anion complexes (shown on the right) and the large pyridinium cation which inhibit crystallization.

aprotic ionic liquids. Therefore, this introduction is limited to the development and investigation of the aprotic ILs, the variation in their chemical structures, applications, physical, and chemical properties. The focus is primarily on introducing aspects relevant to my work concerning the influence of mesoscale organization on dynamics and charge transport. The first aprotic materials to fit the IL description were mixtures of organic and metal salts which formed a low melting point eutectics as discovered in 1951.[110, 111, 112, 109, 43] The most common of these are the chloroaluminates based on mixtures of pyridinium chloride (PyrCl) and aluminum chloride ($AlCl_3$). The field of ionic liquids which we know today was born from the extensive research carried out in the 1970s and 1980s on these eutectics, with notable work in the groups of Bob Osteryoung and Gleb Mamantov.[113, 114] The chemical structures of some early examples of ionic liquids are shown in Figure 3.1. The depression in melting point is attributed to the formation of large anion complexes upon mixing. These large anions, together with the large organic cation, frustrate the efficient packing of molecules into a crystal structure while still satisfying the demands of charge alternation.[115, 111, 43] It should be noted that although the chloroaluminates were the most thoroughly studied they are not the only salt mixtures for which eutectic formation was observed. Other notable examples include additional metal chlorides as well as mixtures of alkali

metal salts such as the last entry in Figure 3.1. The primary applications at this point were as media for the electrodeposition of metals and as solvents for the spectroscopic study of metal complexes.[116, 117] Other major motivations for the development of these ILs was their potential application as heat transfer fluids in nuclear reactors and as battery electrolytes for the extreme conditions encountered in air and spacecraft.[118, 43] Accordingly, much of the initial development of low-melting salts was done at the US Air Force Academy and Oak Ridge National Lab.[111, 43]

A major drawback of these early ionic liquids is their instability under ambient conditions. The anions react rapidly with water to form hydrates which cannot be separated by simple physical drying in a high vacuum. This required all chloroaluminate applications to be carried out in sealed environments completely devoid of water. In addition, the eutectics were only liquid at room temperature over a very narrow composition range. The first water stable ionic liquids, reported in 1992, consisted of imidazolium and pyridinium cations combined with sulfate, nitrate, tetrafluoroborate, triflate, and mesylate anions.[119, 120] These two reports could be considered the birth place of the "modern" aprotic ionic liquids we know today. It was later found that some of the anions such as tetrafluoroborate and hexafluorophosphate do indeed react with water to form hydrofluoric acid. Due to the dangers of HF, care is still needed when handling these ILs. Also, even trace amounts of water can have a strong influence on the physicochemical properties and therefore it is good practice to keep the ILs dry through proper storage and drying protocols. After the emergence of ILs which could be handled on the bench top, their potential for a variety of new applications was soon realized. As these new applications have emerged the library of ionic liquids has also expanded. Figure 3.2 provides the chemical structures of typical modern ionic liquids. This list is by no means exhaustive. It has been estimated that the number of possible unique ionic liquids may be as high as 10^6.[52] This number balloons when we also consider mixtures as unique ionic liquids themselves. Including binary mixtures there are 10^{12} possible variations and with ternary mixtures this number reaches 10^{18}.[52]

The previous applications, electrochemistry, spectroscopic analysis, heat transfer fluids, and electrolytes, continue to be areas of active research. However, the rapid expansion of the ionic liquids field has been driven by the ever expanding variety of applications beyond those originally conceived for molten salts. These include application as solvents in different types of chemical synthesis,[60, 62, 57, 112, 61, 32] for the growth of nanoparticles and

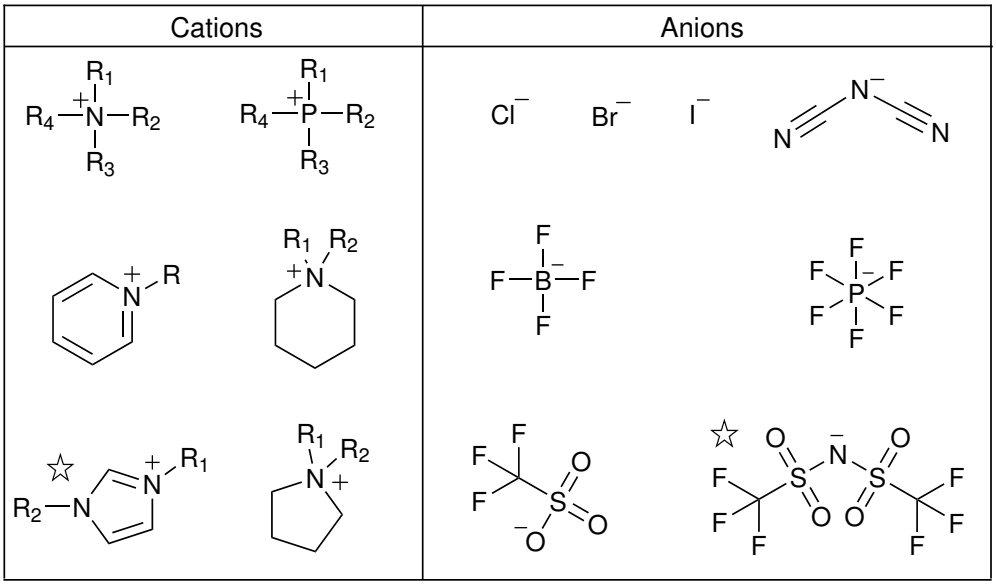

Figure 3.2: Chemical structures of commonly encountered cations and anions in modern ionic liquids. R- represents alkyl chains of varying length substituted on the cation.

other nanostructures,[121, 122, 123, 32, 124], for polymerization,[60] for extraction/separation processes,[32],and as catalysts.[57, 59, 123, 58, 61] ILs are also emerging as important solvents for the dissolution and processing of biomass including cellulose,[48, 125, 123, 112, 32] chitin,[126] and proteins.[48, 32] Their applications as electrolytes continues to expand and now encompasses electrodeposition,[121, 48, 112, 32] batteries,[121, 49, 123, 51] electromechanical actuators,[51, 48] supercapacitors,[50, 127, 51] solar cells,[123, 51] and thermochemical cells.[123, 51] They find application in the medical industry as media for drug delivery as well as antimicrobials.[123, 32] They have potential impact in renewable energy/environmental sustainability as fluids for thermal energy storage[51, 128] and CO_2 capture.[129, 130, 123, 51] There is also potential for more exotic application such as their proposed use as a liquid mirror support in a large moon-based telescope.[131] All of these varied applications arise due to the peculiar combination of properties afforded by the existence of ILs as low-melting point salts.

Ionic liquids are typically characterized as having wide thermal stability windows, wide electrochemical stability windows, moderate ionic conductivities, moderate viscosities, and extremely low volatilities. They have quite a large variability in these properties depending upon the combination of cation and anion. The ability to alter the combination of ions and the large number of possible chemical structures (10^6-10^{18}) opens the possibility of designing ionic liquids with particular

properties for a given application.[112] Accordingly, ionic liquids are often referred to as "tunable" solvents. Taking advantage of this tunability requires a detailed understanding of how the chemical structure of anions and cations contribute to the observed properties. That is, we need very detailed structure/property relationships which allow us to design new ionic liquids without synthesizing and characterizing all of the unique combinations. Rather than giving an overview of all IL properties, we will focus on those most relevant to the experimental results presented in this section including the ionic conductivity, viscosity, and static dielectric permittivity.

The transport properties dc ionic conductivity, σ_0, and fluidity, the inverse of zero-shear viscosity $1/\eta$, are both thermally-activated processes. Temperature-dependent values are given in Figure 3.3 for a prototypical ionic liquid 1-octyl-3-methylimidazolium tetrafluoroborate, C_8MIm BF_4. The dynamics which underlie the viscosity and conductivity, i.e. the structural and ion conductivity relaxations, are accessed experimentally by dynamic mechanical and dielectric spectroscopy, respectively, see the Experimental Methods section. From Maxwell's relation, the structural relaxation rate is determined by, $\omega_\alpha = G_\infty/\eta$, where the glassy shear modulus G_∞ is a few GPa. For numerous aprotic ionic liquids, it has been found that the structural relaxation and ion conduction rates coincide, see the inset of Figure 3.3(a). However, there is some evidence for a slight decoupling of the ion diffusion and structural relaxation rates as the T_g is approached.[132] The temperature dependence of the relaxation rates coincide also with the temperature dependence of σ_0 and $1/\eta$.[133] This indicates that the conductivity and fluidity of ionic liquids are intimately linked to the dynamic glass transition and accordingly to the structural relaxation rate. As the temperature decreases from 240 K and approaches the calorimetric glass transition, T_g, the relaxation rates vary over seven orders of magnitude. The dc ionic conductivities and fluidities, which are shown over a wider temperature range, vary over 10-11 orders of magnitude. An Arrhenius rate law, $\omega = \omega_\infty \exp(E_A/kT)$, corresponds to straight lines in a plot of $\log(\omega)$ *versus* $1000/T$ with slopes corresponding to the activation energy E_A. Rather than straight lines, we observe a gradual increase in the activation energy as the temperature is reduced. The increase in activation energy and the slowing down of molecular motion is common to all glass forming materials and is known as the dynamic glass transition. The temperature dependence of the structural relaxation rate as the temperature approaches the calorimetric glass transition is known as the fragility, $m = d\log(\tau)/d(T_g/T)|_{T=T_g}$.[134] The fragility can vary quite dramatically, especially

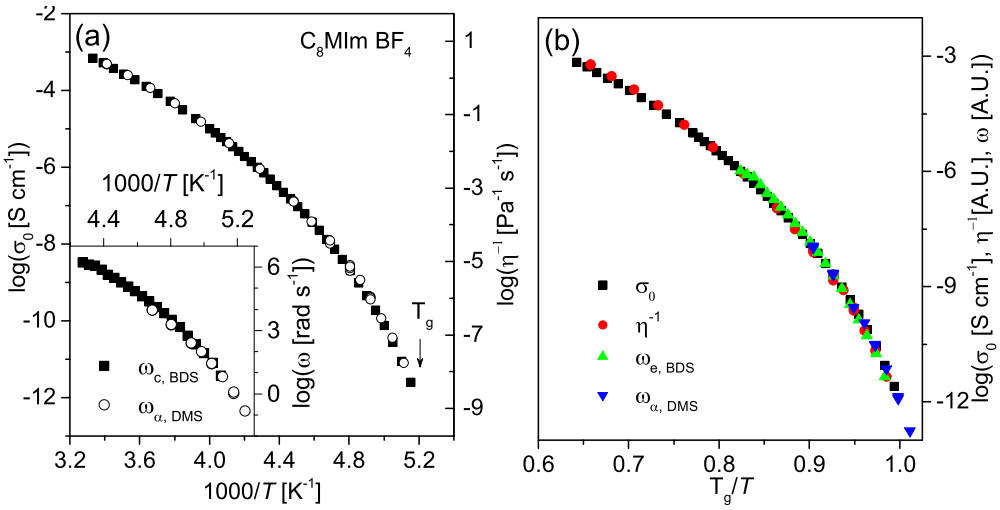

Figure 3.3: (a) DC ionic conductivity, σ_0, and fluidity, η^{-1}, of 1-octyl-3-methylimidazolium tetrafluoroborate (C_8MIm BF_4) *versus* inverse temperature. Inset: Conductivity, $\omega_{e,BDS}$, and structural, $\omega_{\alpha,DMS}$, relaxation rates obtained by dielectric and dynamic-mechanical spectroscopy, respectively. (b) DC conductivity, fluidity, and relaxation rates *versus* temperature normalized by the calorimetric glass transition temperature, T_g. The fluidities and relaxation rates are vertically shifted to illustrate their identical temperature dependence.

with changing cation structure.[135] The close coupling of the dc ionic conductivity with the structural relaxation in ionic liquids makes it necessary to consider how changes to the dynamic glass transition which occur as a result of changes to the chemical structures of the cations and anions can influence the room temperature dc ionic conductivity. The influence of chemical structure changes on charge transport and dynamics is therefore interesting both from the standpoint of developing structure/property relationships for the future application of ILs as well as for the testing and development of theories of the glass transition.

Currently, no theory of glass formation is capable of explaining all experimental observations.[136, 137, 87, 138, 29, 139, 140, 134, 141, 142, 143, 144, 145] The variety IL chemical structures which are easily super-cooled make them useful materials for further study of glass formation physics. For some simple cases and reduced classes of ILs general trends may be highlighted. The primary interaction in ionic liquids is the Coulombic repulsion and attraction experienced between like and un-like charges. By increasing the anion volume while maintaining the same charge, the overall charge density is reduced which decreases the Coulombic interaction strengths. This in turn reduces the cohesion energy of the fluid and the T_g.[115] A similar reduction in the cohesion energy can occur if the van der Waals interactions are weakened

by making the ions less polarizable. Therefore, if the goal is to increase the room-temperature ionic conductivity and fluidity it is best to use a large, highly fluorinated anion. These types of ions are therefore the most common, especially bis(trifluoromethylsulfonyl)imide (NTf_2). They have the added benefit of making the ILs less hygroscopic. This is however only a general trend and a great deal of variability in T_g is found as both the cation and anion are varied.[115, 146, 43] For a given cation, it seems that the size and polarizability effect on the T_g dominate the observed changes in σ_0 and η^{-1}. On the other hand, altering the cation strongly influences both fragility and T_g. A contributing factor to this disparity may be the formation of solvophobic aggregates in the ionic liquids with long alkyl chains substituted on the cation. This type of mesoscopic organization is typically not accounted for in theories of glass formation. However, they may play an important role.[29] The formation of these aggregates is discussed in more detail later.

The dc ionic conductivity is also influenced by the fraction of ions which actually contribute to long-range charge transport. This value is referred to as the ionicity of the IL. It is most often estimated using the qualitative Walden plot analysis. In this analysis, a plot is made of molar conductivity, Λ[S cm^2 mol^{-1}], *versus* fluidity, η^{-1}[Pa^{-1} s].[43] "Good" ion conductors fall higher on this plot while "poor" ion conductors fall lower. In aprotic ionic liquids, where both σ_0 and η^{-1} are coupled to the structural relaxation, the better the ion conductor the higher is its ionicity.[11, 43] An example of a Walden plot for some aprotic ionic liquids is provided in Figure 3.4. In this limited selection of ILs, we can see that the larger quaternary phosphonium ionic liquids which contain a significant non-polar volume fraction tend to have lower ionicities than the smaller pyridinium ILs. A more quantitative estimate of ionicity may be obtained through a combination of the Einstein-Smoluchowski relation and basic electrodynamic theory. From fundamental electrodynamics, we can relate the total ionic conductivity, σ_0, to the mobility, μ, number density, n, and charge, q, of all ions contributing to the ionic conductivity by the equation, $\sigma_0 = \sum_i q_i \mu_i n_i$, where the sum is carried out for all unique ionic species, i. The mobility of ions is related to their diffusivity, D, by the Einstein-Smoluchowski relation, $\mu = qD/kT$.[147, 148] The diffusivity of charge carriers may be found experimentally, for instance by PFG-NMR, or it may be estimated from the ion conductivity rates as, $D = \lambda^2 \omega_e$, where $\lambda \approx 1 - 2$Å is the mean ion-hopping distance. The number density of ions is then given by, $n = \sigma_0 kT/q^2 D$.[149, 150, 151, 152, 153] The ionicities estimated in this manner, n/n_T, where n_T is the total number density of ions, have been found to range from

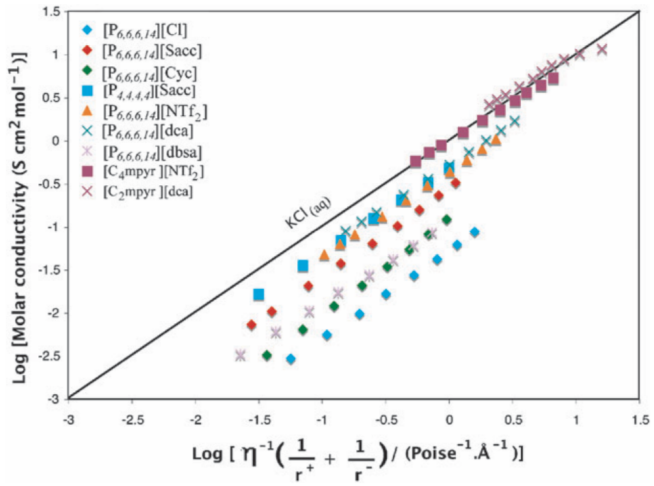

Figure 3.4: Walden plot analysis for a selected group of ionic liquids based on the quaternary phosphonium, $P_{6,6,6,14}$, and pyridinium, Pyr, cations. This is a special type of Walden plot introduced by MacFarlane which includes a correction for differing ion sizes. The line represents data for a 0.01M aqueous HCl solution and is taken as a baseline for a good ion conductor. Reproduced from [11].

30 to 85%.[154, 150] A further, but related, method for estimating ionicity is the Haven ratio. In this approach, the diffusivity obtained by PFG-NMR is used to estimate the molar conductivity via the Nernst-Einstein equation with the assumption that all charge carriers participate in charge transport, $\Lambda_{NMR} = N_A q^2(D)/kT$, where N_A is Avogadro's constant.[155] A ratio is then made with the measured molar conductivity, $\Lambda_{BDS}/\Lambda_{NMR}$. This ratio is equivalent to the ionicity n/n_T. The Haven ratio was originally developed for ion conduction in glassy and crystalline solids. A Haven ratio equal to one indicates that molecular and charge diffusion proceed in the same uncorrelated manner.[156] This is generally only observed in some very dilute electrolytes where the distance separating charges exceeds their Bjerrum length meaning the interaction between charges is weaker than the thermal energy.[157, 158, 159] In pure ionic liquids, the ions are very closely packed and ion motions become more correlated. For instance, when a cation jumps it leaves behind a hole which, considering the preferential interaction of cations with anions rather than other cations, is more likely to be filled by a nearby anion.[156] This correlated motion of cations and anions in the same direction contributes to molecular diffusion, but not charge conduction.[150, 156] Therefore, Haven ratios in more concentrated electrolytes are expected to be less than unity.[160]

Another property critical for the majority of IL applications is their ability to solvate different types of solute molecules and surfaces. This solvation ability is related to the solvent polarity,

defined as the sum of all specific and nonspecific intermolecular interactions between the solvent and solute molecules.[44, 57] There has been a considerable effort to correlate the cation and anion chemical structures to this important property. Solvent polarity can be measured in a number of different ways including: "dielectric constant", Hildebrand solubility parameters, probe-molecule spectroscopy, and Kamlet-Taft parameters.[161, 162, 163, 57, 164] Each of these measures carries its own advantages and limitations. In many instances, the polarity and its trend with chemical structure are significantly different depending on which approach is used.[57, 165, 166] For this reason, universal agreement as to the polarity of ILs has not be reached.[57, 163, 167] However, it is generally found that ILs have only modest polarities with values near those of monohydroxy alcohols.[57]

The static dielectric permittivity (dielectric constant) is one of the most often cited measures of solvent polarity.[57] This value is obtained as the low-frequency limit of the real part of complex dielectric permittivity. It therefore contains contributions from electronic, atomic, dipolar, and ionic polarization, see the Experimental Methods section. Values of the dielectric constant are often reported from dielectric measurements made in the microwave region at room temperature and vary between 10-15.[162, 163, 168, 169, 170] One drawback of measuring in this experimental range is the neglected possibility of contributions from slower relaxations. Recent optical Kerr-effect spectroscopy, neutron spin echo, dielectric, and dynamic light scattering measurements on ILs with long alkyl chains show that such slow relaxation do occur, although their origins remain unclear.[154, 171, 172, 12] The observation of slow, sub-α dynamics in those ILs with extended non-polar alkyl chains suggest that organization induced by the solvophobic segregation of such chains, may contribute to such dynamics.

The commonly used cations shown in Figure 3.2 all have alkyl chains substituted on the charge center. These chains make the cation bulky and aid in the formation of a low-melting ionic liquid. As the length of the alkyl chain is increased, for instance at the R_2 chain on the imidazolium ring, the cation becomes increasingly amphiphilic with a distinct polar(charged) and non-polar(non-charged) region. These cations begin to resemble traditional surfactant molecules which are capable of self-assembly in solution via hydrophobic aggregation to form micellar-type aggregates. Over the past decade, there has been mounting evidence that ionic liquids with short (C≈4) to moderate (C≈12-16) length alkyl chains tend also tend to form similar aggregates. This organization is observed in

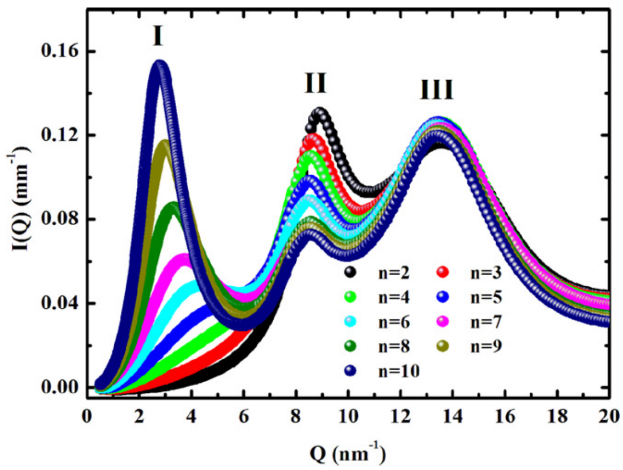

Figure 3.5: Small and wide-angle x-ray scattering of 1-alkyl-3-methylimidazolium bis(trifluoromethylsulfonyl)imide (C_nMIm NTf_2) with alkyl chain lengths varying from ethyl(n=2) to decyl(n=10). The three peaks are assigned based on detailed MD simulations of numerous ILs: peak I is the polar/non-polar alternation peak, peak II the charge-alternation peak, and peak III the adjacency peak. Reproduced from [12].

both the bulk liquid as well as in molecular solvents.[32, 173, 174, 175, 176] This is in contrast to traditional ionic surfactants which form crystalline or amorphous solids at room temp.[44, 177] At longer chain lengths they can transition into liquid crystals.[178] These mesoscale aggregates are formed by the exclusion of the non-polar chains from the polar region occupied by the charged head groups. Due to the absence of water, this mechanism is referred to as solvophobic rather than hydrophobic aggregation. The emergence of this mesoscale organization may, as previously mentioned, influence ε_s if it exhibits a strong dielectric relaxation. It may also have a strong influence on the dynamic glass transition, both the fragility and the T_g, and accordingly on the viscosity and dc ionic conductivity.[29] In addition, it may influence the ionicity and further reduce the ionic conductivity.[179]

The primary experimental observation attributed to the formation of mesoscale solvophobic aggregates is the emergence of a low momentum transfer (q) pre-peak in the small-angle x-ray and neutron scattering intensity profiles of ionic liquids with extended alkyl chains.[32, 55, 180, 21, 20, 181] An example of such a pre-peak is shown in Figure 3.5 for a series of ionic liquids with the 1-alkyl-3-methylimidazolium cation and bis(trifluoromethylsulfonyl)imide anion, chemical structure indicated by a ☆ in Figure 3.2.[12] The development of a peak at a q-value of $\approx 0.3\ \text{Å}^{-1}$ occurs when the alkyl chain length of the R_2 chain is greater than or equal to five carbons.

At a chain length of eight carbons the real space distance corresponding to this correlation is $d \approx 18.9$ Å$= 2\pi/q$. Considering only the geometry of a fully extended, all-trans alkyl chain, Figure 3.6, we can see that this distance is considerably larger than the dimensions of the cation. This indicates a supramolecular origin for the correlation which underlies this pre-peak. The origin of the correlation has been found by numerous molecular dynamics (MD) simulations.[32, 54, 182] Using pair radial distribution functions these MD-simulations give estimates of structure-functions which closely match the experimental scattering profiles.[183, 184] Deconvoluting the contributions to each of the three peaks of Figure 3.5 reveals their molecular origins.[13, 185] These origins are illustrated in Figure 3.6. The pre-peak corresponds to the separation of polar (ionic) regions which are separated by a non-polar region consisting of opposing alkyl chains. The intermediate peak, peak II in Figure 3.5, corresponds to the distance separating ions of like-charge within the polar domain. These peaks are commonly referred to as the polarity and charge alternation peak, respectively. The third peak arises from closer range correlations of both inter- and intramolecular origin and is typically not closely analyzed.[13] MD simulations also provide three dimensional snapshots of the organization (morphology) of the polar and non-polar domains, see Figure 3.7. These snapshots and the analysis of the connectivity of polar and non-polar groups show that in the C_nMIm-based ILs the mesoscale organization may be characterized as bicontinuous with percolating polar and non-polar domains.

The existence of large and separated polar and non-polar regions within an IL can have an important influence on its solvation properties.[186] It can give the ability for the IL to solvate both polar and non-polar molecules. Investigation of probe-molecule dynamics reveal the existence of different dynamics within the two regions.[187, 13] For this reason, there is a great deal of interest in developing our understanding of mesoscale organization. These solvophobic aggregates may be critical to the application of ILs in chemical synthesis, separations, and energy storage.[32]

Scattering experiments and the complementary MD simulations have been carried out for all of the common imidazolium, pyridinium, pyrrolidinium, phosphonium, and ammonium ionic liquids shown in Figure 3.2.[32] Despite this wealth of information on the static mesoscale structure, there is an extremely limited amount of information on the dynamics and lifetimes of the mesoscopic structures. Currently, direct evidence of the mesoscale dynamics is limited to neutron spin echo spectroscopy.[16, 15] Neutron spin echo measurements reveal that the decay in correlation at the

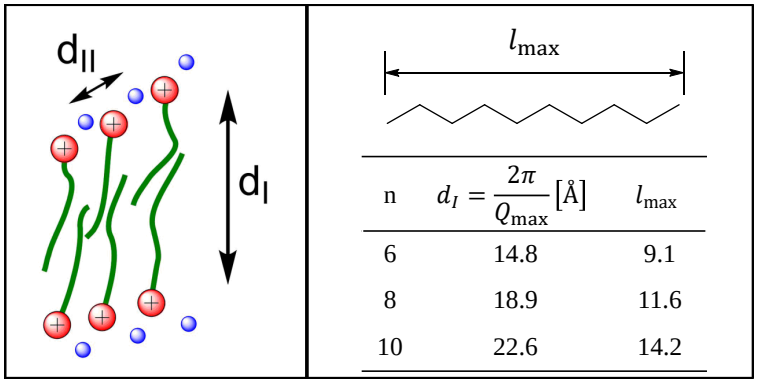

n	$d_I = \frac{2\pi}{Q_{max}}$ [Å]	l_{max}
6	14.8	9.1
8	18.9	11.6
10	22.6	14.2

Figure 3.6: Left: Illustration of the distances corresponding to peak I and peak II in Figure 3.5. Peak I is the distance between polar regions separated by a non-polar domain of opposing alkyl chains. Peak II originates in the ordering of ions within the polar phase and in general represents the distance separating ions of like charge.[13] Right: The real-space distance corresponding to Q_{max}, $d_I = 2\pi/Q_{max}$ is significantly larger than the dimensions of a single molecule. It is , for instance, much larger than the length of an all trans alkyl chain, l_{max}. This indicates the supramolecular origin. The data for d_I correspond to the C_nMIm NTf_2 IL series in Figure 3.5.[12]

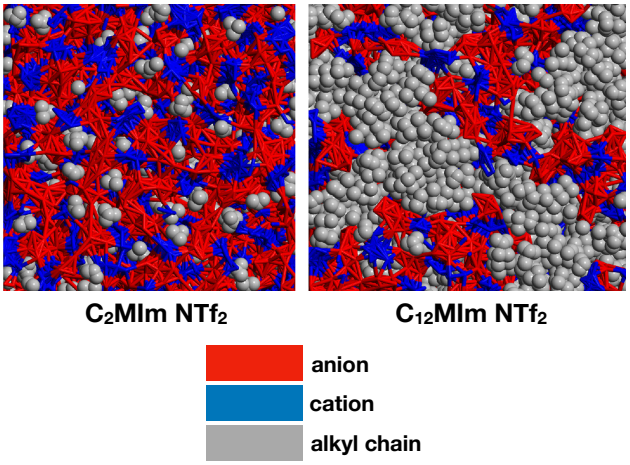

Figure 3.7: Three-dimensional snapshot from a molecular dynamics (MD) simulation of 1-ethyl-3-methylimidazolium bis(trifluoromethylsulfonyl)imide (C_2MIm NTf_2) and 1-dodecyl-methylimidazolium bis(trifluoromethylsulfonyl)imide (C_{12}MIm NTf_2). Reproduced from [14].

pre-peak is significantly slower than at the charge alternation peak. This is a direct evidence that the aggregates fluctuate at rates much slower than the structural relaxation. Drawbacks to these measurements include their difficulty, requiring deuterated samples and days of measurement time per sample, as well as the limited beamtime available at neutron sources. They are also only capable of capturing very fast dynamics from pico- to nanoseconds. Probing the correlation between the mesoscale aggregate organization, dynamics, and ion chemical structure is vital to understand the influence of solvophobic aggregation on the dynamic glass transition, dc ionic conductivity, zero-shear viscosity, and static dielectric permittivity. Therefore, there is a pressing need for additional experimental measurements of the mesoscale aggregate dynamics.

In this chapter, we establish the existence of new experimental probes of mesoscale aggregate dynamics in the dielectric and dynamic mechanical spectra of imidazolium, ammonium, and phosphonium ionic liquids. These dynamics are shown to contribute directly to increases in both the zero-shear viscosity and static dielectric permittivity. Using binary IL mixtures we confirm the mechanism of the dielectric relaxation to be interfacial polarization due to the fluctuation of charge density at the polar/non-polar interfaces. We further demonstrate the application of IL mixtures as a method to tune the viscosity, dc ionic conductivity, and static permittivity of ionic liquids by direct manipulation of mesoscale aggregate shape and volume fraction.

3.2 Dynamic-Mechanical and Dielectric Evidence of Long-Lived Mesoscale Organization in Ionic Liquids

In this section, a series of 1-alkyl-3-methylimidazolium ionic liquids with tetrafluoroborate and bis(trifluoromethylsulfonyl)imide anions are investigated by broadband dielectric and dynamic-mechanical spectroscopy. The length of the alkyl chain substituted on the cation is increased systematically from propyl to octyl. According to x-ray, neutron and MD simulation studies available in the literature, mesoscale organization due to solvophobic aggregation of the non-polar alkyl chains occurs at chain lengths of approximately four to five carbons. We found that at this critical chain length a sub-α relaxation emerges in the dielectric and dynamic-mechanical spectra of these imidazolium-based ionic liquids. The relaxations are tentatively assigned to fluctuations

of the mesoscale aggregates. The dielectric relaxation in particular is attributed to an interfacial polarization mechanism at the polar/non-polar interface with relaxation rates comparable to the slow relaxation probed by neutron spin echo at q-values of the aggregate pre-peak. The static dielectric permittivity, ε_s, and the zero-shear viscosity, η, are both increased due to the additional processes.

This section is a reprinting of a previously published article and its supporting material. My primary contributions to this article include: (i) data analysis, (ii) interpretation of results, and (iii) writing. Changes from the published version consist of the incorporation of supporting information within the main text.

Abstract

Experimental evidence of the dynamics of mesoscopic structure in room temperature ionic liquids—a feature expected to correlate with many physicochemical properties of these materials—remains limited. Here, we report the observation of slow, sub-α relaxations corresponding to dynamics of nanoscale hydrophobic aggregates in a systematic series of 1-alkyl-3-methylimidazolium-based ionic liquids from detailed analysis of dynamic-mechanical and broadband dielectric spectra. The emergence of the sub-α relaxations correlates with increases in the zero-shear viscosity and static dielectric permittivity, constituting direct evidence of the influence of mesoscale aggregation on the physicochemical properties of ionic liquids.

Introduction

Ionic liquids (ILs) are a versatile class of fluids consisting entirely of cations and anions conventionally categorized as having melting temperatures below 100 °C. The molecular structures of the constituent ions and, consequently, the resultant intermolecular interactions, are central to tuning their physicochemical properties such as viscosity, ionic conductivity, density, thermal and electrochemical stability, and polarity. There has been a concerted effort to understand

the impact of molecular organization on physicochemical properties of ILs during the past 2 decades.[44, 188] A recent advance in this respect is the observation of mesoscale organization in bulk ILs arising from the hydrophobic aggregation of extended alkyl tails located on the ionic head groups of a variety of imidazolium, pyridinium, pyrrolidinium, phosphonium, and ammonium cations.[32, 54, 55, 13, 189, 182, 185, 190, 191, 192, 18] Due to their ability to solvate both polar and nonpolar molecules, the formation of such nanoscale aggregates could provide ILs with possible advantages for a variety of solvent applications such as polymerization, organic synthesis and catalysis, as well as nanoparticle growth.[32, 192, 62, 15, 187] Until now, experimental evidence of mesoscale organization has been mainly provided by observation of structural features from low momentum transfer (q) peaks in X-ray and neutron scattering functions. Coupled with molecular dynamics simulations, the structure functions reveal the existence of complex architectures ranging from micellar-like spherical aggregates to extended bicontinuous structures as a function of the alkyl chain length.[54, 55, 13, 189, 182, 185, 190, 191, 192, 18] The influence of these structures on the physicochemical properties of ILs depends strongly on the lifetimes of the nanoscale aggregates.[15, 187, 13] However, neutron spin echo (NSE) spectroscopy is one of the few techniques currently known to be capable of probing such dynamics, albeit at rather short time scales.[15, 133, 16] These measurements are tedious to carry out as they require deuterated IL samples and access to suitable neutron facilities. To date, NSE data for only two ILs, namely, 1-octyl-3-methylimidazolium and 1-hexyl-3-methylimidazolium bis(trifluoromethylsulfonyl)imide, have been reported in the literature.[15, 133, 16] Other studies involving optical Kerr effect and dielectric spectroscopy at time scales faster than nanoseconds have reported slow, sub-α relaxation modes, attributed to the existence of mesoscale aggregation, in the recent past.[172, 193] The question regarding whether the nanostructures observed in imidazolium-based ILs have lifetimes beyond a few nanoseconds has remained unanswered. Despite the rapid and significant advances in our understanding of mesoscale organization in bulk ILs, experimental techniques capable of directly probing the dynamics of such aggregates have thus far been limited to fast time scales. How long-lived are these mesoscopic aggregates and how do they influence the physicochemical properties of ILs? To address these questions, it is necessary to find other experimental techniques that can probe detailed signatures of the mesoscale aggregates and their dynamics over much broader time scales.[15]

In this Letter, we report the observation of slow, sub-α dynamics in the shear-mechanical and dielectric spectra of a series of alkyl imidazolium ILs with tetrafluoroborate and bis(trifluoromethylsulfonyl)imide anions. These features are not present in the imidazolium ILs with alkyl spacer lengths equal to or shorter than butyl but rather emerge only for ILs that have been shown to be capable of hydrophobic aggregation, as evidenced by previous X-ray and neutron scattering experiments complemented by molecular dynamics simulations.[32, 54, 55, 189, 185] The slow, sub-α relaxation is attributed to the motion of extended mesoscale aggregates. This is the first time, to our knowledge, that evidence of long-lived mesoscopic aggregates in ILs is reported from dynamic-mechanical spectroscopy. In addition, the rates of the slow dielectric relaxation agree well with those obtained by NSE, indicating that this is a complementary approach to probe the interplay of aggregate formation, morphology, and dynamics in these complex fluids.

Experimental

The dielectric data for 1-octyl-3-methylimidazolium bis(trifluoromethylsulfonyl)imide, 1-butyl-3-methylimidazolium bis(trifluoromethylsulfonyl)imide, 1-propyl-3-methylimidazolium bis(trifluoromethylsulfonyl)imide, and 1-butyl-3-methylimidazlium tetrafluoroborate as well as rheology data for 1-butyl-3-methylimidazolium tetrafluoroborate are reproduced from previous publications by the authors.[150, 152, 151] 1-octyl-3-methylimidazolium tetrafluoroborate, 1-hexyl-3-methylimidazolium tetrafluoroborate, and 1-hexyl-3-methylimidazolium bis(trifluoromethylsulfonyl)imide were purchased from Iolitec and dried under vacuum (10^{-6} bar) at 60 °C for 24 hours prior to use. Broadband dielectric spectroscopy measurements were made in the frequency range of $10^{-1} - 10^{7}$ Hz using a Novocontrol Alpha Analyzer with a QUATRO liquid nitrogen temperature control system with temperature stability ± 0.1 K. Samples were measured in a parallel plate capacitor geometry with 20mm diameter stainless steel electrodes. A sample thickness of 0.2mm was maintained using Teflon spacers. The dynamic-mechanical spectra of 1-octyl-3-methylimidazolium and 1-hexyl-3-methylimidazolium tetrafluoroborate were obtained via oscillatory shear measurements over the frequency range 0.1-100 Hz with 0.05-2 strain% on an Hybrid Rheometer 2 (TA Instruments) using parallel plate geometry with diameters of 20 mm, 8 mm, and 3 mm. The temperature was controlled by an Environmental Test Chamber with nitrogen as the gas source.

Results and Discussion

The complex shear modulus, $G^* = G'(\omega) + iG''(\omega)$, of glass-forming 1-alkyl-3-methylimidazolium tetrafluoroborate ILs (AlkylMIm BF_4) with alkyl spacer lengths of butyl, hexyl, and octyl are shown in Figure 3.8a. The shift factors are provided in the Figure 3.9. The real and imaginary parts of the complex modulus, G' and G'', are scaled by the high-frequency shear modulus, G_∞, and plotted versus frequency normalized by the structural relaxation rate at the glass transition, ω_α. Simple molecular glass-forming liquids are expected to display a single mechanical relaxation corresponding to the glass transition with low-frequency slopes of 2 and 1 for G' and G'', respectively.[88] As shown in Figure 3.8, this response is observed for 1-butyl-3-methylimidazolium tetrafluoroborate (ButylMIm BF_4). However, upon increasing the alkyl spacer length to octyl, a substantial departure from a simple Maxwell relaxation occurs at time scales slower than the structural relaxation rate. This terminal relaxation in G' is reminiscent of chain relaxations in the rheological response of short-chain polymers.[194, 195] The complex shear modulus, G^*, of 1-octyl-3-methylimidazolium tetrafluoroborate (OctylMIm BF_4) is fit by a combination of two Cole-Davidson-modified Maxwell relaxation models:

$$G' = Re\left[G_\infty\left(1 - \frac{1}{(1 + i\omega\tau_\alpha)^\gamma}\right) + G_{\infty,aggregate}\left(1 - \frac{1}{(1 + i\omega\tau_{slow})^\gamma}\right)\right] \tag{3.1}$$

where G_∞ and $G_{\infty,aggregate}$ are the high-frequency limiting shear moduli of the two relaxations, τ_α and τ_{slow} are the relaxation times of the structural α-relaxation and sub-α relaxation, respectively, and γ is a parameter associated with the spectral shape.[94] The relaxation rate $\omega_\alpha = 1/\tau_\alpha$ and $\omega_{slow} = 1/\tau_{slow}$, extrapolated over a broad temperature range using the shift factors, are presented in Figure 3.12b and discussed later in the current work.

In low-molecular-weight ILs, the primary structural relaxation is coupled to the translational motion of ions, as evidenced by numerous studies utilizing dielectric spectroscopy, dynamic light scattering, differential scanning calorimetry, and rheology.[188, 150] Accordingly, the slow, sub-α relaxation mode must arise from structures significantly larger than those responsible for the primary structural relaxation. X-ray and neutron scattering experiments coupled with molecular dynamics simulations have indicated that 1-alkyl-3-methylimidazolium tetrafluoroborate ILs begin to form distinct hydrophobic aggregates when the alkyl spacer is six carbons long, and nonpolar

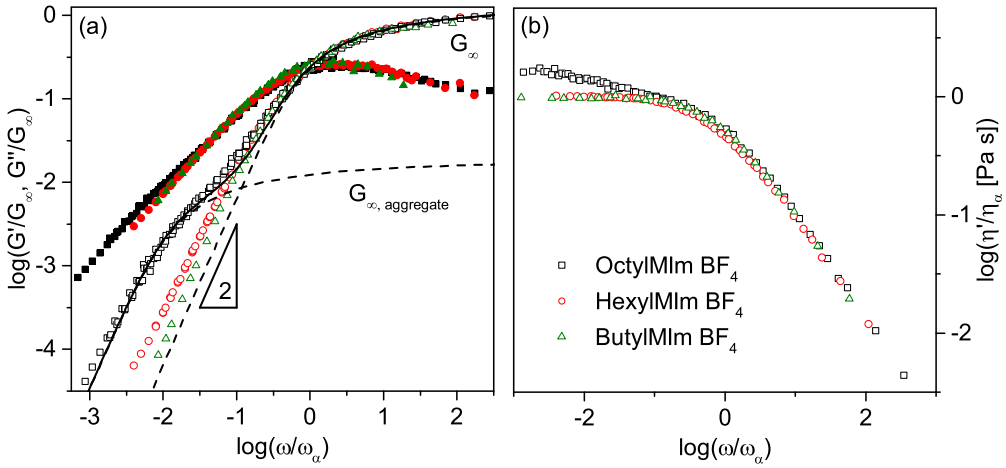

Figure 3.8: (a) Real (G', open symbols) and imaginary (G'', closed symbols) parts of the complex shear modulus, G^*, of 1-alkyl-3- methylimidazolium tetrafluoroborate ILs with alkyl spacer lengths of butyl, hexyl, and octyl. The spectra are normalized with respect to the high-frequency shear modulus, G_∞, and the structural relaxation rate, ω_α. (b) Real part of the complex viscosity normalized by the viscosity contribution of structural α-relaxation.

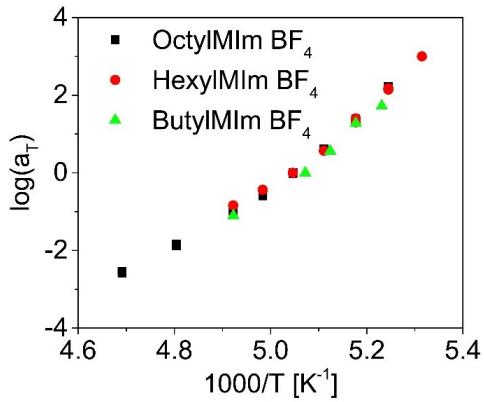

Figure 3.9: Shift factors, a_T, used to construct the dynamic shear modulus master curves in Figure 3.8.

domains percolate the entire material at spacer lengths of approximately eight and longer.[32, 54, 55, 185] The emergence of the new terminal relaxation is therefore attributed to dynamics of these mesoscale aggregates. Similar rheological responses have also been observed in glass-forming monohydroxy alcohols (MAs), systems in which aggregation occurs by intermolecular hydrogen bonding interactions.[94, 196, 197] Recently, compressibility measurements on two representative MAs revealed a similar low-frequency response in the complex adiabatic bulk modulus, thereby linking the terminal relaxation to density fluctuations.[197] A signature of the terminal relaxation is also observed in the broad-band dielectric spectra of MAs, referred to as the slow Debye relaxation due to its approximately single-exponential relaxation time distribution. It is therefore of interest to investigate whether such slow dielectric relaxations associated with dynamics of supramolecular aggregates occur in 1-alkylimidazolium-based ILs as well.

Despite extensive investigations of ILs utilizing dielectric spectroscopy, only two research groups have reported slow, sub-α relaxation dynamics.[172, 193, 171] The origin of the observed slow dynamics remains unclear. To elucidate a possible link between these slow relaxations and mesoscale aggregation, we have revisited the dielectric spectra of a series of 1-alkyl-3-methylimidazolium ILs with varying alkyl spacer lengths and bis(trifluoromethylsulfonyl)imide and tetrafluoroborate anions because imidazolium ILs have been the most widely investigated category using several complementary experimental and computational techniques. The complex dielectric permittivity, $\varepsilon^*(f) = \varepsilon'(f) - i\varepsilon''(f)$, and conductivity, $\sigma^*(f) = \sigma'(f) + i\sigma''(f)$, spectra for the IL 1-octyl-3-methylimidazolium bis(trifluoromethylsulfonyl)imide (OctylMIm NTf_2) are presented in Figure 3.10. Application of the derivative analysis, $\varepsilon''_{der} = (-\pi/2)[\partial\varepsilon'/\partial\ln(f)]$, reveals the existence of two distinct dielectric loss peaks. Fitting the real part of the complex dielectric function, $\varepsilon'(f)$, using eq 3.2, a combination of two Havriliak-Negami functions with a power law function included to account for low-frequency electrode polarization provides an excellent description of the complex permittivity, conductivity, and ε''_{der} spectra:[3]

$$\varepsilon^*(\omega) = \varepsilon_\infty + \frac{\sigma_0}{i\omega\varepsilon_0} + \left(\frac{\Delta\varepsilon_e}{(1+(i\omega\tau_e)^\beta)^\gamma}\right) + \left(\frac{\Delta\varepsilon_{slow}}{(1+(i\omega\tau_{slow})^\beta)^\gamma}\right) + A(\omega)^n \tag{3.2}$$

where $\omega = 2\pi f$, ε_∞ is the high-frequency limiting permittivity, σ_0 the dc ionic conductivity, ε_0 the vacuum permittivity, $\Delta\varepsilon_\alpha$ and $\Delta\varepsilon_{slow}$ are the dielectric strengths, τ_e and τ_{slow} are the relaxation

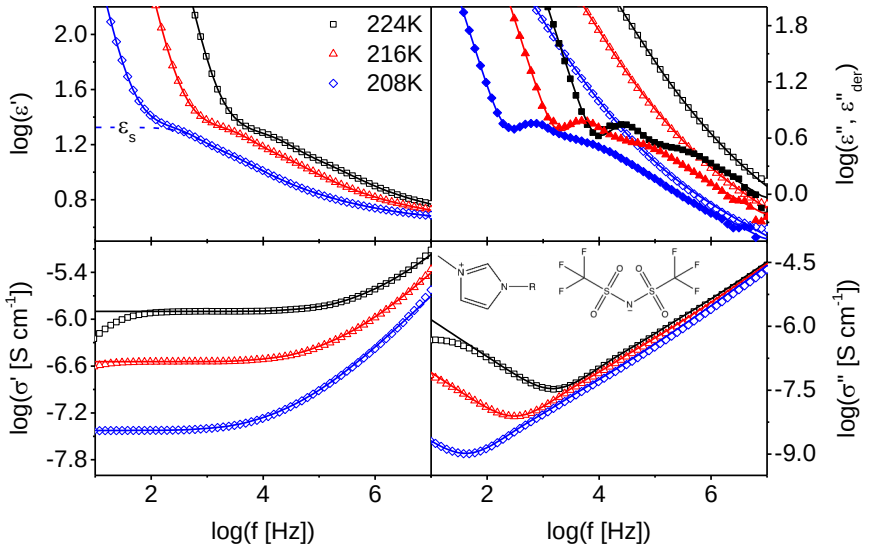

Figure 3.10: Real, ε' and σ', and imaginary, ε'' and σ'', parts of the complex permittivity and conductivity, ε^* and σ^*, of OctylMIm NTf_2. The derivative spectra, $\varepsilon''_{der} = (-\pi/2)[\partial\varepsilon'/\partial \ln(f)]$ (solid symbols), reveal a slow relaxation that is obscured by conductivity in the dielectric loss.

times, and β and γ are stretching parameters. The pre-exponential factor, A, and exponent, n, of the power-law function account for the low-frequency dispersion due to electrode polarization. The mean rate of the faster relaxation corresponds closely to the frequency of the peak in the imaginary part of the complex dielectric modulus, $M''(f)$, as well as rates for fits by the random barrier model and is therefore attributed to ion hopping conduction.[151, 198] It has previously been reported, and is also illustrated in Figure 3.12, that the mean ion hopping rates in these imidazolium-based ILs agrees well with those of the structural relaxation.[150] The slower relaxation is not readily observable in any representation other than the derivative of the real part of the dielectric function, presumably due to the dominant contribution of the ionic conductivity to the dielectric and conductivity spectra. The ε''_{der} spectrum of OctylMIm NTf_2 is compared with that of 1-alkyl-3-methylimidazolium bis(trifluoromethylsulfonyl)imide (AlkylMIm NTf_2) ILs with alkyl lengths of propyl, butyl, and hexyl in Figure 3.11a; a similar comparison is made for the tetrafluoroborate-based series in Figure 3.11b. The derivative spectra of each IL are presented at temperatures where the ion hopping rates are approximately equal. In this representation, a distinct dielectric relaxation, approximately 10-20 times slower than ω_e, is observed at spacer lengths of hexyl and octyl. The dielectric spectra of the ILs with shorter spacer lengths are described by a single Havriliak-Negami

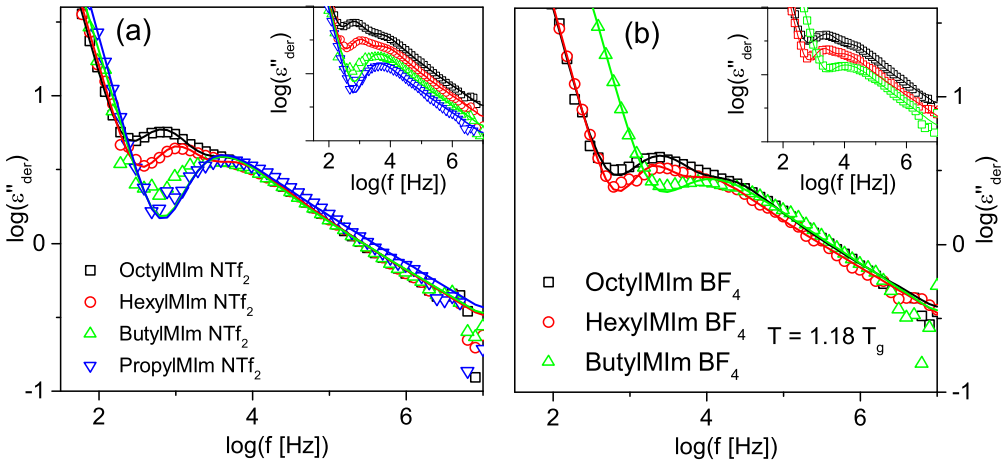

Figure 3.11: Derivative spectra, $\varepsilon''_{der} = (-\pi/2)[\partial\varepsilon'/\partial\ln(f)]$, of 1-alkyl-3- methylimidazolium ILs with (a) bis(trifluoromethylsulfonyl)imide and (b) tetrafluoroborate anions and indicated alkyl spacer lengths at a fixed mean ion hopping rate. Insets: Data are shifted vertically for clarity.

function due to the disappearance of the slow relaxation, although for butyl there appears to be a weak additional spectral contribution at lower frequencies.

The mean relaxation rates of the ion hopping and slow, sub-α dielectric relaxations are presented in Figure 3.12a,b for the bis(trifluoromethylsulfonyl)imide and tetrafluoroborate IL series, respectively. Interestingly, the rates obtained from NSE by Kofu et al. for the low-q peak in OctylMIm NTf_2 and by Russina et al. in HexylMIm NTf_2 are in good agreement with those of the slow dielectric relaxation, as illustrated by a fit using the Vogel-Fulcher-Tammann equation, $\omega = \omega_\infty \exp[B/(T - T_0)]$, where ω_∞ is the high-temperature limit of the relaxation rate, B is the curvature, and T_0 is the Vogel temperature; see the solid lines in Figure 3.12a.[15, 133, 16] Structural and slow, sub-α relaxation rates obtained from the dynamic mechanical spectra for 1-octyl-3-methylimidazolium tetrafluoroborate are compared with the dielectric relaxation rates in Figure 3.12b. The slow, sub-α relaxation rates in the rheological response are slower and more sensitive to the alkyl spacer length than the corresponding dielectric relaxation, as seen in Figures 3.12b, 3.8a, and 3.11b. This discrepancy might be due to sensitivity of the terminal relaxation to the percolation of hydrophobic domains at the octyl spacer length.

The time scales associated with the slow process observed in the broad-band dielectric spectra correlate with those from NSE and dynamic-mechanical data, confirming the existence of long-lived mesoscopic structures. The slow dielectric relaxation is attributed to interfacial polarization

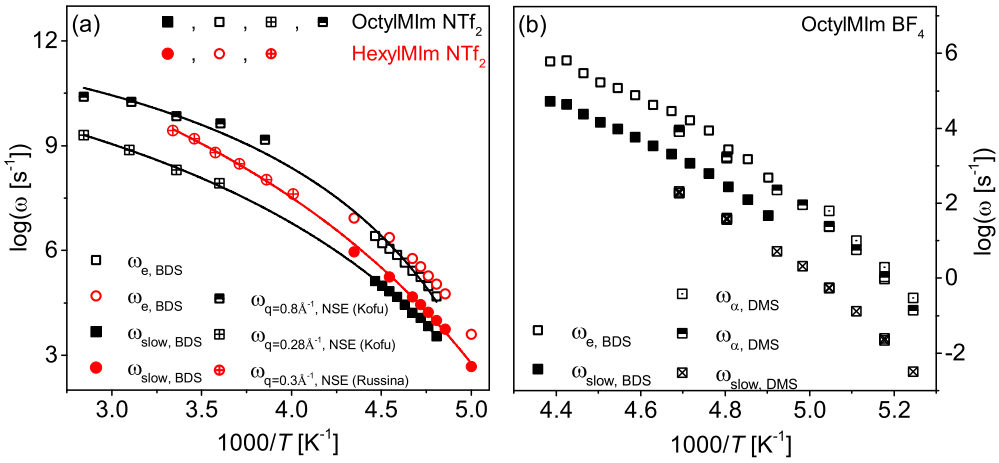

Figure 3.12: (a) Temperature dependence of the dielectric relaxation rates, $\omega_{e,BDS} = 1/\tau_e$ and $\omega_{slow,BDS} = 1/\tau_{slow}$, for AlkylMIm NTf_2 ILs with alkyl spacer lengths of hexyl and octyl, shown as circle and square symbols, respectively. The rates previously reported by NSE, at the indicated q-values, are provided as crossed and half-filled symbols.[15, 16] Lines correspond to fits with the Vogel-Fulcher-Tammann equation, with parameters provided in Tables 3.1 and 3.1. (b) Temperature dependence of the dielectric relaxation rates, $\omega_{e,BDS}$ and $\omega_{slow,BDS}$, and dynamic-mechanical relaxation rates, $\omega_{\alpha,DMS}$ and $\omega_{slow,DMS}$, for 1-octyl-3-methylimidazolium tetrafluoroborate. The crossed and half-filled squares correspond to rates obtained by eq 3.1 and extrapolated using the shift factors. Dotted squares are structural relaxation rates obtained from the crossover frequency of G' and G''.

Table 3.1: Vogel-Fulcher-Tammann fit parameters for the slow, sub-α dielectric relaxation rates, $\omega_{slow,BDS}$.

Ionic Liquid	ω_∞	D	T_0
OctylMIm NTf_2	4.6×10^{12}	5.5	161
HexylMIm NTf_2	1.3×10^{10}	2.4	172
OctylMIm BF_4	1×10^{10}	3.2	172
HexylMIm BF_4	6.70×10^{12}	7.0	156

Table 3.2: Vogel-Fulcher-Tammann fit parameters for the slow, sub-α dielectric relaxation rates, $\omega_{e,BDS}$.

Ionic Liquid	ω_∞	D	T_0
OctylMIm NTf_2	1.1×10^{12}	5.5	161
HexylMIm NTf_2	1.9×10^{14}	14.6	129
OctylMIm BF_4	6.10×10^{9}	4.7	164
HexylMIm BF_4	2.20×10^{10}	4.7	165

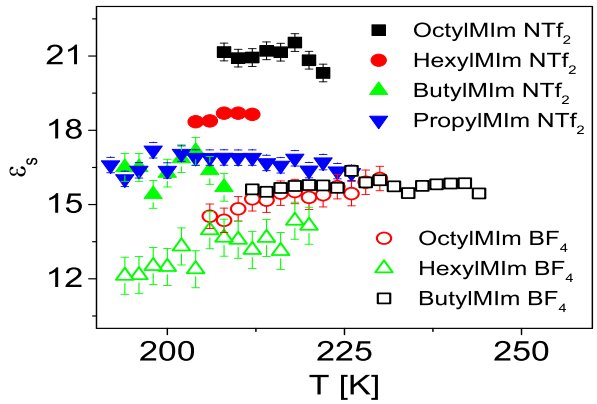

Figure 3.13: Static dielectric permittivities, ε_s, of 1-alkyl-3-methylimidazolium ILs obtained as the low-frequency limit of the fit by eq 3.1; see Figure 3.10.

at the interfaces of the polar and apolar domains. This polarization mechanism may arise from the motion of counterions that surround the aggregate or alternatively by the deformation of aggregates themselves. Further studies are required to assign the definitive molecular mechanism of interfacial polarization in these systems, but it is worth noting that similar interfacial polarizations have been observed in a variety of heterogeneous systems such as aqueous micelles and biopolymers in electrolyte solutions.[198, 199, 200, 201, 202] The rates obtained by NSE correspond to the time scale of the decay in the correlation responsible for the low-q peak. It is therefore directly related to the motion and lifetimes of the aggregates. The fact that the dielectric relaxation occurs at similar rates indicates that it is the deformation of aggregates that is responsible for the slow, sub-α dielectric relaxation.

The emergence of slow, sub-α dynamics in this series of 1-alkyl-3-methylimidazolium ILs has two direct and noticeable effects on the physicochemical properties. The first is an increase in the zero-shear viscosity due to the additional contribution from the slower dynamic-mechanical relaxation, as seen at low frequencies in Figure 3.8b. The second is an increase in the low-frequency, static dielectric permittivity due to contributions from the slow dielectric relaxation, presented in Figure 3.13. These effects on the transport properties in bulk ILs are a direct consequence of mesoscale aggregation and have significant implications for solvent applications such as polymerization, organic synthesis and catalysis, as well as nanoparticle growth.

Conclusion

In summary, the dynamic-mechanical spectra of 1-alkyl-3-methylimidazolium tetrafluoroborate ILs with alkyl lengths of hexyl and octyl exhibit slow relaxation modes reminiscent of the rheological response of short-chain polymers and MAs. This finding confirms the existence of large and long-lived mesoscale aggregates in bulk ILs. A slow, sub-α relaxation in the broad-band dielectric spectra is attributed to polarization at the interfaces of polar and nonpolar domains of the aggregates. These results support the interpretation of the low-momentum transfer (q) peak in the X-ray and neutron scattering functions as evidence of mesoscale organization in numerous ILs. The observed influence of these aggregate dynamics on transport properties illustrates the importance of mesoscale aggregation in developing structureâĹŠproperty relationships in ILs. The ability to probe dynamics of mesoscale aggregation with these experimental techniques provides a new and complementary approach to elucidate the role of aggregate formation and morphology on the physicochemical properties of bulk ILs.

3.3 Mesoscale Aggregate Morphology and Dynamics in Binary Ionic Liquid Mixtures

In this section, the influence of composition on the mesoscale aggregate morphology and dynamics in binary mixtures of imidazolium-based ionic liquids is investigated. It is found that by diluting aggregating 1-octyl-3-methylimidazolium tetrafluoroborate with non-aggregating 1-ethyl-3-methylimidazolium tetrafluoroborate the mesoscale aggregates transition from a bicontinuous morphology to isolated spherical aggregates. This change in morphology is reflected in the mesoscale aggregate dynamics, resulting a 100% increase in the static dielectric permittivity.

The work presented here is compiled from a manuscript draft submitted to Nature Communications, authors Tyler Cosby Utkarsh Kapoor, Jindal K. Shah, and Joshua Sangoro. The molecular dynamics simulations reported herein were performed by Utkarsh Kapoor and Prof. Jindal K. Shah. My contributions include: (i) design of experiments, (ii) data collection and analysis, (iii) interpretation of results, and (iv) writing.

Abstract

The dynamics and morphology of extended, mesoscale polar and non-polar regions are expected to dramatically alter the solvation and transport properties of numerous ionic liquids. Here we present results which reveal a 100% increase in the static dielectric permittivity of binary ionic liquid mixtures relative to their neat constituents. The origin of this increase is traced to a change in the mesoscale aggregate aggregate morphology from bicontinuous, in the neat aggregating IL, to spherical, in the mixtures. These changes to morphology are reflected in the dynamics of mesoscale aggregates probed by dynamic mechanical and broadband dielectric spectroscopy. The transition to spherical aggregates enhances the strength of a slow dielectric relaxation attributed to polarization at the polar/non-polar interfaces, resulting in the substantial increase in ε_s.

Introduction

Due to their outstanding physical and chemical properties, ionic liquids (ILs) have emerged as promising solvents in applications such as chemical synthesis, nanoparticle growth, biomass processing, batteries, solar cells, and supercapacitors.[57, 203, 122, 51, 49, 123, 48, 204] The ability of ILs to self-assemble through solvophobic aggregation of non-polar alkyl chains located on the polar ions promises to further enhance the property and application windows available to these unique materials.[32] Evidence of the mesoscale aggregation emerged in the past decade as the formation of distinct polar and non-polar regions in numerous ILs was recognized in detailed x-ray scattering, neutron scattering, and molecular dynamics simulation studies.[32, 205, 54, 55] Accordingly, the existence of the mesoscale aggregates have been used to qualitatively explain numerous experimental findings which imply the existence of spatially and temporally distinct regions within the bulk liquid. Among these findings is the ability of ILs to solvate both polar and non-polar molecules as well as evidence of dynamic heterogeneity of dissolved polar and non-polar probe molecules.[13, 32] Additionally, recent quasielastic neutron scattering studies have revealed the existence of fast and slow ion diffusion attributed to local diffusion within a single domain and between domains, respectively.[206, 207, 208, 209, 32] Solvophobic aggregation has also been invoked to explain reductions in the viscosity and dc ionic conductivities with increasing volume fraction of aliphatic groups, although the exact mechanism by which this might occur remains

unclear.[179, 210, 211] Critical to all of these phenomena and the associated physicochemical properties is the question of how long the mesoscale aggregates persist. This question is critical, for instance, in chemical synthesis where longer-lived aggregates will allow for multiple solute reactions to occur prior to a complete reorganization of the surrounding solvent environment. Currently, direct experimental insight into aggregate dynamics is limited to neutron spin echo spectroscopy which shows that aggregates do persist to timescales considerably longer than the local motions of ions.[15, 133, 16] The main drawback for NSE experiments are the limited number of beamlines and highly competitive beamtime. To date, only three ILs have been investigated by NSE.[15, 133, 16] It is necessary to find new techniques capable of probing mesoscale aggregate dynamics given the huge number of potential ionic liquids (10^6), many of which are expected to exhibit mesoscale aggregation.[112]

The majority of studies on mesoscopic aggregation in ILs have centered on the evolution of aggregation in neat ILs with systematically increasing alkyl chain length. For instance, substituted 1-alkyl-3-methylimidazolium cations have been shown to progress from globular to bicontinuous polar and non-polar domains as the alkyl chain length increases from butyl to octyl.[189, 54, 55, 185] Recent structural studies indicate that additional and more complex morphologies can be accessed by mixing ILs with differing chain lengths and other chemical structure features.[15] The focus on IL mixtures rather than mixtures with other organic solvents provides a new level of control over IL aggregate morphology while maintaining or improving the properties of the neat ILs, notably their thermal stability. This new experimental space promises to further widen the property and application windows of ILs, but requires a detailed understanding of the influence of mesoscale organization on dynamics and the resultant physicochemical properties of self-assembled ILs, an understanding which is currently non-existent. Therefore there is a pressing need for new approaches to obtain physical insight into the interplay of both mesoscale aggregate dynamics and morphology on the physicochemical properties of ILs.

In this study, we utilize complementary experimental and computational techniques are employed to investigate changes to mesoscale aggregate morphology and dynamics as a function of composition in binary mixtures of the ionic liquids 1-octyl-3-methylimidazolium tetrafluoroborate (C_8MIm BF_4) and 1-ethyl-3-methylimidazolium tetrafluoroborate (C_2MIm BF_4). We find that by mixing these two prototypical imidazolium ILs, which differ only in alkyl chain length, we

can transform the bicontinous morphology of neat C_8MIm BF_4 to more isolated, spherical, non-polar aggregates as probed by x-ray scattering and molecular dynamics simulations. As a result of the composition-dependent evolution in morphology, the mesoscale aggregate dynamics, as determined by dynamic mechanical and broadband dielectric spectroscopy, are significantly altered. Most surprisingly, the changes to aggregate morphology and dynamics result in a 100% increase in the static dielectric permittivity, also known as the "dielectric constant", relative to that of either pure component.

Experimental Methods

1-octyl-3-methylimidazolium tetrafluoroborate and 1-ethyl-3-methylimidazolium tetrafluoroborate were purchased from Iolitec and dried under vacuum (10^{-6} bar) at 60 °C for 24 hours prior to use. Broadband dielectric spectroscopy measurements were made in the frequency range of $10^{-1} - 10^{7}$ Hz using a Novocontrol Alpha Analyzer with a QUATRO liquid nitrogen temperature control system with temperature stability ± 0.1 K. Samples were measured in a parallel plate capacitor geometry with 20 mm diameter gold-plated brass electrodes. A sample thickness of 1.6 mm was maintained using a Teflon spacer. The dynamic-mechanical spectra of the mixtures were obtained via oscillatory shear measurements over the frequency range 0.1 - 100 Hz with $0.05 - 2$ strain% on a Hybrid Rheometer 2 (TA Instruments) using parallel plate geometry with a diameter of 8 mm. The temperature was controlled by an Environmental Test Chamber with nitrogen as the gas source with temperature stability ± 0.1K. Small-angle and wide-angle x-ray scattering measurements were conducted at room temperature using a SAXSLab Ganesha x-ray scattering system. The samples were encased in a button cell with Kapton windows. An empty cell was also measured to enable subtraction of the Kapton background. Differential scanning calorimetry measurements were performed on a TA Instruments Q2000 calorimeter at a cooling rate of 10 K/ min. The calorimetric glass transition temperature, T_g, was determined at the midpoint of the step in the heat flow corresponding to the maximum in the temperature derivative of the heat flow.

Molecular dynamics simulations and the analysis thereof were performed by Utkarsh Kapoor and Prof. Jindal Shah at Oklahoma State University. The computational resources were provided by the High Per-formance Computing Cluster at Oklahoma State University. Structural properties of the ionic liquid systems are described in terms of X-ray structure factors, Voronoi domain

analysis, and aggregate size distribution. Structure factors and domain analysis were computed from MD simulation trajectories using tools implemented in TRAVIS [212, 213] while aggregate size distribution was analyzed using AGGREGATES.[214] Further, the configuration snapshot visualization was rendered using VMD.[215]

Results and Discussion

The structures factors, S(q), of the neat ILs C_8MIm BF_4 and C_2MIm BF_4 as well as their mixtures at 30, 50, and 70mol% C_2MIm BF_4 obtained at room temperature by small- and wide-angle x-ray scattering are presented in Figure 3.14(a). C_8MIm BF_4 exhibits a pre-peak at q = 0.28 Å typical of self-assembled ILs and assigned to the scattering from polar domains separated by a non-polar domain. The higher q peak arises from adjacency correlations of both inter- and intramolecular origins and is common to all ionic liquids.[13] The short-chain, but otherwise identical, C_2MIm BF_4 has no pre-peak and is therefore taken to be non-aggregating. With increasing concentration of C_2MIm BF_4 the pre-peak is reduced in intensity and shifts to slightly lower q-values. Insight into the structural changes which alter the position and intensity of the pre-peak is provided by complementary molecular dynamics (MD) simulations. The MD structure factors, $S(q)$, were calculated using Equation 3.3;

$$S_{ij}(q) = \frac{\rho_o x_i x_j f_i(q) f_j(q) \int_0^R 4\pi r^2 \left[g_{ij}(r) - 1\right] \frac{\sin(qr)}{qr} \left(\frac{\sin(\frac{\pi r}{R})}{\frac{\pi r}{R}}\right) dr}{\left[\sum_i x_i f_i(q)\right]^2}$$

where $S_{ij}(q)$ is the partial structure factor obtained from the Fourier transform of the radial distribution function, $g_{ij}(r)$, between the atoms of type i and j, ρ_o is the average atomic number density, x_i is the atomic fraction of i, q is the scattering vector, and $f_i(q)$ is the X-ray atomic form factor for the atom type i taken from the International Tables for Crystallography.[216] R represents the cutoff distance defined for calculating g_{ij}(r). A Lorch type window function, $\left(\frac{\sin(\frac{\pi r}{R})}{\frac{\pi r}{R}}\right)$, is also used to attenuate the effect of using finite cutoff in calculating the radial distribution function between the atoms types i and j.[217] The structure factors were computed

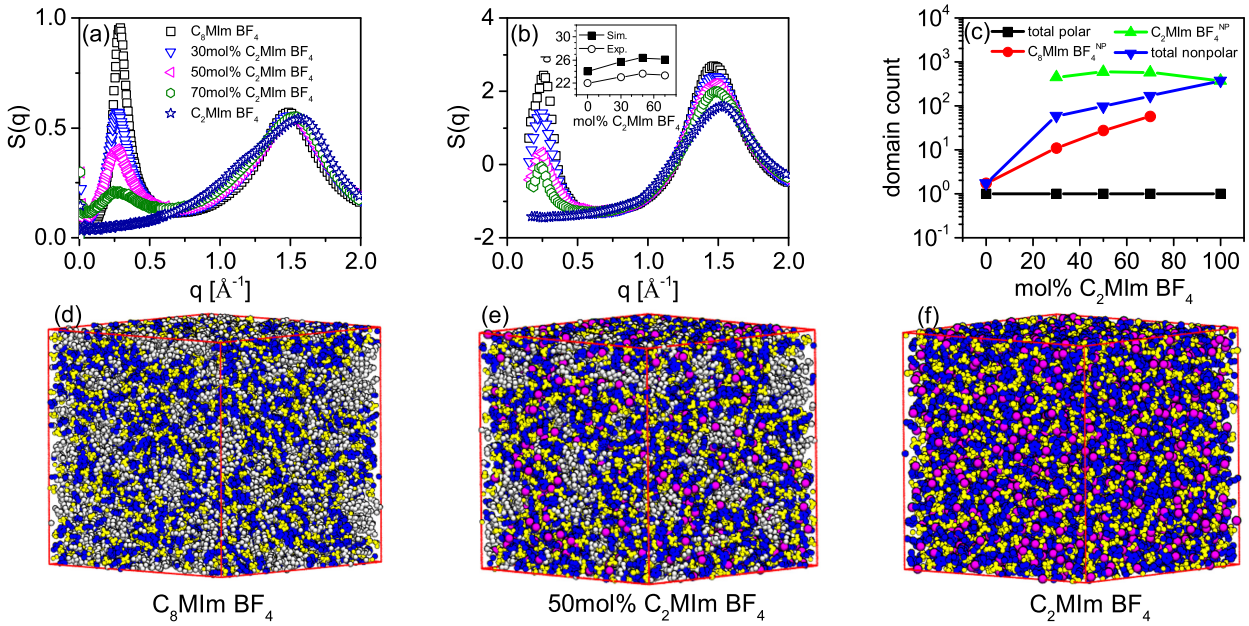

Figure 3.14: (a) Structure factors, S(q), obtained by X-ray scattering. (b) Structure factors computed by MD trajectories. Inset: Comparison of the real-space correlation distance, $d = 2\pi/q_{max}$, of the pre-peak obtained by simulation (sim.) and experiment (exp.). (c) Average domain count of the polar and non-polar domains present in the simulation box as a function of C_2MIm BF_4 concentration. (d-f) Instantaneous snapshots of the equilibrated system of (d) C_8MIm BF_4, (e)50mol% C_2MIm BF_4, and (f) C_2MIm BF_4 with colors corresponding to the following moieties: cation polar (blue), anions (yellow), C_8MIm non-polar (silver), C_2MIm non-polar(pink).

using TRAVIS[212, 213] after including the Lorch type function in the source code. Half of the simulation box length, R, was used as the cutoff distance for these calculations.

The structure factors calculated by MD simluations are shown in Figure 3.14(b). They reproduce the positions and relative intensities of the experimental structure factors reasonably-well over the entire q-range. The real space distances corresponding to the pre-peak, $d = 2\pi/q_{max}$, found by experiment and simulation are presented in the inset of Figure 3.14(b). MD simulations slightly overpredict the experimental values, however, the non-monotonic dependence of the domain distance on composition is well-reproduced. It must be stressed that these distances increase in a non-linear fashion. For example, there is a slight decrease in the non-polar domain distance as the concentration is changed from 50mol% to 70mol% C_2MIm BF_4. A similar non-linear trend in the size of nano-segregated domains has been reported for the mixtures of [C_6mim]Cl - [C_8mim]Cl and [C_6mim]Cl-[C_{10}mim]Cl,[56] and [C_2mim][NTf_2]-[C_6mim][NTf_2].[185]

To understand and visualize the influence of varying concentrations on the morphology of the binary ionic liquid mixtures, static snapshots of the well-equilibrated configurations obtained at the end of MD simulation are provided in Figure 3.14(d), (e), and (f), for neat C_8MIm BF_4, 50mol% C_2MIm BF_4, and neat C_2MIm BF_4, respectively. The results are color-coded in terms of the polar and non-polar groups present in binary ionic liquid mixture systems of C_8MIm BF_4 and C_2MIm BF_4. The polar group of both imidazolium cations contains the imidazolium ring as well as the methyl and methylene groups directly bonded to the ring, while the anion is completely polar. The polar group of the cation and anion together constitutes the overall polar domain. The non-polar regions in the two cations are the respective uncharged carbon groups minus the methylene group directly bonded to the imidazolium ring. The color-scheme is as follows: cation-polar head in blue, anion in yellow, C_8MIm-nonpolar in silver, and C_2MIm-nonpolar in pink. As expected, the cation-polar heads and the anions are always found close to one another, consistent with previous studies.[189, 218, 219, 220] The polar groups form a continuous, percolated polar domain in both of the pure ILs and in all mixtures. The morphology of the non-polar domain, on the other hand, is strongly composition dependent. A bicontinuous, sponge-like morphology is observed for the pure C_8MIm BF_4 with both the polar and non-polar domains percolating throughout the system. This result is consistent with the structures obtained for other C_nMIm-based ionic liquids. [189, 218, 219, 220, 183, 221] With the increase in C_2MIm BF_4 concentration, it is clear that the interconnectivity between the non-polar tails of C_8MIm is highly disrupted, with many tails isolated and surrounded by the non-polar methyl carbon of C_2MIm. Nevertheless, even at the highest concentration of C_2MIm BF_4 considered here, the aggregation of C_8MIm is clearly visible. Such aggregation is responsible for the separation of polar and non-polar domains which is visible as a pre-peak in the structure factors.

The connectivity of the nano-segregated polar–non-polar structure can be examined in a more quantitative manner based on a Voronoi tessellation technique. The concept and the implementation of this technique has been described by Brehm and coworkers.[213] In this analysis, adjacent Voronoi cells sharing a face and belonging to a given subunit constitute a domain. For our purposes, each of the binary ionic liquid mixture systems is characterized in terms of four unique domains: (a) the total polar domain composed of the polar head groups of both the cations and the anion; (b) C_8MIm non-polar; (c) C_2MIm non-polar and (d) total non-polar containing the non-polar groups

from both cations. The uncharged alkyl chain of the cations, are considered unique in order to identify the origin of the structural changes at various concentrations. Figure 3.14(c) provides number of domains based on this classification as a function of the C_2MIm BF_4 concentration. As expected, a domain count of 1 is observed for the polar domain indicating its three-dimensional connectivity for all the ionic liquids mixtures studied here. This observation is in line with previous simulation studies involving a wide range of pure ionic liquids.[189, 218, 219, 220, 213, 212, 32] For pure C_2MIm BF_4, the domain counts for the non-polar group are significantly higher than 1 ($\sim$ 380) indicating that the cation non-polar carbons are dispersed in the system. On the other hand, the domain count for the non-polar tails in the pure C_8MIm BF_4 ionic liquid is between 1 and 2, indicating that the majority of alkyl chains are connected in a single percolated non-polar domain with some possible occurrence of isolated C_8MIm BF_4 non-polar chains. The addition of 30 mol% C_2MIm BF_4 results into a significant disruption of the non-polar connectivity as the large single continuous domain is broken into as many as 10 separate domains and the number reaches a high as 57 at the highest C_2MIm BF_4 concentration. This results corroborates the inferences derived from the qualitative snapshots that there is a transition from a continuous phase to a dispersed phase. We hypothesize that the dispersed subphase of C_2MIm modulates the overall non-polar domain connectivity and morphology in a way that alters the dynamics of the mesoscale aggregates and gives rise to a variation in the static dielectric permittivity as a function of C_2MIm BF_4 concentration, as discussed later.

A prior investigation into the dynamics of the neat IL series C_nMIm BF_4 with systematically increasing alkyl chain length revealed the emergence of unique dynamics at lower than expected rates in the dynamic mechanical and broadband dielectric spectra.[211] These dynamics were attributed to the fluctuations of the mesoscale aggregates at timescales longer than the structural relaxation. The link between the slow dynamics and mesoscale aggregates could only be inferred on the basis of their emergence coinciding with the onset of solvophobic aggregation, as evidenced by the x-ray scattering pre-peak, and by a rough comparison between the rates with those obtained by neutron spin echo spectroscopy.

The real and imaginary parts of complex dynamic shear modulus, $G^* = G' + iG''$, are presented in Figure 3.15(a) for neat C_8MIm BF_4 and the 30, 50, and 70mol% C_2MIm BF_4 mixtures. All liquids exhibit viscoelastic behavior depending upon the experimental timescale. The transition from a

viscous to an elastic response corresponds with an arrest of molecular motion corresponding to the glass transition. The rate of this structural relaxation, $\omega_{\alpha,DMS}$, corresponds to the crossover point of G' and G''. The mechanical relaxation of the majority of liquids deviates from the ideal response of a relaxing Maxwell element due to a broad underlying distribution of relaxations around a mean relaxation rate. Certain liquids which are capable of forming meso- or larger scale heterogeneities also exhibit additional mechanical relaxations at timescales considerably longer than the structural relaxation. A notable example are the glass-forming monohydroxy alcohols.[32] These single-component liquids exhibit a slower relaxation reminiscent of the terminal mode of short chain polymers and attributed to fluctuations associated with the existence of supramolecular hydrogen-bonded chains.[196, 222] This slow relaxation is observed as a low frequency shoulder in the real and imaginary parts of the complex dynamic shear modulus, as a step-change in the real part of complex viscosity and as a peak in the imaginary part of complex viscosity.[94, 223, 197, 224] A very similar relaxation is observed at low frequencies in G' and η' in Figure 3.15(a) and (b). This relaxation was previously observed in the dynamic mechanical spectra of neat C_8MIm BF_4 and tentatively attributed to fluctuations associated with the existence of mesoscale aggregates.[211] The dilution of C_8MIm BF_4 with C_2MIm BF_4 results in a weakening of the slow mechanical relaxation as seen in Figure 3.15(a), and more easily observed in Figure 3.15(b) where the low-frequency contribution to the real part of complex viscosity gradually diminishes with dilution of C_8MIm BF_4. The shear modulus is well-described by a linear combination of two Cole-Davidson-modified Maxwell relaxation models, see Equation 3.3, where ω_{slow}=$1/\tau_{slow}$ and ω_{α}=$1/\tau_{\alpha}$ are the model relaxation rates and G_{slow} and G_{∞} are the high-frequency limiting values of the shear modulus for the slow and structural relaxation, respectively.[211, 94]

$$G' = Re\left[G_{\infty}\left(1 - \frac{1}{(1+i\omega\tau_{\alpha})^{\gamma}}\right) + G_{slow}\left(1 - \frac{1}{(1+i\omega\tau_{slow})^{\gamma}}\right)\right] \tag{3.3}$$

The fit parameters of the Cole-Davidson-modified Maxwell relaxation models, Equation 3.3, are provided in Tables 3.3 and 3.4.

The relaxation rates obtained as fit parameters of this model, $\omega_{slow,DMS}$ and $\omega_{\alpha,DMS}$, correspond to the rate of the slow and structural relaxations, respectively. While the strength of the slow

Table 3.3: Fit parameters of Equation 3.3 for the structural, α-relaxation.

IL	G_∞ [GPa]	γ
C_8MIm BF_4	1.0	0.15
10mol% C_2MIm BF_4	1.0	0.15
30mol% C_2MIm BF_4	1.4	0.15
40mol% C_2MIm BF_4	1.2	0.15
50mol% C_2MIm BF_4	1.5	0.15
70mol% C_2MIm BF_4	0.85	0.15

Table 3.4: Fit parameters of Equation 3.3 for slow, sub-α-relaxation

IL	G_{slow}[MPa]	γ
C_8MIm BF_4	16	0.15
10mol% C_2MIm BF_4	17	0.15
30mol% C_2MIm BF_4	13	0.15
40mol% C_2MIm BF_4	15	0.15
50mol% C_2MIm BF_4	12	0.15
70mol% C_2MIm BF_4	5.6	0.15

mechanical relaxation diminishes with increasing C_2MIm BF_4, the separation between the two relaxation rates remains relatively constant, Figure 3.15(g). This indicates that the volume involved in the mechanical relaxation may not change substantially in the binary mixtures. This is consistent with the relatively slight change in non-polar domain dimensions, as illustrated by the composition dependence of the non-polar correlation distance in the inset of Figure 3.14(b). On the other hand, the weakening of the mechanical relaxation associated with fluctuations of the non-polar domains follows intuitively from the reduction in the overall volume fraction of the non-polar phase and the accompanying reduction in connectivity which occurs upon addition of C_2MIm BF_4.

The broadband dielectric spectra (BDS) of neat ionic liquids are dominated by ion motion. As they are purely ionic materials, the dielectric relaxation associated with ion motion is intimately linked to the structural relaxation. For numerous aprotic ionic liquids, the rate of ion hopping, obtained by BDS, and the structural relaxation rates, as obtained by other techniques such as dynamic mechanical spectroscopy and differential scanning calorimetry, coincide.[150, 153] The real part of complex dielectric permittivity, $\varepsilon^* = \varepsilon' - i\varepsilon''$, as well as the derivative representation of the imaginary part of complex dielectric permittivity, $\varepsilon''_{der} = (-\pi/2)[\partial\varepsilon'/\partial \ln(f)]$, are presented in Figure 3.15(c) and (d), respectively, for neat C_8MIm BF_4, 50mol% C_2MIm BF_4, and 70mol% C_2MIm BF_4. The derivative representation is employed to suppress the contribution of dc ionic

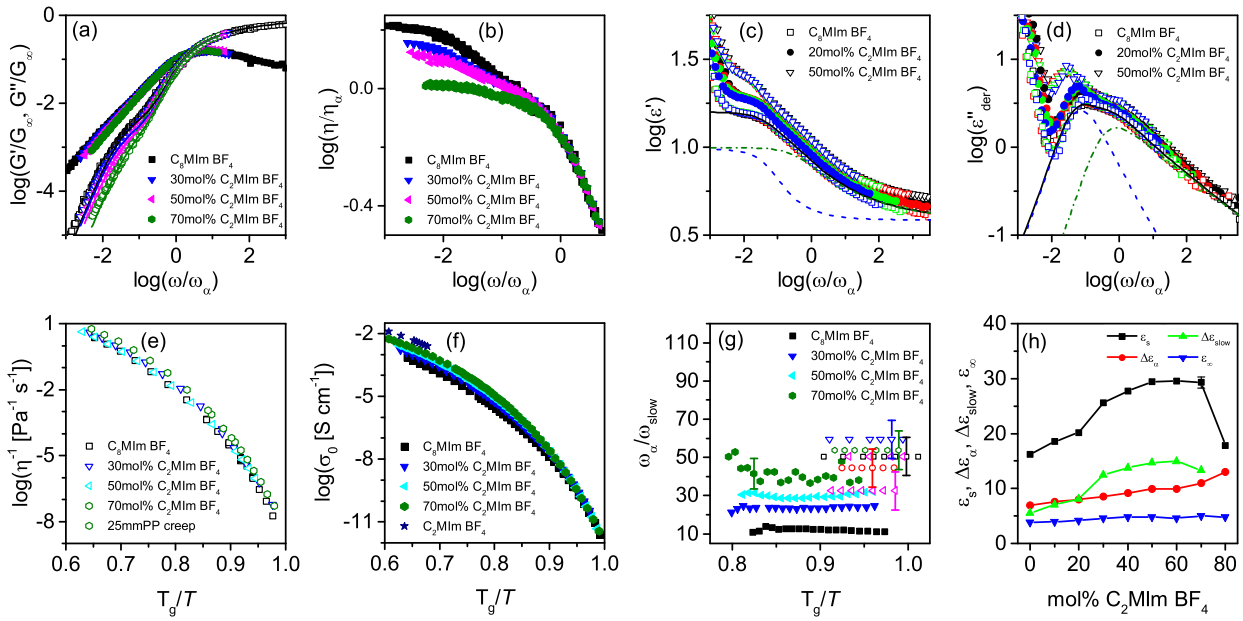

Figure 3.15: (a) The real (open symbols) and imaginary parts (closed symbols) of the complex dynamic shear modulus, $G^*(\omega) = G'(\omega) + iG''(\omega)$, as a function of frequency normalized by the structural relaxation rate, ω_α. Lines represent fits by two Cole-Davidson modified Maxwell-models. (b) The real part of the complex viscosity, $\eta^*(\omega) = \eta'(\omega) - i\eta''(\omega)$. (c) The real part of complex dielectric function, $\varepsilon^*(\omega) = \varepsilon'(\omega) - i\varepsilon''(\omega)$, and (d) the derivative representation of the dielectric loss, $\Delta\varepsilon''_{der} = (-\pi/2)[\partial\varepsilon'/\partial\ln(f)]$. T=204-228K at 8K increments. Solid lines correspond to the total fit of two Havriliak-Negami fit functions for C_8MIm BF_4 at 204K. The dashed and dotted-dashed lines represent the separate Havriliak-Negami functions of the underlying slow and structural relaxations, respectively. (e) Fluidity, η^{-1}, *versus* temperature normalized by T_g. (f) DC ionic conductivities, σ_0, *versus* temperature normalized by T_g. (g) Relaxation rate ratios *versus* temperature normalized by T_g. Closed and open symbols correspond to dielectric and mechanical rates, respectively. (h) Static dielectric permittivity, ε_s, dielectric strength of the α-relaxation, $\Delta\varepsilon_\alpha$, dielectric strength of the slow relaxation, $\Delta\varepsilon_{slow}$, and high-frequency permittivity, ε_∞, *versus* the C_2MIm BF_4 concentration in mol%. T=1.1T_g.

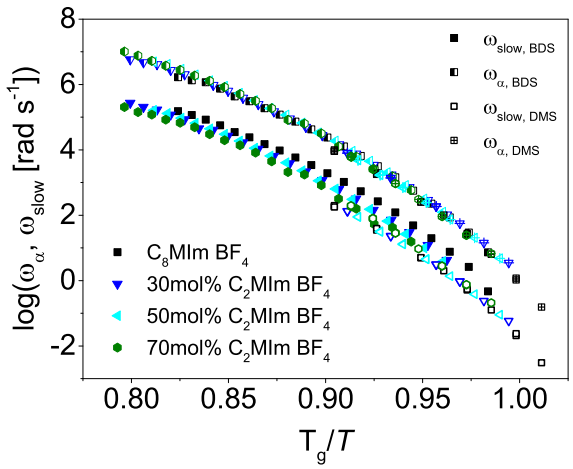

Figure 3.16: Relaxation rates of the structural, α-relaxation, ω_α, and the slow, sub-α relaxation, ω_{slow}, as obtained by dielectric and mechanical spectroscopy *versus* temperature normalized by the calorimetric glass transition temperature, T_g.

conductivity to the dielectric loss.[86, 85] In a typical, non-aggregating ionic liquid, the derivative representation consists of a single broad peak with the peak maximum coinciding with the onset frequency of dc ionic conductivity and the structural relaxation rate.[225, 226, 211] Recently, it was found that the dielectric spectra of neat C_8MIm BF_4 display two closely overlapping peak.[211] The structural relaxation (ion hopping) peak, with relaxation rate ω_α, corresponds to the high frequency shoulder in Figure 3.15(d). The lower frequency peak is then a slower than the structural relaxation. In the previous work, this process was tentatively attributed to the fluctuation of mesoscale aggregates since its emergence coincided with the onset of mesoscale aggregation. The addition of C_2MIm BF_4 reduces the calorimetric glass transition temperature, T_g, but the faster dielectric relaxation rates, $\omega_{\alpha,BDS}$, and the structural relaxation from dynamic mechanical spectroscopy coincide for all measured compositions and scale by the T_g, see Figure 3.16. The composition dependence of T_g, presented in Figure 3.17, follows the Fox equation for the glass transition in amorphous polymer blends.[17] The strength of the slower relaxation increases in the mixtures and shifts to lower frequencies relative to the structural, α relaxation.

The dielectric spectra are well described by a linear combination of two Havriliak-Negami fitting functions, see Equation 3.4, where τ is the model relaxation time, $\Delta\varepsilon$ the dielectric strength, ε_∞ the high-frequency limiting permittivity, σ_0 the dc ionic conductivity, ε_0 the vacuum permittivity, and β and γ are stretching parameters.[80, 3] The temperature dependence of the low-frequency limiting

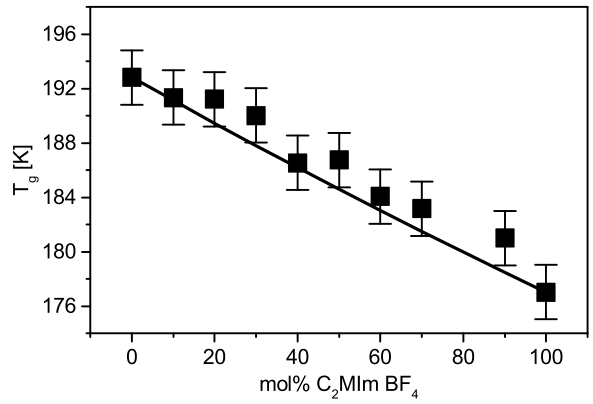

Figure 3.17: Calorimetric glass transition temperatures corresponding to the peak maximum of the derivative of heat flow on cooling. The solid line is the Fox equation, $1/T_g = (x_1/T_{g,1}) + (x_2/T_{g,2})$, where x is mole fraction, ant $T_{g,1}$ and $T_{g,2}$ are the transition temperatures of the neat ILs.[17]

static dielectric permittivity, $\varepsilon_s = \Delta\varepsilon_{slow} + \Delta\varepsilon_\alpha + \varepsilon_\infty$, is presented in Figure 3.18(a). The underlying temperature dependent dielectric strengths and high frequency dielectric permittivities are shown in Figure 3.18(b-d). The shape parameters are provided in Figure 3.19. A comparison of relaxation rates obtained by Equation 3.4 and those obtained by the random barrier model is shown in Figure 3.20 for 50mol% C_2MIm BF_4. In the random barrier model, the ions are taken to be hopping in a randomly varying energy landscape. The onset of dc ionic conductivity, σ_0, corresponds to the time, τ_{RBM}, it takes for ions to overcome the largest energy barrier to form a percolated conducting path. Solved within the continuous time random walk approximation an analytical expression for the complex dielectric function is obtained which contains only two parameters, the dc ionic conductivity and the ion hopping rate, σ_0 and ω_{RBM}, respectively.[4] This model describes the frequency dependence of the real part of complex conductivity for ion conducting liquids and glasses quite well. The strucutral, α-relaxation rates, ω_α coincide with the ion hopping rates, ω_{RBM}.

$$\varepsilon^*(\omega) = \left[\frac{\Delta\varepsilon_{slow}}{[1 + (i\omega\tau_{slow})^\beta]}\right] + \left[\frac{\Delta\varepsilon_\alpha}{[1 + (i\omega\tau_\alpha)^\beta]^\gamma}\right] + \frac{\sigma_0}{i\omega\varepsilon_0} + \varepsilon_\infty \tag{3.4}$$

The dielectric spectra of the 80mol% C_2MIm BF_4 mixture are provided in Figure 3.21 in terms of the derivative representation $\Delta\varepsilon_{der}$. The absence of the slow dielectric relaxation is attributed to a disruption of the mesoscale aggregates above a critical concentration of C_2MIm BF_4.

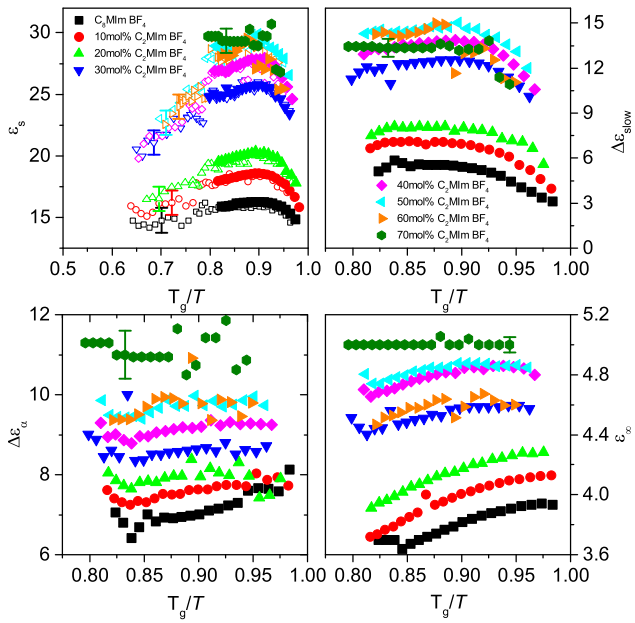

Figure 3.18: Static dielectric permittivities (a), dielectric strength of the slow, sub-α relaxation (b), dielectric strength of the α-relaxation (c), and the high-frequency limit of the real part of dielectric permittivity (d) for all concentrations *versus* temperature normalized by the calorimetric glass transition temperature. The solid symbols are values from fits by Equation 3.4 in the main text. Open symbols are screen-read values of ε_s.

The ratio of $\omega_{\alpha,BDS}$ to $\omega_{slow,BDS}$ increases from approximately 10 in neat C_8MIm BF_4 to approximately 40 in the 70mol% C_2MIm BF_4 mixture, revealing an increasing separation between the two processes, see Figure 3.15(g). The Havriliak-Negami fitting functions also provide the dielectric strengths of the two relaxations, $\Delta\varepsilon_\alpha$ and $\Delta\varepsilon_{slow}$, as well as the high-frequency value of permittivity, ε_∞. The low-frequency limiting value, $\varepsilon_s = \Delta\varepsilon_{slow} + \Delta\varepsilon_\alpha + \varepsilon_\infty$, is commonly referred to as the "dielectric constant". This value excludes the influence of electrode polarization which leads to a strong, lower-frequency dispersion but is not an intrinsic material property. The influence of composition on the static dielectric permittivity and dielectric strengths is shown in more detail in Figure 3.15(h) where the values are taken at a temperature T=1.1T_g. Here, we see that the static dielectric permittivity increases sharply at a composition between 20 and 30mol% C_2MIm BF_4 due to a corresponding increase in $\Delta\varepsilon_{slow}$. The composition-dependent trends in the slow dielectric relaxation stand in sharp contrast to what was observed for the slow mechanical relaxation. This points to a difference in the mechanisms underlying the two relaxations and their sensitivity to the morphology changes which occur as a function of composition.

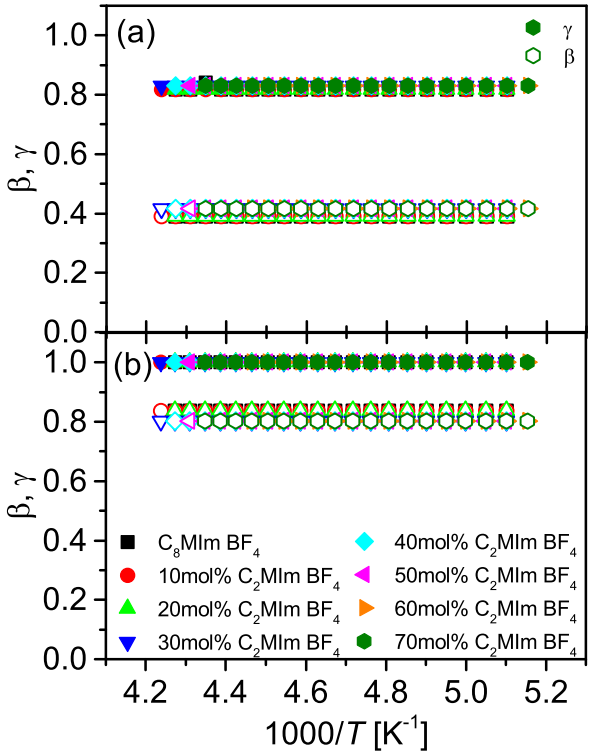

Figure 3.19: Shape parameters, β (open symbols) and γ (closed symbols) of Cole-Cole and Havriliak-Negami equations used to fit the dielectric spectra. (a) Shape parameters of the structural, α relaxation. (b) Shape parameters of the slow, sub-α relaxation.

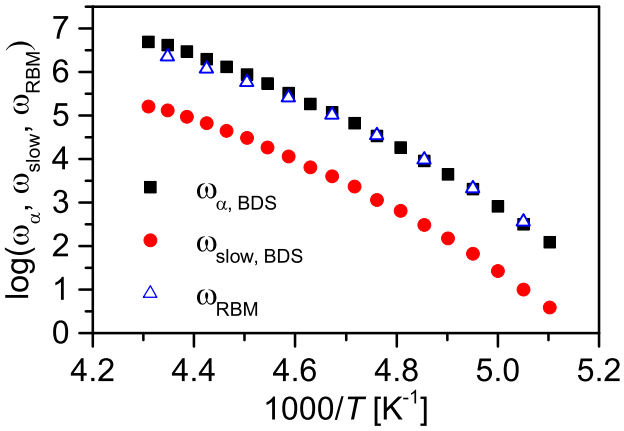

Figure 3.20: Dielectric relaxation rates of 50mol% C_2MIm BF_4 obtained by Equation 3.4 and the random barrier model, ω_{RBM}.[4]

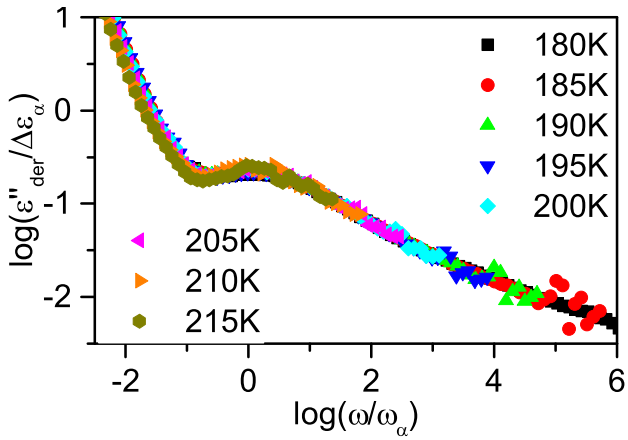

Figure 3.21: The derivative representation of the imaginary part of the complex dielectric function, $\varepsilon''_{der} = (-\frac{\pi}{2})\frac{\partial\varepsilon'}{\partial ln(f)}$, for 80mol% C_2MIm BF_4. The structural, α-relaxation is more fully resolved than at any lower C_2MIm BF_4 concentration and there is no evidence of a slower sub-α relaxation.

It is proposed that the slow dielectric relaxation originates from interfacial polarization occurring at the polar/non-polar interfaces. From numerous studies on heterogeneous liquids and solids it is well established that interfacial polarization is strongly dependent on the shapes of the included domains.[36, 227, 228, 229] A change in the shapes of the aggregates might be the origin of the observed increases in ε_{slow}, therefore it is appropriate to ask, how does composition influence the shape of the mesoscale aggregates in our IL mixtures? To answer this question, we return to the MD simulations. To provide better insight and a quantitative metric to the variety of shapes adopted by the polar and non-polar domains, the isoperimetric quotient, $Q^{\text{peri}} = \left[r_{sphere}(V)/r_{sphere}(A)\right]^6 = 36\pi\left[V^2/A^3\right]$, was computed, where V and A denote the volume and area of a given domain respectively while $r_{\text{sphere}}(V)$ and $r_{\text{sphere}}(A)$ represent the equivalent radii of the sphere with volume V and the sphere with area A, respectively. With this definition, the shape parameter will assume a value of 1 for a perfectly spherical shape while any deviations from sphericity lead to the values lower than 1.[213]

The change in isoperimetric quotient as a function of the C_2MIm BF_4 concentration is shown in Figure 3.22(a). From the figure, it is clear that Q^{peri} for the polar domain shows a negligible dependence on the concentration of C_2MIm BF_4 and is always less than 0.1, which implies that the shape of the polar network differs greatly from sphericity. Further, the non-polar domain present in pure C_8MIm BF_4 ionic liquid has a Q^{peri} value less than 0.25 suggesting a network whose shape is also far from spherical. However, with 30 mol% introduction of C_2MIm BF_4 in C_8MIm BF_4 ionic

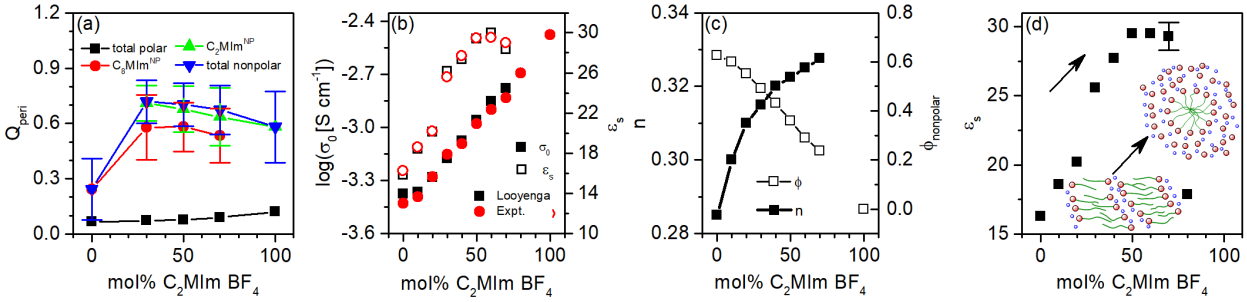

Figure 3.22: (a) Average isoperimetric quotient, Q^{peri}, of respective cation/anion polar and nonpolar domains as a function of C_2MIm BF_4 concentration. Please note that average numerical value and standard deviations were computed by dividing the trajectory into three blocks. (b) DC ionic conductivity, σ_0, at T=1.5T_g (closed squares) and static dielectric permittivity, ε_s, at T=1.1T_g (open squares), as well as estimates of σ_0 and ε_s from the Looyenga EMA (closed and open circles) *versus* C_2MIm BF_4 concentration. (c) Shape parameter, n, and volume fraction of the non-polar phase, $\phi_{nonpolar}$, *versus* mol% C_2MIm BF_4. (d) Concentration dependence of static dielectric permittivity at T= 1.1T_g. The increase in ε_s is due to the concentration-dependent aggregate shapes illustrated by the inset cartoons.

liquid, the Q^{peri} value nearly doubles assuming a value of $\sim$ 0.58 suggesting that a transition in the morphology of the domains which now more closely resemble a sphere in comparison to that in the pure C_8MIm BF_4. The results are even more dramatic when the total non-polar domain of the mixture is considered with values approaching as high as 0.7 at 30 mol% C_2MIm BF_4. Above 30mol%, the Q^{peri} is practically composition independent, indicating that the transition in mesoscale aggrgate shape occurs at or below this concentration.

The influence of the transition to more spherical mesoscale aggregates on interfacial polarization can be ascertained using an effective medium approximation (EMA). EMAs are useful approximate approaches to relate the shape and volume fractions, of filler phases located within host matrices to the overall dielectric properties of the composite, provided the properties of the two phases can be estimated.[230, 3, 229, 231]. Insight into the aggregate shapes and volume fractions may be obtained by probing the ability of EMA to accurately predict the static dielectric permittivities, ε_s, and dc ionic conductivities, σ_0, of the IL mixtures. For this purpose, we employ a form of the symmetric Looyenga equation[230], which is suitable for the conducting phases and intermediate volume fractions found in our IL mixtures.[230] The symmetric Looyenga effective

medium approximation is give in Equations 3.5 and 3.6:

$$\varepsilon_s = \frac{1}{\sigma_0}\left[\sigma_s\varepsilon_1 - \left(\frac{\sigma_2}{\sigma_s}\right)^{-2n}\phi\left(\sigma_2\varepsilon_1 - \sigma_1\varepsilon_2\right)\right] \tag{3.5}$$

$$\sigma_0^{1-2n} = \sigma_1^{1-2n} + \phi\left(\sigma_2^{1-2n} - \sigma_1^{1-2n}\right) \tag{3.6}$$

where subscript 1 signifies the polar phase, subscript 2 the non-polar phase, σ_0 the measured dc ionic conductivity of the mixture taken at T=1.5T$_g$, $\sigma_1 = 3.4 \times 10^{-3}\,\mathrm{S\,cm^{-1}}$ is the dc ionic conductivity of pure C_2MIm BF_4 at T=1.5T$_g$, $\varepsilon_1 = \Delta\varepsilon_\alpha + \varepsilon_\infty$ taken at T=1.1T$_g$ in Figure 3.18, σ_2=$4 \times 10^{-6}\,\mathrm{S\,cm^{-1}}$ $\varepsilon_2 = 1.8$ the static dielectric permittivity of hexane as a reasonable model of the non-polar phase.[232] The remaining variables, ϕ, and n, corresponding to the volume fraction, and shape of the insulating phase, were used as free fit parameters until the two equations gave converging values of ε_s and σ_0 approximately equal to the measured quantities.

The values of ε_s and σ_0 predicted by the Looyenga equation agree very well with the experimental values as shown in Figure 3.22(b). The two fit parameters of this model, n and ϕ, are the shape factor and volume fraction of the non-polar domain. The experimental ε_s and σ_0 are predicted only by an increase in n and a concomitant decrease in ϕ. Due to the assumptions on which an evaluation of the EMA relies, these trends should only be interpreted in a qualitative manner. The overall reduction in volume fraction of the non-polar domain is consistent with the x-ray scattering and MD simulations results. The shape factor, n, is related to the shape of the insulating phase, where $n < 1/3$ corresponds to rod-like inclusions and n = $1/3$ to spherical.[229, 230] The gradual increase in n, and accordingly ε_s, is consistent with the transition to more spherical mesoscale aggregates as indicated by Q^{peri}. The majority of the increase in ε_s occurs over the 20-30mol% C_2MIm BF_4, with a plateau above ≈ 40mol% C2MIm BF_4. This trend mirrors the isoperimetric quotient which is only marginally affected above 30mol% implying that the non-polar domain continues to retain sphere-like morphology above this minimum concentration. Due to the close agreement between these trends found by MD simulation, DMS, and BDS, we attribute the dramatic increase in ε_s and $\Delta\varepsilon_{slow}$ to a transition in the mesoscale aggregate morphology driven by the dilution of non-polar domains upon addition of C_2MIm BF_4. This transition is illustrated alongside the measured static dielectric permittivities in Figure 3.22(d).

In summary, we have demonstrated an ability to tune the properties of ionic liquids simply by mixing two parent ionic liquids. The composition dependent control over mesoscale aggregate morphology and dynamics afforded by the mixtures allows us to increase the measured static dielectric permittivity values, ε_s by approximately 100% relative to either parent compound. The ability to tune ε_s is made more significant by the fact that the vast majority of aprotic ionic liquids have low to moderate values of around 7-15 typical of low polarity solvents.[162, 168, 163, 170] Higher ε_s values are expected to influence IL/solute and IL/solid-surface interactions with potentially critical implications for the application of ILs in biomass processing, chemical synthesis, nanoparticle growth and as electrolytes in solar cells, batteries, and super-capacitors.[48, 57, 127, 233] The substantial increase in ε_s of the IL mixtures and its direct link to aggregate morphology provides a new route to tuning this important physical parameter. More generally, this study highlights the advantage of combining techniques capable of probing composition-dependent changes in mesoscale aggregate morphology as well as mesoscale aggregate dynamics. It is envisioned that future mixture studies on a wide variety of chemical structures will yield ILs with additional and more complex self-assembled morphologies, the dynamics of which may produce ionic liquids with unforeseen and advantageous physical and chemical properties.

3.4 Mesoscale Organization and Dynamics in Quaternary Phosphonium Ionic Liquids

The sub-α dielectric and mechanical relaxations have now been linked more conclusively to the existence of long-lived mesoscale aggregates in imidazolium-based ionic liquids. What happens to these mesoscale dynamics when we move to a different type of cation? X-ray and neutron scattering show that all the common cation classes in Figure 3.2 exhibit the pre-peaks which are indicative of mesoscale aggregates and the snapshots of organization obtained by MD simulations, which reproduce these profiles, are discussed using very similar language.[32] We might therefore expect that each class of ionic liquids should also exhibit similar sub-α relaxations corresponding to the fluctuation of the polar/non-polar domains. In fact, in recent studies of the non-aromatic

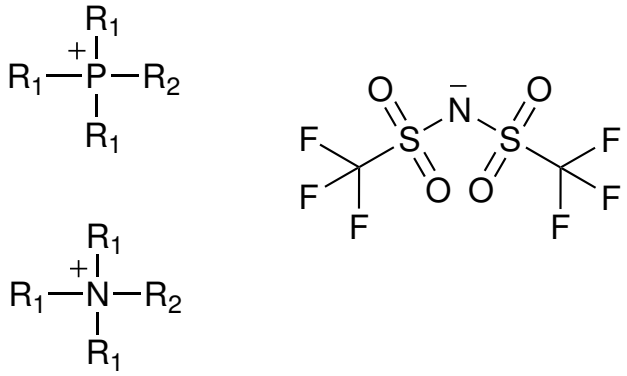

Figure 3.23: Chemical structure of the investigated quaternary phosphonium and ammonium ionic liquids.

and non-heterocyclic triethyl-octyl-phosphonium, triethyl-octyl-ammonium, and methyl-trioctyl-ammonium ionic liquids, sub-α dielectric relaxations have been reported.[171, 154] However, these were not consistently attributed to the motion of the solvophobic aggregates and systematic studies of the influence of alkyl chain length on the mesoscale organization and dynamics of these systems has not been performed. In this study, we investigate the influence of alkyl chain length in the quaternary phosphonium and ammonium ionic liquids on mesoscale organization (probed by small-angle x-ray scattering) and dynamics (probed by broadband dielectric spectroscopy, dynamic mechanical spectroscopy, and differential scanning calorimetry). The general chemical structures of the quaternary phosphonium and ammonium ionic liquids are shown in Figure 3.23. First, we consider a series of two triethyl-alkyl-ammonium ILs. We vary the length of the longer alkyl chain from pentyl to octyl and investigate them by x-ray scattering and dielectric spectroscopy. These results are highlighted in Figure 3.24. We find that the shorter chain triethyl-pentyl-ammonium (TEPA NTf_2) that the x-ray scattering does not show a pre-peak and the dielectric spectra is dominated by a single relaxation with no evidence of a slow, sub$-\alpha$ process. When the length of the long alkyl chain is increased to octyl in triethyl-octyl-ammonium (TEOA NTf_2) an x-ray pre-peak and sub-α dielectric relaxation each emerge. This correlation between the onset of solvophobic aggregation, as evidenced by the pre-peak, and the development of a sub-α dielectric relaxation is entirely consistent with the results obtained for imidazolium-based ILs. Therefore, in these ammonium and phosphonium-based ILs we expect that the pre-peak will indicate long-lived mesoscale organization which contributes a slow, sub-α dielectric relaxation by the same interfacial polarization mechanism which has been found for the imidazolium ILs.

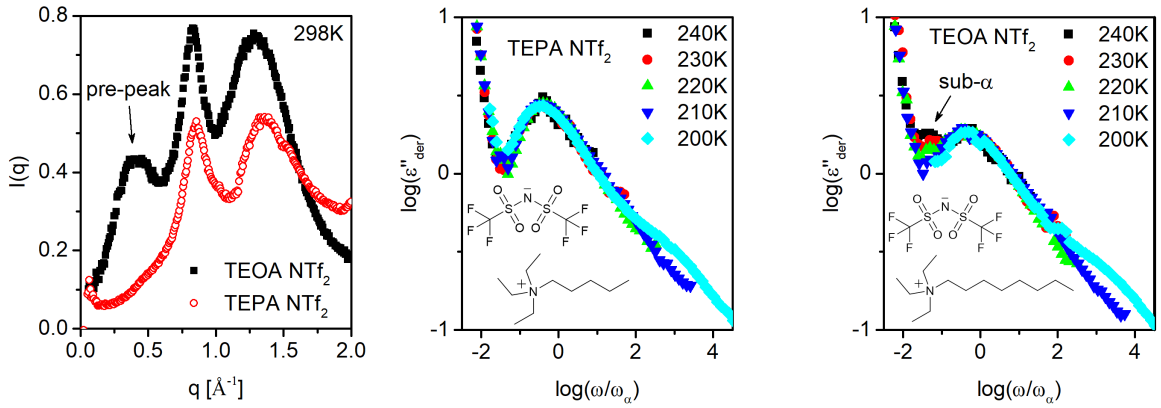

Figure 3.24: Left: X-ray scattering profile of triethyl-octyl-ammonium (TEOA) and triethyl-pentyl-ammonium (TEPA) with the same bis(trifluoromethylsulfonyl)imide (NTf_2) anion. Middle: The derivative representation of imaginary permittivity, ε''_{der} *versus* normalized frequency for TEPA NTf_2. Right: ε''_{der} *versus* normalized frequency for TEOA NTf_2. The existence of an x-ray pre-peak coincides with the emergence of a sub-α dielectric relaxation just as found in the imidazolium-based ILs.

The quaternary phosphonium and ammonium ILs have a wider variety of possible alkyl chain substitutions than the imidazoliums. Depending on the relative lengths of the different chains, the molecules can have a wide range in both the degree of cation asymmetry and the overall non-polar volume. For instance, in the series trimethyl-hexyl-phosphonium, triethyl-dodecyl-phosphonium, and tripropyl-octadecyl-phosphonium the degree of cation asymmetry might be very similar, if taken to be proportional to $R_1/R_2=0.1\bar{6}$, while the overall non-polar volume fraction is increasing significantly. Alternatively, we could make a series such as triethyl-dodecyl-phosphonium, trioctyl-dodecyl-phosphonium, and tetradodecyl-phosphonium. In this series, both the cation asymmetry and non-polar volume fraction are significantly influenced. The relative influence of these types of changes in the chemical structure on mesoscale organization and dynamics in quaternary phosphonium and ammonium ionic liquids are not well understood. In the first series (with constant cation asymmetry) we can expect that gradually increasing the length of the shorter trialkyl chains is gradually reducing the strength of intermolecular interactions between opposite charges within the polar phase. One question arises: what is the effect of the weakening interactions in the polar phase on the formation of long-lived mesoscale aggregates? Is there a crossover point where the aggregates are disrupted? One of the most well-studied of these types of ILs is the cation trihexyl-tetradecyl-phosphonium with the bis(trifluoromethylsulfonyl)imide anion. A pre-peak is observed

in the x-ray scattering profile and this is usually taken as an indication that very similar mesoscale organization is taking place in this liquid as in other ILs which exhibit pre-peaks despite the large hexyl chains which must be incorporated in the polar phase.[180, 22, 190, 234, 235]

In this section, we investigate the relative contribution of cation asymmetry, non-polar volume fractions, and weakening interactions in the polar phase to the formation and dynamics of mesoscale organization in a systematic series of quaternary phosphonium ionic liquids. The ionic liquids are triethyl-octyl, triethyl-dodecyl, tributyl-octyl, and tributyl-dodecyl-phosphonium each with the same bis(trifluoromethylsulfonyl)imide anion. The ionic liquid structures are shown in Figure 3.25. With this systematic variation in cation structure we can investigate the relative influence of cation asymmetry (proportional to R_1/R_2), the overall volume fraction of non-polar groups, and the effect of weakening interactions in the polar phase, (reduced when the length of the trialkyl chains increases from triethyl to tributyl).

The following section is a reprinting of a previously published article and its supporting material. My primary contributions to this article include: (i) design of experiments, (ii) data collection and analysis, (iii) interpretation of results, and (iv) writing. Changes from the published version consist of the incorporation of supporting information within the main text.

Abstract

Mesoscopic aggregation in aprotic ionic liquids due to the microphase separation of polar and nonpolar components is expected to correlate strongly with the physicochemical properties of ionic liquids and therefore their potential applications. The most commonly cited experimental evidence of such aggregation is the observation of a low-q pre-peak in the x-ray and neutron scattering profiles, attributed to the polarity alternation of polar and apolar phases. In this work, a homologous series of phosphonium ionic liquids with the bis(trifluoromethylsulfonyl)imide anion and systematically varying alkyl chain lengths on the phosphonium cation are investigated by small and wide-angle x-ray scattering, dynamic-mechanical spectroscopy, and broadband dielectric spectroscopy. A comparison of the real space correlation distance corresponding to the pre-peak and the presence or absence of the slow sub-α dielectric relaxation previously

associated with the motion of mesoscale aggregates reveals a disruption of mesoscale aggregates with increasing symmetry of the quaternary phosphonium cation. These findings contribute to the broader understanding of the interplay of molecular structures, mesoscale aggregation, and physicochemical properties in aprotic ionic liquids.

Introduction

Ionic liquids (ILs) are valued for their unique characteristics such as low vapor pressure, low flammability, wide liquidus ranges, and electrochemical stability. The large number of potential IL molecular structures with different functional groups makes them promising designer solvents with applications in energy storage, nanoparticle growth, biomass processing, and organic synthesis.[18, 32, 62] Rational design of ILs capable of use in these applications requires the development of detailed structure-property relationships. Considerable progress has been made along these lines through detailed experimental and computational work on a wide variety of cations such as imidazolium, pyrrolidinium, piperidinium, phosphonium, and ammonium combined with a range of anions.[44, 188, 43, 211, 236] An emerging obstacle in this endeavor is the finding that certain ILs aggregate and form long-lived mesostructures that extend over a few nanometers, while others do not show clear evidence of aggregation.[32, 205] This mesoscale organization presumably arises due to the solvophobic separation of polar and non-polar moieties on the cation charge center. Non-polar alkyl groups are excluded from the regions occupied by cations and anions and form extended aggregates surrounded by ionic shells.[32, 13] The existence of these distinct regions provides ILs with the ability to solvate both polar and non-polar molecules, an advantage critical for their applications as solvents in synthesis and material processing.[32, 187]

The primary experimental evidence of the formation of mesoscale structures is the emergence of a low momentum transfer, q, pre-peak in the x-ray and neutron scattering profiles. Computer simulations which reproduce the experimental scattering profiles have also provided snapshots showing the existence of three-dimensional mesoscale organization present in the liquid phase of ILs.[32, 22, 180, 19, 237, 54, 185, 191] Despite the initial uncertainty that the pre-peak may indicate only a local ordering due to cation anisotropy, it is now almost universally attributed to a long-range order induced by hydrophobic aggregation.[18, 32, 181, 183, 238] This assignment

is strengthened by recent results from neutron spin echo (NSE), broadband dielectric spectroscopy (BDS), and dynamic-mechanical spectroscopy (DMS) which reveal aggregate dynamics at timescales considerably longer than the primary structural relaxation.[205, 133, 16, 15, 211] In addition, these slow sub-α relaxations contribute to the increases in the zero-shear viscosity and static dielectric permittivity, highlighting the influence of aggregation on physicochemical properties.[211] However, experimental data on the dynamics of mesoscale aggregates are currently limited to the well studied imidazolium-based ionic liquids. There are numerous open scientific questions regarding the nature and lifetimes of mesoscale aggregates in other classes of aprotic ILs.

In this work, x-ray scattering, dynamic-mechanical spectroscopy, and broadband dielectric spectroscopy are utilized to investigate the influence of chemical structures on the formation and dynamics of mesoscale aggregates in a series of tetraalkylphosphonium bis(trifluoromethylsulfonyl)imide ILs. Unexpectedly, it is observed that increasing the volume fraction of non-polar functional groups in the phosphonium ILs does not necessarily promote mesoscale aggregation. A detailed analysis of the results reveals a disruption of the aggregates with increasing lengths of the shorter alkyl chains as evident from the absence of the sub-α relaxation as well as a substantial reduction in the real-space distance corresponding to the low-q peak. The combination of insights from the experimental techniques capable of probing both the structure and the dynamics of mesoscale aggregates enables us to make this distinction.

Experimental

Four phosphonium-based ionic liquids, triethyl-alkyl-phosphonium and tributyl-alkyl-phosphonium with alkyl chain lengths of octyl and dodecyl, with a common bis(trifluoromethylsulfonyl)imide anion, are the focus of the work reported here. Molecular structures and acronyms of the ionic liquids are provided in Fig. 3.25. The phosphonium ionic liquids were obtained from the Nippon Chemical Industrial Co. The ILs were dried under vacuum (10^{-6} bar) at 50 °C for 24 h prior to experiments. Small-angle and wide-angle x-ray scattering measurements were conducted at room temperature using a SAXSLab Ganesha x-ray scattering system. The samples were encased in a button cell with Kapton windows. An empty cell was also measured to enable subtraction of the Kapton background. Broadband dielectric spectroscopy (BDS) measurements were conducted in the frequency range of $10^{-1} - 10^{7}$ Hz and temperature

range 180-400 K using a Novocontrol High Resolution Dielectric Alpha Analyzer with a QUATRO liquid nitrogen temperature control system with temperature stability better than ±0.1 K. The samples were measured in a parallel plate capacitor geometry with 20 mm diameter gold-plated brass electrodes. A sample thickness of 0.5 mm was maintained using three Teflon spacers. The dynamic-mechanical spectra were obtained via oscillatory shear measurements over the frequency range 0.1-100 Hz with 0.05-2 strain % on Hybrid Rheometer 2 (TA Instruments) using parallel plate geometry with diameters of 8 mm and 3 mm. The temperature was controlled by an Environmental Test Chamber with nitrogen as the gas source with temperature stability ±0.1 K. Differential scanning calorimetry (DSC) measurements were performed on a TA Instruments Q2000 calorimeter at a cooling rate of 10 K/min. The calorimetric glass transition temperature, $T_{g,DSC}$, was determined at the midpoint of the step in heat flow corresponding to the maximum in the temperature derivative of the heat flow.

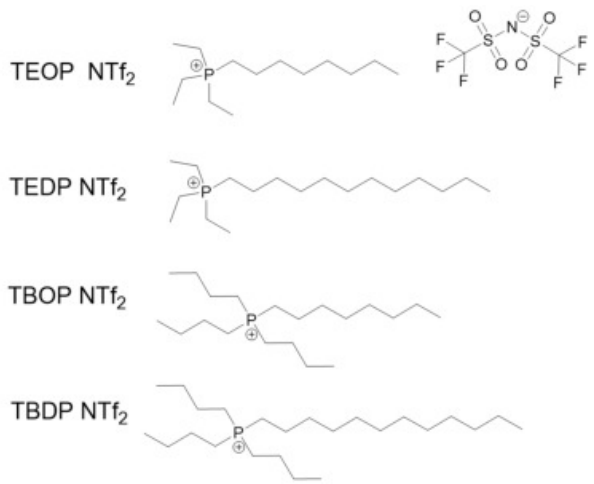

Figure 3.25: Structures of the studied phosphonium ionic liquids.

Results and Discussion

The x-ray scattering profiles are presented in Fig. 3.26 as intensity (I) of scattered x-rays *versus* momentum transfer. Three distinct peaks are observed for each IL. Based on numerous experimental and computational studies of a wide variety of ionic liquids, the highest and middle-q peaks are assigned to adjacency and charge-alternation correlations, respectively.[13, 108] The origin of the adjacency peak is the is the inter and intramolecular correlations of neighboring atoms.[13] The charge-alternation peak arises, as the name implies, from the ordering (alternation)

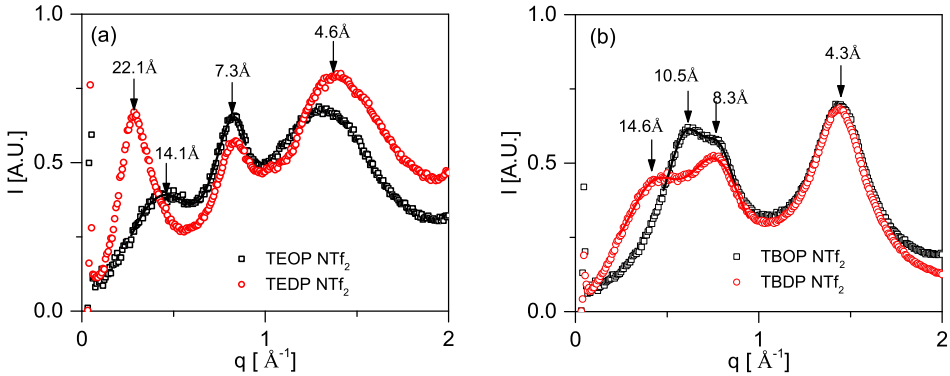

Figure 3.26: X-ray diffraction spectra of the phosphonium-based ionic liquids: (a) triethyloctylphosphonium (TEOP NTf_2) and triethyldodecylphosphonium (TEDP NTf_2) bis(trifluoromethylsulfonyl)imide; (b) tributyloctylphosphonium (TBOP NTf_2) and tributyldodecylphosphonium (TBDP NTf_2) bis(trifluoromethylsulfonyl)imide. Approximate distances in real-space, $d = 2\pi/q_{peak}$, for each major peak are indicated at the arrows. Lines correspond to fits with two Gaussian functions.

of cations and anions mediated by Coulombic interactions and is typical of molten salts. It corresponds to the distance separating two like-charge ions, that is the anion-anion or cation-cation separation distance.[13] In the triethyl-alkyl-phosphoniums, like ionic groups are separated by an average of $d = 7.3$ Å, regardless of the length of the longer alkyl chain, where $d = 2\pi/q_{peak}$. Increasing the short-chain length to four carbons in the tributyl-alkylphosphoniums increases the spacing between the like ionic groups to 8.3 Å.

The lowest q peak, known as the pre-peak or first sharp diffraction peak, is found in aprotic ionic liquids which have sufficiently long non-polar alkyl chains substituted on the cation charge center.[18, 32, 185, 191, 181, 183, 14, 189] The origin of this peak is universally assigned to the existence of alternating polar and non-polar regions resulting in mesoscale heterogeneity; however, there is some debate as to whether it is indicative of a pseudomicellar three-dimensional nanostructure or only local ordering due to cation anisotropy.[181, 183] The formation of hydrophobic aggregates relies on the segregation of neighboring alkyl chains into a non-polar region. In this view, the real-space correlation distance given by the polarity-alternation peak corresponds to the average distance separating ionic regions on the opposite sides of the non-polar inclusions. This distance will therefore depend on the alkyl chain length and the degree of interdigitation of opposing alkyl chains. A significant shift in the length scale corresponding to the pre-peak occurs when the shorter alkyl chains are lengthened from ethyl to butyl. Despite

having the same length of the longest alkyl chain, the distance is decreased from 14.1 Å to 10.5 Å for triethyloctylphosphonium (TEOP) and tributyloctylphosphonium (TBOP) and from 22.1 Å to 14.6 Å for triethyldodecylphosphonium (TEDP) and tributyldodecylphosphonium (TBDP), as indicated in Fig. 3.26. The dependence of aggregate size, d, on the length of the longer alkyl chain, n_c, for the studied phosphonium ionic liquids is compared with other aprotic ionic liquids found in the literature in Fig. 3.32 and discussed later. In accordance with common practice, the existence of the x-ray pre-peak in each of the studied phosphonium ILs might be taken as an indication that they each contain similar mesoscale aggregates. If this is the case, a slow relaxation associated with aggregate dynamics should be present in their dielectric spectra.[211]

Broadband dielectric spectroscopy (BDS) of ionic liquids has previously been used to probe ion dynamics and charge transport over broad temperature and frequency ranges.[150] By comparison with other experimental techniques, the ion dynamics of these purely ionic materials are found to occur at the same timescale as structural α-relaxations. In a recent article, we demonstrated that an additional slow sub-α relaxation emerges with the onset of mesoscale aggregation in two series of 1-alkyl-3-methylimidazolium ionic liquids with bis(trifluoromethylsulfonyl)imide and tetrafluoroborate anions.[211] The timescales of this relaxation were found to correspond with the decay time of the pre-peak as obtained by neutron spin echo (NSE) spectroscopy.[133, 16, 15, 211] The additional dielectric relaxation was therefore attributed to fluctuations of the mesoscale aggregates. It is now our intention to apply a similar analysis presented in that paper to the current series of phosphonium ionic liquids and to relate the trends observed for the slow sub-α relaxation to the length scale of the polarity-alternation peak as well as the molecular structure.

The real and imaginary parts of complex permittivity, $\varepsilon^*(\omega) = \varepsilon'(\omega) - i\varepsilon''(\omega)$, are presented in Fig. 3.27 as functions of the radial frequency, $\omega = 2\pi f$, and over a range of temperatures for TEOP NTf_2. The lines correspond to fits obtained by a combination of the Havriliak-Negami function and Debye equation with a power law to account for low frequency dispersion due to electrode polarization, as given in Eq. (3.7), where ε_∞ is the high frequency limiting permittivity, σ_0 is the dc ionic conductivity, ε_0 the vacuum permittivity, $\Delta\varepsilon_e$ and $\Delta\varepsilon_{aggregate}$ are the dielectric strengths, τ_e and $\tau_{aggregate}$ are the relaxation times, β and γ are the stretching parameters, A is the

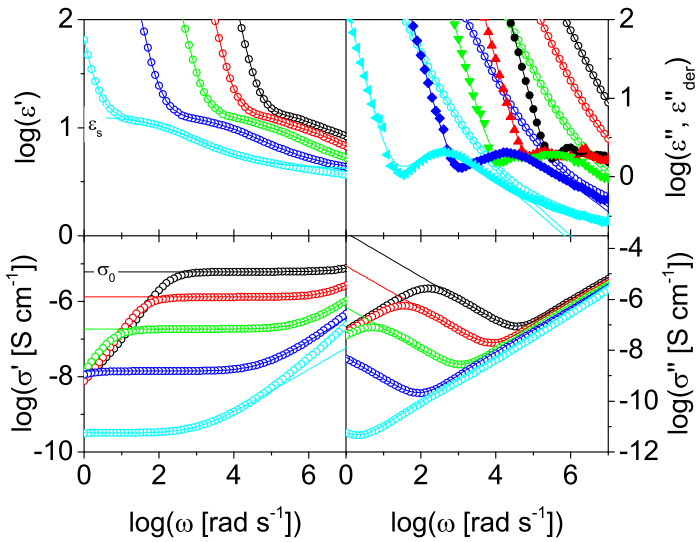

Figure 3.27: Real, ε' and σ', and imaginary, ε'' and σ'', parts of complex permittivity, $\varepsilon^*(\omega) = \varepsilon'(\omega) - i\varepsilon''(\omega)$, and conductivity, $\sigma^*(\omega) = \sigma'(\omega) + i\sigma''(\omega)$, for TEOP NTf_2. A slow sub-α relaxation emerges with increasing temperature, as observed in $\varepsilon''_{der} = (\pi/2)/[\partial\varepsilon'/\partial\ln(\omega)]$. Lines correspond to fits obtained by Eq. (3.7). The static dielectric permittivity, ε_s, is obtained as the low frequency limit of the fit without the contribution of the power law. The long-range ionic (dc) conductivity, σ_0, corresponds to the value of the frequency independent plateau in σ' as indicated.

pre-exponential factor, and n is the exponent:[3]

$$\varepsilon^*(\omega) = \varepsilon_\infty + \frac{\sigma_0}{i\omega\varepsilon_0} + \left(\frac{\Delta\varepsilon_e}{(1+(i\omega\tau_e)^\beta)^\gamma}\right) + \left(\frac{\Delta\varepsilon_{aggregate}}{(1+(i\omega\tau_{aggregate})^\beta)^\gamma}\right) + A(\omega)^n \tag{3.7}$$

The rate of the faster relaxation, $\omega_e = 1/\tau_e$, corresponds closely to the rate of the structural relaxation as measured by dynamic mechanical spectroscopy (see Fig. 3.31), as well as the frequency of the peak in the electric loss modulus, M''. It is therefore attributed to the ion hopping dynamics previously shown to correspond to the structural relaxation in aprotic ionic liquids.[150] The slow sub-α relaxation is most readily observed as a peak in ε''_{der} at frequencies below that of the ion dynamics, where $\varepsilon''_{der} = (-\pi/2)[\partial\varepsilon'/\partial\ln(\omega)]$. The derivative representation is utilized to suppress the dominant contribution of dc ionic conductivity to the dielectric spectra and to enable the observation of dynamics slower than the conductivity relaxation. The existence of the slow relaxation in TEOP NTf_2 and its ammonium homologue was previously reported by Griffin et al.[171] A clearer representation showing the existence of the two relaxations is made by plotting ε''_{der} against the frequency normalized by the frequency of the ion dynamics, ω_e, as presented in

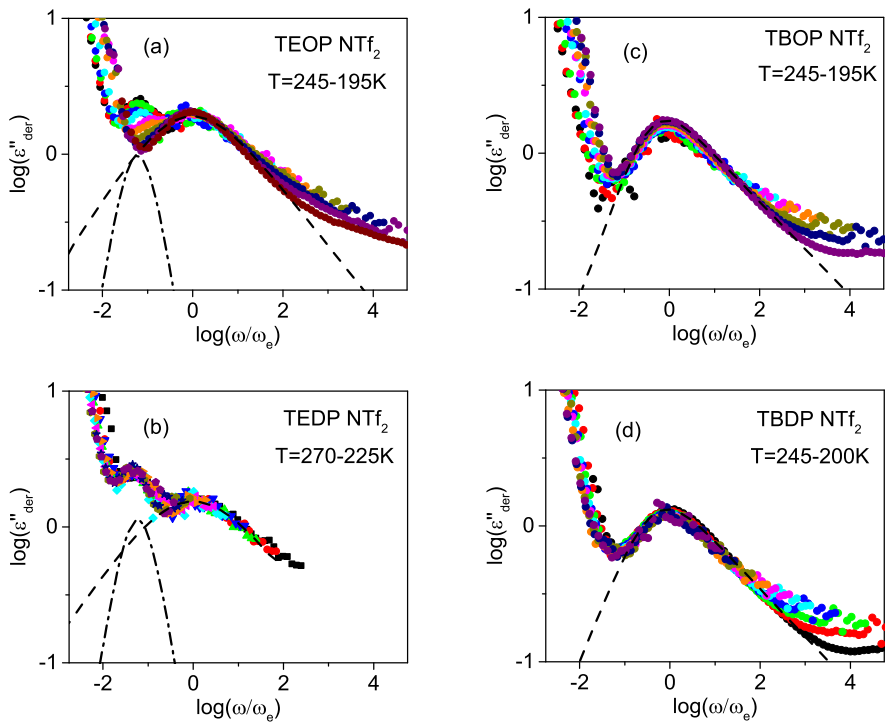

Figure 3.28: Derivative representation of the real part of complex dielectric function, $\varepsilon''_{der} = (-\pi/2)[\partial\varepsilon'/\partial\ln(\omega)]$, of the two series of phosphonium bis(trifluoromethylsulfonyl)imide ionic liquids: (a) triethyloctylphosphonium, TEOP NTf_2; (b) triethyldodecylphosphonium, TEDP NTf_2; (c) tributyloctylphosphonium, TBOP NTf_2; and (d) tributyldodecylphosphonium, TBDP NTf_2.

Fig. 3.28, for all the studied phosphonium ionic liquids. Here, the dashed lines represent the Havriliak-Negami function used to describe the α-relaxation and the dotted-dashed line is the Debye equation used to describe the slow sub-α relaxation. The most obvious difference in the dielectric spectra is the absence of the slower dielectric process in the tributyl-alkyl-phosphonium ionic liquids. In addition, the width of their α-relaxation is noticeably narrower (see Table 3.5) for shape parameters of the Havriliak-Negami fit function. The disappearance of the sub-α relaxation dynamics indicates that long-lived mesoscale aggregates do not form in the two tributyl-alkyl-phosphoniums, in apparent contradiction to the picture from the measured x-ray scattering profiles.

The real and imaginary parts of the complex shear modulus, $G^* = G'(\omega) + iG''(\omega)$, of TEOP NTf_2 and TBOP NTf_2 are presented in Fig. 3.29. The lines correspond to a fit with a single Cole-Davidson function as given in Eq. (3.8), where G_∞ is the high frequency limiting shear modulus, τ_α is the relaxation time of the structural α-relaxation, and γ is a parameter associated with the spectral

Table 3.5: Shape parameters from fits using the Havriliak-Negami function [Eq. (3.7)]

Cation	T [K]	$\beta \pm 0.1$	γ
TEOP	200	0.5	0.8 ± 0.2
TEDP	225	0.4	1.0 ± 0.2
TBOP	200	0.8	0.4 ± 0.1
TBDP	225	0.7	0.5 ± 0.2

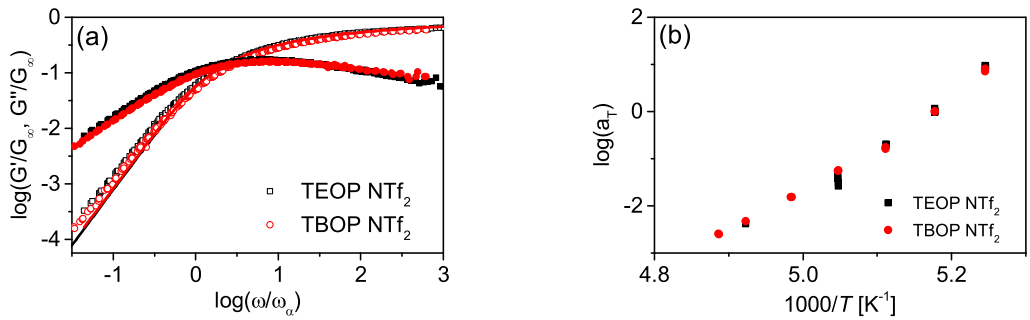

Figure 3.29: (a) Real (open symbols) and imaginary (closed symbols) parts of the complex shear modulus of TEOP NTf_2 and TBOP NTf_2 as measured over the temperature range 190-205 K. Lines correspond to fits by Eq. (3.8). (b) Shift factors, a_T, obtained from time-temperature superposition of the shear modulus over the temperature range 205 K - 190 K.

shape.[94] The shift factors used to create the shear modulus master curve are provided in Figure 3.29(b).

$$G' = Re\left[G_\infty\left(1 - \frac{1}{(1 + i\omega\tau_\alpha)^\gamma}\right)\right] \tag{3.8}$$

In our previous article, a slow sub-α relaxation was also observed by dynamic-mechanical spectroscopy (DMS) for 1-octyl-3-methylimidazolium tetrafluoroborate and attributed to the motion of mesoscale aggregates. However, such a relaxation is not found in either of the phosphonium ionic liquids investigated here. DMS measurements of the longer chain TEDP NTf_2 and TBDP NTf_2 were not successful due to their high propensity to crystallize as shown by the differential scanning calorimetry results in Figure 3.30. The broader frequency range of BDS enables the investigation of the dynamics of interest at temperatures above the crystallization point. The relative magnitude and sharpness of the x-ray pre-peak is much lower in the phosphonium ILs compared to the imidazolium systems. This indicates that even in the triethyl-alkyl-phosphoniums the degree of correlation is much lower than the corresponding imidazolium systems.[181] The sub-α dynamic-mechanical relaxation may be less sensitive to lower extents of aggregation than the dielectric relaxation, as

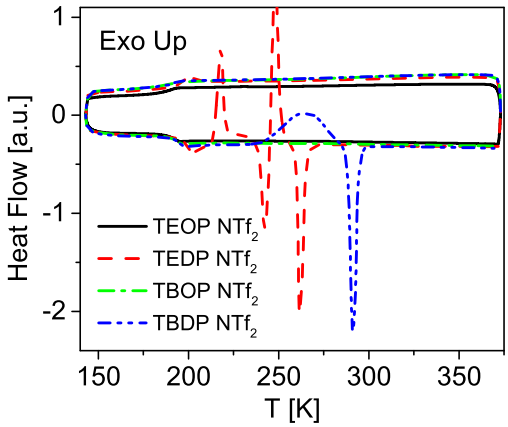

Figure 3.30: Differential scanning calorimetry (10 K min^{-1}) cooling and heating curves for the phosphonium IL series.

is suggested by its response to alkyl chain length in the imidazolium ILs. It is also possible that the mesoscopic domains are disrupted at the low temperatures probed by DMS, as indicated by the disappearance of the slow sub-α dielectric relaxation with decreasing temperature. A decrease in organization at low temperatures has previously been observed in molecular dynamics simulations and x-ray measurements of trihexyl-tetradecyl-phosphonium bis(trifluoromethylsulfonyl)imide and attributed to a reduced ordering of the polar phase.[22, 190, 234] The structural α-relaxation rates, ω_α, obtained by DMS are presented with the relaxation rates obtained by BDS in Fig. 3.31. As stated previously, the ion hopping relaxation rate corresponds closely to the structural relaxation rate, while the slow sub-α relaxation is approximately 20 times slower at the higher temperatures.

The real-space correlation distance corresponding to the low-q, polarity alternation-peak in x-ray scattering of the phosphonium series is presented as a function of the longest alkyl chain length in Fig. 3.32. These values are compared with literature data for the ILs 1-alkyl3-methylimidazolium,[18] 1-alkyl-1-methylpyrrolidinium,[19] 1-alkyl-1-methylpiperidinium,[20] trialkyl-methylammonium,[21] and trihexyl-tetradecyl-phosphonium[22] bis(trifluoromethylsulfonyl)imide. The mesoscale aggregates are characterized by the formation of a non-polar domain consisting of interdigitated alkyl chain tails surrounded by a polar domain of anions and cations. The pre-peak is taken as the distance, $d = 2\pi/q_{peak}$, separating the polar domains on the opposite sides of the non-polar inclusion. The dependence of d on the number of carbons in the alkyl chain, n_c, will depend on the degree of interdigitation, the ratio of trans/gauche

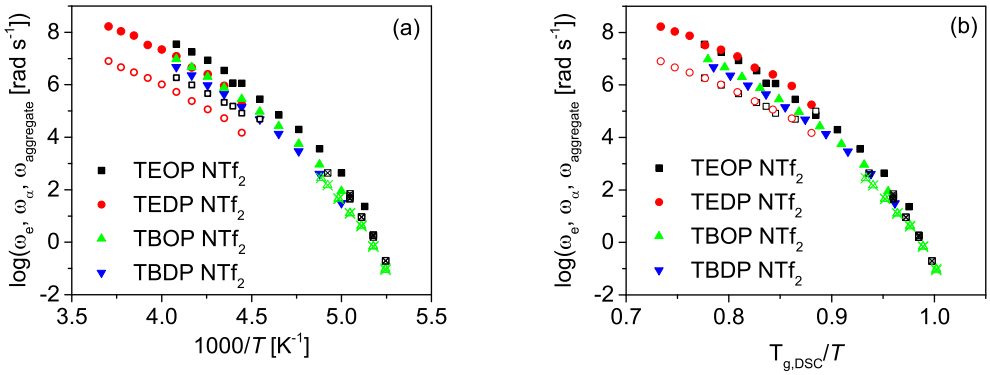

Figure 3.31: (a) Structural relaxation rates, ω_α, obtained by DMS (crossed symbols), ion hopping rates, ω_e, obtained by BDS (closed symbols), and the relaxation rate of the slow sub-α relaxation, $\omega_{aggregate}$, obtained by BDS (open symbols). (b) Relaxation rates *versus* temperature scaled by the calorimetric glass transition temperature obtained by DSC, $T_{g,DSC}$.

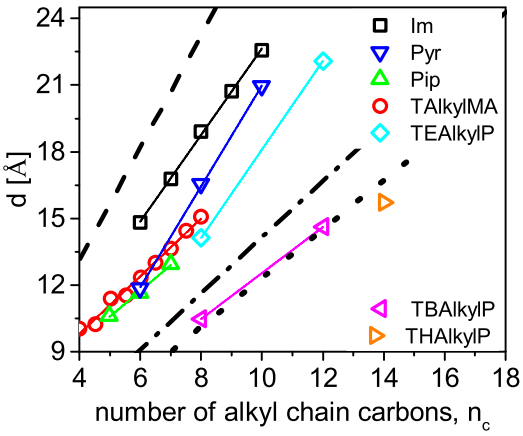

Figure 3.32: Real-space distance of the polarity alternation peak, $d = 2\pi/q_{peak}$, as a function of the number of carbons in the alkyl chain for imidazolium[18] (Im), pyrrolidinium[19] (Pyr), piperidinium[20] (Pip), trialkyl-methylammonium[21] (TAlkylMA), triethyl-alkyl-phosphonium (TEAlkylP), tributylalkyl-phosphonium (TBAlkylP), and trihexyl-tetradecyl-phosphonium[22] (THAlkylP) ionic liquids with the bis(trifluoromethylsulfonyl)-imide anion. The dotted-dashed line is l_{max} given by the Tanford equation, the dashed line is $2l_{max}$, the dotted line is $0.87l_{max}$, and the solid lines are linear fits (parameters are listed in Table 3.6).

Table 3.6: Parameters for the linear fits, corresponding to the solid lines in Fig. 3.32.

IL Series	Slope [Å/CH_2]
Im	2.0
Pyr	2.3
Pip	1.2
TAlkylMA	1.3
TEAlkylP	2.0
TBAlkylP	1.0

isomers, and the location of ions within the polar domain.[18, 239] A further insight into this correlation distance is obtained by comparing d with the length of an extended, all-trans alkyl chain. This distance is given by the Tanford equation, $l_{max} = 1.5\,(\text{Å}) + 1.265(\text{Å}/\text{CH}_2)\text{n}_c$, and is represented in Fig. 3.32 by the dotted-dashed line.[37] The maximum possible size, d_{max}, of a mesoscale aggregate will approximately correspond to an aggregate in which opposing alkyl chains are completely extended and non-interdigitated, $d_{max} = 2l_{max} = 3.0\,(\text{Å}) + 2.53(\text{Å}/\text{CH}_2)\text{n}_c$. This case is represented by the dashed line in Fig. 3.32. The majority of ILs have values of d intermediate of these two extremes, indicating varying degrees of interdigitation as well as possible changes in the organization of the polar phases and trans/gauche ratios. However, the d-spacing of the tributyl-alkyl-phosphonium and trihexyl-tetradecyl-phosphonium is significantly lower. In fact, they fall below the length scale of a single fully extended alkyl chain, revealing that aggregation is no longer necessary to explain the origin of this distance. In addition, the slope is significantly lower for the tri-butyl-alkyl-phosphonium series, see Table 3.6. The d-spacing in these systems is well approximated by $0.87l_{max}$, which is shown as a dotted line in Fig. 3.32, indicating that the only possible mesoscale aggregate capable of producing this length scale would consist of fully interdigitated alkyl chains with some degree of trans/gauche isomerism.[37] Recent atomistic simulations on a series of similar quaternary phosphonium chloride-based ILs reveal even shorter length scales associated with the x-ray scattering pre-peak.[235] Therefore, the dramatic change in the d-spacing upon lengthening the shorter alkyl chains on quaternary phosphonium ILs from ethyl to butyl is attributed to a disruption of the mesoscale hydrophobic aggregates, in agreement with the atomistic simulations which show a breaking of the polar network in the tributyl-alkyl-phosphonium chlorides.[235]

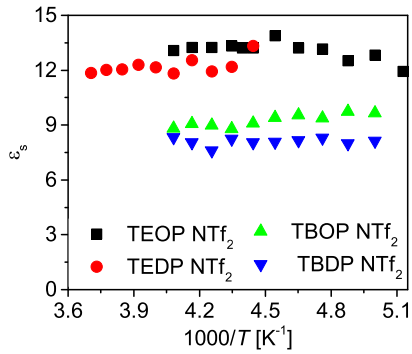

Figure 3.33: Static dielectric permittivity, ε_s, is reduced in the non-aggregating tributyl-alkylphosphoniums relative to the aggregating triethyl-alkylphosphonium series.

The loss of the mesoscale aggregates is corroborated by the absence of the slow sub-α relaxation, which is present in the more highly aggregating imidazolium and triethyl-alkylphosphonium ILs.[211] The existence of a pre-peak is therefore insufficient evidence that similar types of long-lived hydrophobic aggregates are present across ranges of ionic liquids. Rather, the actual distances corresponding to the pre-peak must also correspond to anticipated length scales based on the chemical structure of the IL. In addition, techniques capable of probing the dynamics of mesoscale aggregates, such as dielectric spectroscopy, provide valuable insight into the existence of aggregates as well as their influence on physicochemical properties. The sensitivity of the mesoscale organization to the lengths of the alkyl chains on quaternary phosphonium ILs distinguishes them from other classes of aprotic ionic liquids. These results show that a high degree of tunability of the mesoscale structures is achievable with minor changes to the chemical structure. The mechanism of the disruption is attributed to a weakening of Coulombic interactions within the polar phase due to the increased distance between neighboring ionic groups. This larger separation is evidenced by the increase in charge adjacency distances corresponding to the middle-q x-ray peak (see Fig. 3.26). Studies over a wider range and combination of alkyl chain lengths are currently underway to more fully elucidate the role of chemical structures in the transition from aggregating to non-aggregating phosphonium ILs.

Elucidating the link between the chemical structure and physicochemical properties is a necessary step for the full realization of ionic liquids as truly *designer* solvents. Accordingly, the influence of mesoscale organization on such properties must be identified. With increasing alkyl chain length and the onset of mesoscale aggregation, several authors have reported a reduction

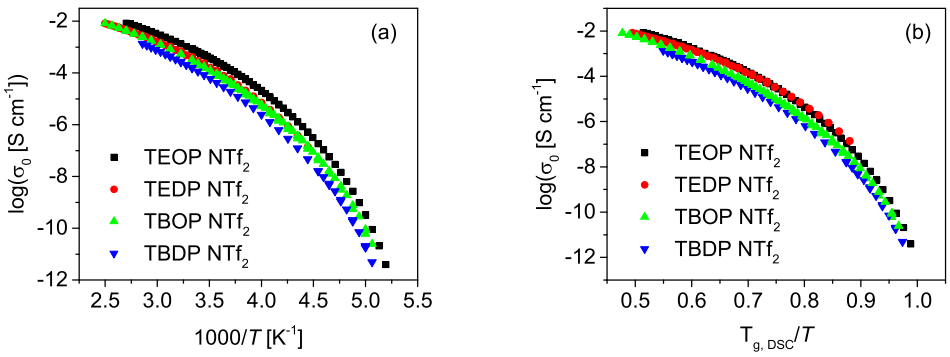

Figure 3.34: Long-range ionic (dc) conductivity as a function of (a) inverse temperature and (b) temperature normalized by the calorimetric glass transition temperature, $T_{g,DSC}$. The ionic conductivity is reduced in the tributyl-alkylphosphoniums.

in ion mobility, leading to a decrease in the ionic conductivity and a simultaneous increase in the zero-shear viscosity.[179, 240, 241, 154] In addition, we have previously reported an increase in the static dielectric permittivity and viscosity due to the additional slow sub-α dielectric and dynamic-mechanical relaxation in aggregating imidazolium ILs. As seen in Figs. 3.33 and 3.34, the transition from triethyl-alkyl-phosphonium to tributyl-alkyl-phosphonium results in a decrease of the static dielectric permittivity as well as the ionic conductivity. The reduction in ionic conductivity might be interpreted as an aggregation induced effect. However, considering the x-ray and BDS evidence presented earlier, this interpretation is not favored. Elucidating whether this decrease is due to the reduced ion mobility or effective number density of charge carriers requires a comparison of diffusivities obtained by pulsed field gradient nuclear magnetic resonance spectroscopy and charge diffusivities as previously accomplished for imidazolium and ammonium ILs.[150, 154] The reduction in static permittivity in the tributyl-alkyl-phosphoniums is consistent with the absence of aggregate induced dynamics. These results highlight the importance of utilizing multiple experimental approaches to investigate the formation of long-lived, mesoscale aggregates, so that changes in physicochemical properties of ionic liquids are not misinterpreted as aggregation induced effects.

Conclusion

In conclusion, the mesoscopic organization, dynamics, and charge transport properties of a series of tetraalkylphosphonium ionic liquids were investigated by small and wide angle x-ray scattering,

broadband dielectric spectroscopy, dynamic-mechanical spectroscopy, and differential scanning calorimetry. A comparison of estimated aggregate size from the Tanford equation with the aggregate size obtained from the x-ray scattering pre-peak indicates a disruption of mesoscale aggregates in tributyl-alkyl-phosphonium ILs. The absence of aggregation is corroborated by the loss of the slow sub-α dielectric relaxation previously linked to the dynamics of mesoscale aggregates. The combination of techniques capable of probing the mesoscale structure with those capable of to distinguish ionic liquids that exhibit an x-ray scattering prepeak due to the formation of long-lived mesoscale aggregates. This distinction is an important step in elucidating the influence of mesoscale aggregation in the physicochemical properties of ionic liquids.

3.5 Anion Dependence of Charge Transport and Dipolar Relaxations in Phosphonium-based Ionic Liquids

In this section, we investigate the influence of anion structure on charge transport and dynamics in a series of ionic liquids with the same cation, tributyl-octyl-phosphonium. In the previous section, we investigated the tributyl-octyl-phosphonium bis(trifluoromethylsulfonyl)imide ionic liquid which, while it exhibits a pre-peak in the x-ray scattering profile, lacks the sub-α dielectric relaxation. Together with an examination of the real-space distance corresponding to the pre-peak correlation, this lack of the sub-α relaxation is taken as an indication that a long-lived mesoscale organization, characterized by a well-defined polar and non-polar domain, is not present in this liquid. Therefore, in this section we turn our attention away from the organization and dynamics at the mesoscale and rather investigate the role of anion chemical structure in a non-aggregating IL with a relatively large non-polar volume fraction.

This section is a reprinting of a previously published article and its supporting material. My primary contributions to this article include: (i) data collection and analysis, (ii) interpretation of results, and (iii) writing. Changes from the published version include the addition of small and wide-angle x-ray scattering profiles.

Abstract

The role of anions in charge transport and localized dipolar relaxations in tributyloctylphosphonium ionic liquids is investigated by broadband dielectric spectroscopy and rheology. The dielectric spectra are quantitatively described by a combination of the random barrier model which accounts for ion transport and empirical Havriliak-Negami functions to characterize dipolar relaxations. Two secondary relaxations are observed at temperatures below the calorimetric glass transition temperature, where the primary structural relaxation is essentially frozen at the relevant experimental time scales. The faster process has an anion independent activation energy of 30 kJ mol^{-1} and is attributed to libration motion of the phosphonium cation. The slower relaxation is similar to a process previously assigned to a Johari-Goldstein relaxation in imidazolium-based ionic liquids; however, the activation energy is significantly higher in the phosphonium systems. For the charge transport dominated regime, it is observed that variation of the anion results in differences in the dc ionic conductivity and characteristic charge transport rates by ∼2.5 decades. Upon scaling by the calorimetric glass transition temperature, both transport quantities are observed to coincide. From these results, a picture of glass transition assisted hopping emerges as the underlying microscopic mechanism of ion conduction, in agreement with recent results obtained for other classes of aprotic ionic liquids.

Introduction

Ionic liquids (ILs) are purely ionic materials with melting points below 100 °C. They are promising for many applications due to their unique solvent properties, large electrochemical windows, low vapor-pressure, high thermal-stability, and high ionic conductivity.[59, 45, 43] Their near-limitless permutations and the substantial effects that minor structural changes have on the electrical and dynamical properties of these mixtures have earned them the designation, "designer solvents." In general, ILs have been a topic of intense investigation for well over two decades, but there is currently no quantitative means of determining the emergent electrical, dynamical, and solvent properties of an ionic liquid from chemical structure alone, hence limiting our ability to design these materials for specific potential applications.

After many years of scientific research on ILs synthesized from nitrogen-based cations, the review work of Bradaric et al. published in 2003 demonstrated that their phosphonium-based counterparts have properties that warrant closer attention too, e.g., the fact that their kinetics of salt formation is, in general, much faster than for amines because their larger radii and higher polarizability make them more nucleophilic.[242, 243] It is worth recalling here that phosphorous is more electronically polarizable than nitrogen.[237] Additionally, it is evident that phosphonium-based ILs have appreciably reduced viscosities and higher ionic conductivities with respect to their ammonium homologues.[244, 245, 246, 247, 248, 249, 250] This has been attributed to the relatively larger volume of the phosphonium cation which in effect decreases the cation charge density and the electrostatic friction between counterions.[246, 251] Thermogravimetric analyses have also shown that although the decomposition point upon heating for neat phosphonium ionic liquids varies depending on the specific anion used, their dynamic thermal stability window is well above 300 °C.[250] In spite of ample evidence that substitution of nitrogen by phosphorus leads to a myriad of changes in the physicochemical properties of the corresponding ILs thereby offering new opportunities for industrial applications, phosphonium-based salts remain a relatively unexplored class of ILs, especially concerning their charge transport and dynamics.[32]

Extensive investigations of charge transport in ionic liquids have shown that the dc conductivity, σ_0, and the characteristic charge transport rate, ω_c, are closely coupled to the structural, α-relaxation rate, ω_α. The latter relaxation process is the molecular basis for the viscosity of liquids as given by Maxwell's relation, $\eta = G_\infty/\omega_\alpha$, where η is the zero-shear viscosity and G_∞ is the high-frequency shear modulus and is associated with the dynamic glass transition.[252, 87] The dynamic glass transition in all liquids is thought to be one of the most fundamental characteristics and is determined by intermolecular interactions.[253, 254] In the well-studied imidazolium-based ILs, variation of the anion produces substantial changes in the relaxation rates as well as the dc conductivity; however, upon scaling by the calorimetric glass transition temperature, T_g, the values coincide.[150] The overlap of charge transport properties upon scaling by T_g indicates that it is the dynamic glass transition which determines the changes in charge transport with anion substitution. There is some evidence indicating that quaternary cations with long, non-polar substituents have a lower fraction of available charge carriers contributing to the ionic conductivity, that is, a lower ionicity, relative to the heterocyclic imidazolium cations.[11, 154] While phosphonium ionic liquids

have been characterized with different cation and anion variants, a systematic study of anion effects has not yet been performed.[255] At time scales faster than the dynamic glass transition, phosphonium systems exhibit a well-defined local dipolar relaxation. Due to the reduction in primary structural mobility at these frequencies and temperatures, the origin of this faster dipolar relaxation may be attributed to a localized fluctuation or libration of the constituent molecules in the glassy state.[3] Similar studies on imidazolium-based ionic liquids have been performed, suggesting that the anion has a detectable effect on the sub-T_g processes, but whether this result holds for phosphonium-based systems is currently unknown.[256, 257]

In this article, a series of tributyloctylphosphonium ionic liquids are investigated using broadband dielectric spectroscopy, rheology, and differential scanning calorimetry to determine the effects of anion change on the charge transport and dynamics in these systems. It is shown that while substitution of the anions results in drastic differences in the charge transport, these changes can be fully accounted for by considering contributions from the dynamic glass transition. Detailed analysis of the high-frequency dielectric spectra reveals the presence of two secondary dielectric relaxations. The faster relaxation exhibits identical thermal activation, suggesting that motion of the cation, rather than the anion, is the origin of this high-frequency dipolar response. The slower relaxation is more highly dependent on the anion as has been observed in imidazolium-based ionic liquids, where it was attributed to a Johari-Goldstein relaxation.

Experimental

The materials investigated in this study are a series of tributyloctylphosphonium (TBOP) ionic liquids paired with the anions: dicyanamide (DCA), bis(trifluoromethylsulfonyl)imide (NTf_2), trifluoromethanesulfonate (OTF), thiocyanate (SCN), trifluoroacetate (TFA), and tetrafluoroborate (TFB). The chemical structures of the cation and anions are displayed in Fig. 3.35. The materials were obtained from Nippon Chemical Industrial Co. and dried in a home-built ultrahigh vacuum setup at 330 K for >24 h prior to use. Broadband dielectric spectroscopy (BDS) measurements were carried out using a Novocontrol Alpha analyzer (frequency range $10^{-1}-10^{7}$ Hz) with a QUATRO temperature control system (120−400 K and temperature stability ±0.1 K) using nitrogen as the cooling and heating gas.[154] Samples were measured using 20 mm stainless steel electrodes in a parallel-plate configuration with 100 µm Teflon spacers to maintain sample thickness. Rheological

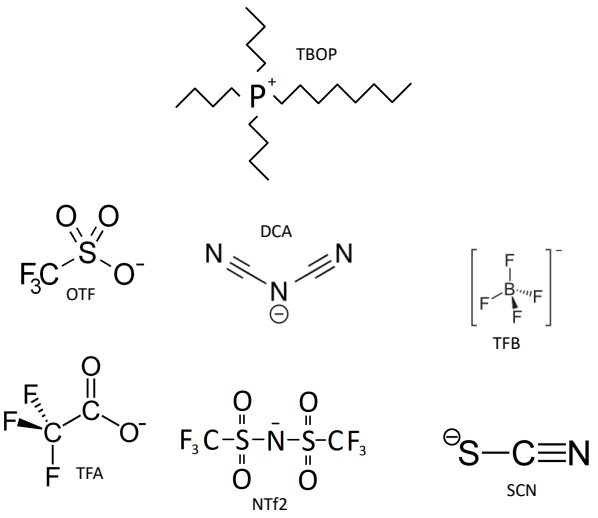

Figure 3.35: The chemical structures of the ionic liquids studied in this work.

creep compliance measurements were performed on a Hybrid Rheometer 2 (TA Instruments) using 25 mm and 3 mm plates. The temperature was controlled by an environmental test chamber with nitrogen as the gas source (temperature stability ± 0.1 K). At each measurement temperature, a constant small stress was applied until a steady strain was observed. The response at the long time limit was used to obtain the zero-shear viscosity of the ILs.[154] Differential scanning calorimetry (DSC) measurements were performed on a TA Instruments Q2000 calorimeter at a cooling rate of 10 K min^{-1}. The calorimetric glass transition temperature, T_g, was determined at the midpoint of the step in the heat flow corresponding to the maximum in the temperature derivative of the heat flow.

Results and Discussion

The complex dielectric function, $\varepsilon^*(\omega) = \varepsilon' - i\varepsilon''$, was measured using broadband dielectric spectroscopy, providing insight into the charge transport and storage in the system with respect to both frequency and temperature. A plot of the real and complex parts of the conductivity and dielectric function is shown in Fig. 3.36 for tributyloctylphosphonium dicyanamide (TBOP DCA). The dielectric spectra are well described by a single empirical Havriliak-Negami (HN) function, which can be viewed as a Debye-process with symmetrical and asymmetrical stretching terms, coupled with an analytical approximation of the Random Barrier Model (RBM), which describes

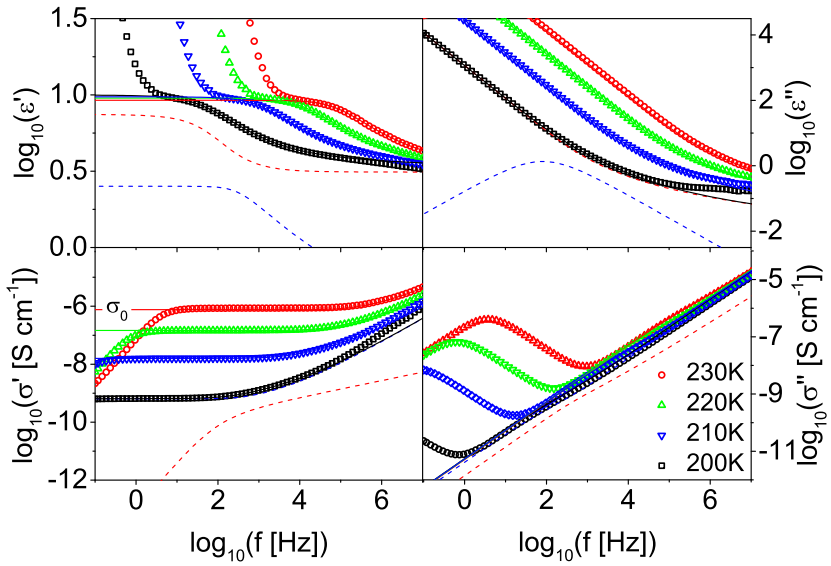

Figure 3.36: The real and imaginary parts of the complex dielectric function, $\varepsilon^*(\omega) = \varepsilon' - i\varepsilon''$, and conductivity, $\sigma^*(\omega) = \sigma' + i\sigma''$, of the ionic liquid tributyloctylphosphonium dicyanamide (TBOP DCA) are shown. The dashed red line represents a Havriliak-Negami fit, while the dashed blue line represents a random barrier model fit. The solid lines represent a linear combination of these two functions. The temperatures range from 230 K to 200 K, going from red circles to black squares.

charge transport within the framework of carrier hopping in a random energy landscape.[81, 4] The RBM has been shown to accurately model the dielectric spectra associated with the ionic conductivity in disordered materials, while the HN function is used extensively to model contributions from dipolar relaxations in general.[256, 151] The combination of the two functions is shown in the following equation, with the first term being the analytical approximation of the random barrier model and the second corresponding to the Havriliak-Negami contribution, where σ_0 is the dc ionic conductivity, ε_∞ is the high-frequency limiting permittivity, $\Delta\varepsilon$ is the dielectric strength, τ_e and τ_{HN} are the relaxation times, and α and γ are stretching parameters:

$$\varepsilon^*(\omega) = \varepsilon_\infty + \frac{\Delta\varepsilon}{(1 + (i\omega\tau_{HN})^\alpha)^\gamma} + \frac{\sigma_0}{i\omega\varepsilon_0}\frac{i\omega\tau_e}{\ln(1 + i\omega\tau_e)} \tag{3.9}$$

The quantitative agreement of Equation 3.9 with the dielectric data indicates that there is a single dipolar process that is strongly coupled with ion motion. This is an interesting observation given that a similar system with shorter alkyl chains, triethyloctylphosphonium, has been shown to have a pronounced sub-α process in earlier studies.[171] Such a slow, sub-α dielectric relaxation has been

Table 3.7: Real-space correlation distances corresponding to the pre-peak positions in Figure 3.37

Anion	$d = 2\pi/q_{max}$ [Å]
OTf	11.3
TFB	11.6
NTf_2	10.5

linked to the motion of supramolecular hydrophobic aggregates in imidazolium ionic liquids and its absence may indicate a disruption of such aggregates in these tributyloctylphosphonium ionic liquids.[211] The primary evidence for the existence of mesoscale aggregates is a pre-peak in the x-ray and neutron scattering profiles of a variety of ionic liquids with extended alkyl chains.[32] The x-ray scattering profiles of three of the TBOP-ILs are shown in Figure 3.37. There is a pre-peak evident at a q-value of 0.6 Å^{-1} which is only weakly dependent on the anion structure, see Table 3.7. The lack of a strong sub-α dielectric relaxation may indicate that the polar domains are simply not well-formed enough to contribute to an interfacial polarization mechanism. The influence of molecular structure on such mesoscale organization and its impact on transport properties of ILs remain an open question which will require a combination of experiments and computation over broad length and time scales to unravel.[179, 258, 259, 15] One of the key parameters from fits using Eq. 3.9 is the dc ionic conductivity, σ_0, which corresponds to the frequency-independent value of the real part of the conductivity spectra, shown in Fig. 3.36. The departure from the plateau value at low frequencies is typically associated with electrode polarization, while the transition into a power law at higher frequencies corresponds to the change from long-range diffusion to sub-diffusive regimes.[4, 260]

The variation of the anion results in differences in the dc ionic conductivity by about 2.5 orders of magnitude (see Fig. 3.38) at lower temperatures across all systems probed. The ordering of the ionic conductivity appears to be non-trivially related to the structure of the anion and attempts to reconcile the observed trend with simple quantities such as molecular volume or weight have, so far, been unsuccessful. This is a different picture if one considers imidazolium systems with spherical-type anions, which yield a systematic trend with respect to anion size.[256] This difference is likely due to variations in the anion shape and charge distribution, but without a comparable anion set for the imidazolium ILs, cation effects or specific intermolecular interactions, like π—π interactions or hydrogen bonding, cannot be excluded. Normalization by the glass transition temperature suggests

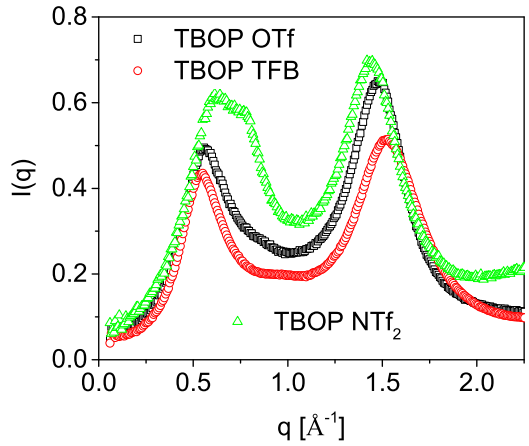

Figure 3.37: X-ray scattering profiles of tributyl-octyl-phosphonium ionic liquids with the trifluoromethanesulfonate (OTf), bis(trifluoromethylsulfonyl)imide (NTf_2), tetrafluoroborate (TFB) anions. The real space correlation distance corresponding to the pre-peak q-value, d=$2\pi/q_{max}$, are provided in Table 3.7

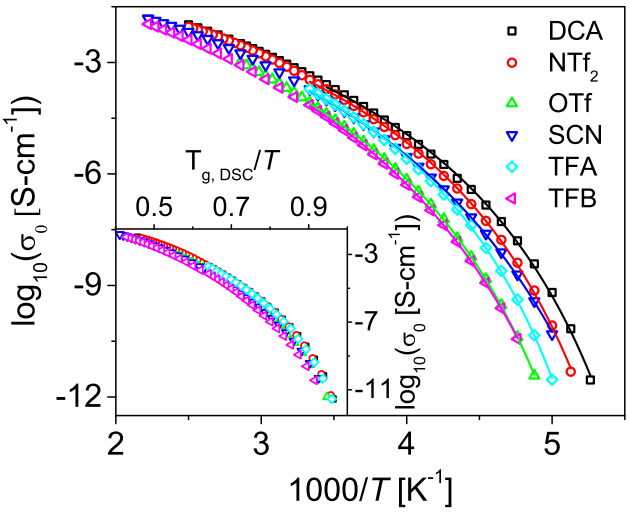

Figure 3.38: The dc ionic conductivity, σ_0, versus inverse temperature for all TBOP samples. Solid lines are fits to the Vogel-Fulcher-Tammann equation. The anion dependence of the conductivity is dominated by the shift in structural relaxation rates as indicated by the inset plot showing dc ionic conductivity normalized by the T_g obtained from DSC. From DCA to TFB, T_g values are 186 K, 192 K, 201 K, 191 K, 196 K, and 202 K. ±2 K for all samples. Cooling rate = 10 K min^{-1}.

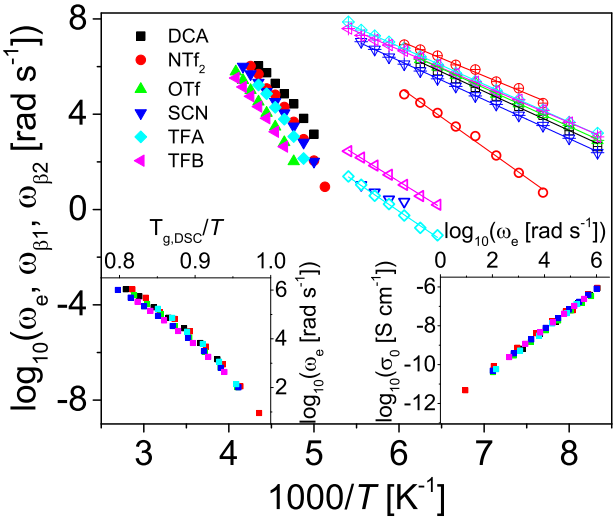

Figure 3.39: The temperature dependence of characteristic relaxation rates for charge transport as well as the β_1 and the β_2 secondary relaxations. Closed symbols show the relaxation rates associated with the conductivity, ω_e. Crossed and open symbols show the rates of the β_1 and β_2 processes, respectively. The rate and presence of the β_2 process is strongly dependent on the anion, whereas the faster β_1 relaxation is relatively unaffected. The left inset shows the values normalized with respect to the glass transition temperatures (DSC heating run). The right inset shows the BNN relations for each of the TBOP samples.

that general ion dynamics of these systems are controlled by the dynamic glass transition.[261, 262] A similar trend is observed for the characteristic rates associated with the dynamics. In Fig. 3.39, the charge hopping and secondary relaxation rates for these materials are shown.

The trend of the characteristic rates of charge transport closely mirrors the order of the magnitudes of the DC conductivity. In fact, plotting the dc conductivity versus the characteristic rate, ω_e, known as the Barton-Nakajima-Namikawa (BNN) relation, a relationship used frequently when discussing the behavior of ionic materials, the conductivity and its associated rate are shown to be directly proportional to one another in a double logarithmic plot (see Fig. 3.39, right inset).[263, 264] Traditionally, the BNN relation illustrates the proportionality of the dc conductivity and characteristic charge transport rate multiplied by the static dielectric permittivity (dielectric constant) or the dielectric strength of the α-relaxation.[265] In the present case, the static permittivities, ε_s, are very similar across all the phosphonium ILs, ranging from 8 to 10, as shown in Fig. 3.40.

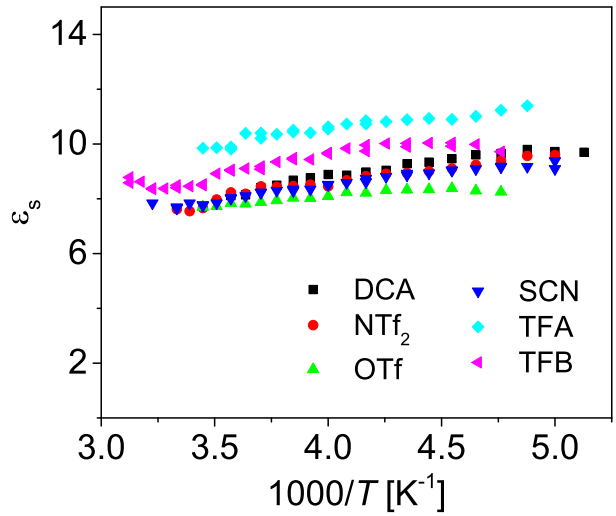

Figure 3.40: Static dielectric permittivities, ε_s, of the phosphonium IL with the indicated anions. The static permittivities are defined by the low frequency limit of the fit by Eq. 3.9 of the real part of the complex dielectric function, as shown in Fig. 3.35.

Mechanical structural α-relaxation rates, ω_α, were also obtained directly from oscillatory shear measurements. Additionally, using Maxwell's relation and the high-frequency shear modulus, the structural α-relaxation rates may be estimated by $\omega_\eta = G_\infty/\eta$. These rates are compared in Fig. 3.41 for TBOP NTf$_2$ with those obtained using the random barrier model (ω_e) and the HN model (ω_{max}) as well as the peak frequency of the imaginary part of complex electric modulus ($\omega_{M''}$), which is often related to the conductivity relaxation rate. The molecular relaxation rate, ω_{max}, is linked to the rate of the Havriliak-Negami function given in Eq. 3.9 by the equation $\omega_{max} = \frac{1}{\tau_{HN}}\left[\sin\left(\frac{\alpha\pi}{2+2\gamma}\right)\right]^{1/\alpha}\left[\sin\left(\frac{\alpha\gamma\pi}{2+2\gamma}\right)\right]^{-1/\alpha}$.

The consistency of the BNN relation between the phosphonium ionic liquids and most other ionic liquids shows that the mode of charge transport in these systems is general.[150] The fact that the characteristic rates for the structural α-relaxations coincide with those corresponding to ion transport unambiguously shows that the mode of charge transport is coupled to the dynamic glass transition in the studied ILs and can be thought of as glass transition assisted hopping.

Figure 3.42 displays rheology data of the measured fluidities of all the samples reported in this work. It is clear that varying the anion leads to significant change in viscosity —a property which is well known to be related to the dynamic glass transition. However, scaling the data with respect to the calorimetrically determined glass transition (see inset, Fig. 3.42) reveals that within the limits of

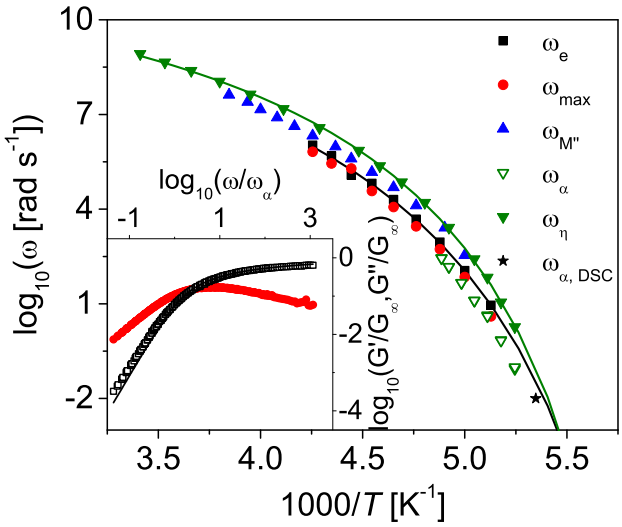

Figure 3.41: Characteristic rates of charge transport and structural relaxation for TBOP NTf_2 as measured by broadband dielectric spectroscopy, rheology, and differential scanning calorimetry (cooling run). Solid lines are fits to the Vogel-Fulcher-Tammann equation. Inset: Superimposed complex dynamic shear modulus at a temperature of 193 K as measured for TBOP NTf_2. The spectrum was constructed for measurements at several temperatures using the time-temperature superposition principle.

experimental accuracy, the samples have the same fragility. The invariance of the fragilities with anion structure is shown more explicitly in Tables 3.8 and 3.9 using the parameters obtained by Vogel-Fulcher-Tammann (VFT) fits, $\sigma_0 = \sigma_\infty[DT_0/(T - T)0)]$, of the dc ionic conductivities and fluidities, respectively. Fragility is a term describing the steepness of the temperature dependence of various transport properties linked to the structural α-relaxation in glass-forming liquids. Three common values related to changes in the fragility are T_g/T_0, D, $m = (DT_0/2.303)T_g/(T_g - T_0)^2$ as given in Tables 3.8 and 3.9. These values show that this series of phosphonium ionic liquids fall into the intermediate range of fragilities as compared to ionic liquids and other types of glass-formers.[134, 266] The lower fragility of phosphonium ionic liquids relative to imidazolium ionic liquids is one reason for their lower room temperature ionic conductivities.[43, 266] This finding is in agreement with a variety of experimental results which indicate that the identity of the cation charge center plays a much more important role in determining the physicochemical properties of ionic liquids.[246, 248]

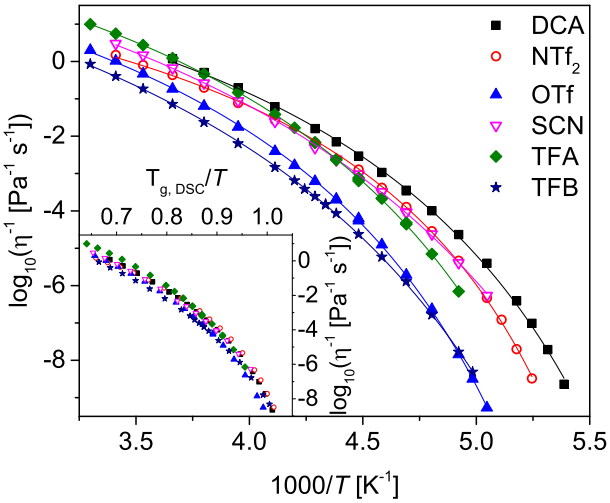

Figure 3.42: Fluidity [the inverse of viscosity, $1/\eta$] for tributyloctylphosphonium-based ionic liquids with different anions, as indicated by the legend. Solid lines are fits to the Vogel-Fulcher-Tammann equation. Inset: Scaling with respect to the calorimetric glass transition temperature measured by DSC (heating run).

Table 3.8: Parameters for the VFT fits of dc conductivity, corresponding to the solid lines in Fig. 3.38, as well as fragilities, m.

Anion	T_0	D	σ_∞ (S cm^{-1})	T_g/T_0	m
DCA	148	7.3	0.44	1.26	60
NTf_2	152	7.0	0.39	1.28	51
OTf	154	8.4	0.60	1.30	52
SCN	142	9.7	1.00	1.36	45
TFA	154	7.7	0.73	1.27	58
TFB	148	10.3	1.47	1.37	46

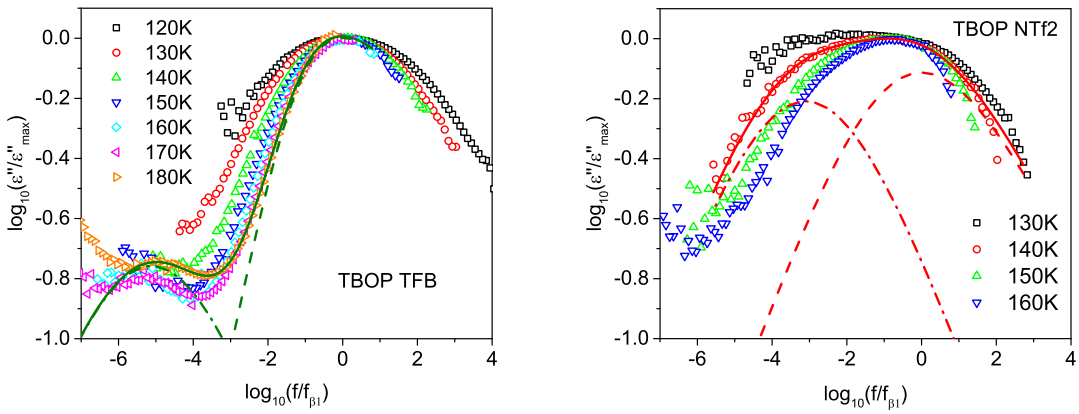

Figure 3.43: Imaginary part of the complex dielectric function, $\varepsilon^*(\omega) = \varepsilon' - i\varepsilon''$, for TBOP TFB and TBOP NTf_2 showing the low temperature, high-frequency Havriliak-Negami functions. Dotted-dashed lines correspond to the slower β_2 relaxation. Dashed lines correspond to the faster β_1 relaxation.

Table 3.9: Parameters for the VFT fits of fluidity, corresponding to the solid lines in Fig. 3.42, as well as fragilities, m.

Anion	T_0	D	η_∞^{-1} (10^4 Pa^{-1} s^{-1})	T_g/T_0	m
DCA	147	7.5	0.6	1.27	58
NTf_2	157	5.7	0.1	1.23	60
OTf	157	8.1	1.0	1.28	56
SCN	137	11.2	5.4	1.40	43
TFA	151	8.7	5.3	1.30	55
TFB	146	10.7	1.7	1.38	45

Analysis of the dielectric spectra at low temperatures reveals the presence of two secondary dipolar relaxations below the glass transition temperature; see Fig. 3.43. A combination of two additional Havriliak-Negami functions is utilized to describe these relaxations.

Since primary structural mobility is generally frozen within experimental time scales below the glass transition temperature, any processes observed at these temperatures must be related to localized or secondary molecular mobility. It is observed that for a given temperature, 150 K in this instance, the magnitudes and frequencies of the faster β_1-process are generally comparable; see Fig. 3.44. The horizontal and vertical normalization in the inset plot also clearly shows a similarity in the shapes of the processes. The practical invariance of the β_1-process despite the changes of the anion suggests that the motion is primarily that of the cation. In studies of imidazolium ILs, a similar dipolar relaxation was attributed to libration motion of the cation.[264] In triethyloctylphosphonium

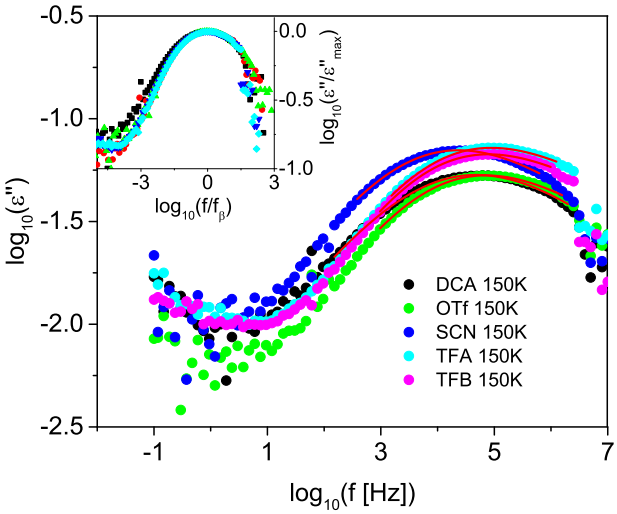

Figure 3.44: Plot of the imaginary component of the permittivity. $T = 150\,\mathrm{K}$. The inset shows the normalized values for the imaginary permittivity. Solid lines are single HN fits.

bis(trifluoromethylsulfonyl)imide (TEOP NTf_2), the β_1-process was attributed to local fluctuations of the alkyl groups based on the observed activation energy of $55\,\mathrm{kJ\,mol^{-1}}$.[171] This is however considerably higher than the $28.3\,\mathrm{kJ\,mol^{-1}}$ activation energy of TBOP NTf_2. It should be noted that in TEOP NTf_2, no β_2-process was reported. The slower β_2-process, observed only for NTf_2, SCN, TFA, and TFB anions, is very similar to an intermediate secondary relaxation observed in 1-butyl3-methylimidazolium bis(trifluoromethylsulfonyl)imide.[257] In that instance, it was attributed to an intrinsic Johari-Goldstein (JG) type relaxation on the basis of its activation energy. JG relaxations are high-frequency processes which are intrinsic to glass-forming materials and do not arise from specific molecular fluctuations. The characteristic rates of secondary relaxations typically show Arrhenius temperature dependences. By fitting using the Arrhenius equation, the activation energy can be determined. The characteristic rates are shown in Fig. 3.39. The activation energies determined from the Arrhenius fit are given in Table 3.10.

It is apparent that the activation energies of the faster relaxation are comparable between anions, further supporting the notion that the motion of the cation is predominately responsible for the β_1-process. The far right column contains the activation energy predicted by an empirical relationship observed for the beta process in many glass-formers.[257] The relationship, $E_\beta = 24RT_g$, has been proposed as the evidence of a Johari-Goldstein (JG) type β-relaxation, where R is the ideal gas

Table 3.10: Activation energies associated with secondary relaxations.

Anion	β_1 E_A (kJ mol^{-1}±1.0)	β_2 E_A (kJ mol^{-1}±1.0)	Johari-Goldstein E_A (kJ mol^{-1}±1.0)
DCA	31.4		37.1
NTf_2	28.3	48.7	38.3
OTf	31.0		40.0
SCN	31.3		38.2
TFA	30.3	46.5	39.0
TFB	29.3	42.5	40.3

constant and T_g is the calorimetric glass transition temperature. It is apparent that the predicted activation energy from a JG process significantly deviates from those experimentally determined in this work, suggesting that neither of the secondary dipolar relaxations can be ascribed to JG-type.

Conclusion

A series of phosphonium-based ionic liquids—with a systematic variation of the anion—has been analyzed using broadband dielectric spectroscopy. It is observed that anion substitution leads to shifts in the characteristic rates and dc conductivities of the sample, but normalization by T_g results in coinciding curves. Furthermore, an adherence to the BNN relation indicates that the nature of the charge transport in phosphonium-based ILs is not altered by the anions, but is rather general for this class of ionic liquids. The coincidence of the characteristic relaxation rates for charge transport and structural relaxation confirms the view that charge hopping in these systems is dominated by the dynamic glass transition. It is observed that two secondary β-relaxations occur in these ILs. The faster relaxation is attributed to libration of the cation, while the origin of the slower relaxation remains unclear. These results further enhance our understanding of the universality of charge transport in ionic liquids and support the physical picture of glass transition-assisted hopping as the underlying mechanism of ion transport in aprotic ionic liquids.

3.6 Conclusions

We have demonstrated that the existence of mesoscale organization in aprotic ionic liquids leads to the emergence of slow, sub-α dynamics in the dielectric and mechanical spectra. The mesoscale organization arises from the solvophobic aggregation of long, non-polar alkyl chains from polar

ionic head groups and counter ions. The additional relaxation dynamics lead to increases in the zero-shear viscosity and static dielectric permittivities. This direct influence of mesoscale organization on physicochemical properties has important implications for the use of ionic liquids as solvents and electrolytes in numerous applications. We further demonstrate the interfacial polarization mechanism of the aggregate dynamics through the use of binary ionic liquid mixtures. By altering the ratio of polar and non-polar volumes the aggregate shapes may be manipulated. This provides a new path to tuning the physicochemical properties of ionic liquids and their mixtures. Futhermore, we show that it is not simply a large volume fraction of non-polar component and asymmetry in the cation which lead to the formation of well-defined and long-lived aggregates. It is also vital that the strength of interactions in the polar phase be strong enough to drive the solvophobic aggregation. In quaternary phosphonium ILs there is a clear transition from aggregating to non-aggregating ILs depending on the aklyl chain substitution. The absence of sub-α relaxations in the tributyl-alkylphosphoniums further demonstrate that the sub-α dielectric relaxation is not associated strictly with the existence of large non-polar regions. Rather, it is necessary that there is both a well-defined polar and a well-defined non-polar domain. This further cements the origin of the sub-α dielectric relaxation in the interfacial polarization at the interfaces of these two distinct domains.

IL aggregate dynamics will be critical for synthesis applications. The lifetimes of aggregates may significantly alter the reaction kinetics of reactants located within either the polar or non-polar phase. When performing polymerizations for instance, the reaction pathway will be significantly altered by the existence of long-lived aggregates. This effect may be even more pronounced in IL mixtures. In this case, it is possible that the polymerization will be analogous to aqueous emulsion polymerizations. The use of IL mixtures to tune the mesoscale organization and dynamics is especially attractive. By altering the interaction of the ionic headgroup of the aggregating ion and the ions which make up the polar phase the mesoscale dynamics may become even more significantly reduced relative to the structural relaxation. In the extreme case these aggregates may be analogous to aqueous surfactant worm-like micelles which are capable of forming supramolecular gels. It is envisioned that IL mixtures will afford an unprecedented opportunity to probe solvophobic aggregate dynamics over extremely broad composition and temperature ranges which are unavailable to traditional surfactant systems.

Going forward, a wider variety of binary ionic liquid mixtures should be investigated. Especially interesting will be mixtures in which the interactions at the aggregate interfaces are altered. This might be possible for instance with mixtures consisting of aromatic and non-aromatic cations. A slight reduction in solubility at the interface is expected to drastically affect the aggregate relaxation dynamics. This type of study is in contrast to our binary ionic liquid mixtures where the chemical structure of the two cations was identical other than the alkyl chain length. With the right choice of cations and anions it may be possible to form much larger extended aggregates which in the extreme case may form systems analogous to worm-like surfactant micelles.

Future studies with a wider range of phosphonium cation chemical structures, especially with tripropyl-alkylphosphonium will allow a better understanding of the evolution of long-lived solvophobic aggregates in these unique systems. It will be necessary to study these ILs with a combination of x-ray scattering, MD simulation, dielectric, and dynamic mechanical spectroscopy to form a coherent picture for how the mesoscale organization and dynamics are depend on the cations chemical structure.

The proposed mechanism of the slow, sub-α dielectric relaxation is sensitive to the shape of the aggregate interface. The aggregate shapes and therefore interface curvature are determined in large part by the relative volumes of the polar and non-polar phases. We demonstrated this through the use of binary ionic liquid mixtures to swell the polar phase while reducing the volume fraction of the non-polar phase. The volume fraction will also be sensitive to the molar volumes of the cations and anions in neat ionic liquids. It will therefore be useful to examine in more detail the influence of various anions on the relaxation rates and dielectric strengths for a common cation and vice versa.

Chapter 4

Hydrogen-bonded Liquids: a Case Study of Imidazoles

In this chapter, the influence of chemical structure, temperature, and diluent concentration on dynamics and charge transport in hydrogen-bonded liquid imidazoles is investigated. Following an introduction to imidazole chemistry, the results of a preliminary study on the impact of levulinic acid additions on charge transport and dynamics in 2-ethyl-4-methylimidazole are presented. Afterwards, a more detailed study with a wider range of additives, compositions, and imidazole chemical structures is discussed. Our findings result primarily from a detailed analysis of slow relaxations linked to the motion of mesoscale hydrogen-bonded chains. It is found that the addition of minute amounts of levulinic acid results in a complete disruption of the hydrogen-bonded chains. These results are discussed within the framework of prior studies on dynamics in hydrogen-bonded monohydroxy alcohols and in the context of previous investigations on ionic conductivity in neat and acid-doped liquid imidazole.

4.1 Introduction and Motivation

Imidazole is a five-membered, aromatic, nitrogen-containing, heterocycle with the chemical structure given in Figure 4.1(a). Imidazoles were first synthesized in the 1850s by Heinrich Debus, the correct chemical structure was introduced by Japp in 1882, and at about the same time the name imidazole was suggested by Kantzsch.[267, 268, 269, 7] It is an amphoteric

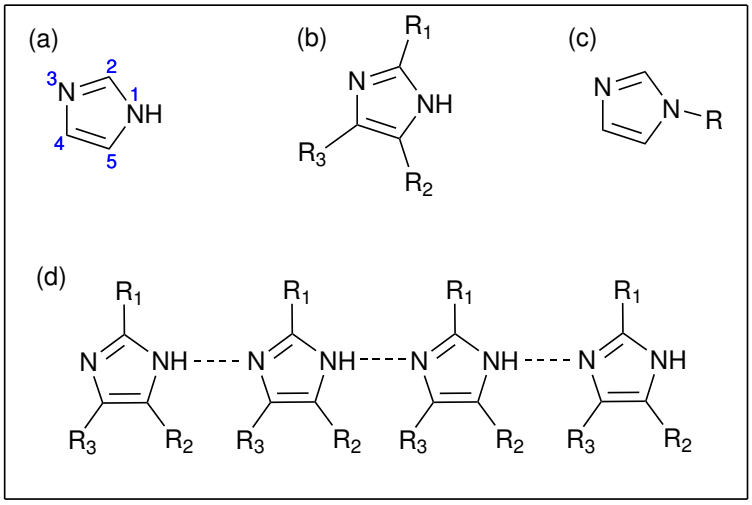

Figure 4.1: Chemical structure of (a) unsubstituted imidazole, (b) with possible substitutions in the Debus-Radziszewski synthesis route, and (c) with substition on the acidic nitrogen which prevents the formation of associated, H-bonded chains. The atoms in (a) are labeled in accordance with all chemical names in this section, i.e. 2-ethyl-4-methylimidazole has an ethyl and methyl group at the 2 and 4 carbons on the heterocycle. (d) A hydrogen-bonded tetramer. Dashed lines represent intermolecular hydrogen bonds.

molecule, possessing both an acidic and basic site. The N-H proton is a weak Brønsted acid with a pKa of 14.9, while the other nitrogen, with its lone pair electrons, is a moderate base with a conjugate acid pKa of 7.0.[7, 270] This allows imidazoles to act as both hydrogen bond donors and acceptors. In addition, the unsaturated carbon-carbon bonds in the heterocycle provide the opportunity for π-bond interactions. The primary interest in imidazoles has long been their biological importance and use in medicinal applications.[271] Imidazole is biologically relevant due to its occurrence in purine, histamine, histidine, and nucleic acids.[272] The ability for imidazole to form intermolecular associations by both hydrogen-bonding and π-π interactions plays a crucial role in a variety of enzymatic processes as well as in the formation of ligands in systems such as hemoglobin, vitamin B12, and metalloproteins.[273, 274, 275, 276, 277, 278]

The location of the acid and base sites, on opposite sides of the planar ring, allows adjacent imidazole molecules to form intermolecular hydrogen-bonds (H-bonds). The repetition of this bonding with multiple molecules leads to the development of extended associated chains, see Figure 4.1(d). In non-polar solution, (in benzene and naphthalene for example) these chains are estimated, by cryoscopic and ebulliometric techniques, to be between 5 and 20 molecules long.[7] A detailed IR study of imidazoles in dilute carbon tetrachloride solution indicates that

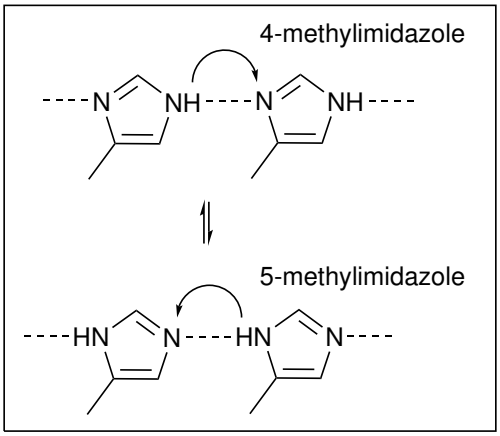

Figure 4.2: Prototropic tautomerism occurs by the intermolecular transfer of a proton along a hydrogen-bond with concomitant π-bond switching.[7]

all oligomers at least up to the dodecamer (12 carbons) are present in significant quantities in the saturated solution.[102] The aromaticity of the heterocycle coupled with this intermolecular association imbues imidazoles with another unusual property, prototropic tautomerism. In this type of tautomerism, the position of the acidic hydrogen, with respect to the nitrogens, is switchable. When a proton is transferred to the basic nitrogen and the acidic proton is transferred to the adjacent imidazole in a chain, the π-bonds within the heterocycle can be switched without reorientation of the molecule. The prototropic tautomerism of 4-methylimidazole, illustrated in Figure 4.2, leads to an equilibrium of 4- and 5-methylimidazole.[7] These tautomers can only be isolated by substituting on the acidic nitrogen, Figure 4.1(c), thus disrupting the intermolecular hydrogen-bonding.[7] Prototropic tautomerism and the closely related ability for imidazoles to rapidly shuttle protons along the hydrogen-bonded chains through fast intermolecular proton transfer have garnered them new attention for technological rather than biological applications.[67] The most significant of these applications include the now familiar field of proton exchange membrane fuel cells as well as the burgeoning field of supramolecular organic ferroelectrics.[65, 279, 280]

Prototropic tautomerism, combined with the formation of H-bonded chains, make crystalline imidazoles promising materials in the developing field of supramolecular ferroelectricity. The imidazole molecule has a large dipole moment, $\approx$ 3.67 - 3.8 D, oriented parallel to the intermolecular hydrogen bonds.[7, 281, 282] The hydrogen-bonds in a single chain are oriented in the same direction thus imparting a large supramolecular dipole moment to each chain. In an appropriate crystal, where the H-bonded chains are all oriented in the same direction, a

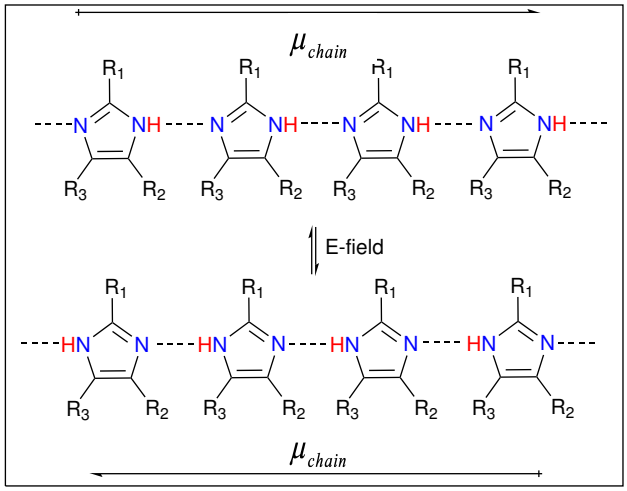

Figure 4.3: Ferroelectric switching of supramolecular dipoles by application of an external electric field. Ferroelectricity is possible due to the ability for imidazoles to transfer a proton along hydrogen bonds in a supramolecular chain with a concomitant switching of the π-bonds in each heterocycle.

permanent polarization may be induced by applying an external electric field of sufficient strength to "switch" all of the acidic protons, in all adjacent chains, to the same direction.[281] So far, such ferroelectricity has been reported in a class of substituted benzimidazoles as well as other appropriate molecular crystals, such as croconic acid.[283, 284, 285] The supramolecular organic ferroelectrics have promising applications in wearable electronics, memory storage, sensors, capacitors, and actuators.[33] A significant advantage of these prototropic tautomerism-based ferroelectrics over traditional inorganic as well as polymer-based, organic ferroelectrics is the low field strength at which their polarization is switched.[284, 286]

The potential for fast proton transfer along the hydrogen-bonded chains and their relatively high intrinsic proton conductivities, see Figure 4.4, has driven an increasing interest in imidazoles as components in proton exchange membrane (PEM) fuel cells. Current state-of-the-art PEM fuel cells are predominately based on sulfonated polymer membranes, e.g. Nafion.[287] These membranes deliver extremely high proton conductivities while restricting the flow of other species between the electrodes. The proton conduction originates from deprotonation of sulfonic acid side groups and proton diffusion in aqueous nanochannels.[287] The high proton conductivities required for efficient operation are only realized at very high hydration levels. The fuel cells must therefore be operated in a high humidity atmosphere which restricts the upper operating temperature to below the boiling point of water, 100 °C.[65] These rather low temperatures necessitate the use of expensive

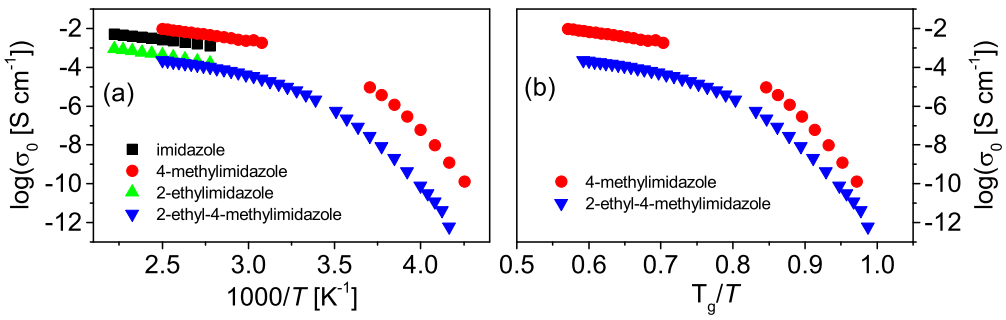

Figure 4.4: DC ionic conductivities, σ_0, of several imidazoles *versus* (a) inverse temperature and (b) temperature normalized by the calorimetric glass transition temperature, T_g.

platinum catalysts.[65] Replacing water with a higher boiling, yet still highly proton conducting material would be very advantageous. Imidazole is one of a number of alternatives which have been explored, including phosphoric acid, triazole, benzimidazole, and pyrazole.[288, 289] Each of these materials have the potential for fast proton transport via intermolecular proton transfer along a hydrogen-bond network such as the supramolecular chains of imidazole. Imidazoles have been incorporated into PEMs as side groups in polymeric backbones, dopants in a polymer membrane, and fillers in the mesoporous channels of metal organic frameworks.[274, 290, 291, 292, 293, 294, 295, 296, 297, 298, 299, 300, 301, 302, 65, 64, 303, 304, 305, 306, 287] Each of these approaches hopes to take advantage of the fast proton transport along supramolecular hydrogen-bonded chains. Therefore, a fundamental understanding of the dominant mechanisms of proton transport in each of these situations is crucial for the application of imidazoles in proton exchange membranes.

The intrinsic conductivity of imidazoles indicates a degree of self-dissociation resulting in protonated imidazolium cations and deprotonated anions. These ions can contribute to charge transport via either a vehicle diffusion or structure diffusion mechanism. In vehicle diffusion, charge transport is linked to the translational diffusion of the whole ionic molecule. This mechanism is analogous to the ion transport typical of the aprotic ionic liquids of the previous chapter where ion conduction is predominantly linked to the structural relaxation and viscosity. Structure diffusion, on the other hand, refers to the ability for certain materials to transfer protons more rapidly along intermolecular hydrogen-bonded networks. This type of proton transport mechanism was first proposed by Grotthuss and is often referred to as the Grotthuss mechanism.[307] It occurs in imidazole by the transference of a proton from one end of a supramolecular chain to the other by rapid shuttling of protons across the intermolecular hydrogen bonds, a picture very

similar to the ferroelectric switching. However, for proton transfer to actually contribute to a dc ionic conductivity, where protons are transported continuously from the cathode to the anode, an additional step is required in which all of the imidazoles in a supramolecular chain reorient so that another proton can be accepted at the same chain end and transferred in the same direction. It is generally accepted that reorientation follows each proton transfer event and is a local process rather than a simultaneous, global reorientation along the entire chain. This molecular view of the structure mechanism in imidazoles has been established by numerous quantum chemical and molecular dynamics simulations.[302, 308, 65, 309, 310, 292, 311, 300] The strongest experimental evidence of a significant contribution from structure diffusion in imidazoles is a Haven ratio less than one. The Haven ratio is defined as the ratio of molecular to ionic diffusivity, $H_R = D_{molecular}/D_\sigma$, where $D_{molecular}$ is the molecular diffusivity obtained by PFG-NMR and D_σ is the ion diffusivity estimated by the Nernst-Einstein equation using the measured conductivity. A Haven ratio less than one indicates a contribution from the ostensibly faster structure diffusion mechanism. In dilute mixtures of imidazole with either sulfanilic or bis(trifluoromethylsulfonyl)imide acid (80 - 100 mol% imidazole), Haven ratios of 0.3-0.7 have been reported, indicating a contribution via fast structure diffusion.[64, 303, 66] Doping imidazoles with small amounts of acid may enhance the contribution of structure diffusion by providing excess protons while reducing the solution viscosity.[302]

In addition to providing a structure diffusion mechanism, the supramolecular hydrogen-bonded chains also strongly influence the static dielectric permittivity (dielectric constant), ε_s. As discussed previously, the molecular dipole moments are aligned with one another in each hydrogen-bonded chain resulting in a supramolecular dipole. This parallel alignment of dipole moments leads to a positive departure from the Onsager relation and a Kirkwood-Fröhlich correlation coefficient greater than one.[282] The static permittivity is therefore expected to be enhanced by the existence of the hydrogen-bonded chains. A higher static permittivity is in turn expected to enhance proton conduction by stabilizing the protonated ions and thereby promoting self-dissociation.[312, 65, 313] However, concrete experimental evidence establishing the interplay between supramolecular hydrogen-bonded networks, static dielectric permittivity, and proton transport in these materials is still lacking.

To contribute to a better understanding of the influence of supramolecular hydrogen-bonded chains on proton transport in liquid imidazoles, we have investigated neat, substituted imidazoles and their mixtures with selected diluents over broad frequency and temperature ranges by broadband dielectric spectroscopy, dynamic mechanical spectroscopy, differential scanning calorimetry, and Fourier transform infrared spectroscopy. We utilize a newly discovered dynamic probe of the supramolecular chains, present as a slow, sub-α Debye-like relaxation in the dielectric spectra, to infer changes in the organization of the chains as a function of temperature, chemical structure, and concentration. The alteration in chain organization, as evidenced by shifts in the timescale and strength of the Debye-like relaxation, is then related to observed changes in the dc ionic conductivity to reveal an underlying influence of supramolecular chains on the proton conductivity. The slow, sub-α, Debye-like dielectric relaxation was previously attributed to the motion of extended supramolecular chains, in agreement with similar dynamics observed in monohydroxy alcohols.[68, 31] Chemical structure-modification, pressure-dependent, and dilution-effect studies on the Debye-like relaxation of monohydroxy alcohols have provided substantial insight into the organization of their hydrogen-bonded network. A brief overview of the monohydroxy alcohol studies is now warranted as our discussion of the imidazole results is strongly colored by these prior works.

Monohydroxy alcohols (MAs) have the ability to associate via intermolecular hydrogen-bonding to form supramolecular chains analogous to those of imidazole, as illustrated in Figure 4.5(a). The original evidence for this association is the departure of the measured static dielectric permittivies, ε_s, from the values expected on the basis of the Onsager relation given the molecular dipole moments and number densities.[23] A positive deviation, to values greater than the Onsager prediction, indicates a parallel orientation of neighboring dipoles while a negative devation indicates antiparallel orientation.[75] These deviations are quantified by modifying the Onsager relation with an additional parameter known as the Kirkwood-Fröhlich correlation factor, g_k. A $g_k > 1$ indicates a parallel orientation and $g_k < 1$ indicates a preference for antiparallel orientation.[75, 3] In the 1960s, detailed dielectric studies by Dannhauser and Johari on a series of isomeric octyl alcohols, with chemical structures depicted in Figure 4.5(b), revealed that the departure from the Onsager relation follows a systematic trend with respect to the chemical structures. Each label in Figure 4.5(b) corresponds to the chemical structure, i.e. 7;2 $\Rightarrow$ 7-methyl-2-heptanol. The

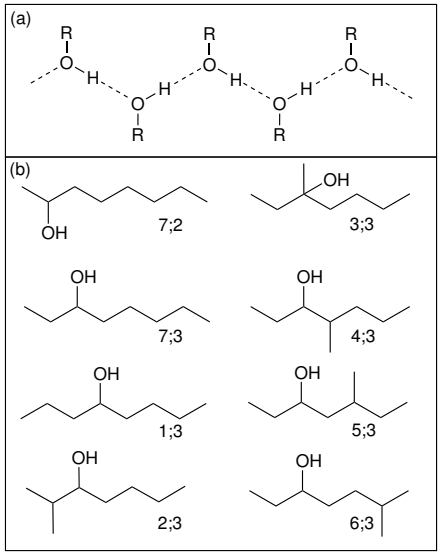

Figure 4.5: (a) Hydrogen-bonding chains of neighboring mono-alcohols as proposed by Oster and Kirkwood.[23] (b) Chemical structures for the series of isomeric octyl alcohols studied by Dannhauser and Johari in the 1960s.[24, 25] Labels correspond to the data in Figure 4.6 and Figure 4.7.

temperature-dependent static dielectric permittivities and g_k's for this series of MAs are given in Figure 4.6 and Figure 4.7, respectively.[24, 25] The monohydroxy alcohols with more terminally-located hydroxyl groups, labeled 7;2, 7;3, 1;3, and 6;3, have larger static dielectric permittivities which increase monotonically. The increase is accompanied by a corresponding increase in g_k to values greater than one as temperature is reduced. The more centrally located and sterically hindered hydroxyl positions, labeled 3;3, 2;3, 4;3, and 5;3, have a non-monotonic temperature dependence in ε_s and their g_k's decrease from one as the temperature is reduced. A qualitative picture of supramolecular organization was introduced to explain these results. The parallel orientation corresponds to the formation of predominantly linear chains. Antiparallel orientation indicates the formation of ring-type structures in which dipoles on opposite sides are oriented in opposite directions. This interpretation is now widely accepted.[31]

In addition to its dielectric strength, the timescale of the Debye-like relaxation also supports its assignment to the relaxation of supramolecular hydrogen-bonded chains. In almost all types of dipolar liquids, the primary, α-dielectric relaxation corresponds rather closely to the structural relaxation of the liquid. The structural relaxation is directly linked to the local molecular motions which determine a liquid's viscosity and dynamic glass transition. Therefore, the structural

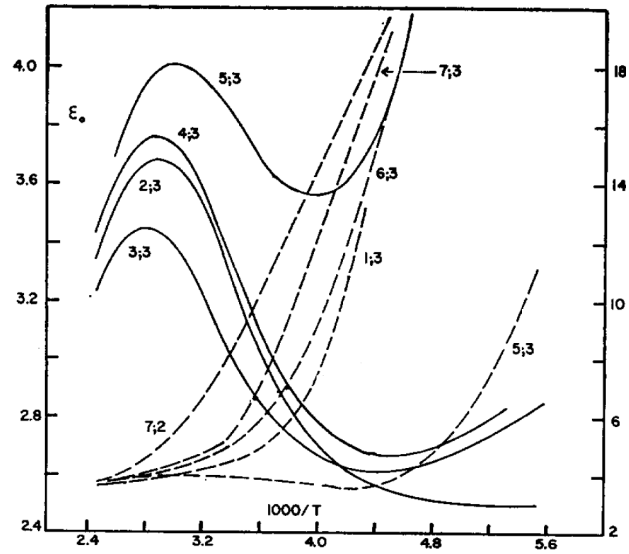

Figure 4.6: Static dielectric permittivities of the series of isomeric octyl alcohols of Figure 4.5 *versus* inverse temperature. Solid and dashed lines correspond to the left and right ordinates, respectively. The permittivities and their temperature dependence vary widely as a function of the chemical structure. This figure is reproduced from [24].

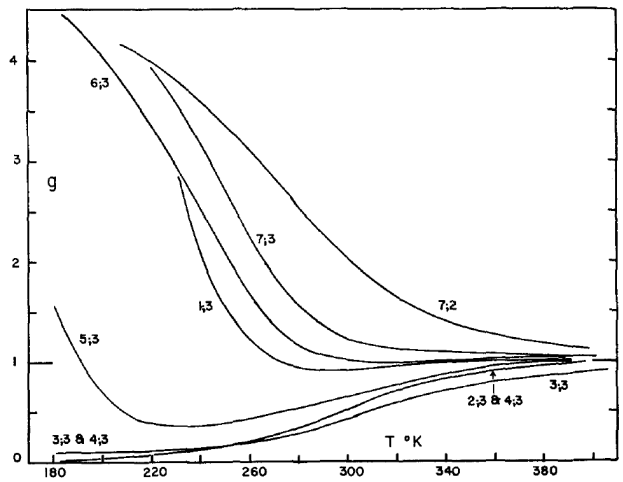

Figure 4.7: Temperature dependence of the Kirkwood-Fröhlich correlation factors of the isomeric octyl alcohols in Figure 4.5. The g_k's approach one at high temperatures. As the temperature is reduced, some of the g_k's increase, others decrease, and in the case of 5-methyl-3-heptanol, both trends are observed. This figure is reproduced from [24].

relaxation is also accessed experimentally in other techniques such as dynamic mechanical spectroscopy(DMS) and differential scanning calorimetry(DSC). The timescales obtained by each of these three techniques for the structural relaxation are roughly comparable. The Debye-like dielectric relaxation of MAs, on the other hand, is considerably slower than their structural relaxation probed by DMS and DSC. The structural relaxation is however still present in their dielectric spectra. The real and imaginary parts of complex dielectric permittivity of 4-methyl-3-heptanol is shown in Figure 4.8. This MA falls in the antiparallel orientation group and therefore has a weak Debye-like relaxation. There are very clearly two relaxation processes at 198 K and below. The slower process, which appears as a low-frequency shoulder, is the Debye-like relaxation while the faster is the α-relaxation with timescales comparable to the structural relaxation probed by DMS and DSC. It is therefore generally referred to as the structural, α-relaxation. The slowness of the Debye-like relaxation relative to the structural suggests the relaxing group is quite large. Estimates of the hydrodynamic radii by the Stokes-Einstein equation yield values much larger than the molecular dimensions, supporting the interpretation that the motion of supramolecular hydrogen-bonded chains are responsible for this relaxation.[31, 314, 315, 77] The Debye-like shape of the relaxation originates in the fast addition and removal of molecules at the chain ends which is responsible for the reorientational motion. In living supramolecular polymers, when chain breaking rates are faster than the chain relaxation rate a narrowing of the relaxation time distribution occurs while the average chain relaxation rate represents an average of the molecular weight distribution.[316, 317] In the case of monohydroxy alcohols, the slow, Debye-like relaxation is the analog of the polymeric chain relaxations. This mechanistic view of the Debye-like relaxation, originated by Gainaru, is known as the transient chain model.[318]

The sensitivity of the strength and timescale of the Debye-like relaxation to the supramolecular structure is made especially clear by considering the temperature-dependence of these parameters. The non-covalent H-bonds between alcohols are relatively weak. As the temperature increases, we expect that at some critical temperature, below the boiling point, the thermal energy will be significantly greater than the H-bond interaction energies and the supramolecular H-bonded chains will be disrupted. In all cases, at elevated temperatures the static dielectric permittivities of MAs approach the value given by the Onsager relation. That is g_k approaches 1 at high temperatures indicating a loss of the supramolecular orientation, see Figure 4.7. Over the same temperature

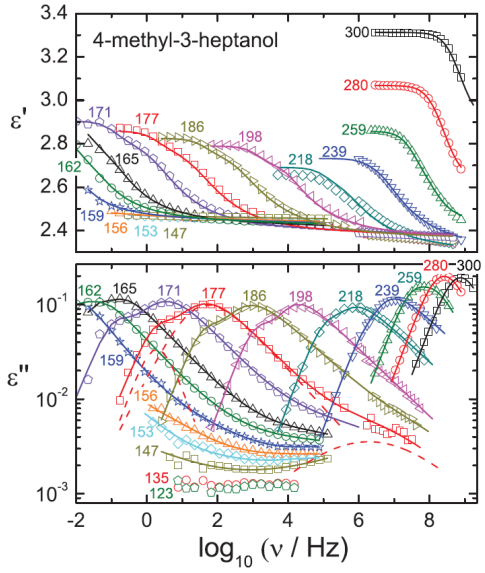

Figure 4.8: Real and imaginary parts of the complex dielectric permittivity, $\varepsilon^* = \varepsilon' - i\varepsilon''$, of 4-methyl-3-heptanol at the indicated temperatures. The slower Debye-like relaxation merges into the structural, α -relaxation at higher temperatures, 239-300 K. Relaxation times are given in Figure 4.7. This figure is reproduced from [26].

range, there is a concomitant increase in the rate of the Debye-like relaxation.[31, 27, 26, 319, 197, 223] When $g_k = 1$ the Debye-like relaxation merges into the structural, α-relaxation and is no longer observable as a distinct relaxation. This is evident in the dielectric spectra of 4-methyl-3-heptanol in Figure 4.8. At temperatures at and above 218 K, the slow, Debye-like relaxation merges into the α. This is also evident in the merging of their timescales as room temperature is approached in Figure 4.9. The observed temperature dependence of g_k and Debye-like relaxation timescales are therefore in agreement with a relaxation mechanism originating in the formation and motion of extended supramolecular hydrogen-bonded chains which can be disrupted at elevated temperatures.

Recently, a slow, sub-α Debye-like relaxation was also found in the dielectric spectra of the glass-forming liquid 2-ethyl-4-methylimidazole (2E4MIm).[68] The similarity in shape and relaxation time, relative to the structural relaxation, indicate that this Debye-like relaxation also reflects the motion of the supramolecular H-bonded chains of imidazole molecules. Therefore, the Debye-like relaxation of 2E4MIm can also be used, in a manner analogous to the MAs, as a sensitive reporter of temperature, chemical structure, and composition dependent changes to the H-bonded chains. 2E4MIm has one exceptional difference, it is capable of self-dissociation and

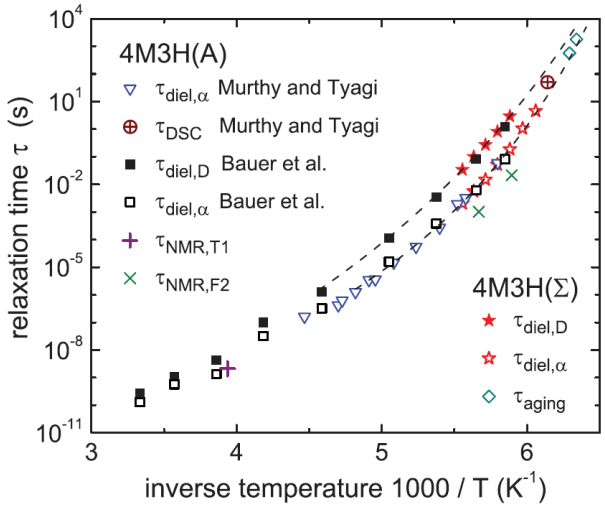

Figure 4.9: Relaxation times of the Debye-like (D) and structural, α-relaxations (α) of 4-methyl-3-hexanol (4M3H) as probed by dielectric spectroscopy (diel), differential scanning calorimetry (DSC). At high temperatures the timescale of the Debye-like relaxation (closed squares) merges into the structural, α-relaxation (open squares). The 4M3H labels, (A) and (Σ), refer to the chemical suppliers Alpha-Aesar and Sigma-Aldrich, respectively. This figure is reproduced from [27].

is therefore an intrinsic proton conductor. This combination of Debye-like relaxation and proton conduction provides a unique opportunity to probe the influence of hydrogen-bond networks on proton conduction in liquids.

4.2 Proton Transport in Imidazoles: Unraveling the Role of Supramolecular Structure

In this section, we investigate the influence of acid-doping on the dynamics, ionic conductivity, and supramolecular H-bonded chains of 2-ethyl-4-methylimidazole. 2E4MIm and mixtures with levulinic acid are investigated by broadband dielectric spectroscopy, dynamic light scattering, differential scanning calorimetry. The results indicate a significant disruption of the H-bonded chains at very low levulinic acid concentrations. This disruption is expected to strongly reduce any contribution of the structure diffusion mechanism to proton conduction. Our findings are at odds with literature results which suggest a contribution from structure diffusion persists at significantly higher concentrations of sulfanilic and bis(trifluoromethylsulfonyl)imide acid than the 2.5mol% of our levulinic acid which is required for a disruption of the H-bonded chains.[64, 303, 66]

This section is a reprinting of a previously published article and its supporting material. My primary contributions to this article include: (i) design of experiments, (ii) data collection and analysis, (iii) interpretation of results, and (iv) writing. Changes from the published version consist of the incorporation of supporting information within the main text.

Abstract

The impact of supramolecular hydrogen bonded networks on dynamics and charge transport in 2-ethyl-4-methylimidazole (2E4MIm), a model proton conducting system, is investigated by broadband dielectric spectroscopy, depolarized dynamic light scattering, viscometry, and calorimetry. It is observed that the slow, Debye-like relaxation reflecting the supramolecular structure in neat 2E4MIm is eliminated upon the addition of minute amounts of levulinic acid. This is attributed to the dissociation of imidazole molecules and the breaking down of hydrogen-bonded chains, which leads to a 10-fold enhancement of ionic conductivity.

Introduction

Hydrogen bonds play prominent roles in numerous physicochemical as well as biological processes. Evidence of hydrogen-bonded networks has been observed in important materials such as water, monohydroxy alcohols, proteins, and nucleic acids, among many others.[31, 320, 321] Due to their technological and fundamental importance, a concerted scientific effort has been directed at understanding the interplay between molecular structure, hydrogen bonding, and dynamics as well as charge transport in these materials. One specific area of fundamental interest has been the origin of the slow, Debye-like processes in monohydroxy alcohols. Using a variety of experimental techniques, several groups have concluded that the Debye-like relaxations in monohydroxy alcohols are due to the dynamics of the supramolecular hydrogen bonded chains inherent in these materials.[31, 196, 322, 319, 318] Recently, it became evident that slow Debye-like relaxations characterize dynamics of hydrogen-bonded networks in supramolecular polymers as well as low molecular weight hydrogen-bonded imidazoles.[68, 323] This expanded class

of materials, especially the imidazoles, provides model systems to investigate the impact of supramolecular hydrogen-bonded networks on the resultant structural dynamics and transport properties. The imidazole ring is an important building block in diverse systems ranging from proton conducting non-aqueous electrolytes to biological systems including histamine, histidine, and vitamin B12.[275, 271, 65, 305, 324, 33, 285, 325, 304] One application for which imidazole has received considerable attention is as a new electrolyte in proton exchange membrane fuel cells.[65, 66, 303] However, detailed understanding of the interplay between the supramolecular structure and dynamics as well as proton transport in these systems remains limited. Proton transport in liquid imidazole has been proposed to occur in one or a combination of two ways: (i) a vehicle mechanism in which the protonated imidazole molecule undergoes long-range diffusion, and, (ii) a Grotthuss mechanism in which a proton is transferred between nitrogen atoms of two neighboring imidazole molecules across a hydrogen-bond, followed by a rate-limiting reorientation step, the time scale of which is presumably controlled by the dynamic glass transition.[321, 65, 302, 292, 326, 309, 327, 328, 308] The amphoteric nature of imidazole allows the molecules to form intermolecular hydrogen bonds, which result in extended, almost linear chains of molecules.[68] The role of the supramolecular structures in proton transport remains unclear, although the high intrinsic conductivity of imidazole, as well as imidazole-rich acid mixtures, has been attributed to fast proton transport by a Grotthuss mechanism.[66, 303] Experimentally, the main signature of these extended supramolecular systems is the slow, Debye-like relaxation process, a feature that was recently revealed by both broadband dielectric spectroscopy and dynamic light scattering techniques.

In this Letter, broadband dielectric spectroscopy, viscometry, calorimetry, and depolarized dynamic light scattering techniques are employed to investigate the impact of the supramolecular hydrogen bond networks on charge transport and the structural dynamics in glass-forming systems of neat 2-ethyl-4-methylimidazole (2E4MIm) and mixtures of 2E4MIm with minute amounts of levulinic acid (LA). It is observed that the slow, Debye-like relaxation characterizing the dynamics of supramolecular structures in the neat 2E4MIm disappears upon the addition of small amounts of LA. A detailed analysis demonstrates that the enhanced ionic conductivities of the mixtures at the low acid concentrations are not due to fast proton motion but are rather due to an increase in the

number density of free charge carriers arising from dissociation of the imidazole and leading to a breaking down of the extended hydrogen bonded chains in the 2E4MIm/LA mixtures.

Experimental Methods

The 2-ethyl-4-methylimidazole (2E4MIm, 99% purity, Acros Organics) and levulinic acid (LA, 98% purity, Sigma-Aldrich) were purchased and used as received. Mixtures were prepared by mixing 2E4MIm and LA at 60 °C in a high purity nitrogen atmosphere. Broadband dielectric spectroscopy measurements were made in the frequency range of $10^{-1} - 2 \times 10^{7}$ Hz and temperature range of 180 - 400 K using a Novocontrol Alpha Analyzer with a QUATRO liquid nitrogen temperature control system with temperature stability ±0.1 K. Stainless steel parallel plate electrodes with a diameter of 20 mm were utilized. Teflon spacers were used to provide a gap of 1 mm between the electrodes. Depolarized dynamic light scattering measurements were performed in 90 degree geometry in an Oxford Optistat cryostat with temperature stability ±0.1 K. The laser wavelength was 647 nm and the power was 15 mW. Differential scanning calorimetry measurements were performed on a TA Instruments Q2000 calorimeter at a cooling rate of 2 K/ min. The calorimetric glass transition temperature, T_g, was determined at the midpoint of the step in heat flow corresponding to the maximum in the temperature derivative of the heat flow. Creep measurements were performed on a Hybrid Rheometer 2 (TA Instruments) with 3 mm and 25 mm parallel plates. In each experiment, a constant small stress was applied to the sample to evaluate its zero-shear viscosity. The temperature was controlled by an Environmental Test Chamber with nitrogen as the gas source.

Results and Discussion

Depolarized dynamic light scattering (DDLS) yields the normalized intensity correlation function (ICF), which provides information regarding the characteristic time scales of reorientational molecular motion. The ICF is well described by a superposition of Kolhrausch-William-Watts (KWW) stretched exponential functions for the normalized electric field correlation function (g_1):

$$g_2(t) - 1 = \gamma \left[g_1(t)^2\right] = \gamma \sum_j \left[a_j \exp\left[\frac{t}{\tau_j}\right]^{\beta_{KWW,j}}\right]^2 \tag{4.1}$$

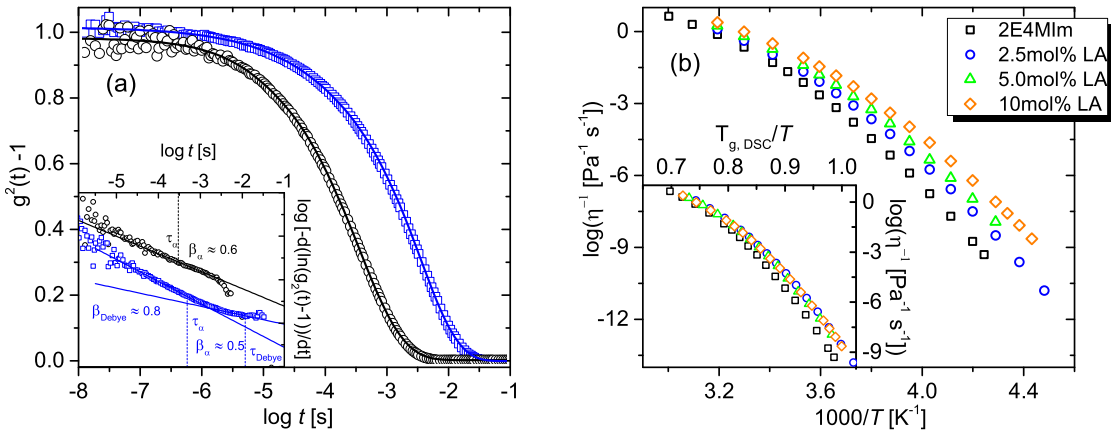

Figure 4.10: (a) Normalized intensity correlation function versus time for neat 2E4MIm and the 2.5 mol % LA mixture at 255 K. Solid lines correspond to fits obtained from superposition of two KWW functions for 2E4MIm, but only one KWW function for the 2.5 mol % mixture. Inset: Double logarithmic plots of the time derivative of the normalized correlation function plotted versus time. The 2.5 mol % LA data exhibits one slope; indicating that there is no detectable slow Debye-like relaxation in this mixture. The R^2 values for the alpha process of 2.5 mol % LA and pure 2E4MIm are both 0.99. The R^2 value for the Debye relaxation of 2E4MIm is 0.98. (b) Fluidities of 2E4MIm and 2.5, 5.0, and 10 mol % LA mixtures obtained by creep measurements versus $1000/T$. Inset: Fluidities of 2E4MIm and 2.5, 5.0, and 10 mol % LA mixtures versus T_g/T. The increase in fluidity at low temperatures when scaled by T_g indicates a weakening of the intermolecular hydrogen-bonding interactions.

where $g_1(t)$ and $g_2(t)$ are the normalized electric field correlation function and ICF, respectively, γ is the spatial coherence factor, a_j ($j = 1, 2$, denoting the number of relaxation processes) is the relative relaxation strength, τ_j is the relaxation time, and $\beta_{KWW,j}$ is the stretching parameter. Figure 4.10(a) presents the ICF of 2.5 mol % LA/2E4MIm mixture alongside that of neat 2E4MIm measured by Wang et al. at a selected temperature.[68] The neat 2E4MIm spectra show two relaxation processes, which correspond to the structural α-relaxation (fast process) and rotational diffusion of supramolecular hydrogen bonded chains of 2E4MIm molecules (slow process). However, upon addition of the 2.5 mol % LA, the mixture exhibits only one process corresponding to structural α relaxation, which is completely described by one KWW function (i.e., $j = 1$ in Equation 4.1) for the experimentally accessible time range. According to the derivative analysis proposed by Wang et al., a relaxation process in DDLS spectra exhibits a single slope in the double logarithmic representation of $-d\ \ln(\mathrm{ICF})/dt$ versus time. Using this derivative analysis, we have verified that

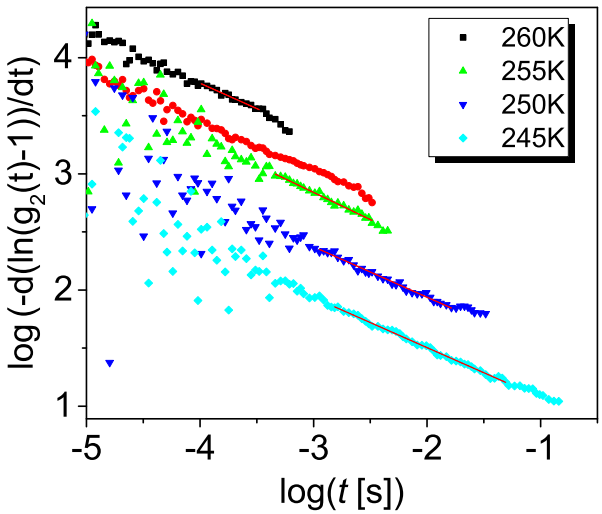

Figure 4.11: Double logarithmic plots of the time derivative of the normalized correlation function plotted versus time for 2.5mol% LA/2E4MIm mixture. The mixture shows only one slope corresponding to the alpha-relaxation. No slow, Debye-like process was found in the DLS spectra of the mixture.

only one relaxation process is present in the DDLS spectra upon addition of 2.5 mol % of LA (Figure 4.10(a) inset). A single relaxation process is observed at all measured temperatures, Figure 4.11.

The disappearance of the slow, Debye-like relaxation dynamics of 2E4MIm upon addition of LA implies a disruption of the hydrogen-bonded 2E4MIm chains. This interpretation is strengthened when considering viscosity data obtained by creep measurements of 2E4MIm and the LA-2E4MIm mixtures. The weakening of the hydrogen bond interactions between imidazole molecules should lead to a decrease in the viscosity.[329, 330, 331] This effect is less significant at high temperatures due to diminishing contributions of hydrogen bonding compared to thermal fluctuations. Figure 4.10(b) presents the fluidities (inverse viscosity) of 2E4MIm and 2.5, 5.0, and 10 mol % 2E4MIm-LA mixtures versus $1000/T$. The increasing fluidity with acid additions is due to the lower calorimetric glass transition temperature (T_g) of the LA and changes in the molecular environment due to breakdown of the hydrogen-bonded networks in the mixtures. The inset of Figure 4.10(b) reveals that the fluidity of the mixtures is higher than the 2E4MIm at low temperatures when scaled by T_g. We attribute this difference to a change in the hydrogen-bonding environment upon the initial addition of LA. For low molecular weight non-hydrogen-bonded glass-forming systems, the zero-shear viscosity η and the structural relaxation time τ_α are interrelated through the Maxwell's relation

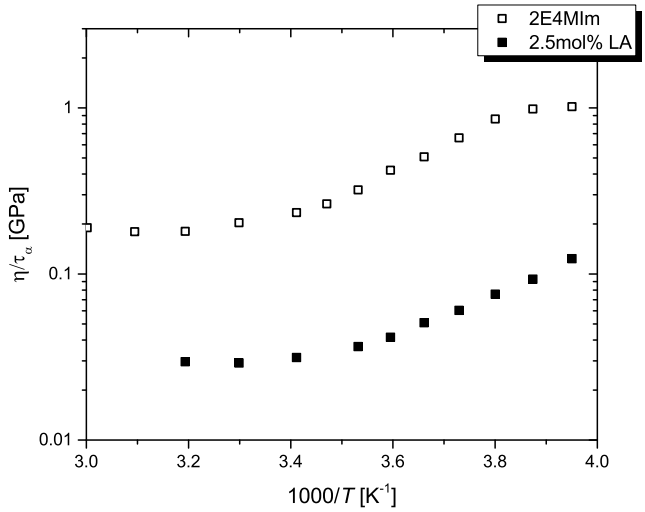

Figure 4.12: Estimates of the high frequency shear modulus obtained by applying the Maxwell's relation to the viscosity and structural α-relaxation times (from DDLS) plotted versus inverse temperature. The shear modulus of the 2.5mol% LA mixture is 8 times lower than that of neat 2E4MIm. This is due to the stronger intermolecular interactions and the existence of the long-lived (compared to timescales of structural relaxation) supramolecular hydrogen-bonded chains.

($\eta = G_\infty \tau_\alpha$, where G_∞ denotes the high frequency shear modulus). However, the supramolecular relaxation mode should make additional contribution to the zero-shear viscosity for hydrogen-bonded systems. In this case, the viscosity can be expressed as $\eta = \tau_\alpha G_\alpha + G_{chain}\tau_{chain}$, where the additional terms correspond to contributions arising from the chains. Utilizing the structural relaxation rates obtained by DDLS, we calculate η/τ_α at 253 K and obtain 1.02 and 0.12 GPa for 2E4MIm and the 2.5 mol % 2E4MIm- LA mixture, respectively see Figure 4.12. The apparent reduction in high frequency shear modulus upon acid addition is attributed to the elimination of the contribution from 2E4MIm chains. The dielectric spectra of many ion-conducting systems are reasonably well described by the Random Barrier Model (RBM) proposed by Dyre.[3, 4, 265] Within the framework of this model, the charge carriers hop in a random spatially varying energy landscape. The mean hopping rate, denoted by the time τ_e, associated with the highest barrier determines the dc conductivity, σ_0, and is one of the characteristic parameters of the model. Solved within the context of continuous-time random walk, an analytical approximation for the complex dielectric function is given by $\varepsilon^*(\omega) = \sigma_0\tau_e/\varepsilon_0[\ln(1 + i\omega\tau_e)$, where ε_0 denotes the permittivity of

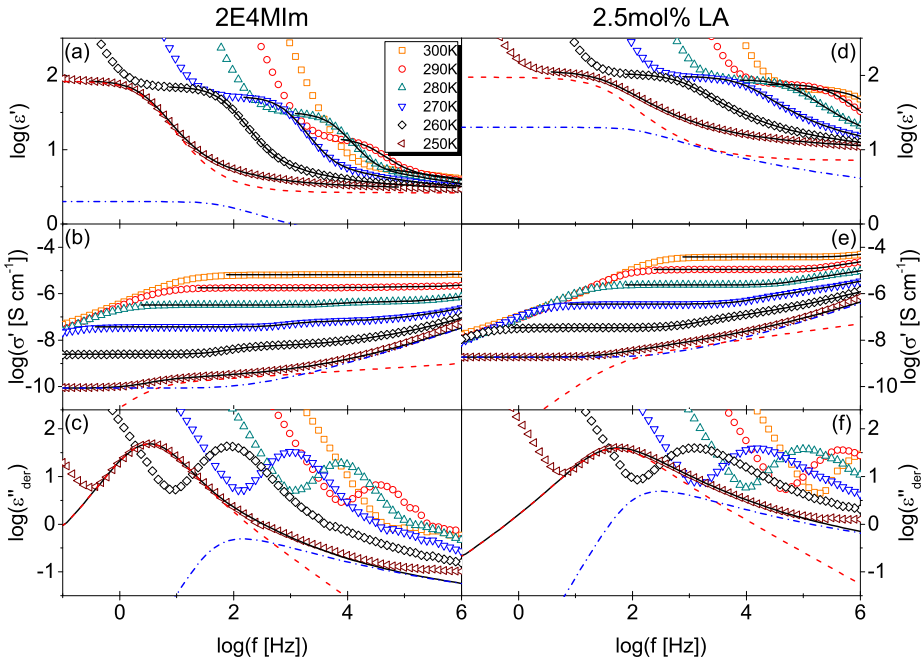

Figure 4.13: Real part of complex dielectric function, $\varepsilon'(f)$, the real part of the complex conductivity, $\sigma'(f)$, and the derivative of $\varepsilon'(f) = \varepsilon''_{der} = (-(\pi/2))\partial\varepsilon'/\partial\ln(f)$, versus frequency for 2E4MIm(a-c) and the 2.5 mol % LA mixture (d-f). Solid lines correspond to fits obtained using Equation 4.2. Dashed and dotted-dashed lines show the individual contributions of the Havriliak-Negami and random barrier models, respectively. The rates of charge transport, ω_e, and dipolar relaxation, ω_{max}, occur at approximately the same frequency in the mixture, whereas in neat 2E4MIm they are separated by at least 1 order of magnitude.

free space. Therefore, the dc conductivity and the characteristic times are sufficient to characterize the dielectric spectra due to charge transport within the framework of the RBM model.

The complex dielectric spectra of the 2E4MIm are dominated by contributions from electrode polarization, charge transport, as well as dipolar relaxations (Figure 4.13(a-c)). To analyze dipolar relaxations, the empirical Havriliak-Negami (HN) equation is employed. In addition, the RBM is used to quantify the contribution of charge transport to the spectra. The resultant linear combination of equations for describing the two contributions is given as

$$\varepsilon^*(\omega) = \left[\varepsilon_\infty + \frac{\Delta\varepsilon}{(1+(i\omega\tau_{HN})^\alpha)^\gamma}\right] + \frac{\sigma_0}{i\omega\varepsilon_0}\left[\frac{i\omega\tau_e}{\ln(1+i\omega\tau_e)}\right] \tag{4.2}$$

where $\Delta\varepsilon$ is the dielectric relaxation strength, ε_∞ denotes the high frequency value of the real part of the dielectric function, τ_{HN} refers to the Havriliak-Negami relaxation time, and α and γ are

shape parameters indicating the symmetric and asymmetric broadening of the complex dielectric function, respectively.[150, 332] The molecular relaxation rates are related to the characteristic time obtained from Equation 4.2 by $\omega_{max} = (1/\tau_{HN})[\sin(\alpha\pi/(2+2\gamma))]^{1/\alpha}[\sin(\alpha\gamma\pi/(2+2\gamma))]^{-1/\alpha}$.[3]

The dielectric spectra of neat 2E4MIm and the 2.5 mol % mixture as described by Equation 4.2 are shown as solid black lines in Figure 4.13. This equation describes the spectra well other than a slight divergence at very high frequencies and low temperatures. This divergence is due to the influence of secondary relaxation processes occurring outside the observable frequency window. The low frequency region described by Equation 4.2 for 2E4MIm is dominated by a slow, Debye-like relaxation attributed to the motion of supramolecular H-bonded chains of imidazole molecules.[68] This process is observed as a peak in the derivative of the imaginary part of the dielectric function.[85] The second contribution to the spectra, attributed to charge transport, is observed as a high-frequency tail of the peak in $\varepsilon''_{der} = (-(\pi/2))\partial\varepsilon'/\partial\ln(f)$. The individual contributions of the HN and RBM to the spectrum at 250 K are given in Figure 4.13 as a red dashed line and a blue dotted-dashed line, respectively.

The dielectric spectra of the 2.5 mol % LA mixture (Figure 4.13(d-f)) display significant differences from that of 2E4MIm. The main relaxation peak in ε''_{der}, now occurs at approximately 1 order of magnitude higher frequencies and the time scale of charge transport and the dipolar relaxations are now practically the same, as shown by the contributions of HN and RBM in Figure 4.13f. Additionally, the dc conductivity, σ_0, corresponding to the frequency-independent region of the real part of the complex conductivity is increased by about 1 order of magnitude in the entire temperature range probed in these experiments. It is also worth noting that the value of the real part of the dielectric function at high frequencies is significantly higher than that of the 2E4MIm.

The characteristic rates of dipolar relaxation, ω_{max}, and charge transport, $\omega_e = 1/\tau_e$, in 2E4MIm as well as the 2.5 mol% mixture are given in Figure 4.14, alongside the rates determined by DDLS, ω_{DLS}. In neat 2E4MIm, there is an order of magnitude difference between the slow, Debye-like relaxation and that of structural α-relaxation (from DDLS) as well as charge transport (from BDS). However, in the 2.5 mol % mixture, the rates of charge transport, dipolar relaxation, and structural relaxation are practically equal. The slow process is no longer detectable at 2.5 mol % acid concentration, while no change in the time scale of the faster dielectric process is observed.

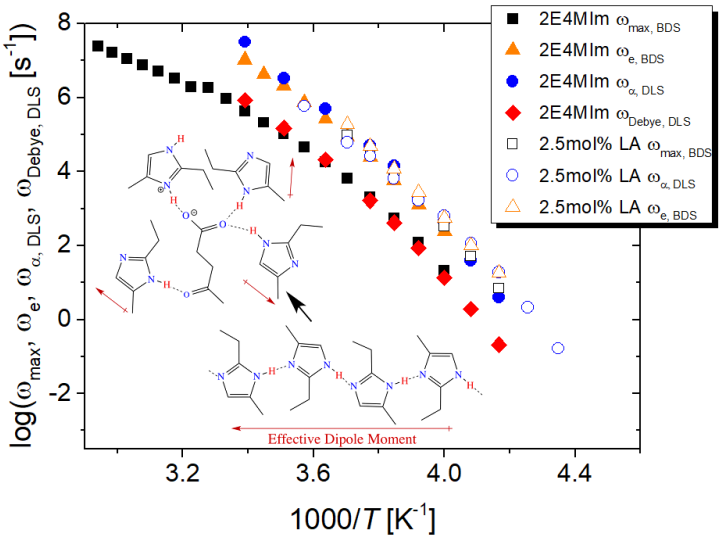

Figure 4.14: Characteristic rates of charge transport and dynamics obtained from the dielectric and depolarized dynamic light scattering spectra of neat 2E4MIm (closed symbols) and the 2.5 mol % LA mixture (open symbols) versus $1000/T$. The neat 2E4MIm has two distinct relaxation rates, one corresponding to the structural relaxation and the slower related to the motion of supramolecular chains of imidazole molecules. The 2.5 mol % LA mixture has only one apparent relaxation rate corresponding to the structural relaxation. Inset: Proposed scheme illustrating the breakdown of the hydrogen-bonded chains of 2E4MIm upon introduction of LA molecules.

This implies no change in the dynamic glass transition, in agreement with the fact that the measured calorimetric T_g of 228 K for the 2.5 mol % mixture and neat 2E4MIm coincide, see Figure 4.15.

The dramatic increase in the ionic conductivity upon addition of LA is now considered with the main objective of understanding the role of supramolecular hydrogen-bonded networks in determining ionic conduction in this class of materials. The dc conductivity, σ_0, can be described by the equation, $\sigma_0 = \sum_i n_i q_i \mu_i$, where n is the effective number density of the free charge carriers, q is the charge, μ is the charge mobility, and i denotes the type of charge carrier. As observed in Figure 4.14, the characteristic charge transport rate obtained by fitting the RBM model to the dielectric spectra coincides with the structural α-relaxation rate obtained by DDLS for both the neat 2E4MIm and the 2.5 mol % mixture. This result is important because it indicates that the rate-limiting process for charge (mainly protons) transport is structural α-relaxation, in agreement with the current understanding of proton conduction, which requires molecular reorientation for successful proton hopping.[65, 308] Therefore, the representation of dc conductivity versus T_g/T can be used to distinguish the dependence of conductivity on variation in charge carrier mobility

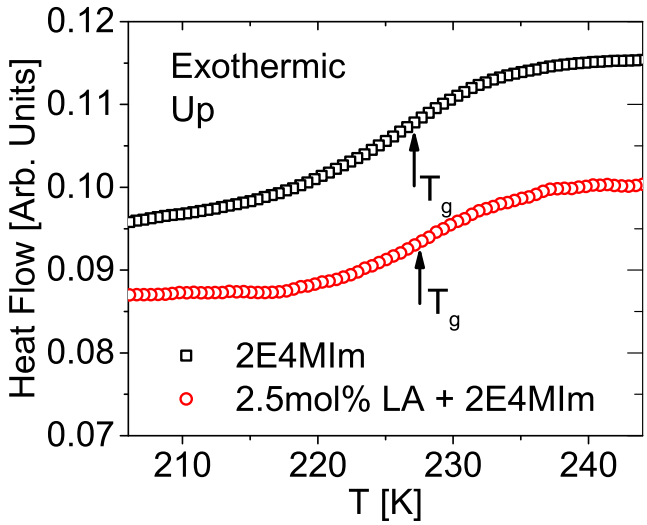

Figure 4.15: Heat flow versus temperature for 2E4MIm and the 2.5mol% LA/2E4MIm mixture. The calorimetric glass transition temperature is unchanged by the addition of a very small amount of levulinic acid.

(Figure 4.16). The increase in ionic conductivity of the 2.5 mol % mixture over the neat 2E4MIm, even when scaled by T_g, indicates an increase in the number density of charge carriers. The scaling of conductivity by T_g at 2.5, 5.0, and 10 mol % LA demonstrates that the increase in effective number density of charge carriers does not continue beyond the initial increase at the 2.5 mol % LA concentration. This trend implies that the increase does not originate strictly from deprotonation of the LA, but rather from an increase in the ionicity of the 2E4MIm molecules themselves.

A quantitative estimate of the number density of charge carriers may be obtained by utilizing a combination of the Einstein and Einstein-Smoluchowski relations expressed as, $n_{H^+} = \sigma_0 k_b T / q^2 \lambda^2 \omega_e$, where λ is the mean ion jump length in the time scale of ω_e. Supposing that the dominant charge carrier is the proton of the charged imidazolium molecules and assuming a mean hopping length $\lambda = 1.0 \pm 0.3$ Å, based on the average bond length in a $N^+{-}H\cdots N$ hydrogen bond, it becomes possible to determine the effective number density of charge carriers as presented in the inset of Figure 4.16.[333] The mean jump length is a rough estimate based on the hydrogen bond length of strong hydrogen bonds such as found in neat 2E4MIm. It should be noted that the mean jump lengths may slightly change upon addition of the acid and this value is only an approximation. The validity of this approach to approximate λ from structural considerations was previously corroborated by detailed infrared studies of a similar proton conducting mixture.[332]

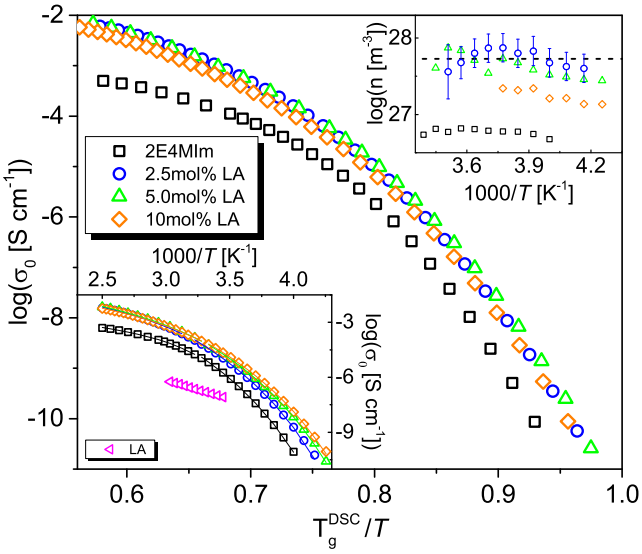

Figure 4.16: DC conductivity, σ_0, of neat 2E4MIm, 2.5, 5.0, and 10 mol % LA mixtures versus T_g/T. The increase in σ_0 when scaled by T_g indicates an increase in the effective number density of charge carriers upon addition of LA. Inset bottom: DC conductivity, σ_0, versus $1000/T$ for 2E4MIm, 2.5, 5.0, 10.0 mol % LA mixture, and LA. Inset top: Estimate of the effective number density of charge carriers versus 1000/T for neat 2E4MIm, 2.5, 5.0, and 10 mol % LA mixtures. The dashed line is the total number density of molecules in 2E4MIm.

A comparison of the number density of free charge carriers in 2E4MIm and the 2.5 mol % LA mixture indicates that the addition of a 2.5 mol % of LA leads to 10-fold increase in the free ion concentration in the mixture compared to the neat 2E4MIm. Further addition of acid molecules leads to a decrease in the number density of charge carriers. This may be due to the formation of ionic aggregates of imidazolium and carboxylate ions leading to a reduction in the number of free ions contributing to charge transport.

Based on the results from the complementary techniques reported in the current article, we propose the scheme in the inset of Figure 4.14 to represent the interaction between LA molecules and the supramolecular chains in 2E4MIm. We conjecture that the introduction of a LA molecule leads to breaking down of a hydrogen-bonded chain, and the resulting molecular moieties contribute to further disruption of the neighboring chains, thereby eliminating the slow, Debye-like dynamics in 2-ethyl-4-methylimidazole and giving rise to higher ionic conductivity as discussed in the current article.

In summary, broadband dielectric spectroscopy, depolarized dynamic light scattering, viscometry, and calorimetry are employed to investigate the impact of hydrogen bond networks on charge

transport and structural dynamics in 2E4MIm and mixtures of 2E4MIm with minute amounts of LA over a broad temperature and frequency range. The addition of LA is found to cause the disappearance of the slow, Debye-like relaxation, which was dominant in neat 2E4MIm, alongside a remarkable 10-fold increase in the ionic conductivity. A detailed analysis demonstrates that the high ionic conductivities are not due to fast proton motion, but are rather due to the change in the number density of free charge carriers arising from dissociation of the 2E4MIm, which leads to the breakdown of the extended hydrogen bonded chains in the 2E4MIm/LA mixtures.

4.3 Associating Imidazoles: Elucidating the Correlation between the Static Dielectric Permittivity and Proton Conductivity

In this section, 2-ethyl-4-methylimidazole and 4-methylimidazole as well as mixtures of 2E4MIm with levulinic acid and butyramide are investigated by broadband dielectric spectroscopy, Fourier transform infrared spectroscopy, and differential scanning calorimetry. An examination of the Debye-like relaxation, both its strength and timescale, of the neat imidazoles reveals the existence of an antiparallel alignment of dipoles not readily explained by the ring-type structures of monohydroxy alcohols. The results are tentatively attributed to an antiparallel alignment of neighboring supramolecular H-bonded chains, whose formation is possibly aided by the π-interactions of imidazole. The investigation of levulinic acid mixtures over broader concentration ranges show the concentration dependent disruption of the supramolecular chains in more detail, a conclusion further strengthened by the FTIR studies. The disruption is shown to depend on the proton-donating ability of the diluent as butyramide has no apparent effect on the size of the H-bonded chains.

This section is a reprinting of a previously published article and its supporting material. My primary contributions to this article include: (i) design of experiments, (ii) data collection and analysis, (iii) interpretation of results, and (iv) writing. Changes from the published version consist of the incorporation of supporting information within the main text.

Abstract

Broadband dielectric spectroscopy is employed to investigate the impact of supramolecular structure on charge transport and dynamics in hydrogen-bonded 2-ethyl-4-methylimidazole and 4-methylimidazole. Detailed analyses reveal (i) an inverse relationship between the average supramolecular chain length and proton conductivity and (ii) no direct correlation between the static dielectric permittivity and proton conductivity in imidazoles. These findings raise fundamental questions regarding the widespread notion that extended supramolecular hydrogen-bonded networks facilitate proton conduction in hydrogen bonding materials.

Introduction

Fundamental understanding of the dominant mechanisms of proton transport in amorphous hydrogen bonded materials is crucial for numerous applications ranging from proton exchange membranes to biological processes.[65, 321] Proton conductivity in these systems is usually attributed either to vehicle and/or structure diffusion mechanisms. Structure diffusion is thought to involve fast proton transfer along supramolecular hydrogen-bonded networks via the Grotthuss mechanism, while vehicle diffusion is associated with transport of the protonated molecules whose rate limiting process is the primary structural relaxation. Computational studies have suggested that structure diffusion contributes significantly to proton conduction in certain amphoteric systems such as imidazoles, pyrazoles, benzimidazoles, triazoles, and phosphoric acid, especially due to the existence of extended supramolecular networks.[311, 334, 288, 312] Therefore, these materials are at the forefront in the search for anhydrous proton exchange membranes with high proton conductivity, especially for applications in fuel cell technologies.[65, 298] However, experimental evidence that extended supramolecular hydrogen-bonded structures actually facilitate proton conductivity through structure diffusion is limited and has, until now, relied on a comparison of charge and molecular diffusivities obtained by the Nernst-Einstein relation and ^{1}H NMR, respectively.[64, 308, 66] Furthermore, some authors have hypothesized that the high static dielectric permittivity (or dielectric constants) in these materials plays an important role in aiding

charge dissociation and thereby increasing the effective number density of charge carriers, as is the case of other ion conducting materials.[65, 288, 308, 313] The premise for this widespread notion is presumably Coulomb's law relating the static dielectric permittivity to the electrostatic force experienced by point charges. Concrete experimental evidence establishing the link between supramolecular hydrogen-bonded networks, static dielectric permittivity, and proton transport in these materials is still lacking. Glass-forming imidazoles such as 2-ethyl-4-methylimidazole and, as we report here for the first time, 4-methylimidazole, exhibit a distinct slow Debye-like relaxation attributed to supramolecular chains and have the ability to dissociate under specific conditions, providing an ideal opportunity to probe the link between supramolecular hydrogen-bonded networks, dielectric constants, and proton transport. Results from these model systems will help in understanding proton conduction in similar supramolecular hydrogen-bonded materials.

A significant body of literature indicates that collective dynamics of supramolecular hydrogen-bonded networks gives rise to a slow, Debye-like relaxation in many hydrogen-bonding liquids such as monohydroxy alcohols, secondary amides, water, and 2-ethyl-4-methylimidazole.[24, 25, 320, 335, 31, 336] The strengths of intermolecular interactions as well as the sizes and orientations of the supramolecular dipoles determine the effective dipole moment and the rate of the slow Debye-like relaxation, ω_{Debye}. Extensive studies of monohydroxy alcohols (MAs) have, for instance, revealed the existence of an equilibrium of ring-type and chain-type supramolecular hydrogen-bonded (H-bonded) structures, with the preferred orientations being sensitive to the molecular structure, pressure, and temperature.[319, 94, 337, 338] Recent rheology and compressibility measurements on MAs revealed a terminal relaxation much slower than the primary structural relaxation, a response analogous to unentangled supramolecular polymers.[339, 223, 196, 340, 197] These studies suggest that the slow, Debye-like relaxation in the hydrogen bonded liquids originates from transient supramolecular chains which reorient by successive addition and removal of monomers at the chain ends. In this case, the Rouse model may be applied to describe the chain dynamics and to provide quantitative estimates of the average sizes of the supramolecular structures. Although these studies enable quantitative estimates of the average lengths of supramolecular chains, MAs cannot easily dissociate due to their chemistry and are therefore not suitable candidates for understanding the correlation between supramolecular hydrogen bonded networks and proton conductivity.

In this study, we employ broadband dielectric spectroscopy to investigate the interplay between the static dielectric permittivity and proton conductivity in glass-forming 2-ethyl-4-methylimidazole and 4-methylimidazole. Detailed analysis of the dielectric data suggests preferential antiparallel alignment of chains comprising approximately seven imidazole molecules at all the temperatures probed. Further experiments using butyramide and levulinic acid as diluents —which either disrupt or preserve the supramolecular structures of 2-ethyl-4-methylimidazole —reveal that longer average chain lengths correlate with lower proton conductivity and higher static dielectric permittivity. These results challenge the longstanding notion that higher static dielectric permittivity in this class of supramolecular hydrogen bonded materials results in enhanced proton conduction. This apparent disparity is attributed to the fact that proton transport in these materials is controlled by the primary structural dynamics while the static dielectric permittivity arises from the additivity of dipole moments comprising the supramolecular chains characterized by dynamics at much longer timescales.

Experimental

2-ethyl-4-methylimidazole (2E4MIm, 95% purity), 4-methylimidazole (4MIm, 98% purity), levulinic acid (LA, 98% purity), and butyramide (BA, 98% purity) were purchased from Sigma-Aldrich and used as received. Mixtures were prepared by mixing at 60 °C in a high purity nitrogen atmosphere. Broadband dielectric spectroscopy measurements were made in the frequency range of $10^{-3} - 10^{7}$ Hz and temperature range of 180 −400 K using a Novocontrol Alpha Analyzer with a QUATRO liquid nitrogen temperature control system with temperature stability ±0.1 K. Stainless steel parallel plate electrodes with a diameter of 20 mm were utilized. Teflon spacers were used to provide a gap of 0.2 mm between the electrodes. Differential scanning calorimetry measurements were made on a TA Instruments Q2000 calorimeter with a heating and cooling rate of 10 K min^{-1}. 2-ethyl-4-methylimidazole is a liquid over the entire temperature range presented. This is confirmed by differential scanning calorimetry measurements which show a well-defined glass transition at 237 K and no evidence of crystallization or melting transitions, see Figure 4.17. Fourier transform infrared spectroscopy (FTIR) measurements were performed on pure 2-ethyl-4-methylimidazole (99% and 95% purity) and mixtures of 2E4MIm with levulinic acid, butyramide, and toluene. Apart

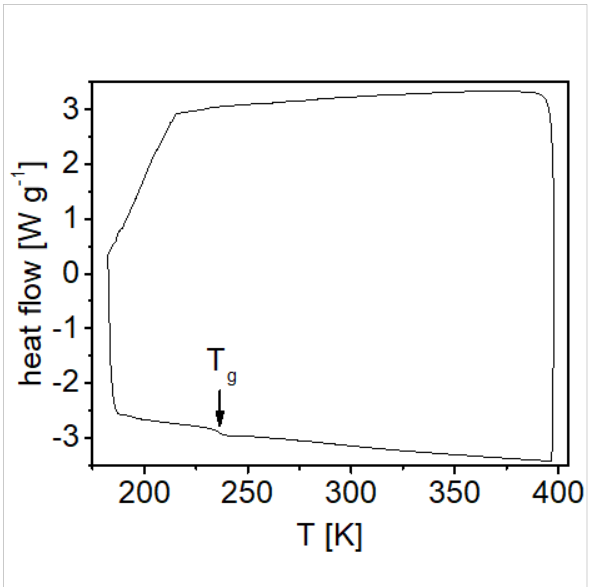

Figure 4.17: Differential scanning calorimetry (DSC) results of 2-ethyl-4-methylimidazole. The heat flow versus temperature indicates this material is cooled without crystallization. The calorimetric glass transition temperature, T_g, is observed as the midpoint of the step in the heat flow rate at 237 K corresponding to a maximum in the derivative of heat flow with respect to temperature.

from the 2.5mol% levulinic acid + 2E4MIm, the 2.5mol% butyramide + 2E4MIm, and temperature-dependent 2E4MIm spectra, all the data in Figures 4.22 - 4.24 were measured at room temperature (298 K) in a Varian FTS 6000e spectrometer over the wavelength range 4000-400 cm^{-1} at a scan resolution of 2 cm^{-1}. Samples were pressed between NaCl windows, placed in a nitrogen-purged atmosphere, and measured in transmission mode for 512 scans. The 2.5mol% levulinic acid + 2E4MIm(95% purity) and 2E4MIm temperature-dependent samples were pressed between BaF_2 windows and measured over the wavelength range 4000-650 cm^{-1} in a Linkam temperature stage mounted on a Hyperion microscope stage attached to a Bruker Vertex 70 spectrometer. The samples were measured in transmission mode at a resolution of 4 cm^{-1} for 282 scans over the temperature range 60 − (−30 °C). The 2.5mol% butyramide + 2E4MIm (95% purity) sample was pressed between BaF_2 windows and measured over the wavelength range 4000 −700 cm^{-1} at 36.85 °C in a Linkam temperature stage mounted on UMA 500 microscope stage attached to the Varian FTS 6000e spectrometer. The sample was measured in transmission mode at a resolution of 1 cm^{-1} for 512 scans over the temperature range 340-200 K.

Table 4.1: Parameters of the Havriliak-Negami fitting functions, Equation.4.3, as obtained for neat 2-ethyl4-methylimidazole at selected temperatures.

T [K]	ε_∞	$\Delta\varepsilon_{Debye}$	β_{Debye}	γ_{Debye}	ω_{Debye} [s^{-1}]	$\Delta\varepsilon_\alpha$	β_α	γ_α	ω_α[s^{-1}]
280	2.5	1.8	0.83	1.0	3.6×10^4	1.4	0.80	0.46	1.3×10^6
270	2.5	5.9	0.88	1.0	3.0×10^3	1.5	0.74	0.52	1.4×10^5
260	2.6	16.3	0.94	1.0	2.3×10^2	1.7	0.75	0.50	8.1×10^3
250	2.6	33.5	0.90	1.0	7.8	1.1	1.00	0.36	6.7×10^2
240	2.6	42.2	0.95	0.93	0.2	1.7	0.72	0.55	5.4

Results and Discussion

Broadband dielectric spectroscopy is a versatile experimental tool for investigating the dynamics of dipolar and ionic materials.[68] Application of an oscillating electric field of small amplitude to these materials over a broad temperature range enables one to probe the dynamics of polar molecular and supramolecular moieties as well as charge transport. The dielectric spectra of the associating imidazoles reveal two relaxations as evident in the real part of complex dielectric permittivity, ε', and its corresponding derivative loss spectra, ε''_{der}, for 2-ethyl-4-methylimidazole (2E4MIm) (Figure 4.18). The derivative representation is employed since it suppresses the contributions of proton conductivity to the dielectric loss while revealing the underlying dielectric relaxations. The solid lines in Figure 4.18 represent fits obtained by a linear combination of two Havriliak-Negami functions:

$$\varepsilon^*(\omega) = \frac{\Delta\varepsilon_{Debye}}{(1+(i\omega\tau_{Debye})^\beta)^\gamma} + \frac{\Delta\varepsilon_\alpha}{(1+(i\omega\tau_\alpha)^\beta)^\gamma} + \varepsilon_\infty + \frac{\sigma_0}{i\omega\varepsilon_0} \tag{4.3}$$

where $\omega = 2\pi f$ is the frequency of the applied electric field, $\Delta\varepsilon$ the dielectric strength, τ the model relaxation time, β and γ shape parameters, ε_∞ the high-frequency limiting permittivity, σ_0 the dc ionic conductivity, and ε_0 the vacuum permittivity. The two molecular relaxation rates are related to their respective model relaxation times by, $\omega_{HN} = (1/\tau_{HN})[\sin(\beta\pi/(2+2\gamma))]^{1/\beta}[\sin(\beta\gamma\pi/(2+2\gamma))]^{-1/\beta}$.[3] The fit parameters obtained by Equation 4.3 for neat 2E4MIm are provided in Table 4.1

The faster dielectric process corresponds to the primary structural, α-relaxation of the 2E4MIm molecules and the slower, Debye-like relaxation is attributed to reorientation of supramolecular hydrogen-bonded chains.[68, 341] The low frequency static dielectric permittivity values, indicated in Figure 4.18(a), show a minimum at 280 K owing to a strong temperature dependence of the

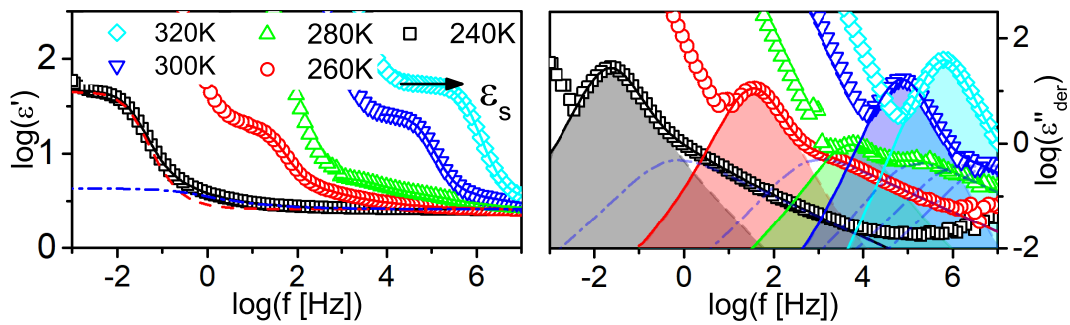

Figure 4.18: Broadband dielectric spectra of 2-ethyl-4-methylimidazole. Real part of the complex dielectric function ε_0 and the derivative spectra $\varepsilon''_{der} = [(-\pi)/2]\{\partial\varepsilon'/\partial\ln(f)\}$ of pure 2-ethyl-4-methylimidazole (2E4MIm) vs frequency. Solid lines represent fits using a combination of two Havriliak-Negami fitting functions. Shaded areas depict the contribution of the slow, Debye-like relaxation and dotted-dashed blue lines correspond to the structural α relaxation.

dielectric relaxation strength $\Delta\varepsilon_{Debye}$. The static dielectric permittivity of associated liquids reflects the supramolecular networks inherent in these materials especially if such networks serve to preferentially orient neighboring dipolar moieties either parallel or antiparallel to one another. The departure from the Onsager relation—which describes the static dielectric permittivity of non-associated dipolar liquids—due to the orientation as described by the Kirkwood-Fröhlich correlation factor, g_K, is quantified by the expression

$$g_K = \frac{9\varepsilon_0 kT}{\eta\mu^2}\frac{(\varepsilon_s - \varepsilon_\infty)(2\varepsilon_s + \varepsilon_\infty)}{\varepsilon_s(\varepsilon_\infty)^2} \tag{4.4}$$

where ε_s is the static dielectric permittivity, ε_∞ the real part of permittivity in the high frequency limit, N the number density of dipoles, and μ the dipole moment.[75, 318] We have calculated g_K using a literature value for the molecular dipole moment of $\mu = 3.84$D and number density of dipoles of $n_{2E4MIm} = \frac{\rho N_A}{M_w}$ =5.3 × 10^{27} m^{-3} and n_{4MIm} =7.5 × 10^{27} m^{-3}.[6] Values of g_K above or below 1 indicate a preference for parallel or antiparallel orientation of neighboring dipoles, respectively.[75] It should be noted that the dielectric strength of $\Delta\varepsilon_\alpha$ is lower than expected from the Onsager relation. The suppression of $\Delta\varepsilon_\alpha$ has also been observed in monohydroxy alcohols and water and is attributed to a reduction in the degrees of freedom available to the molecule at the timescale of the α relaxation.[336, 319, 318]

The static dielectric permittivity, $\varepsilon_s = \Delta\varepsilon_{Debye} + \Delta\varepsilon_\alpha + \varepsilon_\infty$, of 2-ethyl-4-methylimidazole and 4-methylimidazole is given as a function of temperature in Figure 4.19 (closed symbols)

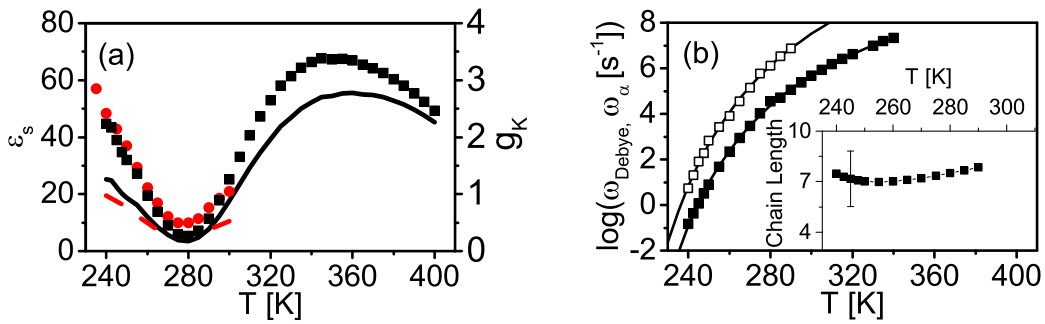

Figure 4.19: (a) Static dielectric permittivity ε_s of pure 2-ethyl-4-methylimidazole (2E4MIm, closed squares) and 4-methylimidazole (4MIm, closed circles). The departure from the Onsager relation is captured by the Kirkwood correlation factor, g_K (solid and dashed lines corresponding to 2E4MIm and 4MIm, respectively). (b) Relaxation rates of the structural, α relaxation (open squares) and slow, Debye-like relaxation (closed squares) of 2E4MIm. Solid lines represent fits by the Vogel-Fulcher-Tammann equation, $\omega = \omega_\infty \exp[B/(T - T_0)]$, fit parameters are provided in Table 4.2. Inset: Estimated number of molecules participating in a chain, chain length $\approx (\omega_\alpha/\omega_{Debye})^{1/2}$.

Table 4.2: Vogel-Fulcher-Tammann Fit Paramters for 2E4MIm relaxation rates.

Relaxation	ω_∞ [s^{-1}]	β	T_0 [K]
α	1.3×10^{15}	2240	172
Debye	2.2×10^{12}	1850	180

alongside the corresponding g_K (lines), revealing competing parallel and antiparallel orientations of neighboring imidazole dipoles. In monohydroxy alcohols, such a temperature dependence of static permittivity is associated with a shifting orientation of the relaxing supramolecular structures, as first suggested by Dannhauser in the 1960s.[24, 25] As temperature is decreased, ring-type supramolecular structures begin to form followed by a transition to predominantly linear chains at the lowest temperatures. The transition from rings to chains would geometrically require lengthening of the supramolecular structures and therefore a concomitant decrease in ω_{Debye} with respect to ω_α has been observed in all MAs showing this type of temperature dependent static dielectric permittivity. The decrease in values of ω_{Debye} has been confirmed by dielectric and shear-mechanical spectroscopy as well as compressibility measurements.[319, 197, 223, 26, 27, 342, 343] However, in the case of 2E4MIm the ratio between ω_{Debye} and ω_α remains approximately constant over the entire temperature range in which g_K transitions from above to below 1, suggesting that the average lengths of the supramolecular structures remain relatively unaltered in the entire range.

Evidence of the formation of a variety of linear oligomers in imidazoles has been reported from solution infrared studies; however, the formation of cyclic oligomers with less than 10 repeat molecules would result in strained hydrogen bonds and are therefore highly unlikely.[102] The transient chain mechanism, which describes the slow, Debye-like relaxation of MAs, provides an avenue to estimate an average length of supramolecular chains by applying models developed to describe polymer dynamics.[196, 318, 344, 345, 316, 346] The Rouse model, which describes the dynamics of short chain polymers, reveals a temperature independent average chain length, $n \approx \sqrt{\omega_\alpha/\omega_{Debye}}$, of approximately seven 2-ethyl-4-methylimidazole molecules [inset of Figure 4.19(b)]. Therefore, if the depression in static permittivity vs temperature were due to a shift in the equilibrium of chain and ring structures, the average lengths of the structures would need to drastically increase as temperature is decreased. However, the ratio $\omega_\alpha/\omega_{Debye}$ is temperature independent over the range 240-290 K (Figure 4.19), indicating that the average length of the chains remains unaltered. Furthermore, the slow Debye-like relaxation in 2E4MIm has been observed up to 450 K by Brillouin-Raman spectroscopy with negligible reduction in the ratio $\omega_\alpha/\omega_{Debye}$.[68] Therefore, we suggest that the antiparallel orientation of 2E4MIm originates not from ring formation, but from an increase in the preference for antiparallel alignment of linear chains. While the precise reason for the change in preferred alignment cannot be conclusively determined from the current results, we conjecture that the ability of imidazole molecules to engage in π - π interactions is a contributing factor to this mechanism. Further experimental and computational work, out of the scope of the current work, are required to unravel the role of π - π interactions in determining supramolecular hydrogen bonding in this class of materials.

Further insight into the influence of supramolecular structure on the charge transport and dynamics of 2E4MIm is provided by examining the influence of additives on the average lengths of the supramolecular structures, the dielectric strength of the slow, Debye-like relaxation, and the measured proton conductivity. In a previous work, we proposed that the supramolecular chains of 2-ethyl-4-methylimidazole are disrupted by addition of 2.5 mol % levulinic acid (LA) as indicated by shifts in the rates obtained by dynamic light scattering and broadband dielectric spectroscopy as well as a reduction in the viscosity.[341] An inspection of the dielectric spectra over a broader acid concentration range reveals a gradual increase in ω_{Debye}, attributed to a shortening of the average chain lengths, Figure 4.20(a). Because of the decreasing separation between ω_α and ω_{Debye}, the

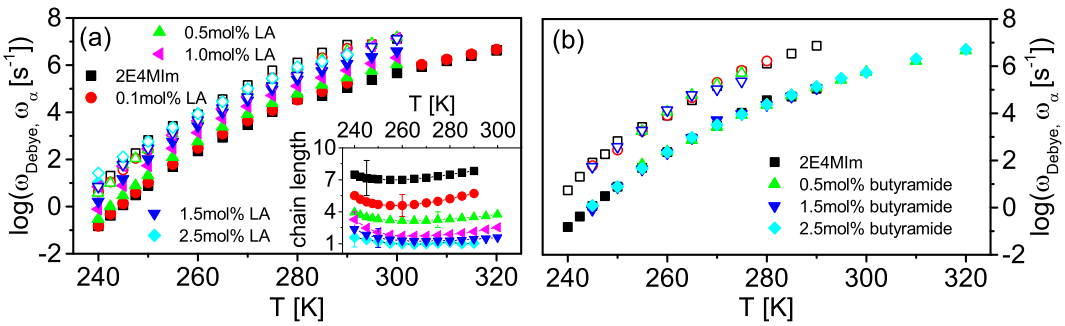

Figure 4.20: Relaxation rate vs temperature for the slow, Debye-like relaxation (closed symbols) and structural, α relaxation (open symbols) of pure 2-ethyl-4-methylimidazole and low concentration (a) levulinic acid and (b) butyramide mixtures as obtained from the broadband dielectric spectra.

dielectric spectra of the acid mixtures are fit with a combination of one HavriliakNegami function, to account for the slow, Debye-like relaxation, and the random barrier model (RBM), to account for the faster charge hopping process:

$$\varepsilon^*(\omega) = \frac{\Delta\varepsilon_{Debye}}{(1+(i\omega\tau_{Debye})^{\beta})^{\gamma}} + \frac{\sigma_0}{i\omega\varepsilon_0}\frac{i\omega\tau_e}{\ln(1+i\omega\tau_e)} + \varepsilon_\infty \tag{4.5}$$

The structural, α-relaxation rate of pure 2E4MIm corresponds with the charge hopping rate, $\omega_e = 1/\tau_e$, obtained by the RBM as seen in Figure 4.20. Based on the separation of the two relaxation rates, it is apparent that the extended supramolecular hydrogen-bonded chains are disrupted at and above 1.5 mol % LA. The disruption in supramolecular structure is sensitive to the type of diluent and appears to rely on its ability to donate protons as shown by the invariance of relaxation rates upon addition of nonproton donating butyramide, Figure 4.20(b).

The loss of linear hydrogen-bonded structures upon addition of levulinic acid is expected to reduce the parallel correlations of neighboring dipoles. That is, it will decrease the static dielectric permittivity in the regime where $g_K > 1$. Because of the unknown influence of the shortening of hydrogen-bonded chains on the interplay between parallel and antiparallel orientations of neighboring dipoles, the actual influence of acid addition on ε_s is not so straightforward, as seen in Figure 4.21(a). Despite this, two observations may still be made: (i) values where $g_K < 1$ continue to be observed up to 2.5 mol % LA and (ii) the values and temperature dependence of ε_s approach the prediction of Onsager's relation for pure 2E4MIm at 10 mol % LA. The observation of antiparallel orientation at concentrations where the chains are significantly shorter is a strong indication that

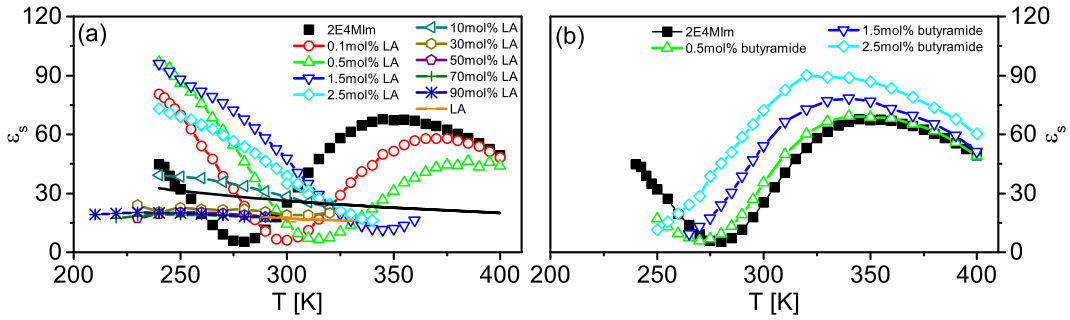

Figure 4.21: Static dielectric permittivity vs temperature of 2-ethyl-4-methylimidazole and its mixtures with (a) levulinic acid and (b) butyramide. Solid line is the static permittivity predicted for pure 2E4MIm by the Onsager relation.

such orientation does not originate in ring-type supramolecular structures. The continued departure from Onsager's relation up to approximately 10 mol % LA indicates a contribution from linearly H-bonded structures. The interpretation of the dielectric spectra in terms of a disruption of the 2E4MIm hydrogen bond network upon addition of proton-donating levulinic acid is qualitatively supported by Fourier-transform infrared spectroscopy measurements of 2E4MIm and the levulinic acid mixtures.

Infrared spectroscopy probes intramolecular, and in certain cases intermolecular, vibrational molecular dynamics.[347, 348, 349, 350, 340, 351, 352] The room-temperature mid-IR spectrum of pure 2-ethyl-4-methylimidazole (2E4MIm) is presented in Figure 4.22. The vibrational modes of gas phase and crystalline imidazole as well as in aqueous and carbon tetrachloride solution have been thoroughly investigated.[102, 348, 353, 354, 355, 356, 357, 358, 103] The region between 3500-2300 cm^{-1} consists of a broad band with several distinct sub-bands. The fundamental NH stretching band located within this region will be sensitive to a change in the strength of intermolecular hydrogen bonds brought about by the addition of levulinic acid. In extremely dilute solutions, where imidazole is "free", the NH stretch band is located at 3500 cm^{-1}. In slightly less dilute solutions, where imidazole begins to associate via intermolecular hydrogen bonds, this peak begins to shift and may be located as low as $\approx$2850 cm^{-1}.[9] However, even in these dilute solutions the peak is obscured by strongly absorbing sub-bands which appear in this region due to Fermi resonance of stretching vibrations with overtones or combination tones of bands in the 1600-900 cm^{-1} range.[9] These Fermi resonance bands are insensitive to the hydrogen bond strength.[9] Therefore, this region cannot easily be utilized to investigate hydrogen bonding in bulk

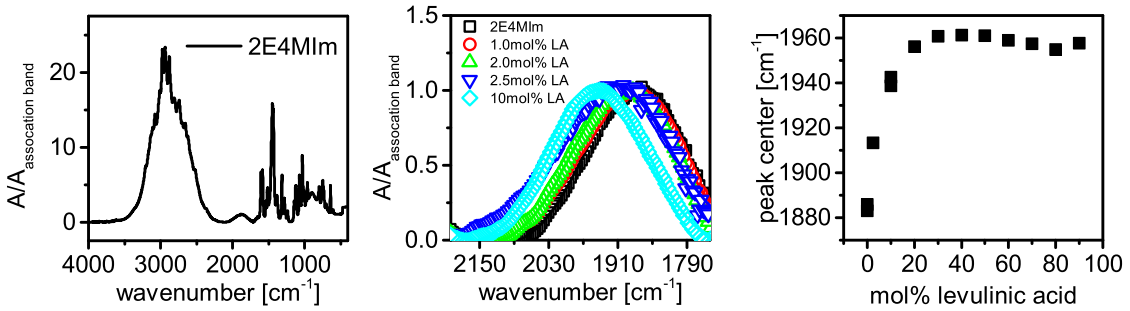

Figure 4.22: Left:Mid-IR spectrum of liquid 2-ethyl-4-methylimidazole at room temperature. The spectrum is normalized by the maximum absorbance of the broad association peak centered at 1875cm^{-1}. Middle: Normalized absorbance versus wavenumber for 2E4MIm and low concentration levulinic acid mixtures. Upon addition of acid the association band shifts to higher frequency. Solid lines correspond to fits with a Gaussian function. Right: Concentration dependence of the association band peak position. The largest shift in position occurs over the concentration range 0-10mol% LA. Peak centers are found by Gaussian fits of the association band.

liquid imidazoles. The fingerprint region between 1200-400 cm^{-1} contains additional contributions from NH bending and wagging modes which will also be sensitive to hydrogen-bond strengths. However, the large number of closely-overlapping modes in this region also inhibits the isolation and assignment of these peaks.

A broad and weak band centered at 1880 cm^{-1} in liquid 2E4MIm is far from the frequency of any fundamental vibrational modes. A similar band in liquid water, located near 2100 cm^{-1}, is termed the "association" peak and arises from a combination of H-O-H bending and libration modes[359, 360, 361, 362]. The position of the association peak is highly sensitive to the strength of the H-bond network. Kosmotropic and chaotropic ions, which strengthen and weaken the H-bond network of water, have an inverse influence on the peak position. Kosmotropic ions blue-shift the peak while chaotropic ions red-shift it to lower frequencies[360]. The similarity in position, shape, and intensity of the association band of liquid water and the band at 1880 cm^{-1} in 2E4MIm encourages its possible application as a reporter of the hydrogen bond network of bulk, liquid imidazoles. The position of the association band of 2E4MIm is temperature-independent over the temperature range 240-330 K, see Figure 4.23. Therefore, if this peak is a reporter of the H-bond network we can suppose that the strength and number density of intermolecular hydrogen bonds is not strongly dependent on temperature in this region. This observation is in agreement with our previous observation of constant separation in the relaxation rates of the slow, Debye-like relaxation and structural, α-relaxation over the same temperature range, Figure 4.19.

In contrast to temperature, the addition of levulinic acid has a strong influence on the peak position of the association band in 2E4MIm. Upon addition of even minute amounts of levulinic

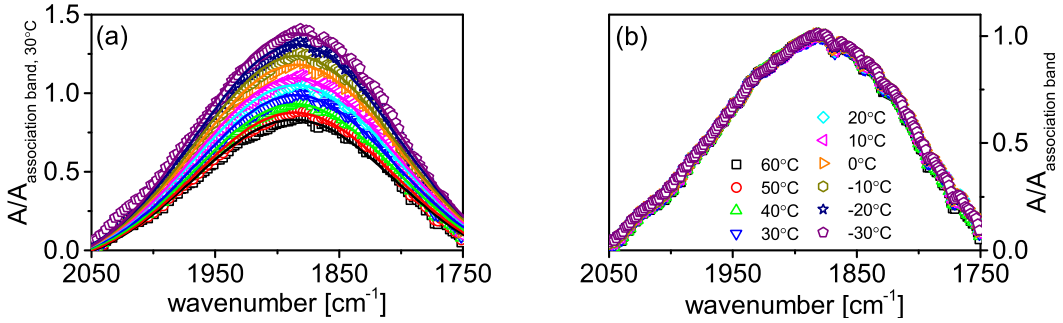

Figure 4.23: Temperature dependence of the 2E4MIm association band. (a) Absorbance normalized by the peak maximum at 30 °C versus wavenumber for pure 2E4MIm. Solid lines correspond to fits with a Gaussian function. (b) Absorbance normalized by the peak maximum at each respective temperature versus wavenumber. The intensity of the band decreases with increasing temperature, however, the peak position is temperature independent over the measured range.

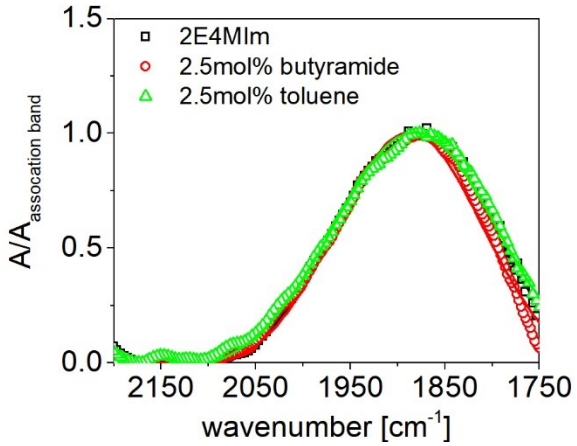

Figure 4.24: Absorbance normalized by the peak maximum versus wavenumber for 2E4MIm and low concentration butyramide and toluene mixtures. The association band is not influenced by the addition of the non-proton donating additives. Solid lines correspond to fits with a Gaussian function.

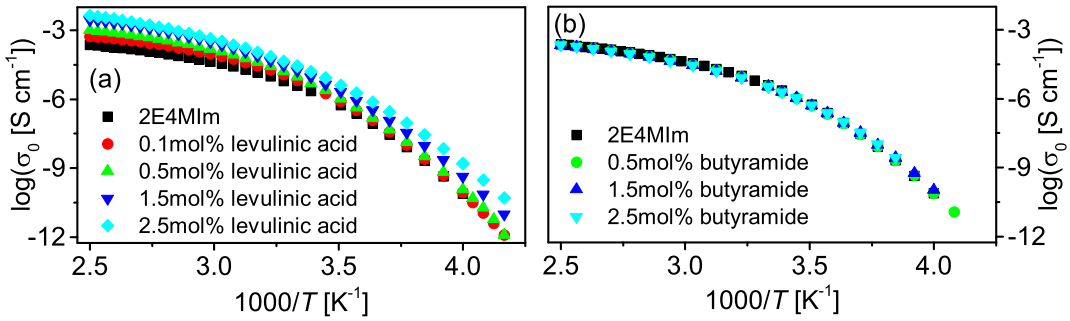

Figure 4.25: Ionic conductivity σ_0 as a function of inverse temperature for (a) levulinic acid and (b) butyramide mixtures with 2-ethyl-4-methylimidazole. Minute amounts of levulinic acid substantially increase the ionic conductivity, while butyramide has no effect.

acid, the peak begins to shift to higher frequencies. The majority of the shift occurs at the lowest acid concentrations with no significant change above 20mol% levulinic acid. At 20mol% it has blue-shifted by approximately 80 cm^{-1}, as shown in Figure 4.22. The concentration dependence coincides with the disruption of hydrogen-bonded chains as deduced from changes in supramolecular dynamics observed in dielectric spectroscopy and previously by dynamic light scattering, Figure 4.10. This observation provides qualitative support that the addition of levulinic acid has a significant influence on the hydrogen-bond network of 2E4MIm at very low concentrations. The addition of other non-proton donating diluents, butyramide and toluene, has no influence on the position of the "association" band, see Figure 4.24. This further supports the notion that it is the proton-donating ability of levulinic acid which disrupts the H-bond network.

The exact origin of the association band of liquid 2E4MIm is unknown. The majority of imidazole IR studies are performed in dilute solution or solid phase.[102, 348, 363, 353, 354, 355, 356, 357] To our knowledge there is no discussion of the association band of bulk, liquid imidazole in the current literature. Indeed, despite the long history of liquid water IR studies, it is only very recently that this band has been utilized as a probe of the hydrogen bond network.[360, 362, 361] The blue-shift in peak position upon adding levulinic acid to 2E4MIm is opposite that observed in water upon addition of a chaotrope. This may be due to a different fundamental mode underlying the association band in 2E4MIm as compared to water. It suggests that one of the underlying modes is a stretching band, possibly the N-H—N stretch located near 100 cm^{-1} in liquid imidazole.[348]

A significant increase in the ionic conductivity accompanies the disruption of the extended supramolecular chains, see Fig. 4.25. Fast proton transport by structure diffusion mechanism

Table 4.3: Parameters of the Havriliak-Negami fitting functions of Equation4.3 as obtained for the 2.5mol% butyramide + 2E4MIm mixture.

T [K]	ε_∞	$\Delta\varepsilon_{Debye}$	β_{Debye}	γ_{Debye}	ω_{Debye} [s^{-1}]	$\Delta\varepsilon_\alpha$	β_α	γ_α	ω_α[s^{-1}]
280	2.8	38.4	1	0.98	2.6×10^4	2.3	0.76	0.53	6.1×10^5
270	2.8	23.7	1	1	3.4×10^3	2.2	0.76	0.56	1.1×10^5
260	2.8	15.1	1	0.82	2.2×10^2	1.5	0.76	0.56	1.4×10^4
250	2.8	7.1	1	0.73	9.6	1.8	0.76	0.56	3.9×10^2

should be strongly hindered by the reduction in the average lengths of the extended hydrogen-bonded structures.[346] In contrast, it is observed that the ionic conductivity is enhanced at all acid concentrations measured. The increase may be attributed to an increase in the effective number density of mobile charge carriers.

The constant average chain length upon addition of the hydrogen bonding, but non-proton donating butyramide molecule is illuminating. The static dielectric permittivity, by comparison, is significantly influenced upon addition of butyramide, Figure 4.21(b). The minimum shifts to lower temperatures while the value at the maximum increases from 68 to 88. The dielectric spectra of the 2.5mol% butyramide + 2E4MIm mixture are shown in Figure 4.26. The fit parameters obtained from Equation 4.3 for the 2.5mol% butyramide + 2E4MIm mixtures are provided in Table 4.3. Here we see that the shift in ε_s is due to changes in the dielectric strength of the slow, Debye-like relaxation, $\Delta\varepsilon_{Debye}$. Alongside the continued presence of the minimum in ε_s at lower temperatures this suggests that it is still a shift in the supramolecular structures of 2E4MIm which is responsible for this increase even in the butyramide mixtures. However, the butyramide molecules will also contribute to the measured ε_s due to their high dipole moments even when their concentration is low.

It is worth noting that a similar effect on ε_s of 2E4mIm is observed when one compares the magnitude of the static dielectric permittivity for neat 2E4MIm of different purities of 95% and 99%, reported in the previous studies and shown together in Figure 4.27.[68, 341] In both cases, slightly shifted minima in the plot of the ε_s vs temperature are observed, but the characteristic timescales remain unaltered. It should be noted that in previous studies of 2-ethyl-4-methylimidazole, no analysis and discussion of the temperature dependence of ε_s was provided.[68] Therefore, any direct correlation between the average length of the supramolecular chains and the static dielectric

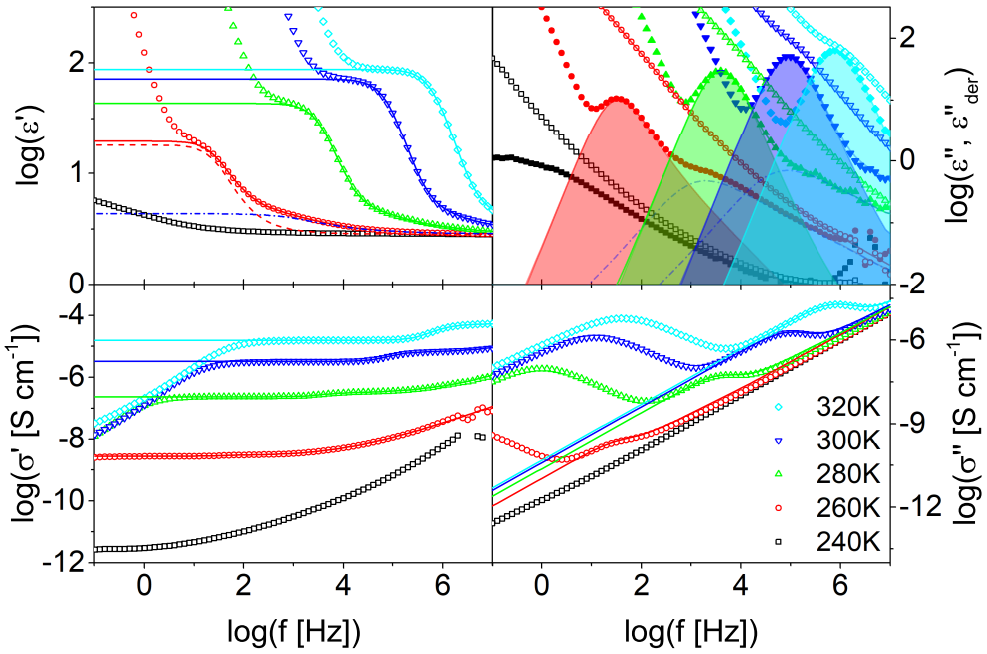

Figure 4.26: Real and imaginary parts of complex permittivity, ε^* and conductivity, σ^* of 2.5mol% butyramide+2E4MIm. Solid lines correspond to fits by Equation 4.3. Fit parameters are provided in Table 4.3. Closed symbols in the upper right panel correspond to the derivative representation of imaginary permittivity, ε''_{der}. Shaded areas depict the contribution of the slow, Debye-like relaxation and dotted-dashed blue lines correspond to the structural α-relaxation.

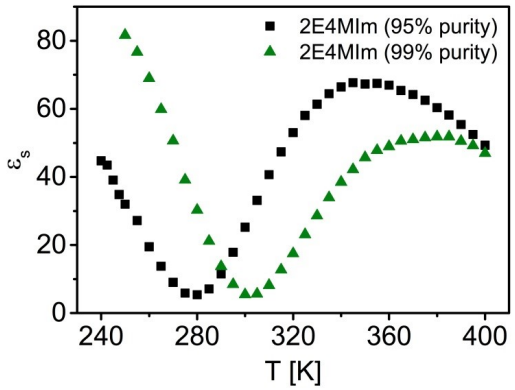

Figure 4.27: Static dielectric permittivity, ε_s, of pure 2-ethy-4-methylimidazole obtained from Sigma Aldrich (95% purity, squares) and Acros Organics (99% purity, triangles)

permittivity as well as proton conductivity could not be established. In addition, although we conjectured that addition of levulinic acid to 2-ethyl-4-methylimidazole leads to disruption of the supramolecular hydrogen-bonded chains, this hypothesis could not be confirmed since much higher concentrations (≥2.5 mol%) of the acid were used in the previous study.[341]

In addition to the new insights obtained from the present study regarding the interplay between the static dielectric permittivity and proton transport, the use of suitable diluents makes it possible to verify the previous hypothesis regarding the shortening of the supramolecular chains upon addition of levulinic acid. The measured ionic conductivity σ_0 shows no change over the same butyramide concentrations. Because of the strongly temperature dependent static dielectric permittivity of neat 2E4MIm and the absence of a direct correlation between static dielectric permittivity with ionic conductivity in the butyramide mixtures, we conclude that the static dielectric permittivity in imidazoles with slow, sub-α relaxation dynamics is not directly linked to proton conductivity, in contrast to prevailing opinion in the current scientific literature.[65, 288, 312, 313] We attribute this apparent discrepancy to the fact that proton transport in these materials is controlled by the structural, α-relaxation while the static dielectric permittivity arises from the vector addition of the dipole moments comprising the supramolecular chains, for which the characteristic timescales of dynamics are much slower.

In summary, we have reported a strong non-monotonic temperature dependence of the static dielectric permittivity in glass-forming 4-methylimidazole and 2-ethyl-4-methylimidazole. Deviations from the Onsager relation indicate preferential antiparallel alignment of neighboring imidazole molecules. Using the Rouse model, it is found that the supramolecular chains in neat 2-ethyl-4-methylimidazole consist of approximately seven imidazole molecules at all the temperatures probed. Further experiments using butyramide and levulinic acid as diluents reveal that longer average chain lengths of the supramolecular chains correlate with lower proton conductivity and higher static dielectric permittivity. These results challenge the longstanding notion that higher static dielectric permittivity (or constant) in this class of supramolecular hydrogen bonded materials enhances proton conduction. The apparent disparity is attributed to the fact that proton transport in these materials is determined by the primary structural dynamics while the static dielectric permittivity arises from the additivity of dipole moments comprising the supramolecular chains with dynamics at much longer characteristic timescales.

4.4 Conclusions

Mesoscale hydrogen-bonded (H-bonded) networks may exist in liquids which are capable of forming two or more intermolecular hydrogen bonds per molecule.[8, 333, 270, 364] This mesoscale organization can drastically alter the physicochemical properties of these liquids. The hydrogen bonded networks in water, phosphoric acid, and liquid imidazoles, for example, are believed to be critical to proton conduction in materials which contain these molecules, including polymeric proton exchange membranes in fuel cells as well as biological membranes.[64, 65, 321, 308, 302, 310] In addition, in many H-bonded networks the organization of molecular dipoles occurs in such a way that the network itself has an overall supramolecular dipole moment derived from the additivity of the molecular dipole moments. The reorientation of these supramolecular dipoles produces a slow, Debye-like dielectric relaxation, the strength of which is strongly dependent on the relative ratio of parallel versus antiparallel orientation of molecular dipoles within the network. The intrinsic proton conductivity of liquid imidazoles coupled with their linear-chain type H-bond networks provides a new and unique opportunity to probe the influence of mesoscale organization on proton transport in hydrogen-bonded liquids.[68] The formation of extended linear chains enables the analysis of supramolecular dynamics by models originally developed to describe the dynamics of polymers. For instance, by applying the Rouse model, an average chain length may be estimated as, $N = (\omega_\alpha/\omega_{Debye})^{1/2}$, where ω_α is the structural relaxation rate and ω_{Debye} is the rate of the slow, Debye-like relaxation.[318]

In mixtures of 2-ethyl-4-methylimidazole with low concentrations of levulinic acid [LA], the rate of the slow, Debye-like relaxation is rapidly increased until it coincides with the structural, α-relaxation at only 2.5mol% levulinic acid. This merging of the relaxation rates, in view of the Rouse model estimates of the average chain length, indicates a disruption of the supramolecular H-bonded chains over the concentration range from 0 to 2.5mol% LA. Fourier transform infrared spectroscopy measurements of the "association" band, a sensitive reporter of the H-bond network, supports this interpretation. A comparison with the hydrogen-bonding, but not proton-donating butyramide as the diluent reveals the important role of the proton-donating ability to the disruption of the H-bonded chains. If the fast structure diffusion of protons along the hydrogen-bond network is the dominant mechanism contributing to the overall proton conductivity, it is expected that such

a significant alteration in the network as caused by the addition of such small amounts of levulinic acid would reduce the dc ionic conductivity. However, at all levulinic acid concentrations a steady increase in dc ionic conductivity is observed. We also highlight the importance of antiparallel and parallel orientations of linear supramolecular H-bonded imidazole chains to the measured static dielectric permittivities. The high static dielectric permittivity of imidazole is often cited as contributing to its high intrinsic proton conductivities by stabilizing the imidazolium cations. However, the static dielectric permittivity is strongly temperature dependent, passing through a minimum at 280 K, and can be influenced by addition of butyramide without any apparent effect on the dc ionic conductivity. This indicates that the measured static permittivity values may not actually be assisting in the formation of protonated imidazoles due to their supramolecular origin. These results provide new insight into the organization and dynamics of the mesoscale hydrogen-bonded network of liquid imidazoles and their influence of charge transport. This insight will be useful in the future design of ion conducting liquids and furthers our understanding of the nature of mesoscale organization and dynamics in general.

Disruption of imidazole chains: The detailed study of levulinic acid concentration has only been performed for 2-ethyl-4-methylimidazole. Other imidazoles, 4-methylimidazole and imidazole, have higher room temperature proton conductivities. This is a potential indication of a more substantial contribution from a structure diffusion-type proton transport mechanism in these systems. Future studies on the influence of acid concentration on dc ionic conductivity of other imidazoles may reveal an initial drop in dc ionic conductivity not found for 2E4MIm. This could indicate the contribution of the structure diffusion mechanism in these imidazoles. We attribute the disruption of the H-bonded chains to the proton-donating abilities of the levulinic acid. However, we have not directly measured the transfer of protons from levulinic acid to imidazole. A potentially interesting future work would make a more detailed study of the influence of additive pKa on the concentration dependence of the disruption of the H-bonded chains.

Temperature-dependent supramolecular organization of neat imidazoles: This work represents only a first step to understanding the unusual temperature dependence of the supramolecular organization of neat imidazoles. We have demonstrated that imidazoles have stark differences in their organization and dynamics compared to monohydroxy alcohols. The exact mechanism contributing to the antiparallel orientation of imidazole dipoles has not been conclusively found.

Using mixtures to elucidate this mechanism is difficult given the additional complexity added by the influence of additive interactions and motion to the dielectric spectra. Still, further diluent studies, especially with diluents capable of interacting with imidazole through π-π stacking may be helpful. Future studies with new imidazoles with wider varying chemical structures may also be helpful in elucidating this mechanism. A challenge in this respect is finding imidazoles with substituents which allow it to be supercooled without crystallization. Imidazoles with extended alkyl chains substituted at the 2 and 4 position, similar to monohydroxy alcohols, are a promising direction and can be synthesized with current procedures.[365, 7] These materials will need to be capable of super-cooling while avoiding crystallization to allow for studies over the experimentally relevant frequency range, as was possible for the 4-methyl and 2-ethyl-4-methylimidazoles of the current study.

Chapter 5

Conclusions

The aim of this dissertation is to contribute to a fundamental understanding of the influence of mesoscale organization and dynamics on the physical and chemical properties of structured liquids. To accomplish this objective, we have focused on two case studies: (i) ionic liquids and (ii) imidazoles. At the outset, we highlighted several fundamental scientific questions to which we sought answers. We now return to these questions and supply the answers as informed by our studies.

1. *How do the chemical structures of ionic liquids alter organization and dynamics at the mesoscale?*

   We have demonstrated the emergence of slow mesoscale aggregate relaxation dynamics in the dielectric and dynamic mechanical spectra of long alkyl chain, solvophobically aggregating ILs. Additionally, in quaternary phosphonium ionic liquids it was found that the formation of long-lived mesoscale aggregates is not simply a function of the volume fraction of non-polar groups, as often believed, but depends more subtly on the chemical structure of the cation and its ability to form strong coulombic interactions in the polar ionic phase.

   These results can found in the following publications:

   (i) Cosby, T., Vicars, Z., Wang, Y., and Sangoro, J., Dynamic-Mechanical and Dielectric Evidence of Long-lived Mesoscale Organization in Ionic Liquids. *Journal of Physical Chemistry Letters*, 8(15), 3544-3548, 2017.

   (ii) Cosby T., Vicars Z., Heres M., Tsunashima, K. Sangoro J., Dynamic and Structural

Evidence of Mesoscopic Aggregation in Phosphonium Ionic Liquids. *The Journal of Chemical Physics*, 148, 193815, 2018.

(iii) Cosby T., Vicars Z., Mapesa, E., Tsunashima, K. Sangoro J., Charge Transport and Dipolar Relaxations in Phosphonium-based Ionic Liquids. *The Journal of Chemical Physics*, 147, 234504, 2017.

2. *In turn, how do changes to the mesoscale organization and dynamics alter the physical and chemical properties of ionic liquids?*

   The existence of the slow mesoscale aggregate dynamics in the dielectric and dynamic mechanical spectra were demonstrated to increase the static dielectric permittivities and zero-shear viscosities, respectively.

   These results can found in the following publications:

   (i) Cosby, T., Vicars, Z., Wang, Y., and Sangoro, J., Dynamic-Mechanical and Dielectric Evidence of Long-lived Mesoscale Organization in Ionic Liquids. *Journal of Physical Chemistry Letters*, 8(15), 3544-3548, 2017.

   (ii) Cosby T., Vicars Z., Heres M., Tsunashima, K. Sangoro J., Dynamic and Structural Evidence of Mesoscopic Aggregation in Phosphonium Ionic Liquids. *The Journal of Chemical Physics*, 148, 193815, 2018.

3. *What design strategies be formulated which allow the physicochemical properties of ionic liquids to be tuned via control of mesoscale aggregate morphology and dynamics?*

   Binary ionic liquid mixtures can be utilized to provide composition-dependent control of the mesoscale aggregate morphology and dynamics. By mixing the aggregating 1-octyl-3-methylimidazolium tetrafluoroborate with non-aggregating 1-ethyl-3-methylimidazolium tetrafluoroborate, the mesoscale aggregate morphologies are altered from bincontinuous to isolated spheres. As a result, the dielectric strength of the mesoscale aggregate relaxation is significantly increased resulting in a 100% increase in the static dielectric permittivity versus the neat IL constituents.

   These results are found in a *to be submitted* manuscript, authors Tyler Cosby, Utkarsh

Kapoor, Jindal Shah, and Joshua Sangoro. The manuscript constitutes Chapter 3.3.

4. *How do temperature, chemical structure, and acid concentration influence the size and dynamics of mesoscale hydrogen-bonded chains in liquid imidazoles?*

   The addition of minute amounts of levulinic acid is found to disrupt the hydrogen-bonded chains of 2-ethyl-4-methylimidazole. In neat imdidazoles, there exists a competition between parallel and antiparallel alignment of molecular dipoles, as evidenced by the temperature dependence of static dielectric permittivity. The origin of the antiparallel alignment is tentatively attributed to a tendency for neighboring hydrogen-bonded chains to orient in opposite directions, perhaps aided by the ability for imidazole to participate in π-bonding.

   These results can found in the following publications:

   (i) Cosby, T., Holt, A., Griffin, P. J., Wang, Y. Y., and Sangoro, J., Proton Transport in Imidazoles: Unraveling the Role of Supramolecular Structure. *Journal of Physical Chemistry Letters*, 6(19), 3961-3965, 2015.

   (ii) Cosby T., Vicars Z., Heres M., Sangoro J., Associating Imidazoles: Elucidating the Correlation between the Static Dielectric Permittivity and Proton Conductivity. *Physical Review Letters*, 120, 136001, 2018.

5. *What is the influence of the size and dynamics of mesoscale hydrogen-bonded chains on proton transport in liquid imidazoles?*

   The loss of the hydrogen-bonded chains in 2-ethyl-4-methylimdazole correlates with an increase in the dc ionic conductivity and a reduction in the static dielectric permittivity. The addition of the non-proton donating butyramide increases the static dielectric permittivity, attributed to a change in the antiparallel alignment of imidazole chains, while dc ionic conductivity is unaffected. Together, these results call into question the inference that hydrogen-bonded chains should influence dc ionic conductivity either by fast proton transport via structure diffusion or by their influence on the static dielectric permitttivity.

   These results can found in the following publications:

   (i) Cosby, T., Holt, A., Griffin, P. J., Wang, Y. Y., and Sangoro, J., Proton Transport in Imidazoles: Unraveling the Role of Supramolecular Structure. *Journal of Physical Chemistry*

Letters, 6(19), 3961-3965, 2015.

(ii) Cosby T., Vicars Z., Heres M., Sangoro J., Associating Imidazoles: Elucidating the Correlation between the Static Dielectric Permittivity and Proton Conductivity. *Physical Review Letters*, 120, 136001, 2018.

5.1 Future Outlook

The newly discovered experimental probes of mesoscale dynamics in ionic liquids provide an exciting new ability to investigate the interplay of chemical structure, mesoscale aggregate morphology, and mesoscale aggregate dynamics in determining the resultant physical and chemical properties of ionic liquids. These studies on neat imidazolium and phosphonium-based ILs and simple binary IL mixtures are a first step in this direction. The vast number of potential unique chemical structures alongside the ability to tune mesoscale morphology by mixing two or more ILs makes this an exciting direction. It is expected that by using these approaches to further alter the aggregate morphology and dynamics, new abilities to tune the static dielectric permittivity, dc ionic conductivity, and zero-shear viscosity will be realized.

In the imidazole studies, we question the influence of mesoscale hydrogen-bonded chains on proton transport in liquid imidazoles. We also highlighted the unusual temperature-dependent antiparallel alignment of adjacent chains. This is an unexpected departure from the findings of hydrogen-bonded networks in the related monohydroxy alcohols and points to an additional level of previously unrealized organization in imidazoles. Further work with a wider variety of chemical structures and diluents will hopefully shed more light on this mesoscale organization and its influence on static dielectric permittivity.

Bibliography

[1] Arthur R. Von Hippel. *Dielectrics and Waves*. John Wiley & Sons, Inc., 1954. x, 9, 13, 14, 15

[2] C J F Böttcher, O C Van Belle, P Bordewijk, and A Rip. *Theory of Electric Polarization*, volume 1. Elsevier Scientific Publishing Company, New York, 1973. x, 8, 13, 14

[3] Friedrich Kremer and Andreas Schönhals. *Broadband Dielectric Spectroscopy*. Springer, Berlin, 2003. x, 13, 14, 15, 16, 24, 55, 71, 76, 87, 98, 118, 129, 131, 140

[4] Jeppe C. Dyre. The random free energy barrier model for ac conduction in disordered solids. *Journal Applied Physics*, 64(5):2456–2468, 1988. x, xvii, 18, 19, 72, 74, 100, 101, 129

[5] Robert L Danley. New heat flux DSC measurement technique. *Thermochimica Acta*, 395(1):201–208, 2002. xi, 27, 28

[6] Alan R Katritzky, Christopher A Ramsden, John A Joule, and Viktor V Zhadankin. *Handbook of Heterocyclic Chemistry*. Elsevier, Amsterdam, 3rd edition, 2010. xii, 3, 31, 32, 141

[7] Klaus Hofman. *The Chemistry of Heterocycyclic Compounds: Imidazole and its Derivatives, Part I*. Wiley-Interscience, New York, 1953. xii, xxi, 3, 31, 32, 112, 113, 114, 154

[8] Serge. N Vinogradov and Robert. H Linnell. *Hydrogen Bonding*. Van Nostrand Reinhold Company, New York, N.Y., 1971. xii, 3, 31, 32, 152

[9] H Wolff and Helm Müller. Substructure of the NH stretching vibrational band of imidazole. *The Journal of Chemical Physics*, 60(7):2938–2939, 1974. xii, 31, 32, 33, 145

[10] Loïc Barré. Contribution of Small-Angle X-Ray and Neutron Scattering (SAXS and SANS) to the Characterization of Natural Nanomaterials. In *X-ray and Neutron Techniques for Nanomaterials Characterization*, pages 665–716. Springer Berlin Heidelberg, Berlin, Heidelberg, 2016. xiii, 35

[11] Douglas R MacFarlane, Maria Forsyth, Ekaterina I Izgorodina, Andrew P Abbott, Gary Annat, and Kevin Fraser. On the concept of ionicity in ionic liquids. *Physical Chemistry Chemical Physics*, 11(25):4962–4967, 2009. xiii, 43, 44, 97

[12] Olga Russina, Alessandro Triolo, Lorenzo Gontrani, Ruggero Caminiti, Dong Xiao, Larry G Hines, Richard A Bartsch, Edward L Quitevis, Natalia Plechkova, and Kenneth R Seddon. Morphology and intermolecular dynamics of 1- alkyl-3-methylimidazolium bis{(trifluoromethane)sulfonyl}amide ionic liquids: structural and dynamic evidence of nanoscale segregation. *Journal of Physics: Condensed Matter*, 21:424121, 2009. xiv, 45, 46, 48

[13] Juan C. Araque, Jeevapani J. Hettige, and Claudio J. Margulis. Modern Room Temperature Ionic Liquids, a Simple Guide to Understanding Their Structure and How It May Relate to Dynamics. *The Journal of Physical Chemistry B*, 119(40):12727–12740, oct 2015. xiv, 2, 36, 47, 48, 51, 61, 64, 82, 84, 85

[14] Duncan W. Bruce, Christopher P. Cabry, José N. Canongia Lopes, Matthew L. Costen, Lucía D'Andrea, Isabelle Grillo, Brooks C. Marshall, Kenneth G. McKendrick, Timothy K. Minton, Simon M. Purcell, Sarah Rogers, John M. Slattery, Karina Shimizu, Eric Smoll, and María A. Tesa-Serrate. Nanosegregation and Structuring in the Bulk and at the Surface of Ionic-Liquid Mixtures. *Journal of Physical Chemistry B*, 121(24):6002–6020, 2017. xiv, 48, 85

[15] Olga Russina, Fabrizio Lo Celso, Natalia V. Plechkova, and Alessandro Triolo. Emerging Evidences of Mesoscopic-Scale Complexity in Neat Ionic Liquids and Their Mixtures. *Journal of Physical Chemistry Letters*, 8(6):1197–1204, 2017. xv, 2, 47, 51, 57, 58, 62, 83, 86, 101

[16] Maiko Kofu, Michihiro Nagao, Takeshi Ueki, Yuzo Kitazawa, Yutaro Nakamura, Syota Sawamura, Masayoshi Watanabe, and Osamu Yamamuro. Heterogeneous Slow Dynamics of Imidazolium-Based Ionic Liquids Studied by Neutron Spin Echo. *Journal of Physical Chemistry B*, 117(9):2773–2781, 2013. xv, 47, 51, 57, 58, 62, 83, 86

[17] P C Hiemenz and T P Lodge. *Polymer Chemistry*. CRC Press, New York, 2nd edition, 2007. xvii, 20, 21, 24, 30, 71, 72

[18] Olga Russina, Alessandro Triolo, Lorenzo Gontrani, and Ruggero Caminiti. Mesoscopic Structural Heterogeneities in Room-Temperature Ionic Liquids. *Journal of Physical Chemistry Letters*, 3(1):27–33, 2012. xix, 51, 82, 85, 90, 91, 92

[19] Cherry S. Santos, Harsha V. R. Annapureddy, N. Sanjeeva Murthy, Hemant K. Kashyap, Edward W. Castner, and Claudio J. Margulis. Temperature-dependent structure of methyl-tributylammonium bis(trifluoromethylsulfonyl)amide: X ray scattering and simulations. *The Journal of Chemical Physics*, 134:64501, 2011. xix, 82, 90, 91

[20] Alessandro Triolo, Olga Russina, Barbara Fazio, Giovanni Battista Appetecchi, Maria Carewska, and Stefano Passerini. Nanoscale organization in piperidinium-based room temperature ionic liquids. *The Journal of Chemical Physics*, 130(16):164521, 2009. xix, 46, 90, 91

[21] Tanja Pott and Philippe Méléard. New insight into the nanostructure of ionic liquids: a small angle X-ray scattering (SAXS) study on liquid tri-alkyl-methyl-ammonium bis(trifluoromethanesulfonyl)amides and their mixtures. *Physical Chemistry Chemical Physics*, 11(26):5469–5475, 2009. xix, 46, 90, 91

[22] Jeevapani J Hettige, Juan C Araque, Hemant K Kashyap, and Claudio J Margulis. Communication: Nanoscale structure of tetradecyltrihexylphosphonium based ionic liquids. *The Journal of Chemical Physics*, 144(12), 2016. xix, 81, 82, 90, 91

[23] Gerald Oster and John G Kirkwood. The Dielectric Constant of Water and the Saturation Effect. *The Journal of Chemical Physics*, 11:6353, 1943. xxii, 118, 119

[24] Walter Dannhauser. Dielectric Study of Intermolecular Association in Isomeric Octyl Alcohols. *Journal of Chemical Physics*, 48(5):1911–1917, 1968. xxii, 2, 119, 120, 137, 142

[25] G P Johari and W Dannhauser. Dielectric Study of the Pressure Dependence of Intermolecular Association in Isomeric Octyl Alcohols. *Journal of Chemical Physics*, 48(11):5114–5122, 1968. xxii, 119, 137, 142

[26] S Bauer, K Burlafinger, C Gainaru, P Lunkenheimer, W Hiller, A Loidl, and R Böhmer. Debye relaxation and 250 K anomaly in glass forming monohydroxy alcohols. *Journal of Chemical Physics*, 138(9):11, 2013. xxii, 122, 142

[27] S Bauer, H Wittkamp, S Schildmann, M Frey, W Hiller, T Hecksher, N B Olsen, C Gainaru, and R Böhmer. Broadband dynamics in neat 4-methyl-3-heptanol and in mixtures with 2-ethyl-1-hexanol. *Journal of Chemical Physics*, 139(13):10, 2013. xxii, 122, 123, 142

[28] Takashi Nakanishi. *Supramolecular Soft Matter*. Wiley, 2011. 1

[29] Hajime Tanaka. Bond orientational order in liquids: Towards a unified description of water-like anomalies, liquid-liquid transition, glass transition, and crystallization. *The European Physical Journal E*, 35(10):1–84, 2012. 1, 42, 43, 46

[30] Hajime Tanaka. Importance of many-body orientational correlations in the physical description of liquids. *Faraday Discussions*, 167(0):9–76, 2013. 1

[31] R Böhmer, C Gainaru, and R Richert. Structure and dynamics of monohydroxy alcohols-Milestones towards their microscopic understanding, 100 years after Debye. *Physics Reports-Review Section of Physics Letters*, 545(4):125–195, 2014. 1, 2, 15, 16, 118, 119, 121, 122, 124, 137

[32] Robert Hayes, Gregory G. Warr, and Rob Atkin. Structure and Nanostructure in Ionic Liquids. *Chemical Reviews*, 115(13):6357–6426, 2015. 1, 2, 36, 39, 40, 46, 47, 51, 52, 55, 61, 67, 68, 78, 82, 85, 97, 101

[33] Sachio Horiuchi, Reiji Kumai, and Yoshinori Tokura. A supramolecular ferroelectric realized by collective proton transfer. *Angewandte Chemie International Edition*, 46(19):3497–3501, 2007. 1, 2, 115, 125

[34] Jacob N. Israelachvili. *Intermolecular and surface forces*. Academic Press, 2011. 1

[35] Stephen H. Donaldson, Anja Røyne, Kai Kristiansen, Michael V. Rapp, Saurabh Das, Matthew A. Gebbie, Dong Woog Lee, Philipp Stock, Markus Valtiner, and Jacob

Israelachvili. Developing a General Interaction Potential for Hydrophobic and Hydrophilic Interactions. *Langmuir*, 31(7):2051–2064, feb 2015. 1

[36] Salvatore Torquato. *Random Heterogeneous Materials: Microstructure and Macroscopic Properties*. Springer-Verlag, New York, 2002. 1, 75

[37] Charles Tanford. *The Hydrophobic Effect: Formation of Micelles and Biological Membranes*. John Wiley & Sons, Inc., New York, 1980. 1, 92

[38] J. D. Bernal. The Bakerian Lecture, 1962. The Structure of Liquids. *Proceedings of the Royal Society A: Mathematical, Physical and Engineering Sciences*, 280(1382):299–322, jul 1964. 1

[39] David. Tabor. *Gases, liquids, and solids : and other states of matter*. Cambridge University Press, 1991. 1

[40] W Dannhauser, L W Bahe, R Y Lin, and A F Flueckinger. Dielectric Constant of Hydrogen Bonded Liquids. IV. Equilibrium and Relaxation Studies of Homologous Neo Alcohols. *The Journal of Chemical Physics*, 43(1):257–266, 1965. 2

[41] Lokendra P. Singh and Ranko Richert. Two-channel impedance spectroscopy for the simultaneous measurement of two samples. *Review of Scientific Instruments*, 83(3):033903, mar 2012. 2

[42] Simona Capponi, Simone Napolitano, and Michael Wübbenhorst. Supercooled liquids with enhanced orientational order. *Nature Communications*, 3:1233, 2012. 2

[43] C Austen Angell, Younes Ansari, and Zuofeng Zhao. Ionic Liquids: Past, present and future. *Faraday Discussions*, 154(0):9–27, 2012. 2, 38, 39, 43, 82, 96, 105

[44] Barbara Kirchner. *Ionic Liquids*. Topics in Current Chemistry. Springer-Verlag Berlin Heidelberg, 1 edition, 2009. 2, 45, 46, 51, 82

[45] Edward W Castner and James F Wishart. Spotlight on ionic liquids. *The Journal of Chemical Physics*, 132(12):120901, 2010. 2, 96

[46] M Petkovic, K R Seddon, L P Rebelo, and C Silva Pereira. Ionic liquids: a pathway to environmental acceptability. *Chemical Society Reviews*, 40(3):1383–1403, 2011. 2

[47] Masayoshi Watanabe, Morgan L Thomas, Shiguo Zhang, Kazuhide Ueno, Tomohiro Yasuda, and Kaoru Dokko. Application of Ionic Liquids to Energy Storage and Conversion Materials and Devices. *Chemical Reviews*, 117(10):7190–7239, 2017. 2

[48] Michel Armand, Frank Endres, Douglas R MacFarlane, Hiroyuki Ohno, and Bruno Scrosati. Ionic-liquid materials for the electrochemical challenges of the future. *Nature Materials*, 8:621, jul 2009. 2, 40, 61, 78

[49] Mohammed Harun Chakrabarti, Farouq Sabri Mjalli, Inas Muen AlNashef, Mohd Ali Hashim, Mohd Azlan Hussain, Laleh Bahadori, and Chee Tong John Low. Prospects of applying ionic liquids and deep eutectic solvents for renewable energy storage by means of redox flow batteries. *Renewable and Sustainable Energy Reviews*, 30:254–270, 2014. 2, 40, 61

[50] Rongying Lin, Pierre-Louis Taberna, Sébastien Fantini, Volker Presser, Carlos R Pérez, François Malbosc, Nalin L Rupesinghe, Kenneth B K Teo, Yury Gogotsi, and Patrice Simon. Capacitive Energy Storage from 50 to 100 C Using an Ionic Liquid Electrolyte. *The Journal of Physical Chemistry Letters*, 2(19):2396–2401, 2011. 2, 40

[51] Douglas R MacFarlane, Naoki Tachikawa, Maria Forsyth, Jennifer M Pringle, Patrick C Howlett, Gloria D Elliott, James H Davis, Masayoshi Watanabe, Patrice Simon, and C Austen Angell. Energy applications of ionic liquids. *Energy & Environmental Science*, 7(1):232–250, 2014. 2, 40, 61

[52] Natalia V. Plechkova and Kenneth R. Seddon. Applications of ionic liquids in the chemical industry. *Chem. Soc. Rev.*, 37(1):123–150, dec 2008. 2, 39

[53] José N Canongia Lopes, Telma C Cordeiro, José M. S. S. Esperança, Henrique J. R. Guedes, Susanne Huq, Luís P N Rebelo, and Kenneth R Seddon. Deviations from Ideality in Mixtures of Two Ionic Liquids Containing a Common Ion. *The Journal of Physical Chemistry B*, 109(8):3519–3525, 2005. 2, 36

[54] José N A Canongia Lopes and Agí lio A H Pádua. Nanostructural Organization in Ionic Liquids. *The Journal of Physical Chemistry B*, 110(7):3330–3335, 2006. 2, 36, 47, 51, 52, 55, 61, 62, 82

[55] A Triolo, O Russina, H J Bleif, and E Di Cola. Nanoscale Segregation in Room Temperature Ionic Liquids. *Journal of Physical Chemistry B*, 111(18):4641–4644, 2007. 2, 46, 51, 52, 55, 61, 62

[56] Olga Russina and Alessandro Triolo. New experimental evidence supporting the mesoscopic segregation model in room temperature ionic liquids. *Faraday Discussions*, 154(0):97–109, 2012. 2, 65

[57] Jason P Hallett and Tom Welton. Room-Temperature Ionic Liquids: Solvents for Synthesis and Catalysis. 2. *Chemical Reviews*, 111(5):3508–3576, 2011. 2, 39, 40, 45, 61, 78

[58] H Olivier-Bourbigou, L Magna, and D Morvan. Ionic liquids and catalysis: Recent progress from knowledge to applications. *Applied Catalysis A: General*, 373(1-2):1–56, 2010. 2, 40

[59] Rajni Ratti. Ionic Liquids: Synthesis and Applications in Catalysis. *Advances in Chemistry*, 2014:1–16, oct 2014. 2, 40, 96

[60] Przemysław Kubisa. Ionic liquids as solvents for polymerization processes Progress and challenges. *Progress in Polymer Science*, 34(12):1333 – 1347, 2009. 2, 39, 40

[61] Thomas Welton. Room-Temperature Ionic Liquids. Solvents for Synthesis and Catalysis. *Chemical Reviews*, 99(8):2071–2084, 1999. 2, 39, 40

[62] Robin D. Rogers and Kenneth R. Seddon. Ionic liquids - Solvents of the future? *Science*, 302(5646):792–793, 2003. 2, 39, 51, 82

[63] Peter Wasserscheid and Thomas Welton. *Ionic Liquids in Synthesis*. Wiley-VCH Verlag, Weinheim, 2008. 2

[64] K. D. Kreuer, A. Fuchs, M. Ise, M. Spaeth, and J. Maier. Imidazole and pyrazole-based proton conducting polymers and liquids. *Electrochimica Acta*, 43(10-11):1281–1288, 1998. 3, 116, 117, 123, 136, 152

[65] Klaus-Dieter Kreuer, Stephen J Paddison, Eckhard Spohr, and Michael Schuster. Transport in Proton Conductors for Fuel-Cell Applications: Simulations, Elementary Reactions, and Phenomenology. *Chemical Society Reviews*, 104:41, 2004. 3, 114, 115, 116, 117, 125, 132, 136, 137, 151, 152

[66] Tomohiro Yasuda and Masayoshi Watanabe. Protic ionic liquids: Fuel cell applications. *MRS Bulletin*, 38(7):560–566, 2013. 3, 117, 123, 125, 136

[67] Noam Agmon. The Grotthuss mechanism. *Chemical Physics Letters*, 244(5):456–462, 1995. 3, 114

[68] Yangyang Wang, Philip J Griffin, Adam Holt, Fei Fan, and Alexei P Sokolov. Observation of the slow, Debye-like relaxation in hydrogen-bonded liquids by dynamic light scattering. *The Journal of Chemical Physics*, 140(10):104510, 2014. 3, 118, 122, 124, 125, 127, 131, 140, 143, 149, 152

[69] Michael Faraday. I. Experimental researches in electricity. âĹŠâĹŠ eleventh series. *Philisophical Transactions of the Royal Society of London*, 128:1–40, 1838. 6, 7

[70] James Clerk-Maxwell. *The Electrical Researches of the Honourable Henry Cavendish*. Cambride University Press, Cambridge, 1879. 6

[71] Frank A. J. L. James, editor. *The Correspondence of Michael Faraday, Volume 2: 1832-1840*. Peter Peregrinus Ltd, 1991. 7

[72] Peter Debye. *Polar Molecules*. Lancaster Press, Inc., Lancaster, PA, 1929. 9, 12, 15

[73] Evaristo. Riande and Ricardo Díaz Calleja. *Electrical properties of polymers*. Marcel Dekker, Inc., New York, 2004. 13

[74] F Kremer, A Serghei, J R Sangoro, M Tress, and E U Mapesa. Broadband dielectric spectroscopy in nano-(bio)-physics. *Annual Report - Conference on Electrical Insulation and Dielectric Phenomena*, (Copyright (C) 2013 American Chemical Society (ACS). All Rights Reserved.):730–735, 2009. 14

[75] Herbert Fröhlich. *Theory of Dielectrics*. Clarendon, Oxford, 1958. 14, 118, 141

[76] M. Doi and S. F. Edwards. *The Theory of Polymer Dynamics*. Clarendon, Oxford, 1986. 15

[77] P Debye. Dielectric Properties of Pure Liquids. *Chemical Reviews*, 19(3):171–182, 1936. 15, 121

[78] Kenneth S. Cole and Robert H. Cole. Dispersion and Absorption in Dielectrics II. Direct Current Characteristics. *The Journal of Chemical Physics*, 10(2):98–105, feb 1942. 16

[79] D. W. Davidson and R. H. Cole. Dielectric Relaxation in Glycerine. *The Journal of Chemical Physics*, 18(10):1417–1417, oct 1950. 16, 24

[80] S. Havriliak and S. Negami. A complex plane analysis of α-dispersions in some polymer systems. *Journal of Polymer Science Part C: Polymer Symposia*, 14(1):99–117, mar 1966. 16, 71

[81] S Havriliak and S Negami. A Complex Plane Representation of Dielectric and Mechanical Relaxation Processes in Some Polymers. *Polymer*, 8:161–210, 1967. 16, 100

[82] C Hansen, F Stickel, T Berger, R Richert, and E W Fischer. Dynamics of glass-forming liquids. III. Comparing the dielectric a- and b-relaxation of 1-propanol and o-terphenyl. *The Journal of Chemical Physics*, 107:1086–1093, 1997. 16

[83] Th. Bauer, M. Michl, P. Lunkenheimer, and A. Loidl. Nonlinear dielectric response of Debye, α, and β relaxation in 1-propanol. *Journal of Non-Crystalline Solids*, 407:66–71, jan 2015. 16

[84] A Serghei, M Tress, J R Sangoro, and F Kremer. Electrode polarization and charge transport at solid interfaces. *Physical Review B*, 80(18):5, 2009. 18

[85] M L Jiménez, F J Arroyo, J van Turnhout, and A V Delgado. Analysis of the dielectric permittivity of suspensions by means of the logarithmic derivative of its real part. *Journal Colloid Interface Science*, 249(2):327–335, 2002. 19, 71, 131

[86] Michael Wübbenhorst and Jan van Turnhout. Analysis of complex dielectric spectra. I. One-dimensional derivative techniques and three-dimensional modelling. *Journal of Non-Crystalline Solids*, 305(1-3):40–49, jul 2002. 19, 71

[87] S V Nemilov. Relaxation processes in inorganic melts and glasses: An elastic continuum model as a promising basis for the description of the viscosity and electrical conductivity. *Glass Physics and Chemistry*, 36(3):253–285, 2010. 19, 23, 42, 97

[88] H M Wyss. Rheology of Soft Materials. In A Fernandez-Nieves Puertas and A Manuel, editors, *Fluids, Colloids and Soft Materials: An Introduction to Soft Matter Physics*. John Wiley & Sons, Inc., Hoboken, NJ, USA., 2016. 19, 21, 23, 53

[89] R. Byron Bird, Warren E. Stewart, and Edwin R. Lightfoot. *Transport Phenomena*. John Wiley & Sons, Inc., 2nd edition, 2002. 21

[90] H. A. Barnes, J. F. Hutton, and K. Walters. *An Introduction to Rheology*. Elsevier Science Publishers B.V., Amsterdam, 1st edition, 1989. 21

[91] K. Walters. *Rheometry*. Chapman and Hall, London, 1st edition, 1975. 21, 22

[92] John D. Ferry. *Viscoelastic Properties of Polymers*. John Wiley & Sons, Inc., New York, 3rd edition, 1980. 21, 22

[93] D. W. Davidson and R. H. Cole. Dielectric Relaxation in Glycerol, Propylene Glycol, and nPropanol. *The Journal of Chemical Physics*, 19(12):1484–1490, dec 1951. 24

[94] C. Gainaru, M. Wikarek, S. Pawlus, M. Paluch, R. Figuli, M. Wilhelm, T. Hecksher, B. Jakobsen, J. C. Dyre, and R. Böhmer. Oscillatory shear and high-pressure dielectric study of 5-methyl-3-heptanol. *Colloid and Polymer Science*, 292(8):1913–1921, 2014. 24, 53, 55, 68, 89, 137

[95] B. Wunderlich. Development towards a single-run DSC for heat capacity measurements. *Journal of Thermal Analysis*, 32(6):1949–1955, nov 1987. 25, 30

[96] Bernhard Wunderlich. *Thermal Analysis of Polymeric Materials*. Springer, New York, 2005. 25, 30

[97] E. S. Watson, M. J. O'Neill, Joshua. Justin, and Nathaniel. Brenner. A Differential Scanning Calorimeter for Quantitative Differential Thermal Analysis. *Analytical Chemistry*, 36(7):1233–1238, jun 1964. 25

[98] Paul C. Painter, Michael M. Coleman, and Jack L. Koenig. *The Theory of Vibrational Spectroscopy and Its Application to Polymeric Materials*. Wiley-Interscience, New York, 1982. 30, 31

[99] Peter R. Griffiths and James A. de Haseth. *Fourier Transform Infrared Spectroscopy*. John Wiley & Sons, Inc., Hoboken, NJ, second edition, 2007. 30, 31

[100] Brian C. Smith. *Fundamentals of Fourier Transform Infrared Spectroscopy*. CRC Press, Boca Raton, 2 edition, 2011. 30, 31

[101] L. J. Bellamy. *The Infrared Spectra of Complex Molecules*. Chapman and Hall Ltd, 3rd edition, 1975. 31, 33

[102] D M W Anderson, J L Duncan, and F J C Rossotti. The hydrogen bonding of imidazole in carbon tetrachloride solution. *Journal of the Chemical Society*, (0):2165–2171, 1961. 32, 114, 143, 145, 148

[103] Anne-Marie Bellocq and Chatal Garrigou-Lagrange. Spectres de vibration de quelques sels d'imidazolium et d'imidazolium (D2) 1,3. *Spectrochimica Acta Part A: Molecular Spectroscopy*, 27(7):1091–1104, 1971. 33, 145

[104] A. Hewish, editor. *Seeing Beyond the Visible*. American Elsevier Publishing Company, Inc., New York, 1970. 34

[105] Geoge L. Clark, editor. *Encyclopedia of X-Rays and Gamma Rays*. Reinhold Publishing Corporation, New York, 1963. 34

[106] Andre Guinier and Gérard Fournet. *Small-Angle Scattering of X-rays*. John Wiley & Sons, Inc., New York, 1955. 34, 35

[107] O. Glatter and O. Kratky. *Small-Angle X-ray Scattering*. Academic Press, New York, 1982. 35

[108] Thomas Murphy, Rob Atkin, and Gregory G Warr. Scattering from ionic liquids. *Current Opinion in Colloid & Interface Science*, 20(4):282–292, 2015. 36, 84

[109] Marcelle Gaune-Escard and Kenneth R. Seddon, editors. *Ionic Liquids and Molten Salts: Never the Twain?* John Wiley & Sons, Inc., 2010. 37, 38

[110] Frank H. Hurley and Thomas P. Wier. Electrodeposition of Metals from Fused Quaternary Ammonium Salts. *Journal of The Electrochemical Society*, 98(5):203, may 1951. 38

[111] John S. Wilkes. A short history of ionic liquids from molten salts to neoteric solvents. *Green Chemistry*, 4(2):73–80, apr 2002. 38, 39

[112] Natalia V. Plechkova and Kenneth R. Seddon. Applications of ionic liquids in the chemical industry. *Chemical Society Reviews*, 37(1):123–150, 2008. 38, 39, 40, 41, 62

[113] J. Robinson and R. A. Osteryoung. An electrochemical and spectroscopic study of some aromatic hydrocarbons in the room temperature molten salt system aluminum chloride-n-butylpyridinium chloride. *Journal of the American Chemical Society*, 101(2):323–327, jan 1979. 38

[114] J. Braunstein, G. Mamantov, and G. P. Smith, editors. *Advances in Molten Salt Chemistry*. Plenum Press, New York, 1971. 38

[115] C. A. Angell, I. M. Hodge, and P. A. Cheeseman. Physico-Chemical and Computer Simulation Studies of the Role of Cation Coordination Numbers on Melt Physical Properties. *ECS Proceedings Volumes*, 1976-6:138–154, jan 1976. 38, 42, 43

[116] John S. Wilkes, Joseph A. Levisky, Robert A. Wilson, and Charles L. Hussey. Dialkylimidazolium chloroaluminate melts: a new class of room-temperature ionic liquids for electrochemistry, spectroscopy and synthesis. *Inorganic Chemistry*, 21(3):1263–1264, mar 1982. 39

[117] Denise Appleby, Charles L. Hussey, Kenneth R. Seddon, and Janet E. Turp. Room-temperature ionic liquids as solvents for electronic absorption spectroscopy of halide complexes. *Nature*, 323:614–616, oct 1986. 39

[118] B. F. Hitch and Charles F. Baes. Electromotive force study of molten lithium fluoride-beryllium fluoride solutions. *Inorganic Chemistry*, 8(2):201–207, feb 1969. 39

[119] Emanuel I. Cooper and Eugene J. M. O'Sullivan. New, Stable, Ambient-Temperature Molten Salts. *ECS Proceedings Volumes*, 1992-16:386–396, jan 1992. 39

[120] John S Wilkes and Michael J Zaworotko. Air and Water Stable I-Ethyl-3-methylimidazolium Based Ionic Liquids. Technical report, 1992. 39

[121] Frank Endres and Sherif Zein El Abedin. Air and water stable ionic liquids in physical chemistry. *Physical Chemistry Chemical Physics*, 8:2101–2116, 2006. 40

[122] Markus Antonietti, Daibin Kuang, Bernd Smarsly, and Yong Zhou. Ionic Liquids for the Convenient Synthesis of Functional Nanoparticles and Other Inorganic Nanostructures. *Angewandte Chemie International Edition*, 43(38):4988–4992, 2004. 40, 61

[123] M. Smiglak, J. M. Pringle, X. Lu, L. Han, S. Zhang, H. Gao, D. R. MacFarlane, and R. D. Rogers. Ionic liquids for energy, materials, and medicine. *Chemical Communications*, 50(66):9228–9250, 2014. 40, 61

[124] Zhiqi He and Paschalis Alexandridis. Ionic liquid and nanoparticle hybrid systems: Emerging applications, 2017. 40

[125] Bruno Medronho, Anabela Romano, Maria Graça Miguel, Lars Stigsson, and Björn Lindman. Rationalizing cellulose (in)solubility: reviewing basic physicochemical aspects and role of hydrophobic interactions. *Cellulose*, 19(3):581–587, 2012. 40

[126] Simone S. Silva, João F. Mano, and Rui L. Reis. Ionic liquids in the processing and chemical modification of chitin and chitosan for biomedical applications. *Green Chemistry*, 19(5):1208–1220, mar 2017. 40

[127] Taeyoung Kim, Hyun Chang Kang, Tran Thanh Tung, Jung Don Lee, Hyeongkeun Kim, Woo Seok Yang, Ho Gyu Yoon, and Kwang S Suh. Ionic liquid-assisted microwave reduction of graphite oxide for supercapacitors. *RSC Advances*, 2:8808–8812, 2012. 40, 78

[128] Brooks D. Rabideau, Kevin N. West, and James H. Davis. Making good on a promise: ionic liquids with genuinely high degrees of thermal stability. *Chemical Communications*, 54(40):5019–5031, may 2018. 40

[129] Wei Shi and Dan C Sorescu. Molecular Simulations of CO2 and H2 Sorption into Ionic Liquid 1-n-Hexyl-3-methylimidazolium Bis(trifluoromethylsulfonyl)amide ([hmim][Tf2N]) Confined in Carbon Nanotubes. *The Journal of Physical Chemistry B*, 114(46):15029–15041, 2010. 40

[130] Jason E. Bara, Dean E. Camper, Douglas L Gin, and Richard D Noble. Room-Temperature Ionic Liquids and Composite Materials: Platform Technologies for CO2 Capture. *Accounts of Chemical Research*, 43(1):152–159, 2010. 40

[131] Ermanno F. Borra, Omar Seddiki, Roger Angel, Daniel Eisenstein, Paul Hickson, Kenneth R. Seddon, and Simon P. Worden. Deposition of metal films on an ionic liquid as a basis for a lunar telescope. *Nature*, 447(7147):979–981, jul 2007. 40

[132] Philip Griffin, Alexander L Agapov, Alexander Kisliuk, Xiao-Guang Sun, Sheng Dai, Vladimir N Novikov, and Alexei P Sokolov. Decoupling charge transport from the structural dynamics in room temperature ionic liquids. *The Journal of Chemical Physics*, 135:114509, 2011. 41

[133] Kevin R J Lovelock. Quantifying intermolecular interactions of ionic liquids using cohesive energy densities. *Royal Society Open Science*, 4(12), 2017. 41, 51, 57, 62, 83, 86

[134] Li-Min Wang, C. Austen Angell, and Ranko Richert. Fragility and thermodynamics in nonpolymeric glass-forming liquids. *Journal of Chemical Physics*, 125(7):74505, 2006. 41, 42, 105

[135] Wu Xu and C. Austen Angell. Solvent-free electrolytes with aqueous solution - Like conductivities. *Science*, 302(5644):422–425, 2003. 42

[136] Jeppe C Dyre. Colloquium: The glass transition and elastic models of glass-forming liquids. 2006. 42

[137] Mark D Ediger and Lian Yu. Polymer glasses: From gas to nanoglobular glass. *Nature Materials*, 11(4):267–268, 2012. 42

[138] Vassiliy Lubchenko and Peter G Wolynes. Theory of Structural Glasses and Supercooled Liquids. *Annual Review of Physical Chemistry*, 58(1):235–266, 2007. 42

[139] Walter Kauzmann. The Nature of the Glassy State and the Behavior of Liquids at Low Temperature. *Chemical Reviews*, 43(2):219–256, 1948. 42

[140] L Berthier, G Biroli, J P Bouchaud, L Cipelletti, D El Masri, D L'Hote, F Ladieu, and M Pierno. Direct Experimental Evidence of a Growing Length Scale Accompanying the Glass Transition. *Science*, 310(5755):1797–1800, 2005. 42

[141] Gregory B. McKenna. Diverging views on glass transition. *Nature Physics*, 4(9):673–673, sep 2008. 42

[142] Rob Zondervan, Ted Xia, Harmen Van Der Meer, Cornelis Storm, Florian Kulzer, Wim Van Saarloos, and Michel Orrit. Soft glassy rheology of supercooled molecular liquids. *Proceedings of the National Academy of Sciences*, 105(13):4993–4998, 2008. 42

[143] Tina Hecksher, Albena I. Nielsen, Niels Boye Olsen, and Jeppe C. Dyre. Little evidence for dynamic divergences in ultraviscous molecular liquids. *Nature Physics*, 4(9):737–741, 2008. 42

[144] J C Dyre, T Hechsher, and K Niss. A brief critique of the Adam-Gibbs entropy model. *Journal of Non-Crystalline Solids*, 355(10-12):624–627, 2009. 42

[145] Inyong Chang and Hans Sillescu. Heterogeneity at the Glass Transition:âĂĽ Translational and Rotational Self-Diffusion. *The Journal of Physical Chemistry B*, 101(43):8794–8801, 1997. 42

[146] V. Bocharova, Z. Wojnarowska, Peng-Fei Cao, Y. Fu, R. Kumar, Bingrui Li, V. N. Novikov, S. Zhao, A. Kisliuk, T. Saito, Jimmy W. Mays, B.G. Sumpter, and A. P. Sokolov. Influence of Chain Rigidity and Dielectric Constant on the Glass Transition Temperature in Polymerized Ionic Liquids. *The Journal of Physical Chemistry B*, 121(51):11511–11519, dec 2017. 43

[147] A Einstein. Über die von der molekularkinetischen Theorie der Wärme geforderte Bewegung von in ruhenden Flüssigkeiten suspendierten Teilchen. *Annalen der Physik*, 322(8):549–560, 1905. 43

[148] M von Smoluchowski. Zur kinetischen Theorie der Brownschen Molekularbewegung und der Suspensionen. *Annalen der Physik*, 326(14):756–780, 1906. 43

[149] J R Sangoro, A Serghei, S Naumov, P Galvosas, J Karger, C Wespe, F Bordusa, and F Kremer. Charge transport and mass transport in imidazolium-based ionic liquids. *Physical Review E*, 77(5 Pt 1):51202, 2008. 43

[150] J R Sangoro and F Kremer. Charge transport and glassy dynamics in ionic liquids. *Accounts of Chemical Research*, 45(4):525–532, 2012. 43, 44, 52, 53, 56, 69, 86, 87, 94, 97, 104, 131

[151] J R Sangoro, C Iacob, S Naumov, R Valiullin, H Rexhausen, J Hunger, R Buchner, V Strehmel, J Kärger, and F Kremer. Diffusion in ionic liquids: the interplay between molecular structure and dynamics. *Soft Matter*, 7(5):1678–1681, 2011. 43, 52, 56, 100

[152] J Sangoro, C Iacob, A Serghei, S Naumov, P Galvosas, J Kärger, C Wespe, F Bordusa, A Stoppa, J Hunger, R Buchner, and F Kremer. Electrical conductivity and translational diffusion in the 1-butyl-3-methylimidazolium tetrafluoroborate ionic liquid. *The Journal of Chemical Physics*, 128(21):214509, 2008. 43, 52

[153] Joshua Sangoro, Tyler Cosby, and Friedrich Kremer. Rotational and Translational Diffusion in Ionic Liquids, 2016. 43, 69

[154] Philip J. Griffin, Adam P. Holt, Yangyang Wang, Vladimir N. Novikov, Joshua R. Sangoro, Friedrich Kremer, and Alexei P. Sokolov. Interplay between hydrophobic aggregation and charge transport in the ionic liquid methyltrioctylammonium bis(trifluoromethylsulfonyl)imide. *Journal of Physical Chemistry B*, 118(3):783–790, 2014. 44, 45, 79, 94, 97, 98, 99

[155] Hiroyuki Tokuda, Seiji Tsuzuki, Md. Abu Bin Hasan Susan, Kikuko Hayamizu, and Masayoshi Watanabe. How ionic are room-temperature ionic liquids? An indicator of the physicochemical properties. *Journal of Physical Chemistry B*, 110(39):19593–19600, 2006. 44

[156] Alfred R. Cooper. The Haven Ratio in Terms of the Self-Diffusion of Charge. In George Simkovich and Vladimir S. Stubican, editors, *Transport in Nonstoichiometric Compounds*, pages 127–137. Plenum Press, New York, 1985. 44

[157] R. A. Robinson and R. H. Stokes. *Electrolyte Solutions*. Dover, 1st edition, 1965. 44

[158] K.L. Ngai. *Relaxation and Diffusion in Complex Systems*. Spring-Verlag, New York, 1 edition, 2011. 44

[159] W. B. Russel, D. A. Saville, and W. R. Schowalter. *Colloidal Dispersions*. Cambridge University Press, Cambridge, 1989. 44

[160] C. Gainaru, E. W. Stacy, V. Bocharova, M. Gobet, A. P. Holt, T. Saito, S. Greenbaum, and A. P. Sokolov. Mechanism of Conductivity Relaxation in Liquid and Polymeric Electrolytes: Direct Link between Conductivity and Diffusivity. *The Journal of Physical Chemistry B*, 120(42):11074–11083, oct 2016. 44

[161] S Pandey, S N Baker, and G A Baker. Fluorescent Probe Studies of Polarity and Solvation within Room Temperature Ionic Liquids: A Review. *Journal of Fluorescence*, 22(5):1313–1343, 2012. 45

[162] Hermann Weingartner. The static dielectric permittivity of ionic liquids. *Journal of Molecular Liquids*, 192:185–190, 2014. 45, 78

[163] H Weingärtner. Understanding ionic liquids at the molecular level: Facts, problems, and controversies. *Angewandte Chemie-International Edition*, 47(4):654–670, 2008. 45, 78

[164] M A Ab Rani, A Brant, L Crowhurst, A Dolan, M Lui, N H Hassan, J P Hallett, P A Hunt, H Niedermeyer, J M Perez-Arlandis, M Schrems, T Welton, and R Wilding. Understanding the polarity of ionic liquids. *Physical Chemistry Chemical Physics*, 13(37):16831–16840, 2011. 45

[165] G A Baker, A A Rachford, F N Castellano, and S N Baker. Ranking Solvent Interactions and Dielectric Constants with Pt(mesBIAN)(tda) : A Cautionary Tale for Polarity Determinations in Ionic Liquids. *Chemphyschem*, 14(5):1025–1030, 2013. 45

[166] Cinzia Chiappe, Marco Malvaldi, and Christian Silvio Pomelli. Ionic liquids: Solvation ability and polarity. *Pure and Applied Chemistry*, 81(4):767–776, 2009. 45

[167] Mark N Kobrak. The relationship between solvent polarity and molar volume in room-temperature ionic liquids. *Green Chemistry*, 10(1):80–86, 2008. 45

[168] Mian-Mian Huang, Yanping Jiang, Padmanabhan Sasisanker, Gordon W. Driver, and Hermann Weingärtner. Static Relative Dielectric Permittivities of Ionic Liquids at 25 degrees C. *Journal of Chemical and Engineering Data*, 56(4):1494–1499, 2011. 45, 78

[169] Sen Mou, Andrea Rubano, and Domenico Paparo. Complex Permittivity of Ionic Liquid Mixtures Investigated by Terahertz Time-Domain Spectroscopy. *The Journal of Physical Chemistry B*, 121(30):7351–7358, 2017. 45

[170] Chihiro Wakai, Alla Oleinikova, Magnus Ott, and Hermann Weingärtner. How polar are ionic liquids? Determination of the static dielectric constant of an imidazolium-based ionic liquid by microwave dielectric spectroscopy. *Journal of Physical Chemistry B*, 109(36):17028–17030, 2005. 45, 78

[171] P J Griffin, A P Holt, K Tsunashima, J R Sangoro, F Kremer, and A P Sokolov. Ion Transport and Structural Dynamics in Homologous Ammonium and Phosphonium-based Room Temperature Ionic Liquids. *Journal of Chemical Physics*, 142(8):84501, 2015. 45, 55, 79, 87, 100, 108

[172] D A Turton, J Hunger, A Stoppa, G Hefter, A Thoman, M Walther, R Buchner, and K Wynne. Dynamics of Imidazolium Ionic Liquids from a Combined Dielectric Relaxation and Optical Kerr Effect Study: Evidence for Mesoscopic Aggregation. *Journal of the American Chemical Society*, 131(31):11140–11146, 2009. 45, 51, 55

[173] Gary A Baker, Siddharth Pandey, Shubha Pandey, and Sheila N Baker. A new class of cationic surfactants inspired by N-alkyl-N-methyl pyrrolidinium ionic liquids. *Analyst*, 129(10):890–892, 2004. 46

[174] N A Smirnova and E A Safonova. Micellization in solutions of ionic liquids. *Colloid Journal*, 74(2):254–265, 2012. 46

[175] X Q Fan and K S Zhao. Aggregation behavior and electrical properties of amphiphilic pyrrole-tailed ionic liquids in water, from the viewpoint of dielectric relaxation spectroscopy. *Soft Matter*, 10(18):3259–3270, 2014. 46

[176] H.-W Cheng, H Weiss, P Stock, Y.-J Chen, C R Reinecke, J.-N Dienemann, M Mezger, and M Valtiner. Effect of Concentration on the Interfacial and Bulk Structure of Ionic Liquids in Aqueous Solution. *Langmuir*, 34:2637–2646, 2018. 46

[177] Promod Kumar and K.L. Mittal, editors. *Handbook of Microemulsion Science and Technology*. Marcel Drekker, Inc., New York, 1999. 46

[178] Charles M. Gordon, John D. Holbrey, Alan R. Kennedy, and Kenneth R. Seddon. Ionic liquid crystals: hexafluorophosphate salts. *Journal of Materials Chemistry*, 8(12):2627–2636, jan 1998. 46

[179] Philip J. Griffin, Yangyang Wang, Adam P. Holt, and Alexei P. Sokolov. Communication: Influence of nanophase segregation on ion transport in room temperature ionic liquids. *Journal of Chemical Physics*, 144(15):151104, 2016. 46, 62, 94, 101

[180] Lorenzo Gontrani, Olga Russina, Fabrizio Lo Celso, Ruggero Caminiti, Gary Annat, and Alessandro Triolo. Liquid Structure of Trihexyltetradecylphosphonium Chloride at Ambient Temperature: An X-ray Scattering and Simulation Study. *The Journal of Physical Chemistry B*, 113(27):9235–9240, 2009. 46, 81, 82

[181] Christopher Hardacre, John D Holbrey, Claire L Mullan, Tristan G. A. Youngs, and Daniel T Bowron. Small angle neutron scattering from 1-alkyl-3-methylimidazolium hexafluorophosphate ionic liquids (C(n)mim PF6 , n=4, 6, and 8). *Journal of Chemical Physics*, 133(7):74510, 2010. 46, 82, 85, 89

[182] B L Bhargava, R Devane, M L Klein, and S Balasubramanian. Nanoscale Organization in Room Temperature Ionic Liquids: A Coarse Grained Molecular Dynamics Simulation Study. *Soft Matter*, 3(11):1395–1400, 2007. 47, 51

[183] Harsha V R Annapureddy, Hemant K Kashyap, Pablo M De Biase, and Claudio J Margulis. What is the Origin of the Prepeak in the X-ray Scattering of Imidazolium-Based Room-Temperature Ionic Liquids. *Journal of Physical Chemistry B*, 114:16838, 2010. 47, 66, 82, 85

[184] Hongjun Liu and Stephen J Paddison. Direct calculation of the X-ray structure factor of ionic liquids. *Physical Chemistry Chemical Physics*, 18(16):11000–11007, 2016. 47

[185] Karina Shimizu, Margarida F Costa Gomes, Agílio A H Pádua, Luís P N Rebelo, and José N Canongia Lopes. Three Commentaries on the Nano-Segregated Structure of Ionic Liquids. *Journal of Molecular Structure: THEOCHEM*, 946(1-3):70–76, 2010. 47, 51, 52, 55, 62, 65, 82, 85

[186] Margarida F Costa Gomes, José N. Canongia Lopes, and Agílio A. H. Pádua. Thermodynamics and Micro Heterogeneity of Ionic Liquids. In Barbara Kirchner, editor, *Ionic Liquids*, pages 161–183. Springer Berlin Heidelberg, Berlin, Heidelberg, 2010. 47

[187] M D Fayer. Dynamics and Structure of Room Temperature Ionic Liquids. *Chemical Physics Letters*, 616:259–274, 2014. 47, 51, 82

[188] M (Ed) Paluch. *Dielectric Properties of Ionic Liquids (Advances in Dielectrics)*. Advances in Dielectrics. Springer Verlag, 2016. 51, 53, 82

[189] Karina Shimizu, Carlos E. S. Bernardes, and José N. Canongia Lopes. Structure and Aggregation in the 1-Alkyl-3-Methylimidazolium Bis(trifluoromethylsulfonyl)imide Ionic Liquid Homologous Series. *Journal of Physical Chemistry B*, 118(2):567–576, 2014. 51, 52, 62, 66, 67, 85

[190] Hemant K Kashyap, Cherry S Santos, Harsha V R Annapureddy, N Sanjeeva Murthy, Claudio J Margulis, and Jr. Castner Edward W. Temperature-Dependent Structure of Ionic Liquids: X-ray Scattering and Simulations. *Faraday Discussions*, 154:133–143, 2012. 51, 81, 90

[191] Karina Shimizu and José N. Canongia Lopes. Comparing the Structure of Different Ionic Liquid Series: Bistriflamide v. Hexafluorophosphate; Pure v. Equimolar Mixtures. *Fluid Phase Equilibria*, 418:181–191, 2016. 51, 82, 85

[192] Karina Shimizu, Mohammad Tariq, Adilson A. Freitas, Agílio A. H. Pádua, and José N. C. Lopes. Self-Organization in Ionic Liquids: From Bulk to Interfaces and Films. *Journal of the Brazilian Chemical Society*, 27(2):349–362, 2016. 51

[193] Thomas Sonnleitner, David A. Turton, Stefan Waselikowski, Johannes Hunger, Alexander Stoppa, Markus Walther, Klaas Wynne, and Richard Buchner. Dynamics of RTILs: A Comparative Dielectric and OKE Study. *Journal of Molecular Liquids*, 192:19–25, 2014. 51, 55

[194] C M Roland. *Viscoelastic Behavior of Rubbery Materials*. Oxford University Press, Oxford, 2011. 53

[195] R W Gray, G Harrison, and J Lamb. Dynamic Viscoelastic Behavior of Low-Molecular-Mass Polystyrene Melts. *Proceedings of the Royal Society of London Series a-Mathematical Physical and Engineering Sciences*, 356(1684):77–102, 1977. 53

[196] C Gainaru, R Figuli, T Hecksher, B Jakobsen, J C Dyre, M Wilhelm, and R Böhmer. Shear-Modulus Investigations of Monohydroxy Alcohols: Evidence for a Short-Chain-Polymer Rheological Response. *Physical Review Letters*, 112(9), 2014. 55, 68, 124, 137, 143

[197] T Hecksher. Communication: Linking the dielectric Debye process in mono-alcohols to density fluctuations. *Journal of Chemical Physics*, 144(16):4, 2016. 55, 68, 122, 137, 142

[198] Leandro Lanzi, Marcello Carla, and Cecilia M C Gambi. A New Insight on the Dynamics of Sodium Dodecyl Sulfate Aqueous Micellar Solutions by Dielectric Spectroscopy. *Journal of Colloid and Interface Science*, 330(1):156–162, 2009. 56, 59

[199] R Polacek and U Kaatze. Monomer Exchange Kinetics, Radial Diffusion, and Hydrocarbon Chain Isomerization of Sodium Dodecylsulfate Micelles in Water. *Journal of Physical Chemistry B*, 111(7):1625–1631, 2007. 59

[200] R. Buchner, C. Baar, P. Fernandez, S. Schrödle, and W. Kunz. Dielectric Spectroscopy of Micelle Hydration and Dynamics in Aqueous Ionic Surfactant Solutions. *Journal of Molecular Liquids*, 118(1-3):179–187, 2005. 59

[201] Gerhard Schwarz. Dielectric-Relaxation of Biopolymers in Solution. *Advances in Molecular Relaxation Processes*, 3:281–295, 1972. 59

[202] Toshiyuki Shikata and Shin-ichiro Imai. Dielectric Relaxation of Surfactant Micellar Solutions. *Langmuir*, 14(24):6804–6810, 1998. 59

[203] Zhiqi He and Paschalis Alexandridis. Nanoparticles in ionic liquids: interactions and organization. *Physical Chemistry Chemical Physics*, 17(28):18238–18261, 2015. 61

[204] Dannie J. G. P. van Osch, Laura J. B. M. Kollau, Adriaan van den Bruinhorst, Sari Asikainen, Marisa A. A. Rocha, and Maaike C. Kroon. Ionic liquids and deep eutectic solvents for lignocellulosic biomass fractionation. *Physical Chemistry Chemical Physics*, 19(4):2636–2665, 2017. 61

[205] Olga Russina, Fabrizio Lo Celso, Natalia Plechkova, Charl J Jafta, Giovanni Battista Appetecchi, and Alessandro Triolo. *Mesoscopic organization in ionic liquids*, volume 375. 2017. 61, 82, 83

[206] Quentin Berrod, Filippo Ferdeghini, Jean-Marc Zanotti, Patrick Judeinstein, Didier Lairez, Victoria García Sakai, Orsolya Czakkel, Peter Fouquet, and Doru Constantin. Ionic Liquids: evidence of the viscosity scale-dependence. *Scientific Reports*, 7(1):2241, 2017. 61

[207] Filippo Ferdeghini, Quentin Berrod, Jean-Marc Zanotti, Patrick Judeinstein, Victoria Garcia Sakai, Orsolya Czakkel, Peter Fouquet, and Doru Constantin. Nanostructuration of ionic liquids: impact on the cation mobility. A multi-scale study. *Nanoscale*, 9(5):1901–1908, 2017. 61

[208] Tatsiana Burankova, Giovanna Simeoni, Rolf Hempelmann, Juan F Mora Cardozo, and Jan P Embs. Dynamic Heterogeneity and Flexibility of the Alkyl Chain in Pyridinium-Based Ionic Liquids. *The Journal of Physical Chemistry B*, 121(1):240–249, 2016. 61

[209] Bachir Aoun, Miguel A González, Jacques Ollivier, Margarita Russina, Zunbeltz Izaola, David L Price, and Marie-Louise Saboungi. Translational and Reorientational Dynamics of an Imidazolium-Based Ionic Liquid. *The Journal of Physical Chemistry Letters*, 1(17):2503–2507, 2010. 61

[210] Yanting Wang and Gregory A. Voth. Tail Aggregation and Domain Diffusion in Ionic Liquids. *The Journal of Physical Chemistry B*, 110(37):18601–18608, 2006. 62

[211] Tyler Cosby, Zachariah Vicars, Yangyang Wang, and Joshua Sangoro. Dynamic-Mechanical and Dielectric Evidence of Long-Lived Mesoscale Organization in Ionic Liquids. *The Journal of Physical Chemistry Letters*, 8:3544–3548, jul 2017. 62, 67, 68, 71, 82, 83, 86, 93, 101

[212] Martin Brehm and Barbara Kirchner. TRAVIS - A Free Analyzer and Visualizer for Monte Carlo and Molecular Dynamics Trajectories. *Journal of Chemical Information and Modeling*, 51(8):2007–2023, aug 2011. 64, 65, 67

[213] Martin Brehm, Henry Weber, Martin Thomas, Oldamur Hollóczki, and Barbara Kirchner. Domain Analysis in Nanostructured Liquids: A Post-Molecular Dynamics Study at the Example of Ionic Liquids. *ChemPhysChem*, 16(15):3271–3277, oct 2015. 64, 65, 66, 67, 75

[214] Carlos E. S. Bernardes. AGGREGATES: Finding structures in simulation results of solutions. *Journal of Computational Chemistry*, 38(10):753–765, apr 2017. 64

[215] William Humphrey, Andrew Dalke, and Klaus Schulten. VMD: Visual molecular dynamics. *Journal of Molecular Graphics*, 14(1):33–38, feb 1996. 64

[216] P J Brown, A G Fox, E N Maslen, M A O'Keefe, and T M Willis. International Tables for Crystallography. *Prince, E., Ed. International Union of Crystallography: Dordrecht,The Netherlands*, C:554–595, 2004. 64

[217] E Lorch. Neutron Diffraction by Germania, Silica and Radiation-Damaged Silica Glasses. *J. Phys. C: Solid State Phys.*, 2(8):229–237, mar 1969. 64

[218] Carlos E. S. Bernardes, Karina Shimizu, Ana I. M. C. Lobo Ferreira, Luís M. N. B. F. Santos, and José N. Canongia Lopes. Structure and Aggregation in the 1,3-Dialkyl-imidazolium Bis(trifluoromethylsulfonyl)imide Ionic Liquid Family: 2. From Single to Double Long Alkyl Side Chains. *The Journal of Physical Chemistry B*, 118(24):6885–6895, jun 2014. 66, 67

[219] Karina Shimizu and José N. Canongia Lopes. Probing the structural features of the 1-alkyl-3-methylimidazolium hexafluorophosphate ionic liquid series using Molecular Dynamics simulations. *Journal of Molecular Liquids*, 210:257–263, oct 2015. 66, 67

[220] Karina Shimizu, Adilson A. Freitas, and José N. Canongia Lopes. Structural characterization of the [CnC1im][C4F9SO3] ionic liquid series: Alkyl versus perfluoroalkyl side chains. *Journal of Molecular Liquids*, 226:28–34, jan 2017. 66, 67

[221] Marina Macchiagodena, Lorenzo Gontrani, Fabio Ramondo, Alessandro Triolo, and Ruggero Caminiti. Liquid structure of 1-alkyl-3-methylimidazolium-hexafluorophosphates by wide angle x-ray and neutron scattering and molecular dynamics. *The Journal of Chemical Physics*, 134(11):114521, mar 2011. 66

[222] Tsuyoshi Yamaguchi, Makina Saito, Koji Yoshida, Toshio Yamaguchi, Yoshitaka Yoda, and Makoto Seto. Structural Relaxation and Viscoelasticity of a Higher Alcohol with Mesoscopic Structure. *The Journal of Physical Chemistry Letters*, 9(2):298–301, jan 2018. 68

[223] Tina Hecksher and Bo Jakobsen. Communication: Supramolecular structures in monohydroxy alcohols: Insights from shear-mechanical studies of a systematic series of octanol structural isomers. *Journal of Chemical Physics*, 141(10):101104, 2014. 68, 122, 137, 142

[224] S. Arrese-Igor, A. Alegría, and J. Colmenero. Multimodal character of shear viscosity response in hydrogen bonded liquids. *Physical Chemistry Chemical Physics*, 2018. 68

[225] Tyler Cosby, Zachariah Vicars, Emmanuel Urandu Mapesa, Katsuhiko Tsunashima, and Joshua Sangoro. Charge transport and dipolar relaxations in phosphonium-based ionic liquids. *The Journal of Chemical Physics*, 2017. 71

[226] Tyler Cosby, Zachariah Vicars, Maximilian Heres, Katsuhiko Tsunashima, and Joshua Sangoro. Dynamic and structural evidence of mesoscopic aggregation in phosphonium ionic liquids. *The Journal of Chemical Physics*, 148(19):193815, 2018. 71

[227] Tuck C Choy. *Effective Medium Theory*. Oxford University Press, New York, 1999. 75

[228] H Looyenga. Dielectric Constants of Heterogeneous Mixtures. *Physica*, 31(3):401–&, 1965. 75

[229] L K H van Beek. Dielectric Behavior of Heterogeneous Systems. In J B Birks, editor, *Progress in Dielectrics*, volume 7. Heywood Books, London, 1967. 75, 76, 77

[230] M H Boyle. The Electrical-Properties of Heterogeneous Mixtures Containing an Oriented Spheroidal Dispersed Phase. *Colloid and Polymer Science*, 263(1):51–57, 1985. 76, 77

[231] Makoto Mizoshiri, Takena Nagao, Yuri Mizoguchi, and Makoto Yao. Dielectric permittivity of room temperature ionic liquids: A relation to the polar and nonpolar domain structures. *The Journal of Chemical Physics*, 132(16):164510, 2010. 76

[232] Frederick I Mopsik. Dielectric Constant of N-Hexane as a Function of Temperature, Pressure, and Density. *Journal of Research of the National Bureau of Standards -A. Physics and Chemistry*, 71(4), 1967. 77

[233] Maxim V Fedorov and Alexei A Kornyshev. Ionic Liquids at Electrified Interfaces. *Chemical Reviews*, 114(5):2978–3036, 2014. 78

[234] Jeevapani J Hettige, Hemant K Kashyap, and Claudio J Margulis. Communication: Anomalous temperature dependence of the intermediate range order in phosphonium ionic liquids. *The Journal of Chemical Physics*, 140(11):111102, 2014. 81, 90

[235] Yong Lei Wang, Bin Li, Sten Sarman, and Aatto Laaksonen. Microstructures and dynamics of tetraalkylphosphonium chloride ionic liquids. *The Journal of Chemical Physics*, 147(22):224502, 2017. 81, 92

[236] Joshua R. Sangoro. Charge transport and dipolar relaxations in an alkali metal oligoether carboxylate ionic liquid. *Colloid and Polymer Science*, 292(8):1933–1938, aug 2014. 82

[237] H K Kashyap, C S Santos, R P Daly, J J Hettige, N S Murthy, H Shirota, E W Castner, and C J Margulis. Structure of 1-Alkyl-1-methylpyrrolidinium Bis(trifluoromethylsulfonyl)amide Ionic Liquids with Linear, Branched, and Cyclic Alkyl Groups. *The Journal of Physical Chemistry B*, 117:1130, 2013. 82, 97

[238] Kenta Fujii, Ryo Kanzaki, Toshiyuki Takamuku, Yasuo Kameda, Shinji Kohara, Mitsuhiro Kanakubo, Mitsuhiro Shibayama, Shin-ichi Ishiguro, and Yasuhiro Umebayashi. Experimental evidences for molecular origin of low-Q peak in neutron/x-ray scattering of 1-alkyl-3-methylimidazolium bis(trifluoromethanesulfonyl)amide ionic liquids. *The Journal of Chemical Physics*, 135(24):244502, 2011. 82

[239] General discussion. *Faraday Discussions*, 154(0):189–220, 2012. 92

[240] J Sun, M Forsyth, and D R MacFarlane. Room-Temperature Molten Salts Based on the Quaternary Ammonium Ion. *The Journal of Physical Chemistry B*, 102(44):8858–8864, 1998. 94

[241] D R McFarlane, J Sun, J Golding, P Meakin, and M Forsyth. High conductivity molten salts based on the imide ion. *Electrochimica Acta*, 45(8):1271–1278, 2000. 94

[242] Christine J Bradaric, Andrew Downard, Christine Kennedy, Allan J Robertson, and Yuehui Zhou. Industrial preparation of phosphonium ionic liquids âĂă. *Green Chemistry*, 5(143):143–152, 2003. 97

[243] William A. Henderson and Carol J. Schultz. The Nucleophilicity of Amines. *The Journal of Organic Chemistry*, 27(12):4643–4646, dec 1962. 97

[244] Chainika Jangu and Timothy E Long. Phosphonium cation-containing polymers: From ionic liquids to polyelectrolytes. *Polymer*, 55:3298–3304, 2014. 97

[245] Nazira Karodia, Steven Guise, Craig Newlands, and Jo-Ann Andersen. Clean catalysis with ionic solvents-phosphonium tosylates for hydroformylation. *Chemical Communications*, 0(21):2341–2342, 1998. 97

[246] P J Carvalho, S P M Ventura, M L S Batista, B Schröder, F Gonçalves, J Esperança, F Mutelet, and J A P Coutinho. Understanding the impact of the central atom on the ionic liquid behavior: Phosphonium vs ammonium cations. *Journal of Chemical Physics*, 140(6):12, 2014. 97, 105

[247] M H Ghatee and M Bahrami. Emergence of innovative properties by replacement of nitrogen atom with phosphorus atom in quaternary ammonium ionic liquids: Insights from ab initio calculations and MD simulations. *Chemical Physics*, 490:92–105, 2017. 97

[248] Rebecca K Blundell and Peter Licence. Quaternary ammonium and phosphonium based ionic liquids: a comparison of common anions. *Physical Chemistry Chemical Physics*, 16(29):15278–15288, 2014. 97, 105

[249] M D Green, C Schreiner, and T E Long. Thermal, Rheological, and Ion-Transport Properties of Phosphonium-Based Ionic Liquids. *Journal of Physical Chemistry A*, 115(47):13829–13835, 2011. 97

[250] Kevin J. Fraser and Douglas R. MacFarlane. Phosphonium-Based Ionic Liquids: An Overview. *Australian Journal of Chemistry*, 62(4):309–321, 2009. 97

[251] Hideaki Shirota, Hiroki Fukazawa, Tomotsumi Fujisawa, and James F Wishart. Heavy Atom Substitution Effects in Non-Aromatic Ionic Liquids: Ultrafast Dynamics and Physical Properties. *The Journal of Physical Chemistry B*, 114(29):9400–9412, 2010. 97

[252] J C Dyre. Colloquium: The glass transition and elastic models of glass-forming liquids. *Reviews of Modern Physics*, 78(3):953–972, 2006. 97

[253] Walter Kauzmann. The Nature of the Glassy State and the Behavior of Liquids at Low Temperatures. *Chemical Reviews*, 43(2):219–256, 1948. 97

[254] E Donth. *The Glass Transition*. Springer Series in Materials Science. Springer-Verlag, Berline Heidelberg, 1 edition, 2001. 97

[255] Katsuhiko Tsunashima and Masashi Sugiya. Physical and Electrochemical Properties of Room Temperature Ionic Liquids Based on Quaternary Phosphonium Cations. *Electrochemistry*, 75:734–736, 2007. 98

[256] C Krause, J R Sangoro, C Iacob, and F Kremer. Charge Transport and Dipolar Relaxations in Imidazolium-Based Ionic Liquids. *Journal of Physical Chemistry B*, 114(1):382–386, 2010. 98, 100, 101

[257] Alberto Rivera and Ernst A Rössler. Evidence of secondary relaxations in the dielectric spectra of ionic liquids. *Physical Review B*, 73(21):212201, 2006. 98, 108

[258] Kenneth R Harris. Can the Transport Properties of Molten Salts and Ionic Liquids Be Used To Determine Ion Association? *The Journal of Physical Chemistry B*, 120(47):12135–12147, 2016. 101

[259] Hemant K Kashyap, Harsha V R Annapureddy, Fernando O Raineri, and Claudio J Margulis. How Is Charge Transport Different in Ionic Liquids and Electrolyte Solutions? *The Journal of Physical Chemistry B*, 115(45):13212–13221, 2011. 101

[260] Thomas B Schrøder and Jeppe C Dyre. Computer simulations of the random barrier model. *Physical Chemistry Chemical Physics*, 4(14):3173–3178, 2002. 101

[261] S Murugavel and B Roling. ac Conductivity Spectra of Alkali Tellurite Glasses: Composition-Dependent Deviations from the Summerfield Scaling. *Physical Review Letters*, 89(19):195902, 2002. 103

[262] D Zielniok, H Eckert, and C Cramer. Direct Correlation between Nonrandom Ion Hopping and Network Structure in Ion-Conducting Borophosphate Glasses. *Physical Review Letters*, 100(3):35901, 2008. 103

[263] J Ross Macdonald. Universality, the Barton Nakajima relation, ad scaling for dispersive ionic materials. *Physical Review B*, 71(18):184307, 2005. 103

[264] P Pal and A Ghosh. Dynamics and relaxation of charge carriers in poly(methylmethacrylate)-lithium salt based polymer electrolytes plasticized with ethylene carbonate. *Citation: Journal of Applied Physics*, 120:045108, 2016. 103, 107

[265] Jeppe C Dyre and Thomas B Schrøder. Universality of ac conduction in disordered solids. *Reviews of Modern Physics*, 72(3):873–892, 2000. 103, 129

[266] Wu Xu, Emanuel I. Cooper, and C. Austen Angell. Ionic liquids: Ion mobilities, glass temperatures, and fragilities. *Journal of Physical Chemistry B*, 107(25):6170–6178, 2003. 105

[267] Heinrich Debus. Ueber die Einwirkung des Ammoniaks auf Glyoxal. *Annalen der Chemie und Pharmacie*, 107(2):199–208, 1858. 112

[268] A. Hantzsch. Allgemeine Bemerkungen über Azole. *Annalen der Chemie*, 249:1–6, 1888. 112

[269] A. Hantzsch and J. H. Weber. Ueber Verbindungen des Thiazoles (Pyridins der Thiophenreihe. *Berichte der deutschen chemischen Gesellschaft*, 20:3118–3132, 1887. 112

[270] Gastone Gilli and Paola Gilli. *The Nature of the Hydrogen Bond*. Oxford University Press, New York, 2009. 113, 152

[271] L Zhang, X M Peng, G L V Damu, R X Geng, and C H Zhou. Comprehensive Review in Current Developments of Imidazole-Based Medicinal Chemistry. *Medicinal Research Reviews*, 34(2):340–437, 2014. 113, 125

[272] Klaus Ebel, Hermann Koehler, Armin O Gamer, and Rudolf Jäckh. Imidazole and Derivatives. In *Ullmann's Encyclopedia of Industrial Chemistry*. American Cancer Society, 2000. 113

[273] E. A. Barnard and W. D. Stein. The Roles of Imidazole in Biological Systems. In F. F. Nord, editor, *Advances in Enzymology and Related Areas of Molecular Biology*. Interscience Publishers, Inc., New York, 1958. 113

[274] C G Overberger and Vorchhei.N. Imidazole-containing Polymers. Synthesis and Polymerization of the Monomer 4(5)- Vinylimidazole. *Journal of the American Chemical Society*, 85(7):951–955, 1963. 113, 116

[275] R J Sundberg and R B Martin. Interactions of histidine and other imidazole derivatives with transition-metal ions in chemical and biological-systems. *Chem. Rev.*, 74(4):471–517, 1974. 113, 125

[276] Georg Zundel. Proton Polarizability of Hydrogen Bonds: Infrared Methods, Relevance to Electrochemical and Biological Systems. *Methods in Enzymology*, 127:439–455, 1986. 113

[277] Cassandra D M Churchill and Stacey D Wetmore. Noncovalent Interactions Involving Histidine: The Effect of Charge on pi-pi Stacking and T-Shaped Interactions with the DNA Nucleobases. *Journal of Physical Chemistry B*, 113(49):16046–16058, 2009. 113

[278] Jacob D. Graham, Allyson M. Buytendyk, Di Wang, Kit H. Bowen, and Kim D. Collins. Strong, Low-Barrier Hydrogen Bonds May Be Available to Enzymes. *Biochemistry*, 53(2):344–349, 2014. 113

[279] S Horiuchi. Organic Ferroelectrics. *Nature Materials*, 7:10, 2008. 114

[280] Alok S Tayi, Adrien Kaeser, Michio Matsumoto, Takuzo Aida, and Samuel I Stupp. Supramolecular ferroelectrics. *Nature Chemistry*, 7(4):281–294, 2015. 114

[281] Andrzej Katrusiak. Stereochemistry and transformations of NH—N hydrogen bonds - Part I. Structural preferences for the hydrogen site. *Journal of Molecular Structure*, 474:125–133, 1999. 114, 115

[282] Vladimir I Minkin, Osip A Osipov, and Yurii A Zhdanov. *Dipole Moments in Organic Chemistry*. Plenum Press, New York, 1970. 114, 117

[283] S Horiuchi, F Kagawa, K Hatahara, K Kobayashi, R Kumai, Y Murakami, and Y Tokura. Above-room-temperature ferroelectricity and antiferroelectricity in benzimidazoles. *Nat Commun*, 3:1308, 2012. 115

[284] Sachio Horiuchi, Kensuke Kobayashi, Reiji Kumai, and Shoji Ishibashi. Proton tautomerism for strong polarization switching. *Nature Communications*, 8, 2017. 115

[285] S Horiuchi, R Kumai, and Y Tokura. Hydrogen-bonding molecular chains for high-temperature ferroelectricity. *Advanced Materials*, 23(18):2098–2103, 2011. 115, 125

[286] Yuki Noda, Toshikazu Yamada, Kensuke Kobayashi, Reiji Kumai, Sachio Horiuchi, Fumitaka Kagawa, and Tatsuo Hasegawa. Few-Volt Operation of Printed Organic Ferroelectric Capacitor. *Advanced Materials*, 27(41):6475–6481, nov 2015. 115

[287] Alexander Kraytsberg and Yair Ein-Eli. Review of Advanced Materials for Proton Exchange Membrane Fuel Cells. *Energy Fuels*, 28(12):7303–7330, 2014. 115, 116

[288] H Steininger, M Schuster, K D Kreuer, A Kaltbeitzel, B Bingol, W H Meyer, S Schauff, G Brunklaus, J Maier, and H W Spiess. Intermediate temperature proton conductors for PEM fuel cells based on phosphonic acid as protogenic group: A progress report. *Physical Chemistry Chemical Physics*, 9(15):1764–1773, 2007. 116, 136, 137, 151

[289] Zhen Zhou, Rui Liu, Jenghan Wang, Siwen Li, Meilin Liu, and Jean-Luc Brédas. Intra- and Intermolecular Proton Transfer in 1H(2H)-1,2,3-Triazole Based Systems. 2006. 116

[290] A Bozkurt, W H Meyer, J Gutmann, and G Wegner. Proton conducting copolymers on the basis of vinylphosphonic acid and 4-vinylimidazole. *Solid State Ionics*, 164(3-4):169–176, 2003. 116

[291] A Bozkurt and B Karadedeli. Copolymers of 4(5)-vinylimidazole and ethyleneglycol methacrylate phosphate: Synthesis and proton conductivity properties. *Reactive & Functional Polymers*, 67(4):348–354, 2007. 116

[292] G F Mangiatordi, V Butera, N Russo, D Laage, and C Adamo. Charge transport in poly-imidazole membranes: a fresh appraisal of the Grotthuss mechanism. *Physical Chemistry Chemical Physics*, 14(31):10910–10918, 2012. 116, 117, 125

[293] M D Green, M H Allen, J M Dennis, D la Cruz, R L Gao, K I Winey, and T E Long. Tailoring macromolecular architecture with imidazole functionality: A perspective for controlled polymerization processes. *European Polymer Journal*, 47(4):486–496, 2011. 116

[294] R Skouta, S J Wei, and R Breslow. High Rates and Substrate Selectivities in Water by Polyvinylimidazoles as Transaminase Enzyme Mimics with Hydrophobically Bound Pyridoxamine Derivatives as Coenzyme Mimics. *Journal of the American Chemical Society*, 131(43):15604–+, 2009. 116

[295] A Sezgin, U Akbey, R Graf, A Bozkurt, and A Baykal. Proton Conductivity Survey of the Acid Doped Copolymers Based on 4-Vinylbenzylboronic Acid and 4(5)-Vinylimidazole. *Journal of Polymer Science Part B-Polymer Physics*, 47(13):1267–1274, 2009. 116

[296] Manita Jithunsa, Kohji Tashiro, Suzana Pereira Nunes, and Suwabun Chirachanchai. Preparation of 4(5)-vinylimidazole-co-acrylic acid copolymer and thermal performances related to applicability as PEM fuel cells. *Polymer Degradation and Stability*, 93(7):1389–1395, 2008. 116

[297] Chikkannagari Nagamani, Usha Viswanathan, Craig Versek, Mark T Tuominen, Scott M Auerbach, and S Thayumanavan. Importance of dynamic hydrogen bonds and reorientation barriers in proton transport. *Chemical Communications*, 47(23):6638–6640, 2011. 116

[298] Y B Chen, M Thorn, S Christensen, C Versek, A Poe, R C Hayward, M T Tuominen, and S Thayumanavan. Enhancement of anhydrous proton transport by supramolecular nanochannels in comb polymers. *Nature Chemistry*, 2(6):503–508, 2010. 116, 136

[299] Patric Jannasch. Recent developments in high-temperature proton conducting polymer electrolyte membranes. *Current Opinion in Colloid & Interface Science*, 8(1):96–102, 2003. 116

[300] Usha Viswanathan, Dipankar Basak, Dhandapani Venkataraman, Justin T. Fermann, and Scott M. Auerbach. Modeling Energy Landscapes of Proton Motion in Nonaqueous, Tethered Proton Wires. *Journal of Physical Chemistry A*, 115(21):5423–5434, 2011. 116, 117

[301] Qinfang F. Sun, Jacob A. Harvey, Katherine V. Greco, and Scott M. Auerbach. Molecular Simulations of Hydrogen Bond Cluster Size and Reorientation Dynamics in Liquid and Glassy Azole Systems. *Journal of Physical Chemistry B*, 120(39):10411–10419, 2016. 116

[302] Hanning Chen, Tianying Yan, and Gregory A Voth. A computer simulation model for proton transport in liquid imidazole. *The Journal of Physical Chemistry A*, 113(16):4507–4517, 2009. 116, 117, 125, 152

[303] Akihiro Noda, Md. Abu Bin Hasan Susan, Kenji Kudo, Shigenori Mitsushima, Kikuko Hayamizu, and Masayoshi Watanabe. Brønsted Acid-Base Ionic Liquids as Proton-Conducting Nonaqueous Electrolytes. *The Journal of Physical Chemistry B*, 107(17), 2003. 116, 117, 123, 125

[304] S Bureekaew, S Horike, M Higuchi, M Mizuno, T Kawamura, D Tanaka, N Yanai, and S Kitagawa. One-dimensional imidazole aggregate in aluminium porous coordination polymers with high proton conductivity. *Nature Materials*, 8(10):831–836, 2009. 116, 125

[305] Emanuel Eisbein, Jan-Ole Joswig, and Gotthard Seifert. Proton Conduction in a MIL-53(Al) Metal–Organic Framework: Confinement versus Host/Guest Interaction. *The Journal of Physical Chemistry C*, 118(24):13035–13041, 2014. 116, 125

[306] Emanuel Eisbein, Jan-Ole Joswig, and Gotthard Seifert. Enhanced proton-transfer activity in imidazole@MIL-53(Al) systems revealed by molecular-dynamics simulations. *Microporous and Mesoporous Materials*, 216:36–41, 2015. 116

[307] C J T De Grotthuss. Memoir on the decomposition of water and of the bodies that it holds in solution by means of galvanic electricity. *Annales de Chimie*, 58:54–74, 1806. 116

[308] W Munch, K D Kreuer, W Silvestri, J Maier, and G Seifert. The diffusion mechanism of an excess proton in imidazole molecule chains: first results of an ab initio molecular dynamics study. *Solid State Ionics*, 145(1-4):437–443, 2001. 117, 125, 132, 136, 137, 152

[309] Milan Kumar and Arun Venkatnathan. Quantum chemistry study of proton transport in imidazole chains. *Journal of Physical Chemistry B*, 119(7):3213–3222, 2015. 117, 125

[310] A L Li, Z Cao, Y Li, T Y Yan, and P W Shen. Structure and Dynamics of Proton Transfer in Liquid Imidazole. A Molecular Dynamics Simulation. *Journal of Physical Chemistry B*, 116(42):12793–12800, 2012. 117, 152

[311] S Scheiner and M Y Yi. Proton transfer properties of imidazole. *Journal of Physical Chemistry*, 100(22):9235–9241, 1996. 117, 136

[312] Worapong Bua-ngern, Sermsiri Chaiwongwattana, Parichart Suwannakham, and Kritsana Sagarik. Dynamics of proton transfer in imidazole hydrogen-bond chains. *RSC Advances*, 6(101):99391–99403, 2016. 117, 136, 151

[313] Jittima Thisuwan and Kritsana Sagarik. Proton dissociation and transfer in a phosphoric acid doped imidazole system. *RSC Advances*, 4(106):61992–62008, 2014. 117, 137, 151

[314] John T Edward. Molecular Volumes and the Stokes-Einstein Equation. *Journal of Chemical Education*, 47(4):261–270, 1970. 121

[315] Pierre Girard and Paul Abadie. Experimental Curves of Losses and of Anomalous Dispersion as a Basis of a Spectral Method. *Transactions of the Faraday Society*, 42:A040–A047, 1946. 121

[316] M Monkenbusch, M Krutyeva, W Pyckhout-Hintzen, W Antonius, C H Hövelmann, J Allgaier, A Brás, B Farago, A Wischnewski, and D Richter. Molecular View on Supramolecular Chain and Association Dynamics. *Physical Review Letters*, 117(14):147802, 2016. 121, 143

[317] M E Cates. Reptation of living polymers: dynamics of entangled polymers in the presence of reversible chain-scission reactions. *Macromolecules*, 20(9):2289–2296, 1987. 121

[318] C Gainaru, R Meier, S Schildmann, C Lederle, W Hiller, E A Rössler, and R Böhmer. Nuclear-Magnetic-Resonance Measurements Reveal the Origin of the Debye Process in Monohydroxy Alcohols. *Physical Review Letters*, 105(25):4, 2010. 121, 124, 141, 143, 152

[319] L P Singh and R Richert. Watching Hydrogen-Bonded Structures in an Alcohol Convert from Rings to Chains. *Physical Review Letters*, 109(16):5, 2012. 122, 124, 137, 141, 142

[320] M. A. Floriano and C. A. Angell. On the relaxation between Debye and nonexponential relaxation in supercooled monohydric alcohols and water: A solution study. *The Journal of Chemical Physics*, 91(4):2537–2543, aug 1989. 124, 137

[321] J T Daycock, G P Jones, J R N Evans, and J M Thomas. Rotation of imidazole in solid state and its significance in deciding nature of charge migration in biological materials. *Nature*, 218(5142):672–673, 1968. 124, 125, 136, 152

[322] M Preuß, C Gainaru, T Hecksher, S Bauer, J C Dyre, R Richert, and R Böhmer. Experimental studies of Debye-like process and structural relaxation in mixtures of 2-ethyl-1-hexanol and 2-ethyl-1-hexyl bromide. *Journal of Chemical Physics*, 137(14):144502, 2012. 124

[323] N Lou, Y Y Wang, X P Li, H X Li, P Wang, C Wesdemiotis, A P Sokolov, and H M Xiong. Dielectric Relaxation and Rheological Behavior of Supramolecular Polymeric Liquid. *Macromolecules*, 46(8):3160–3166, 2013. 124

[324] Douglas E. Friesen, Travis J.A. Craddock, Aarat P. Kalra, and Jack A. Tuszynski. Biological wires, communication systems, and implications for disease. *Biosystems*, 127:14–27, 2015. 125

[325] Jingtao Wang, Xiujun Yue, Zizhuo Zhang, Zheng Yang, Yifan Li, Han Zhang, Xinlin Yang, Hong Wu, and Zhongyi Jiang. Enhancement of Proton Conduction at Low Humidity by Incorporating Imidazole Microcapsules into Polymer Electrolyte Membranes. *Advanced Functional Materials*, 22(21):4539–4546, 2012. 125

[326] L Vilciauskas, M E Tuckerman, J P Melchior, G Bester, and K D Kreuer. First principles molecular dynamics study of proton dynamics and transport in phosphoric acid/imidazole (2:1) system. *Solid State Ionics*, 252:34–39, 2013. 125

[327] Zaneta Wojnarowska, Krzysztof J. Paluch, Evgeni Shoifet, Christoph Schick, Lidia Tajber, Justyna Knapik, Patryk Wlodarczyk, Katarzyna Grzybowska, Stella Hensel-Bielowka, Sergey P. Verevkin, and Marian Paluch. Molecular origin of enhanced proton conductivity in anhydrous ionic systems. *Journal of the American Chemical Society*, 137(3):1157–1164, 2015. 125

[328] A Kawada, A R McGhie, and M M Labes. Protonic Conductivity in Imidazole Single Crystal. *The Journal of Chemical Physics*, 52(6):3121–3125, 1970. 125

[329] I V Stiopkin, C Weeraman, P A Pieniazek, F Y Shalhout, J L Skinner, and A V Benderskii. Hydrogen bonding at the water surface revealed by isotopic dilution spectroscopy. *Nature*, 474(7350):192–195, 2011. 128

[330] S K Tang, G A Baker, and H Zhao. Ether- and alcohol-functionalized task-specific ionic liquids: attractive properties and applications. *Chemical Society Reviews*, 41(10):4030–4066, 2012. 128

[331] Z B Zhou, H Matsumoto, and K Tatsumi. Low-melting, low-viscous, hydrophobic ionic liquids: Aliphatic quaternary ammonium salts with perfluoroalkyltrifluoroborates. *Chemistry-A European Journal*, 11(2):752–766, 2005. 128

[332] Philip J Griffin, Tyler Cosby, Adam P Holt, Roberto S Benson, and Joshua R Sangoro. Charge Transport and Structural Dynamics in Carboxylic-Acid-Based Deep Eutectic Mixtures. *The Journal of Physical Chemistry B*, jul 2014. 131, 133

[333] George A Jeffrey. *An Introduction to Hydrogen Bonding*. Topics in Physical Chemistry. Oxford University Press, New York Oxford, 1997. 133, 152

[334] I Fischbach, H W Spiess, K Saalwachter, and G R Goward. Solid state NMR spectroscopic investigations of model compounds for imidazole-based proton conductors. *Journal of Physical Chemistry B*, 108(48):18500–18508, 2004. 136

[335] Li-Min Wang and Ranko Richert. Debye type dielectric relaxation and the glass transition of alcohols. *Journal of Physical Chemistry B*, 109(22):11091–11094, 2005. 137

[336] Jesper S Hansen, Alexander Kisliuk, Alexei P Sokolov, and Catalin Gainaru. Identification of Structural Relaxation in the Dielectric Response of Water. *Physical Review Letters*, 116(23):5, 2016. 137, 141

[337] D. Fragiadakis, C. M. Roland, and R. Casalini. Insights on the origin of the Debye process in monoalcohols from dielectric spectroscopy under extreme pressure conditions. *Journal of Chemical Physics*, 132(14):9, 2010. 137

[338] K Adrjanowicz, B Jakobsen, T Hecksher, K Kaminski, M Dulski, M Paluch, and K Niss. Communication: Slow supramolecular mode in amine and thiol derivatives of 2-ethyl-1-hexanol revealed by combined dielectric and shear-mechanical studies. *The Journal of Chemical Physics*, 143(18):6, 2015. 137

[339] B Jakobsen, C Maggi, T Christensen, and J C Dyre. Investigation of the shear-mechanical and dielectric relaxation processes in two monoalcohols close to the glass transition. *Journal of Chemical Physics*, 129(18):7, 2008. 137

[340] S Bauer, K Moch, P Munzner, S Schildmann, C Gainaru, and R Böhmer. Mixed Debye-type liquids studied by dielectric, shear mechanical, nuclear magnetic resonance, and near-infrared spectroscopy. *Journal of Non-Crystalline Solids*, 407:384–391, 2015. 137, 145

[341] T Cosby, A Holt, P J Griffin, Y Y Wang, and J Sangoro. Proton Transport in Imidazoles: Unraveling the Role of Supramolecular Structure. *Journal of Physical Chemistry Letters*, 6(19):3961–3965, 2015. 140, 143, 149, 151

[342] Lokendra P Singh, Ahmed Raihane, Christiane Alba-Simionesco, and Ranko Richert. Dopant effects on 2-ethyl-1-hexanol: A dual-channel impedance spectroscopy and neutron scattering study. *Journal of Chemical Physics*, 142(1):8, 2015. 142

[343] Lokendra P. Singh, Christiane Alba-Simionesco, and Ranko Richert. Dynamics of glass-forming liquids. XVII. Dielectric relaxation and intermolecular association in a series of isomeric octyl alcohols. *Journal of Chemical Physics*, 139(14):13, 2013. 142

[344] S Arrese-Igor, A Alegría, and J Colmenero. Dielectric relaxation of 2-ethyl-1-hexanol around the glass transition by thermally stimulated depolarization currents. *The Journal of Chemical Physics*, 142(21):214504, 2015. 143

[345] S Arrese-Igor, A Alegría, and J Colmenero. On the non-exponentiality of the dielectric Debye-like relaxation of monoalcohols. *The Journal of Chemical Physics*, 146(11):114502, 2017. 143

[346] R A Munson and M E Lazarus. The Influence of Ionic Solutes upon the Conductivity of Molten Phosphoric Acid. *Journal of Physical Chemistry*, 71(10):3245–&, 1967. 143, 149

[347] Periklis Papadopoulos, Wilhelm Kossack, and Friedrich Kremer. Intra- and inter-molecular dynamics in glass-forming liquids. *Soft Matter*, 9(5):1600–1603, 2013. 145

[348] C. Perchard and A. Novak. Far-Infrared Spectra and Hydrogen-Bond Frequencies of Imidazole. *The Journal of Chemical Physics*, 48(7):3079–3084, 1968. 145, 148

[349] John T Reilly, Arun Thomas, Aileen R Gibson, Chi Y Luebehusen, and Marc D Donohue. Analysis of the Self-Association of Aliphatic Alcohols Using Fourier Transform Infrared

(FT-IR) Spectroscopy. *Industrial & Engineering Chemistry Research*, 52(40):14456–14462, 2013. 145

[350] Wycliffe Kiprop Kipnusu, Wilhelm Kossack, Ciprian Iacob, Philipp Zeigermann, Malgorzata Jasiurkowska, Joshua Rume Sangoro, Rustem Valiullin, and Friedrich Kremer. The interplay between inter- and intra-molecular dynamics in a series of alkylcitrates. *Soft Matter*, 9(18):4681–4686, 2013. 145

[351] Koichi Fumino, Alexander Wulf, and Ralf Ludwig. The Cation–Anion Interaction in Ionic Liquids Probed by Far-Infrared Spectroscopy. *Angewandte Chemie International Edition*, 47(20):3830–3834, 2008. 145

[352] K Fumino, K Wittler, and R Ludwig. The Anion Dependence of the Interaction Strength between Ions in Imidazolium-Based Ionic Liquids Probed by Far-Infrared Spectroscopy. *Journal of Physical Chemistry B*, 116(31):9507–9511, 2012. 145

[353] Wiktor Tatara, Marek J Wójcik, Jan Lindgrin, and Michael Probst. Theoretical study of structures, energies, and vibrational spectra of the imidazole-imidazolium system. *Journal of Physical Chemistry A*, 107(39):7828–7831, 2003. 145, 148

[354] Marek J Wójcik, Jacek Kwiendacz, Marek Boczar, Łukasz Boda, and Yukihiro Ozaki. Theoretical and spectroscopic study of hydrogen bond vibrations in imidazole and its deuterated derivative. *Chemical Physics*, 372(1):72–81, 2010. 145, 148

[355] Koji Hasegawa, Taka-aki Ono, and Takumi Noguchi. Vibrational spectra and ab initio DFT calculations of 4-methylimidazole and its different protonation forms: Infrared and raman markers of the protonation state of a histidine side chain. *Journal of Physical Chemistry B*, 104(17):4253–4265, 2000. 145, 148

[356] M Majoube, P Millié, and G Vergoten. Vibrational spectra of 4-methylimidazole-assignments of modes and calculation of raman and resonance raman intensities at the ab-initio 6-31G level. *Journal of Molecular Structure*, 344(1-2):21–36, 1995. 145, 148

[357] F Billes, H Endrédi, and G Jalsovszky. Vibrational spectroscopy of diazoles. *Journal of Molecular Structure: THEOCHEM*, 465(2):157–172, 1999. 145, 148

[358] Seulki Lee, Seung Jun Lee, Ahreum Ahn, Yusic Kim, Ahreum Min, Myong Yong Choi, and Roger E. Miller. Infrared Spectroscopy of Imidazole Trimer in Helium Nanodroplets: Free NH Stretch Mode. *Bulletin of the Korean Chemical Society*, 32(3):885–888, 2011. 145

[359] Anne B McCoy. The Role of Electrical Anharmonicity in the Association Band in the Water Spectrum. *The Journal of Physical Chemistry B*, 118(28):8286–8294, 2014. 146

[360] Pramod Kumar Verma, Achintya Kundu, Matthew S Puretz, Charvanaa Dhoonmoon, Oriana S Chegwidden, Casey H Londergan, and Minhaeng Cho. The Bend+Libration Combination Band Is an Intrinsic, Collective, and Strongly Solute-Dependent Reporter on the Hydrogen Bonding Network of Liquid Water. *The Journal of Physical Chemistry B*, 122(9):2587–2599, 2017. 146, 148

[361] Sergio Giuffrida, Grazia Cottone, and Lorenzo Cordone. The water association band as a marker of hydrogen bonds in trehalose amorphous matrices. *Physical Chemistry Chemical Physics*, 19(6):4251–4265, 2017. 146, 148

[362] Sergio Giuffrida, Grazia Cottone, Fabio Librizzi, and Lorenzo Cordone. Coupling between the Thermal Evolution of the Heme Pocket and the External Matrix Structure in Trehalose Coated Carboxymyoglobin. *The Journal of Physical Chemistry B*, 107(47):13211–13217, 2003. 146, 148

[363] D H Bonsor, B Borah, R L Dean, and J L Wood. Complex hydrogen-bonded cations - imidazole-imidazolium complex cation. *Canadian Journal of Chemistry-Revue Canadienne De Chimie*, 54(15):2458–2464, 1976. 148

[364] Gautam R Desiraju. A Bond by Any Other Name. *Angewandte Chemie International Edition*, 50(1):52–59, 2011. 152

[365] Marcus F Brackeen, Jeffrey A Stafford, Paul L Feldman, and Donald S Karanewsky. An efficient and mild synthesis of highly substituted imidazoles. *Tetrahedron Letters*, 35(11):1635–1638, 1994. 154

Vita

Tyler is originally from the Shores Community of Giles County, Tennessee. He graduated from Tennessee Technological University with a B.S. in Chemical Engineering (Magna Cum Laude) in the Spring of 2013. In the summer of 2012 and 2013 he participated in the Technology Internship Program(TIP) at SABIC Innovative Plastics in Mount Vernon, IN. While there he worked in the bisphenol A (BPA) production plant developing a spray drying apparatus designed to more effectively separate the BPA product from excess phenol. He started the PhD program at the University of Tennessee in the Fall of 2013 and quickly joined the soft materials research group of Dr. Joshua Sangoro. After completing his PhD, he will begin a postdoctoral position at the US Naval Academy with Prof. Paul Trulove. There he will continue to investigate structure/property relationships in soft materials with a particular emphasis on ionic liquids and their application in the processing of natural fibers.